Borate polyanion-based systems as Li- and Mg-ion cathode materials

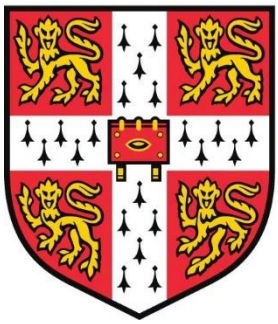

Hugh F. J. Glass

Department of Physics
University of Cambridge

This dissertation is submitted for the degree of

Doctor of Philosophy

Girton College

May 2017

Declaration

This dissertation is the result of my own work and includes nothing which is the outcome of work done in collaboration except as declared in the Preface and specified in the text.

It is not substantially the same as any that I have submitted, or, is being concurrently submitted for a degree or diploma or other qualification at the University of Cambridge or any other University or similar institution except as declared in the Preface and specified in the text. I further state that no substantial part of my dissertation has already been submitted, or, is being concurrently submitted for any such degree, diploma or other qualification at the University of Cambridge or any other University or similar institution except as declared in the Preface and specified in the text

It does not exceed the prescribed word limit for the relevant Degree Committee.

Acknowledgments

I am very grateful to Dr. Siân Dutton for giving me the opportunity to work in the Quantum Matter group, and for all she has taught me over the last few years. Also to Professor Clare Grey for her invaluable scientific contribution to a project I have thoroughly enjoyed. I have been lucky enough to work in two fantastic research groups, and would particularly like to thank members of Team-Mg: Zigeng Liu for teaching me electrochemistry and running the NMR experiments, Professor Dominic Wright and Evan Keyzer for providing the Mg-ion electrolytes and help with electrochemical set ups, and Jeongjae Lee for his calculations which made interpretation of the NMR possible. Also, to Paromita Mukherjee for her help during the neutron diffraction experiments at the ILL, Michael Gaultois for running the XANES experiments, and to the whole of the QM and Grey groups for providing such an enjoyable environment to work in.

I would like to thank all those involved in the NanoDTC for providing so many opportunities to learn and develop new skills throughout my time at Cambridge. I would also like to thank the EPSRC Cambridge NanoDTC, EP/G037221/1, and The Winton Programme for the Physics of Sustainability for providing financial support to the project.

Outside of Cambridge I have collected data from the neutron diffraction facility at the ILL, Grenoble, and the Diamond Light Source, neither of which would have been possible without the support and patience of the local contacts, Emma Suard and Giannantonio Cibin. Thanks also to Shou-Hang Bo who provided the BVS calculation software and helped with the synthesis of borates during his visit to Cambridge.

And finally, to my parents Richard and Hester for their continual support, and Sophie, without whose love and encouragement this would not have been possible.

Abstract

The aim of this thesis is to investigate pyroborates, $M_2B_2O_5$, and orthoborates, $M_3(BO_3)_2$, where M = Mg, Mn, Co, or Ni, as high capacity and high voltage Li- and Mg-ion cathode materials.

We explore the layered orthoborates, $M_3(BO_3)_2$, which, to our knowledge, have not been previously considered as Li- or Mg-ion cathodes, perhaps due to the lack of Li analogues. Structural analysis shows that mixed metal orthoborates form a solid solution, with preferential site occupancy of the Mg and transition metal driven by the presence of directional *d* orbitals. Electrochemical studies show that Mg can be removed from the structure and replaced with Li in a ~1:1 ion ratio. In the Mg-rich $Mg_2Mn(BO_3)_2$ 0.86 Mg^{2+} can be removed, giving a capacity of 209.9 mAh g^{-1}. To balance the 2-electron process Mn^{2+} is oxidised to Mn^{4+}, which is evident by two distinct features in the electrochemistry. Up to 1 Li^+ replaces each Mg^{2+} ion removed on cycling vs. a Li anode. The capacities of $MgMn_2(BO_3)$ and $Mg_2Co(BO_3)_2$, however, are limited by the amount of Mg on site *M*1, the more mobile site as determined by bond valence sum calculations.

The pyroborates ($M_2B_2O_5$) are an unexplored family of borate polyanions, which offer higher theoretical capacities and voltage than Li$M$$BO_3$ due to their more condensed frameworks. There are no known Li-containing pyroborates, therefore we use electrochemical ion exchange, with the aim of replacing each Mg^{2+} with 2 Li^+, to form $Li_xMB_2O_5$. The stoichiometry can be varied to alter the redox couple utilised and the Mg available for removal. $Mg_xM_{2-x}B_2O_5$ has been synthesised for M = Mn, Co, Fe and Ni and all forms have been shown to form a solid solution with cation ordering over the two M sites. In $MgMnB_2O_5$ we have shown that Mg can be fully removed while retaining the pyroborate structure. Subsequently up to 1.1 Li^+ can be inserted giving discharge capacities of 240 mAh g^{-1} above 1.5 V. After 1000 cycles 1.8 Li^+ can be reversibly cycled giving a capacity of 314 mAh g^{-1}. The insertion of Li^+ has been confirmed by ^{7}Li NMR and the oxidation state changes in Mn have been investigated by SQUID magnetometry and XANES spectroscopy. Electrochemical studies in materials where M = Fe, Co, and Ni show high voltage plateaus (>3.5 V) but limited capacity at room temperature. Increased temperatures improve the cycling, with Co and Fe based compounds reaching full theoretical capacitiy (>200 mAh g^{-1}).

As Mg can be removed from the structure, the pyroborates could be of interest in Mg-ion batteries, which offer benefits in energy density, cost, and safety. Mg-ion battery research is still in its infancy, therefore here we develop methods to reliably test Mg-ion cathodes and electrolytes. The previously unstudied Mg-ion electrolyte salt $Mg(PF_6)_2$ is also shown to

support reversible Mg deposition on a variety of working electrodes, as well as Mg^{2+} intercalation into the Chevrel phase (Mo_6S_8). We demonstrate that despite significant side reactions, 0.5 Mg can be reversibly cycled in the $MgMnB_2O_5$ system in a full Mg-ion cell, giving capacities of ~150 mAh g^{-1}. Cyclic voltammetry in a 3-electrode cell shows reversible electrochemical reactions occur in $MgMnB_2O_5$ above 2.6 V, which is consistent with galvanostatic electrochemistry observed in both the Li- and Mg-ion coin cells. This shows that pyroborates are a promising family of materials for high capacity, high voltage Mg-ion cathodes.

This study demonstrates that the pyroborates and orthoborates are good candidates for Li- and Mg-ion cathode materials, with the light-weight structure leading to high specific capacities. The ability to replace Mg for Li in polyanion materials without disrupting the crystal structure opens a new way to search for novel, high energy density, Li-ion cathodes.

List of Publications

Chapter 4 contains material from the publication:

Glass, H. F. J.; Liu, Z.; Bayley, P. M.; Suard, E.; Bo, S.-H.; Khalifah, P. G.; Grey, C. P.; Dutton, S. E. $Mg_xMn_{2-x}B_2O_5$ Pyroborates ($2/3 \leq x \leq 4/3$): High Capacity and High Rate Cathodes for Li-Ion Batteries. *Chem. Mater.* **2017**, *29*, 3118–3125.

Chapter 6 contains material from the publication:

Keyzer, E. N.; **Glass, H. F. J.**; Liu, Z.; Bayley, P. M.; Dutton, S. E.; Grey, C. P.; Wright, D. S. $Mg(PF_6)_2$-Based Electrolyte Systems: Understanding Electrolyte-Electrode Interactions for the Development of Mg-Ion Batteries. *J. Am. Chem. Soc.* **2016**, *138*, 8682–8685.

Publications not included in this thesis:

Liu, Z.; Lee, J.; Xiang, G.; **Glass, H. F. J.**; Keyzer, E. N.; Dutton, S. E.; Grey, C. P. Insights into the Electrochemical Performances of Bi Anodes for Mg Ion Batteries Using ^{25}Mg Solid State NMR Spectroscopy. *Chem. Commun.* **2017**, *53*, 743–746.

King, T. C.; Matthews, P. D.; **Glass, H. F. J.**; Cormack, J. A.; Holgado, J. P.; Leskes, M.; Griffin, J. M.; Scherman, O. A.; Barker, P. D.; Grey, C. P.; Dutton, S. E.; Lambert, R. M.; Tustin, G.; Alavi, A.; Wright, D. S. Theory and Practice: Bulk Synthesis of C_3B and Its H_2- and Li-Storage Capacity. *Angew. Chem. Int. Ed. Engl.* **2015**, *54*, 5919–5923.

Matthews, P. D.; King, T. C.; **Glass, H. F. J.**; Magusin, P. C. M. M.; Tustin, G. J.; Brown, P. A. C.; Cormack, J. A.; García-Rodríguez, R.; Leskes, M.; Dutton, S. E.; Barker, P. D.; Grosche, F. M.; Alavi, A.; Grey, C. P.; Wright, D. S. Synthesis and Extensive Characterisation of Phosphorus Doped Graphite. *RSC Adv.* **2016**, *6*, 62140-62145.

Jellicoe, T. C.; Richter, J. M.; **Glass, H. F. J.**; Tabachnyk, M.; Brady, R.; Dutton, S. E.; Rao, A.; Friend, R. H.; Credgington, D.; Greenham, N. C.; Böhm, M. L. Synthesis and Optical Properties of Lead-Free Cesium Tin Halide Perovskite Nanocrystals. *J. Am. Chem. Soc.* **2016**, *138*, 2941-2944.

Amigues, A. M.; **Glass, H. F. J.**; Dutton, S. E. $LiMnTiO_4$ with the $Na_{0.44}MnO_2$ Structure as a Positive Electrode for Lithium-Ion Batteries. *J. Electrochem. Soc.* **2016** 163 (3), A396-A400.

Zhao, B.; Abdi-Jalebi, M.; Tabachnyk, M.; **Glass, H. F. J.**; Kamboj, V. S.; Nie, W.; Pearson, A. J.; Puttisong, Y.; Godel, K. C.; Beere, H. E.; Ritchie, D. A.; Mohite, A. D.; Dutton, S. E.; Friend, R. H.; Sadhanala, A. High Open-Circuit Voltages in Tin-Rich Low-Bandgap Perovskite-Based Planar Heterojunction Photovoltaics. *Adv. Mater.* **2016,** 29, 1604744-1604752.

Contents

List of Abbreviations

ACN	Acetonitrile
BVS	Bond valence sum
CIF	Crystallographic information file
CSA	Chemical shift anisotropy
CV	Cyclic voltammetry
DMC	Dimethyl carbonate
EC	Ethylene carbonate
EXAFS	Extended X-ray absorption fine structure
GITT	Galvanostatic intermittent titration technique
LSV	Linear sweep voltammetry
MACC	Magnesium aluminium chloride complex
MAS NMR	Magic angle spinning nuclear magnetic resonance
OCV	Open circuit voltage
PND	Powder neutron diffraction
PXRD	Powder X-ray diffraction
SEM	Scanning electron microscopy
SQUID	Super conducting quantum interference device
TFSI	Bis(trifluoromethane)sulfonimide
THF	Tetrahydrofuran
TM	Transition metal
XANES	X-ray absorption near edge structure

Chapter 1. Introduction

1.1 Background

The desire to decrease the reliance on fossil fuels as an energy source (due to dwindling resources and fears over environmental and health impacts) means that new forms of energy production and storage are required. Renewable energy sources such as wind or solar could eventually replace, or at least complement, other forms of production, however they are intermittent; energy production is not always possible at the times it is needed.[1] Therefore, efficient and large scale energy storage systems are required to level out the load.

Replacement of fossil fuels in vehicles is another burgeoning area, with hybrid car sales having taken off in the last few years (although the first hybrid was built in 1909!)[2] and a number of governments announcing national targets for the introduction of all-electric vehicles, which are fast becoming competitive against combustion engines both in terms of cost and range.[3] The recent surge in electric vehicle market share is largely driven by cost, with Lithium ion (Li-ion) battery prices having been cut by ¼ since 2008.[4] However, to cement electric vehicles as the best option for all vehicle types further improvements in energy density (and therefore range), power, charging time, lifetime, and safety are required.

The recent advances in Li-ion technology have also allowed for widespread adoption of portable electronics. Yet the continual advance of technology and consumer demands for functionality put an ever-increasing strain on the Li-ion batteries that power them. Continual improvements in power, energy density and safety are required to keep up with the changes in technology.

1.2 How batteries work

Batteries are simple in concept, so their slow development compared to other areas of technology is initially surprising. The difficulties in development come from a lack of suitable materials and complexities in understanding and controlling the reactions between them which deviate from the simple, idealised model.[5]

Secondary (rechargeable) batteries rely on the movement of a working ion between two electrodes, through an ionic conductor, to produce a current in an external circuit. The principal components are the cathode, anode and electrolyte-soaked separator. Figure 1-1 shows how these components are arranged to produce a rechargeable battery in a typical Li-ion cell. When the electrodes are connected electrons flow spontaneously from the anode to the cathode (from

the higher chemical potential to lower chemical potential electrode), Figure 1-2.[6] Simultaneously, Li-ions move through the electrolyte and are reduced at the cathode, while electrons are forced around the external circuit to balance the charge, providing useful energy. On charge, lithium ions are forced to migrate from the cathode to the anode due to an applied electrical potential (greater than the voltage produced by spontaneous discharge), with the oxidized cathode providing electrons to the circuit while the anode receives electrons to reduce lithium ions from the electrolyte. A typical Li-ion cell is based on those produced by Sony in 1990 and uses a graphitic intercalation anode, $LiCoO_2$ layered intercalation cathode and $LiPF_6$ in ethylene carbonate/dimethyl carbonate electrolyte.[7] The half-cell reactions and overall reaction for this cell are given in Equation 1, Equation 2 and Equation 3.

Anode: $$C + xLi^+ + xe^- \leftrightarrow Li_xC$$ Equation 1

Cathode: $$LiCoO_2 \leftrightarrow Li_{1-x}CoO_2 + xLi^+ + xe^-$$ Equation 2

Overall: $$LiCoO_2 + C \leftrightarrow Li_{1-x}CoO_2 + Li_xC$$ Equation 3

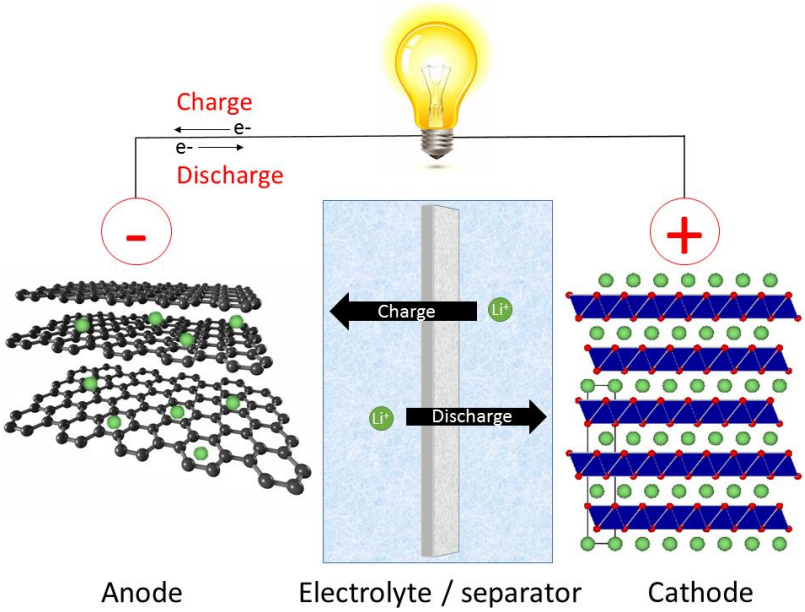

Figure 1-1: Illustration of a typical Li-ion battery system. Here both the anode and cathode are intercalation materials. The difference in chemical potential between the electrodes results in a voltage across the cell.

The difference in chemical potentials between the two electrodes dictates the open circuit voltage of the cell, V_{oc}, Equation 4, Figure 1-2.

$$V_{oc} = \frac{(\mu_A - \mu_C)}{e} \qquad \text{Equation 4}$$

Where e is the charge on an electron and μ_A and μ_C are the chemical potential of the anode and cathode respectively. The voltage on discharge, V_{dis}, is lower than V_{oc} as there is impedance (η) to the movement of cations in the cell at current, I_{dis}, Equation 5.

$$V_{dis} = V_{oc} - \eta_{dis} I_{dis} \qquad \text{Equation 5}$$

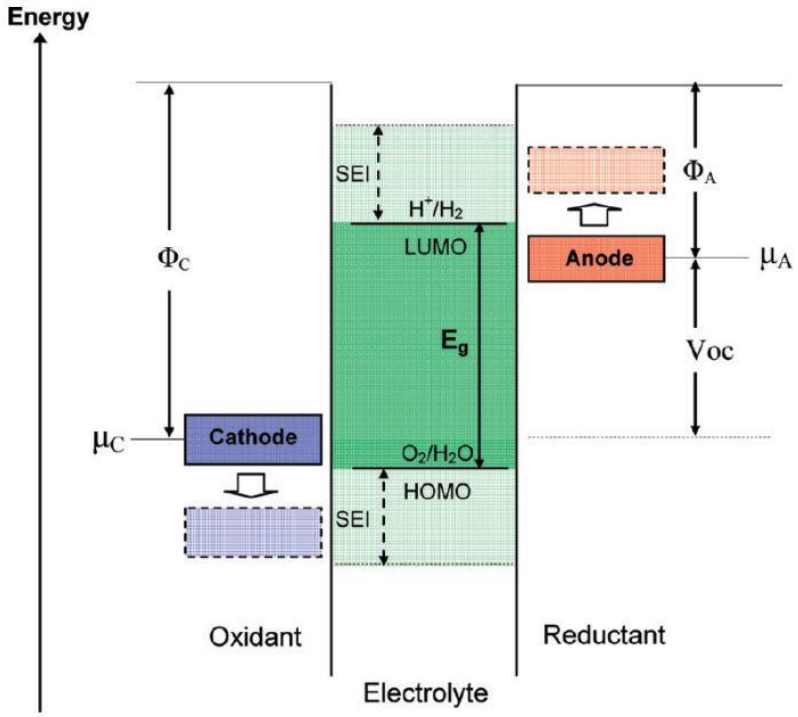

Figure 1-2: Energy diagram of a typical battery comprising of a cathode and anode, separated by an electrolyte. Φ_c and Φ_a are the work functions of the cathode and anode. $E_g$is the stability window of the electrolyte. μ_c and μ_a are the chemical potentials of the cathode and anode. If $\mu_c <$ HOMO or $\mu_a >$ LUMO a surface electrolyte interphase (SEI) is required to stabilise the system. In most Li-ion systems an anode SEI layer is required. Figure from Goodenough and Kim.[6]

The theoretical capacity, Q, of a cell is the amount of charge per unit mass (specific) or volume (volumetric) that can be transferred across the cell. For a given electrode the theoretical specific capacity can be calculated by Equation 6.

$$Q = \frac{\Delta x \times F \times 1000}{M_w \times 3600} \qquad \text{Equation 6}$$

Where Δx is the number electrons transferred, F is the Faraday constant and M_w is the molecular weight. The constants 1000 and 3600 give the capacity in units of mAh g^{-1} (as the Faraday constant has units of sA mol^{-1}). The actual capacity achieved during discharge is the amount of charge transported around the cell and is therefore the product of the current, *I*, and the time taken to complete the reaction.[8]

The energy that a battery can deliver is the product of the voltage on discharge and the capacity per unit mass or volume. Therefore, to increase the energy stored in a cell the potential difference between the electrodes can be increased (increased V_{dis}), or the mass/volume per electron transferred can be reduced (increased Q). Both of these can be achieved by manipulating the chemistry of the electrodes, hence the drive to develop new cathode materials.

Another important property of modern cells is power, or the rate at which energy can be extracted from a cell. This is measured in watts and is the product of the discharge voltage and the current drawn from the cell. The power of a cell is a property of both cell design and an intrinsic property of the electrode material, and can therefore be improved by altering the chemistry of the active materials used. The same properties dictate the rate of charge, C, where a rate of C/t takes t hours to charge. Equation 7 is used to calculate the current required, *I*, to fully charge a mass of active material, m, with capacity Q in a given time, t.

$$I = \frac{Q \times m}{t} \qquad \text{Equation 7}$$

1.3 Intercalation cathodes

Intercalation materials are compounds where a guest ion is mobile between sites within a host network, and where the guest ions can be removed while maintaining the host framework. Ideally they would be electronically as well as ionically conducting, however, most are poor electronic conductors so a conductive additive such as carbon black is often added.[9] On addition or removal of the guest ion the host often undergoes significant volume expansion or contraction. To accommodate the volume change, a polymeric binder is used to produce a cathode film that maintains particle connectivity and therefore conductivity. For an

intercalation material to be considered a good candidate for a cathode it should have certain characteristics, including:

- A low Fermi energy – achieved by high oxidation state transition metal or the inductive effect.
- Allow reversible intercalation of large quantities of the working ion.
- Form stable or metastable structures throughout the range of ion (de)intercalation.
- Undergo no side reactions, *i.e.* be chemically stable to the electrolyte and other battery components.
- Be electronically conductive (can be improved by forming composites with carbon).
- Be low cost - use inexpensive and abundant starting materials and low energy synthesis.

1.3.1 Intercalation mechanisms

So far we have described the cathode materials as intercalation hosts, where an ion can move into and out of a structure, while maintaining the original framework. However, in reality there are several types of intercalation mechanisms that can occur, two-phase (or solid solution) and single-phase transformations, Figure 1-3.

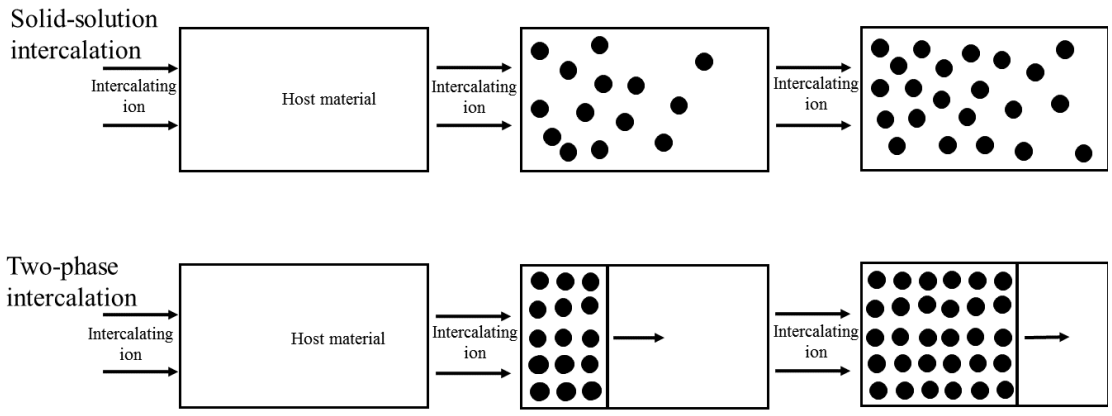

Figure 1-3. Simplified schematics of solid-solution and two-phase intercalation mechanisms.

If intercalation causes a modification to the host structure, forming a new, ordered phase, then insertion can progress with a moving interface separating two phases in a single particle. Therefore, a particle will contain two distinct phases (A and B) with composition, 1-yA + yB. If there are several different sites with varying energies, insertion will usually occur in one site first, followed by other, higher energy sites, when the concentration of guest ions or the applied potential is high enough. As the composition of the original material is not changing as intercalation proceeds, the reaction occurs with a constant potential for each transformation.

The nucleation of a new phase within a particle has an energy penalty associated with the interface, which is compensated for by a decrease in the volume free energy as the particle grows, and is eventually overcome at a critical radius, r^*, Figure 1-4.[10] The nucleation energy leads to an activation barrier which can reduce capacity retention at high cycle rates and cause a large overpotential at the start of charge/discharge.[11]

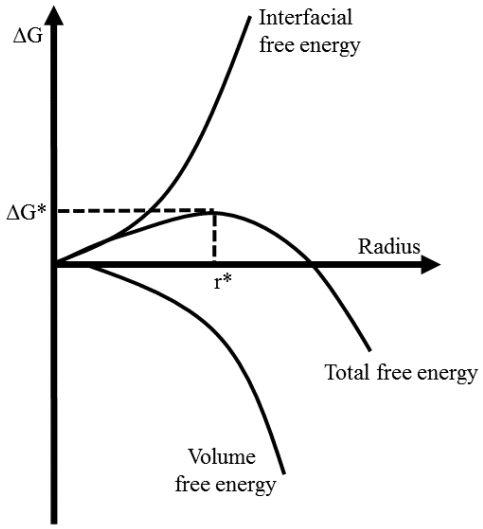

Figure 1-4 Total free energy of nucleation, ΔG, where the energy penalty of the interface is overcome by the volume free energy at a critical particle radius, r*. Adapted from Porter *et al.*[10]

A solid-solution transformation is when a material has a composition gradient, or variable stoichiometry, throughout a crystal. This occurs when the guest ion randomly occupies sites in the host, gradually filling all sites as guest concentration increases, so a particle consists of a single phase of $A_{1-y}B_y$, Figure 1-3.[9] As the composition changes gradually so must the potential, therefore solid solutions have a constantly varying potential on (de)intercalation (discharge/charge). As single-phase transformations do not involve nucleation and crystal growth they generally have lower activation barriers and therefore can handle higher rates of charge and discharge. However, the sloping voltage response leads to a loss of energy compared to a two-phase reaction with the same initial voltage.

1.4 Li-ion batteries

1.4.1 Advantages and limitations

Research into using lithium as the working ion in a battery began in the 1950's with Li_xTiS_2 layered materials, as the Li^+ ion has low equivalent weight and high redox potential (3.04 V vs. the standard hydrogen electrode (SHE)). These early cathode materials were stable over wide ranges of *x* and showed good reversibility, but side reactions occurred at low voltages limiting cell life.[12] It was later realised that oxide materials had similar structures to the sulphides yet were lighter and cycled at higher voltages, and therefore could do more useful work.[13] The first commercial Li-ion battery was released by Sony in 1991 containing a $LiCoO_2$ cathode with a carbon anode. Due to its unrivalled energy density this technology quickly surpassed competing systems, and derivatives of this chemistry remain the battery of choice for the majority of uses today.[14] Although this breakthrough in materials science lead to the portable electronics revolution, and the re-emergence of electric vehicles there are still many improvements in energy density, safety and cost that can, and need, to be made if batteries are to power future technological advancements.

The main limitations for current Li-ion cells include:

1. The energy density; current state of the art cells have just $1/10^{th}$ the energy density of gasoline.
2. Safety concerns; Co and the electrolyte solvents are toxic, and dendrite formation leads to short circuits.
3. Cost; cathodes constitute ~12% of total battery price and cobalt is significantly more expensive than other transition metals.[15]

A huge body of research has been dedicated to improving cathode materials since the 1990's, and a description of the most common cathodes and their properties is given below.

1.4.2 Layered Li-ion cathode materials

$LiCoO_2$ is the most common of the $LiMO_2$ family of layered rock salt cathode materials (*M* = Co, Mn, Ni, Mg, Al *etc.*). These contain close-packed arrays of oxygen with *M* occupying half the octahedral sites, Figure 1-5. The CoO_2 sheets provide a framework for reversible Li-ion insertion into octahedral sites forming the O3-type layered structure. The two dimensional layers of octahedrally coordinated Li allow reversible (de)intercalation of up to 50% of the ions while retaining a stable structure, at an electrode potential of 3.6 V vs. Li/Li^+.[13] The transition metal undergoes redox reactions as Li is (de)intercalated, by providing or removing electrons from the external circuit to maintain charge balance, and it is the high lithium chemical potential

associated with the $Co^{3+/4+}$ couple that leads to high cell voltages. The theoretical capacity of Li_xCoO_2 is 280 mAh g^{-1} for complete removal of Li, however at deep charge ($x < 0.5$) the material is structurally unstable and forms the spinel Co_3O_4, via the loss of O_2. Therefore, the practical capacity is ~140 mAh g^{-1} with $0.5 \leq x \leq 1$. $Li_{0.5}CoO_2$ represents the charged state of the material, whereupon discharge the material accepts electrons from the external circuit and so is reduced to $LiCoO_2$.

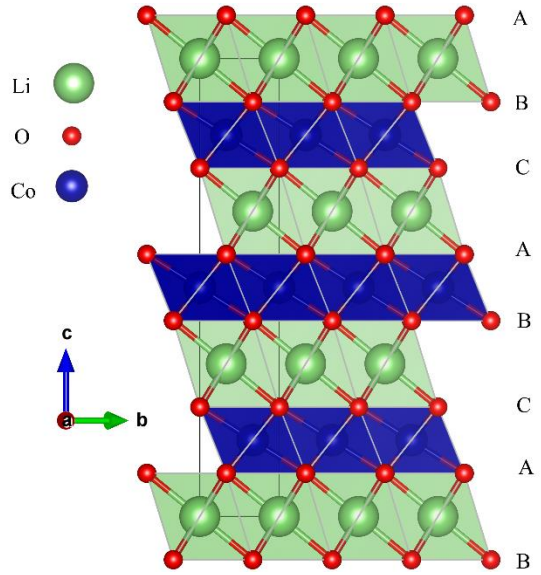

Figure 1-5: Rhombohedral structure of $LiCoO_2$. Co octahedra shown in blue, Li octahedra in green and the oxygen stacking is indicated by A, B and C.

As previously stated the use of Co is not ideal due to concerns over cost and safety, as well as structural instability limiting capacity and cycle life. Therefore, replacing the Co with cheaper and safer transition metals, or using non-transition metal ions to improve structural stability has been a productive area of research. For example, the addition of Ni and Mn to form $LiNi_{1-y-z}Mn_yCo_zO_2$ (NMC) leads to increased stability and power as the presence of Mn^{4+} and utilisation of $Ni^{2+/4+}$ reduces reliance on $Co^{3+/4+}$ at high delithiation. The cell voltage is also increased to 3.8 V vs. Li and capacity to 160 mAh g^{-1}. $LiNi_{1-y-z}Co_yAl_zO_2$ (NCA) uses the $Ni^{3+/4+}$ redox couple so also has a higher voltage than the pure Co version, while the Al helps increase both stability and capacity (180 mAh g^{-1}). Both have been successfully commercialised as lower cost and higher power alternatives to $LiCoO_2$.[16]

1.4.3 Manganese spinel Li-ion cathode materials

Lithium manganese spinel, $LiMn_2O_4$, is not a layered material and yet displays good Li-ion conduction through channels in the MnO_2 framework, leading to high power cells, Figure 1-6.[17] The structure is cubic with a close packed O^{2-} lattice and octahedrally coordinated Mn, as in the layered structures, however the Li environment differs. Whereas in the layered structure Li occupies octahedral sites for all stages of intercalation ($0 \leq x \leq 1$), in the spinel $Li_xMn_2O_4$ (where $0 \leq x \leq 2$), Li is tetrahedrally coordinated when $x < 1$ and octahedrally coordinated when $x > 1$. This change in environment leads to the observed voltage plateau dropping from 4 V to 3 V during discharge.[18] In practice cycling is limited to between Mn_2O_4 and $LiMn_2O_4$ ($x \leq 1$), the higher voltage process which utilises the three-dimensional tetrahedral Li network, and has a capacity of 148 mAh g^{-1}. The sensitivity of voltage to small changes in chemistry is displayed even within this narrow region of intercalation. Within the higher voltage process ($x < 1$) a small step is seen when $x = 0.5$ due to ordering of the lithium vacancies, forming a stable phase with a subtly different chemical potential to the parent phase.

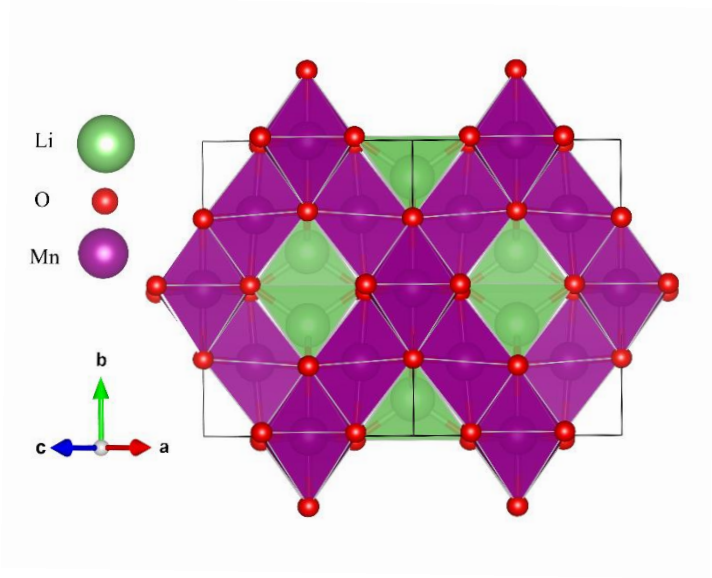

Figure 1-6 Structure of $LiMn_2O_4$ showing Li diffusion channels with Mn in the centre of purple octahedra, and Li in the green tetrahedra.

The spinel is attractive for transportation and grid-scale technologies due to its low cost and desirable safety attributes. However, it suffers from poor rate capability due to slow ionic diffusion and serious capacity fade over extended cycling due to Mn dissolution and structural changes at high Li content.[19] The structural changes occur as on lithiation Mn^{4+} (d^3 ion) are reduced to Mn^{3+} (d^4 ion), (the final product is more correctly written $LiMn^{3+}Mn^{4+}O_4$), leading to Jahn-Teller distortion of the manganese octahedra.[20] Further increasing the Li content causes

a greater proportion of the Mn to become Jahn-Teller distorted, eventually leading to a cooperative Jahn-Teller distortion which causes significant changes in lattice parameters and a cubic to tetragonal phase change. This eventually results in structural failure of the particles and disproportionation to Mn^{2+} and Mn^{4+}. The Mn^{2+} is soluble in the organic electrolyte and is therefore leached from the material.[17,18,21]

1.4.4 Polyanion cathode materials

Although the layered and spinel oxides have enjoyed obvious success, their instability at deep charge and after many cycles limits their practical capacity. The instability partly arises from the use of highly oxidised redox couples such as $Co^{3+/4+}$ and $Mn^{3+/4+}$, which offer cell voltages around 4.0 V. Therefore, when Padhi *et al.* showed full Li extraction from a phospho-olivine material ($LiFePO_4$) it was suggested that polyanion cathodes could achieve similar, or higher, voltages than the oxides using more stable, lower-valence redox couples.[22,23] Since the original publication in 1997 LiMPO$_4$ (M = Co, Fe, Mn) have attracted much interest for their high voltages as well as their improved cycle life, high rates, low cost, and non-toxic nature.[24–26] Other polyanion systems with the general formula LiM_b(XO$_a$) where M = transition metal and X = P, B, Si, S have also been explored as the strong covalent bonds in XO$_a$ lead to more stable compounds than the oxides.

1.4.5 Phosphate polyanions

1.4.5.1 LiMPO$_4$

The orthorhombic $LiFePO_4$ consists of PO_4^{3-} units with strong covalent bonds between the P^{5+} and oxygen ions, and chains of FeO_6 octahedra, Figure 1-7. Li migration occurs through one-dimensional channels in the *b*-direction and full removal of the Li gives a theoretical capacity of 170 mAh g^{-1} at a voltage of 3.5 V. The redox couple of $Fe^{2+/3+}$ would normally result in a low voltage (1.5 V in $Li_xFe_2O_3$)[27] and therefore low energy cells, however the presence of electronegative groups lowers the redox couple through the inductive effect, therefore increasing the cell voltage compared to oxide analogues. This effect is related both to the amount of covalency between the groups (higher covalency = higher voltage) and the local environments around the transition metal.[6,28] Figure 1-8 shows how the $Fe^{3+/2+}$ couple varies with a range of phosphate polyanions. A recent publication by Ceder *et al.*[29] calculated the theoretical voltage for a huge range of potential polyanions, and showed that in the vast majority of cases the polyanions based on P, Si, B or S had higher voltages than their oxide counterparts.

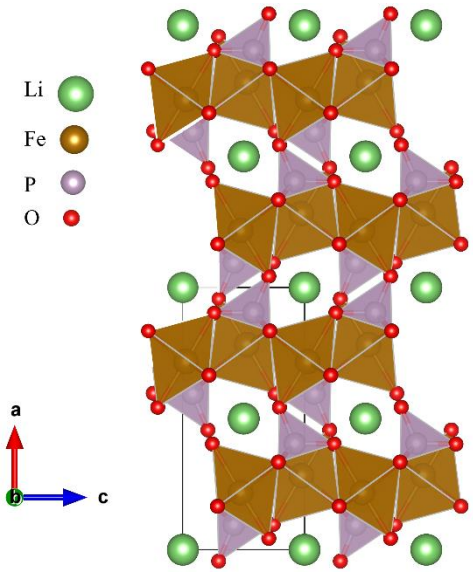

Figure 1-7 Structure of $LiFePO_4$ demonstrating Li channels between layers of FeO_6 octahedra connected by PO_4 tetrahedra.

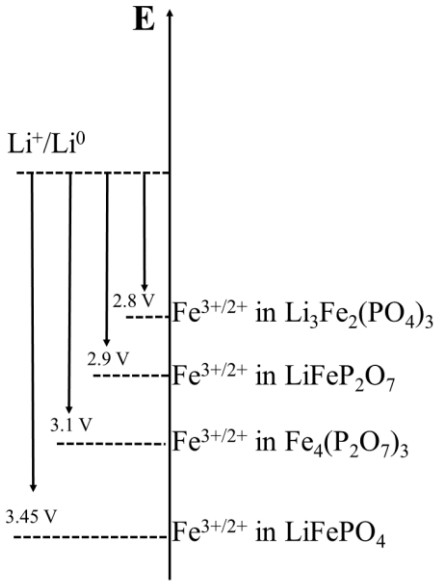

Figure 1-8 Position of the Fe^{3+}/Fe^{2+} redox couple relative to lithium in different polyanion phosphates. Adapted from Goodenough and Kim.[6]

Diffusion of Li^+ through one dimensional channels is thought to be more sluggish than through layers, and the presence of anti-site defects (Li on an Fe site or Fe on a Li site) blocks these channels, further hindering diffusion.[30] The (de)intercalation rate is also reduced by the PO_4 units rendering the material inherently electronically insulating, as they remove *M*-*M* or *M*-O-*M* connectivity. These limitations can be mitigated by nano-sizing which shortens Li diffusion pathways, and forming carbon composites which increase electronic conductivity.[31,32] The relatively low voltage, and therefore decreased energy density of the Fe based phosphate resulted in research into Mn, Co and Ni olivines, raising the operating voltage to 4.1 V, 4.8 V

and 5.0 V vs. Li respectively, and therefore offer much higher energy densities.[26,33,34] However, all three have considerably worse electrochemical performance, associated with reduced electronic conductivity. Therefore, research switched to solid solutions containing a mix of transition metals to optimise properties with the general structure $LiM_xM'_{1-x}PO_4$. By combining Co and Fe or Mn and Fe the electrochemical properties can be manipulated to give higher voltages and better structural stability than the non-substituted parent phases.[35,36] It is also possible to substitute non-transition metal ions such as Mg on the Fe site, and this has been shown to improve structural stability and reduce antisite defects, therefore significantly improving ionic diffusion and cycle life, at the expense of capacity.[37]

1.4.5.2 Alternate phosphate polyanions

The Li*M*PO_4 family of materials are attractive as they are more stable and therefore safer than the oxides and provide good specific capacities. However, the need for nanosizing reduces volumetric capacities, restricting their use to applications where volume is not an issue. These limitations and the need for ever increasing capacity have led to the investigation of a wide variety of polyanions.

Polyanions that can cycle multiple Li per unit cell have been a keen area of investigation with the pyrophosphates ($Li_2MP_2O_7$) and $Li_3Mo_4P_5O_{24}$ being proposed as promising candidates.[38,39] Both display higher voltages than the corresponding olivine compounds (3.5 V and 3.8 V vs. Li respectively) but not all the Li can be removed from the structures and the heavier polyanion frameworks lead to reduced capacities (110 mAh g^{-1} and 113 mAh g^{-1}). The cabanophosphate $Na_3MnPO_4CO_3$ displays two-electron cycling in a Na-ion cell, utilising the $Mn^{2+/3+}$ and $Mn^{3+/4+}$ redox couples to give capacities ~125 mAh g^{-1}.[40]

The Tavorite structure, Li*M*(*Z*O_4)*X* where *M* is a transition metal, *Z* is P, Si or S and *X* is commonly O, OH or F, contains linear chains of corner-sharing *M*O_4X_2 octahedra linked by *Z*O_4 tetrahedra, forming a three-dimensional network of Li-conduction channels.[41] This family of materials can offer high capacities and high voltages, especially when F is the *X* atom, as this raises the voltage even further, exemplified by $LiVPO_4F$ with a capacity of 156 mAh g^{-1} at 4.2 V.[42]

1.4.6 Borate polyanions

As polyanions introduce inactive mass it is beneficial to try and reduce the weight while maintaining the benefits of stability and the inductive effect. The BO_3^{3-} borate is the lightest polyanion group and therefore gives high theoretical capacities ($LiFePO_4$ = 170 mAh g^{-1}, $LiFeBO_3$ = 220 mAh g^{-1}, ~3 V vs. Li).[43] The strength of the inductive effect of this lightweight

framework sits between the silicates and phosphates (PO_4 > BO_3 > SiO_4) and leads to much higher voltages than the simple oxides, which, when combined with high capacities leads to high energy densities. For example, the calculated voltages for the $Mn^{2+/3+}$ redox couple in $LiMnSO_4$, $LiMnBO_3$ and $LiMnPO_4$ are 3.0 V, 3.7 V and 4.8 V vs. Li respectively.[28] Li*M*BO_3 where *M* = Mn, Co and Fe have been studied, and although initial electrochemical performance was poor (removal of ~0.2 Li per unit cell),[44] subsequent research has steadily improved the reversible capacity to around 100% of theoretical.[37,43–46] This has been achieved through nano-sizing, careful construction of cathode films to avoid oxidation ($Fe^{2+/3+}$ in particular) and forming mixed metal phases such as $LiMn_xCo_yBO_3$ and $LiFe_{0.5}Co_{0.5}BO_3$ which combine the good electrochemical performance of Mn and Fe phases with the high voltages of Co.[47,48] Good cycle life at high voltages, especially for the Mn and Fe borates, means there is continued interest in these systems.

As with the phosphates there are a range of borate frameworks, with *M*BO_3 being analogous to the *M*PO_4 with the same *M*:polyanion-cation ratio. The pyroborates ($M_2B_2O_5$), however, have not been studied as battery cathodes previously, presumably because the Li analogue cannot be synthesised directly, and as *M* is in a 2+ oxidation state Li cannot be directly intercalated into the material without reduction to unusual oxidation states. Unlike the pyrophosphates, where the heavier $P_2O_7^{4-}$ group compromises the overall capacity,[39] the lighter boron atom (and fewer oxygen atoms) means that a move from borates to pyroborates does not compromise the theoretical capacity.

1.4.7 The Anode

The voltage difference between the cathode and anode should be maximized in order to boost power output from the cell. Therefore the ideal anode for a Li-ion battery would be lithium metal, but due to dendrite formation and consumption of the electrolyte this is not a viable option. Instead, graphitic carbon is used as Li_xC_6 is formed at low voltages vs. Li/Li^+. Even when using a graphitic anode, expensive copper current collectors must be used as Li forms an alloy with stainless steel at low potentials. The specific capacity of carbon is 372 mAh g^{-1}, far lower than the ideal 3860 mAh g^{-1} of pure lithium metal, but greater than any cathode currently on the market. Therefore, at present, cathode technologies limit Li-ion battery capacity.[49]

1.4.8 Electrolytes

Good electrolytes are ionically conductive but electronically insulating and have a band gap large enough that the redox energies of the electrodes do not cause reaction with the electrolyte. It is, in some cases, possible to have redox energies outside of the electrolyte band gap by formation of a stabilising surface/electrolyte interphase (SEI), Figure 1-2. This layer on the

electrode is electronically insulating and inhibits further reaction between electrode and electrolyte, but allows Li ion diffusion so the charge and discharge processes are not inhibited. After many cycles (often thousands) the battery capacity fades due to loss of Li to the SEI, though this is a minor side effect of avoiding complete degradation early in the battery's life.[50] The electrolyte is usually a lithium salt dissolved in an appropriately stable solvent, most commonly $LiPF_6$ in a carbonate solvent.[12]

1.5 Beyond Li-ion batteries

Much of the research carried out since Sony released the first commercial Li-ion battery in 1991 has focused on improving this technology, be it capacity, charge rates, safety or operating voltage. The impressive progress achieved leaves Li-ion technologies with little room for improvement meaning new battery systems are required if performance is to continue increasing. New technologies aim to become viable for use in larger applications such as electric vehicles or grid storage, while being cheaper and safer to manufacture than Li-ion based cells. Alternatives to Li-ion include Mg-ion, Na-ion, Li-S and Li-air batteries. Each provides its own set of benefits and comes with different obstacles which must be understood and overcome before any commercial success can be achieved.

1.5.1 Alloying compounds: Li-S and Li-Si

Sulphur has a very high theoretical capacity for Li insertion, 1675 mAh g^{-1} forming Li_2S, and is very abundant, therefore low cost, making it a promising candidate for the next generation of batteries. Nevertheless, there are significant limitations; the low working voltage (2.1 V vs. Li) and low density lead to poor energy densities, while inherently low conductivity, an 80% volume expansion and dissolution of intermediate reaction products limits cell lifetimes and coulombic efficiency.[42,51] Much research has been dedicated to overcoming these difficulties. Encapsulating sulphur in carbon or polymers limits dissolution and mitigates volume expansion.[52] Producing carbon nanocomposites with Li_2S improves conductivity and as the film is cast with the highest volume phase, film integrity is maintained on cycling.[53,54] The electrolyte can also be modified to prevent polysulphide dissolution by adding additives that form a stable SEI or using solid state electrolytes.[55]

Another well studied example is the alloying reaction with Si which achieves capacities of 8365 mAh cm^{-3} and 3590 mAh g^{-1} compared to 975 mAh cm^{-3} and 372 mAh g^{-1} for the commercialised graphitic anodes. The viability of its use is restricted by low electrical conductivity and large volume changes which occur on (de)lithiation, and cause significant capacity fade. The 300% expansion on lithiation causes instability in the SEI which therefore

reforms each cycle, consuming the electrolyte.[56] As with sulphur many studies have attempted to overcome these issues by using additives, forming composites, or nano-structuring.[57,58]

1.5.2 Na-ion

Na-ion cells offer little advantage over Li-ion in terms of electrochemical performance. The redox potential of sodium is slightly higher than that of lithium (Table 1-1) and it has the same charge but with greater weight, giving capacities which are at best equivalent to current Li-ion technology. The drive for commercialisation of Na-ion systems arises from their differing chemistries, leading to a number of practical advantages. Na^+ has a larger ionic radius than Li^+ which leads it adopt both the P2- and O3-layered oxide structures, where Na sits in either trigonal prismatic sites or octahedral sites between the transition metal layers, whereas Li always adopts the O3 structure. The P2 structure is less prone to structural transformation to the spinel phase than the O3, so capacity retention is greater.[59] Na does not form alloys with Al (unlike Li) therefore cheap Al current collectors, rather than Cu, can be used on both electrodes. Finally, Na itself is significantly cheaper than Li due to its natural abundance, further reducing manufacturing costs.[60]

Although the differing chemistry between Na and Li leads to improved performances in the layered oxides, with capacities of >200 mAh g^{-1} retained over hundreds of cycles, the Na-ion performance in high voltage cathodes is limited. The polyanion structures that have good electrochemical performance with Li have low (<100 mAh g^{-1}) reversible capacities and low voltage (< 3 V vs. Na) in Na-ion systems. There are also problems at the anode as Na does not intercalate into graphite, so hard carbons or low voltage intercalation compounds such as $Na_2Ti_3O_7$ are used, further reducing the operating voltage of the cell.[51,60,61]

1.5.3 Conversion cathodes

All commercialised Li cells are based on intercalation materials, however metal oxide electrodes that react with Li via conversion reactions offer capacities up to 5 times those of current electrodes and often use cheap, environmentally friendly materials.[62] Unlike intercalation materials, on (de)lithiation the material undergoes a significant structural change, with the general formula:

$$M_aX_b + (b\times n)\mathrm{Li} \leftrightarrow aM + b\mathrm{Li}_nX$$

Where M is a transition metal, X is an anion (usually O, S) and n is the oxidation state of X.

This transformation involves complete reduction of the metal and formation of a new lithium compound, leading to very high capacities. However, the energy required to reverse the reaction can be significant, leading to voltage hysteresis and therefore reduced energy density. This is mitigated when the resulting product is nano-particulate, with very high surface areas and the subsequent reactivity being key to a reversible reaction. The voltage at which transformation occurs is reliant on both the transition metal redox chemistry and the anion present, with voltages ranging from 0.2 V vs. Li for Cr_2O_3 (1166 mAh g^{-1})[63] to 3.55 V vs. Li for CuF_2 (~528 mAh g^{-1})[64] so very high capacity cells using both conversion anode and cathode can be envisioned.

Conversion reactions in polyanions have also been investigated, with the layered borate $Cu_3^{2+}(BO_3)_2$ reacting with up to 6 Li per unit cell to form Cu^0 with a capacity >600 mAh g^{-1} on first discharge. With normal film preparation and cell conditions this capacity fades very quickly, with the first charge achieving just half this capacity (after full discharge), forming a Cu^{1+} compound with less than 50 mAh g^{-1} reversible capacity after just 10 cycles. The use of 65% conductive carbon in cathode films greatly improves capacity retention by improving the electrical conductivity. This makes oxidation back to Cu^{2+} possible and capacities over 400 mAh g^{-1} are achieved after 10 cycles.[65]

1.5.4 Multivalent working ions

The continual progress of Li-ion intercalation materials has shown that electrochemical performance is limited primarily by how well the crystal structure withstands insertion/removal of ions and the intrinsic redox properties (number of electrons transferable and the voltage at which this occurs). Therefore, a breakthrough in performance could be achieved by developing materials that can accommodate multiple ions, or electron, transfer.

Multivalent cations, such as Mg^{2+}, Ca^{2+}, Zn^{2+} and Al^{3+} can transfer multiple electrons per ion, therefore fewer ions need to be moved across the cell to achieve a given capacity. This potentially offers a large increase in energy density over the monovalent Li- or Na-ion technologies. The insertion of a single multivalent cation may also reduce the volume expansion compared to insertion of multiple Li ions, therefore material stability may be improved. Additionally, the ability to use the less reactive metals as anodes (Mg, Ca, Zn or Al) means reduced weight, volume and expense in comparison to Li-ion cells, which require carbon anodes and copper current collectors. Although the energy density is predicted to be higher for the multivalent ions, their redox potentials, and therefore predicted voltages, are lower than Li, Table 1-1.[66,67]

Table 1-1 Comparison of univalent and multivalent standard electrode potentials and theoretical anode capacities.

Ion	Standard Electrode Potential (V)	Theoretical Capacity	
		Specific Capacity (mAh g^{-1})	Volumetric Capacity (mAh cm^{-3})
Li^+	-3.05	3829	2044
Na^+	-2.71	1165	1128
Mg^{2+}	-2.36	2234	3882
Ca^{2+}	-2.87	1337	2073
Zn^{2+}	-0.76	820	5854
Al^{3+}	-1.66	2980	8046

1.6 Mg-ion

Mg-ion primary (single use) batteries have been well understood and commercialised for many years. They are low voltage aqueous cells used primarily as emergency power sources as they can be stored indefinitely "dry" and when required salt water is added as the electrolyte. The first non-aqueous rechargeable batteries were postulated by Gregory *et al.* in 1990, where they demonstrated reversible magnesium plating from organo-magnesium compounds, however, these electrolytes were incompatible with the binary oxides and sulphides tested.[68] It was not until 2000 when Aurbach *et al.* demonstrated reversible Mg intercalation into the Chevrel phase, Mo_6S_8, that research into rechargeable Mg-ion batteries really took off.[69]

Secondary Mg-ion batteries, although still in their infancy, have a number of potential advantages over lithium. The bivalent Mg^{2+} ion leads to high theoretical capacities, with a volumetric capacity nearly double that of Li. Mg is inexpensive and abundant; Mg is 2,000 times more abundant in the earth's crust than Li and $1/25^{th}$ of the cost. Mg can also be used as the anode as extended cycling does not lead to dendrite formation, therefore cells could be produced which are safer and have higher energy densities.[70] Although the redox potential of Mg is higher than that of Li (-2.36 compared to -3.05), it is sufficiently negative such that with the right cathode, high voltage cells can be envisioned.

As magnesium forms a divalent working ion its chemistry is quite different to that of lithium and therefore it is not necessarily possible to infer what will make a good Mg-ion battery cathode from analysis of Li-ion literature. Some of the differences and potential difficulties of switching from Li to Mg include:

1. An inherently lower voltage (by ~0.73 V), hence the need to look at transition metal oxide or polyanion based materials.
2. The 2+ ion may hinder diffusion, be more likely to become trapped in defects and have slower kinetics.
3. Mg has differing preferences for coordination site (Mg has a preference for octahedral coordination, while Li sits in either tetrahedral or octahedral sites), which affects the structures adopted and the diffusion of the ions.[71,72] For example, in the Li-ion cathode Li_2MnSiO_4, where magnesium doping is used to stabilise the monoclinic structure, magnesium occupies the transition metal site, not the lithium site, to form $Li_2Mn_{1-x}Mg_xSiO_4$.[73]
4. The change in valence shifts the stoichiometry of the materials formed *e.g.* $Mg_aM_bO_c$ rather than $Li_{2a}M_bO_c$ (*M* = transition metal) if the oxidation state of the transition metal remains the same. The oxidation state of the transition metal could be tuned so as to give greater capacity. For example, replacing Li_2 with Mg_2 by reducing the transition metal oxidation state, giving 4 electrons per unit rather than 2.
5. Current electrolytes are not well understood and significant side reactions occur that limit battery capacity, voltage window, and cell life.[74,75]

1.6.1 Rechargeable cathodes

The motivation for focusing on novel Mg-ion cathodes is that those published so far have been limited to capacities below 200 mAh g^{-1} over a limited number of cycles, and voltages below 2.0 V vs. Mg, and are therefore not currently competitive against Li-ion technologies. A summary of the intercalation materials investigated in the literature is given at the end of the section, Table 1-2.

1.6.1.1 The Chevrel phase

The Chevrel phase, Mo_6S_8, was initially demonstrated using a halo-alkyl aluminate complex in ether solvents (now known as the Grignard based electrolyte, as synthesis involves mixing R_2Mg with a $AlCl_{3-n}R_n$ Lewis acid) and achieved capacities of around 70 mAh g^{-1} up to 1.3 V vs. Mg, maintained over 2000 cycles. The rhombohedral crystal structure of Mo_6S_8 is formed of Mo_6S_8 blocks with cubic cavities between them, Figure 1-9a. These cavities contain 6 tetrahedral sites which the Mg^{2+} ion can occupy, however electrostatic repulsion limits insertion to 1 Mg per cavity. The theoretical capacity of the Chevrel phase is 122 mAh g^{-1}, significantly more than was originally achieved, with the limiting factor thought to be sluggish diffusion and charge trapping of the high charge/radius ratio Mg^{2+} in low energy sites caused by slight distortions in the structure. Two plateaus are observed in the electrochemistry relating to

insertion of Mg^{2+} into these tetrahedral sites. The first Mg insertion (to form $MgMo_6S_8$) randomly occupies a tetrahedral site in one cavity, with the second Mg^{2+} occupying an adjacent, higher energy, site.[76] Later studies demonstrated that substituting S with the more polarizable Se helps to stabilise the system and reduce charge trapping, leading to the full theoretical capacity being achieved, Figure 1-9b.[76,77] Cycling at elevated temperatures also improves the achieved capacity in the unsubstituted Mo_6S_8 due to increased diffusion kinetics of Mg^{2+}.

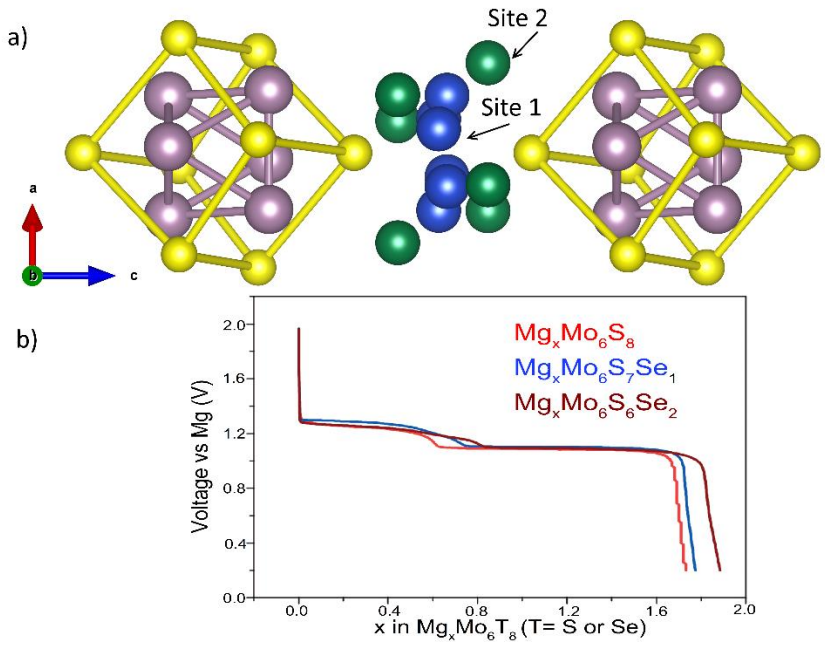

Figure 1-9. a) Mo_6S_8 clusters and the two tetrahedral intercalation sites formed between them. S atoms are displayed in yellow, and Mo atoms in pink. b) Electrochemistry of nanoparticulate $Mo_6S_{8-y}Se_y$ from Aurbach *et al.*[77]

1.6.1.2 Layered oxides and sulphides

Subsequent studies have aimed at investigating Mg-ion (de)intercalation in higher voltage cathodes, primarily oxides with a few of the well-studied Li polyanions also explored. The layered oxide V_2O_5 has received particular attention and has demonstrated good reversible capacity at high voltage (up to 250 mAh g^{-1} at ~3.0 V vs. Mg).[78] However, a large activation barrier to diffusion limits the charge rates and results in high overpotentials. The layered structure consists of both edge and corner sharing VO_5 square pyramids with a corner sharing tetrahedral cation insertion site. A tetrahedral site could be thought to be beneficial for Mg^{2+} diffusion as four coordinate sites are not the preferred site, and therefore diffusion barriers are lower than when occupying octahedral sites. However, the diffusion pathway takes the cation through a high energy three-coordinated face, leading to a >1.3 eV activation energy (the Li^+ activation energy in the same material is 0.2 eV).[72] Compare this to the Chevrel phase where

both the stable and intermediate site are tetrahedral, and good Mg^{2+} mobility is observed, though this is also aided by the increased polarizability of S over O.

It has been shown that using thin films, carbon composites or nano-sizing V_2O_5 can improve rate capability and capacity retention by reducing Mg^{2+} diffusion distances.[79,80] It has also been suggested that reversible intercalation is only possible with water present in the electrolyte. There is debate as to the role water plays and whether it is intercalated with the Mg^{2+} or that solvation by water aids (de)solvation of Mg^{2+} from the electrolyte.[81–83] Increasing the water content was shown to improve the achieved capacity for the first few cycles but leads to severe capacity fade, and recent characterisation of the intercalated phase suggests H^+ ions may be contributing the high capacities observed.[81] The need for water in an electrolyte is a major disadvantage as it prohibits the use of a Mg metal anode due passivation of the surface.

The use of amorphous aerogels of V_2O_5 to increase the interlayer spacing significantly improves rate capability and reduces the overpotential, but again the presence of water hinders practical application.[84,85] The ability to expand the interlayer spacing of layered materials by exfoliation or ion exchange has led to improved Mg^{2+} diffusing in both MoS_2 and MoO_2, with capacities of ~70 mAh g^{-1} at 0.7 V and ~150 mAh g^{-1} at 3 V vs. Mg respectively, double that achieved with the same materials prepared in the standard way.[83,86–88]

1.6.1.3 Spinel $MgMn_2O_4$

The spinels with general formula M_2O_4 where M = Mn, Co and Ni have been shown to intercalate Mg^{2+} with open circuit potentials >3 V vs. Mg and theoretical capacities ~270 mAh g^{-1}, however due to the instability of electrolytes at the high voltages required for cycling full electrochemical testing is inconclusive.[89–91] The effect of water (and therefore protons) present in the electrolyte is also not fully understood, with "wet" electrolytes giving capacities up to 150 mAh g^{-1} while dry electrolytes lead to significantly lower capacities (30 mAh g^{-1}).[91,92] The reversibility of Mg intercalation into the tetrahedral sites of Mn_2O_4 has been confirmed by ^{25}Mg NMR where vacancies were created by acid leaching in $LiMn_2O_4$, followed by electrochemical insertion of Mg^{2+} from an aqueous electrolyte to form $MgMn_2O_4$, utilising the $Mn^{3+/4+}$ redox couple.[92] The use of MMn_2O_4 (M = Li, Ag, K) as the starting material is important as this cubic spinel exhibits less cation disorder than the tetragonal spinel formed by $MgMn_2O_4$ (induced by Mn^{3+} Jahn-Teller distortions and the similarity in size of Mg^{2+} and Mn^{2+}).[93] Cation disorder leads to slower ion mobility and Mn disproportionation to Mn^{2+} and Mn^{4+} which reduces the structural integrity of the crystal.[91] The high capacity and high voltage of the spinels, coupled with the use of a Mg anode could lead to energy densities that exceed all currently available commercial cells.

1.6.1.4 Polyanions

Along with spinels, the olivine type materials are the highest voltage Mg-ion cathodes studied so far. As in Li-ion batteries the polyanion framework offers increased voltages and stability that should aid energy densities and cycle life. One of the most promising of these is the orthorhombic manganese silicate $MgMnSiO_4$ which, when nano-sized via ball milling or sol-gel synthesis can reach capacities of up to 244 mAh g^{-1} with two discharge plateaus at 1.55 V and 1.05 V vs. Mg. The two plateaus are attributed to two distinct cation octahedral sites, over which Mg and Mn are randomly distributed. The analogous $MgFeSiO_4$ also exhibits promising electrochemical properties with 125 mAh g^{-1} achieved with plateaus at 1.6 V and 1.2 V vs. Mg, with 91.4% capacity retention after 20 cycles and a similar voltage profile to the Mn version.[94] Electrochemical ion exchange from Li_2FeSiO_4 and cycling at 55 ˚C leads to much higher capacities (up to 300 mAh g^{-1}) with a discharge voltage ~2.4 V vs. Mg.[95] The Co analogue, $MgCoSiO_4$ has been synthesised with a mesoporous structure that results in capacities approaching 300 mAh g^{-1} with discharge plateaus at 1.7 V and 1.1 V vs. Mg.[96] It is worth noting that the ratio of these plateaus is quite different from the Mn and Fe versions, with much less capacity from the lower voltage plateau in the Co version. This could be attributed to a greater degree of cation ordering, where the Co and Mg are not randomly distributed over the two sites, instead *M*1 is 66% Co, 33% Mg and *M*2 33% Co, 66% Mg.[97]

Bond valence sum calculations, which have been used to explore ion transport in cathode materials (detail on the method can be found in Chapter 2), suggest the pyroborate $Mg_{2/3}Fe_{4/3}B_2O_5$ may be another polyanion in which the Mg is mobile and is therefore a promising cathode candidate.[98] There are also some structural similarities with the silicates, where Mg and the transition metal are both disordered over two octahedral sites, with the Co displaying greater ordering than Mn or Ni. This is further discussed in Chapter 4 and Chapter 5.

Table 1-2. Comparison of the capacity and voltage achieved for various Mg^{2+} intercalation cathodes investigated in the literature. Cells were cycled at room temperature unless otherwise stated.

Cathode material	Capacity achieved (Theoretical capacity) (mAh g^{-1})	Voltage vs. Mg (V)	Notes	References
Mo_6S_8	70 (128 forming $MgMo_6S_8$)	1.1	>2000 cycles. Full capacity achieved when cycling at 60 °C).	69
Layered - TiS_2	20 (260 forming $MgTiSe_2$)	< 0.75	Cycled at 60 °C. Significant capacity fade.	99,100
Spinel – TiS_2	200 (260 forming $MgTiSe_2$)	1.2	Using the All-Phenyl Complex electrolyte. 90 mAh g^{-1} when using $Mg(AlCl_2 BuEt)_2$ electrolyte.	101
Layered - MoS_2	70 (168 forming $MgMoS_2$)	0.7	Significant capacity fade.	102,103
$TiSe_2$	108 (260.5 forming $MgTiSe_2$)	1.0		104
WSe_2	203 (157.2 forming $MgWSe_2$)	1.6	Requires nanowires for appreciable capacity. $Mg_{0.67}WSe_2$ is formed, giving 105 mAh g^{-1}; it is unclear how the extra capacity arises.	105
Layered MoO_3	200 (372 forming $MgMoO_3$)	2.25	Only partially reversible, dependent on nanostructure. "Wet" electrolytes give greatest capacities so proton intercalation may play a role.	78
Ortho-V_2O_5	130 as a powder, 250 as a gel (295 forming MgV_2O_5)	~3.0	Poor diffusion kinetics, aided by formation of gels (aero- or xero-) or high temperatures.	78,106
α-MnO_2	~100 (308 forming $Mg_{0.5}MnO_2$)	<2.25	Tunnel structure. Significant capacity loss due to conversion to MgO and Mn^{2+}dissolutions.	83,107
δ-MnO_2 (Birnessite)	Up to 230 (308 forming $Mg_{0.5}MnO_2$)	~2.8	Capacity achieved dependent on electrolyte. "Wet" electrolytes give greater capacities, proton involvement demonstrated.	86,87
Mn_2O_4	150 in aqueous electrolytes, 35 in non-aqueous (308 forming $MgMn_2O_4$)	2.5 – 3.0	Significant capacities only achieved in aqueous electrolytes. Mg intercalation proven even in aqueous system.	91,92
$Mg_xMn_8O_{16}$	180 (154 forming $Mg_2Mn_8O_{16}$)	2.7	α-MnO_2 structure synthesised containing Ag or K.	93
$FeSiO_4$	330 (362 forming $MgFeSiO_4$)	~2.5	Cell life of 5 cycle in non-aqueous electrolytes.	95
$MnSiO_4$	240 for sol-gel (364 forming $MgMnSiO_4$)	1.6 and 1.1	Low current densities used. 80 mAh g^{-1} as powder.	108
$FePO_4$	<12 (178 forming $Mg_{0.5}FePO_4$)	~1.9	DFT calculations indicate prohibitively high diffusion barrier.	89,109
$MgFePO_4F$	53 (138 forming$FePO_4F$)	2.6	Complete Mg/Fe cation mixing.	110

1.6.2 Anodes

One of the major benefits of using magnesium as the working ion is that Mg metal can be used as the anode, giving a significant enhancement to specific and volumetric densities over commercial Li-ion cells. By simply replacing the graphitic carbon currently used in Li-ion cells with Mg metal, the anode volumetric density is increased from 756 mAh cm^{-1} to 3833 mAh cm^{-1} and the gravimetric from 372 mAh g^{-1} to 2203 mAh g^{-1}.[111] Li metal anodes are used in laboratory cells but the risk of thermal runaway, fire and poor cycle life means use in commercial cells in not feasible. The switch to a Mg-metal anode is achievable primarily due to Mg plating forming far more uniform layers than Li plating. Uniform layers have lower surface area and therefore decreased reactivity with the electrolyte, which would normally reduce cycle life and increase the cell temperature. There is also the reduced risk of dendrites forming which can short circuit cells and leads to catastrophic failure of a cell. However, the full benefits of a Mg metal anode have not yet been achieved as developing an electrolyte that allows reversible stripping and plating which is also compatible with the Mg surface and current collectors (*i.e.* which is stable over a wide voltage range) has proved difficult.

The incompatibility of Mg metal with existing Mg-ion electrolytes has led to investigation of several anode alternatives. Sn (~900 mAh g^{-1}, 0.15 V vs. Mg) and Bi (~400 mAh g^{-1}, 0.2 V vs. Mg) have been investigated as alloying anodes with flat, low voltage plateaus, and $Li_4Ti_5O_{12}$ (175 mAh g^{-1}, below 1.5 V vs. Mg) as a highly reversible insertion anode with a higher, sloping, voltage response.[106,112,113] Mg^{2+} does not intercalate into graphite even though Mg intercalated carbons can be synthesised directly. However, by increasing the interlayer spacing from 3.35 Å to >5 Å through formation of a nano-porous carbon, intercalation of Mg is possible, though with a higher voltage than would be expected for crystalline graphite.[114]

1.6.3 Electrolytes

Despite the many advantages Mg-ion offers development has been limited, in part due to lack of suitable electrolytes hindering both cell construction and analysis of electrodes that require a stable electrolyte to operate in. Only a small number of electrolyte families display reversible Mg plating, and none are without compromises.

1.6.3.1 Grignard type

Early magnesium electrolytes were based on inorganic salts such as $Mg(ClO_4)_2$ or $Mg(BF_4)$ in carbonate solvents and displayed high initial current densities but very short cell lifetimes, due to passivation of the Mg anode with an insulating film.[115] As previously stated the development of Grignard based electrolyte such as $Mg(AlCl_{3-nR}R_n)$ in THF where R is C_2H_5 or C_4H_9 with anodic stability up to ~2.2 V vs. Mg and conductivity comparable to Li-ion electrolytes (a few

mS, dependent on the nature of *R* and concentration) allowed for the first demonstration of the Chevrel phase system.[69] This system was later optimised by using phenol *R* groups that avoid β-hydride elimination and extend the anodic stability to 3.3 V vs. Mg. However, the sensitivity to moisture and high overpotential for Mg deposition limits its practical application. The cathodic stability of this family of electrolytes is generally around -2 V vs. Mg which is well outside the normal operating voltage of an electrode.[75]

1.6.3.2 Aluminium complexes

The nature of the species formed in-situ and their role in reversible plating is complex and not well understood. The magnesium dimer, $[Mg_2Cl_3(THF)_6]^+$ has been crystallised from various Grignard type electrolytes suggesting that this may be the active species.[116] This led to several studies on chloride based complexes, one of the most used and studied of which is the magnesium aluminium chloride complex (MACC) which is prepared simply by dissolving $MgCl_2$ and $AlCl_3$ in tetrahydrofuran (THF). This electrolyte supports high efficiency reversible deposition and has anodic stability up to 3.4 V vs. Mg.[117] As with the Grignard electrolytes synthesis is relatively simple but the speciation is complex, exemplified by the fact that as-prepared MACC does not allow reversible deposition, and requires extended conditioning before the favourable properties emerge.[118] Conditioning involves cycling the electrolyte on a Pt working electrode above 0 V vs. Mg until the desired stripping and plating behaviour is achieved. During this process aluminium is deposited onto the working electrode until the Mg:Al ratio is 2.6:1, irrespective of the starting ratio. Switching to a fresh working electrode after conditioning has demonstrated that the enhancement of electrochemical properties is due to changes in the solution rather changes to the electrode surface.[118,119] Characterisation of the active species again shows a Mg dimer is involved, this time $[Mg_2(\mu\text{-}Cl)_3 \cdot 6THF]^+$ but also that the concentration of free Cl^- is increased. It is thought that although the dimer is the active electrochemical species the free Cl^- aids deposition by depassivating the Mg anode surface.[119] This hypothesis is supported by other work which shows that the addition of $MgCl_2$ to inorganic salt based electrolytes improves performance.[120,121]

1.6.3.3 Inorganic salts

The search for electrolytes that do not require formation of the dimer (and therefore the conditioning step) has led to a number of inorganic salts being studied with varying success. The Hauser base amines show good reversibility and stability towards sulphur compounds, but less so on oxide cathodes.[75] While borohydrides and carboranes display promising performance as halide free electrolytes with high anodic stabilities (2.5 - 3.2 V vs. Mg) with the carborane cluster $[1\text{-}(1,7\text{-}C_2B_{10}H_{11})]MgCl$ achieving high coulombic efficiency reversible deposition

(>98%) and high anodic stability (ca. 3.2 V vs. Mg). The use of halide free electrolytes is desirable in order to limit corrosion of the cell.[89,122]

Magnesium bis(trifluoromethane)sulfonimide or $Mg(TFSI)_2$ is another promising electrolyte, displaying high anodic stability (3.5 V vs. Mg) and efficient deposition of Mg. The electrochemical performance seems to be dependent on the solvent used, with glymes giving high efficiencies but high overpotentials and acetonitrile and THF having lower efficiencies and anodic stability but also lower overpotentials. The addition of $MgCl_2$ also has a large effect on conductivity, with a 2.5:1 $MgCl_2$:$Mg(TFSI)_2$ ratio having twice the conductivity of a 1:4 ratio at room temperature (5.8 S cm^{-1} compared to 2.9 S cm^{-1}).[89,123]

1.7 Aim

The aim of this thesis is to investigate the pyroborates, $M_2B_2O_5$, and orthoborates, $M_3(BO_3)_2$, where M = Mg, Mn, Co, Ni, as high capacity and high voltage Li- and Mg-ion cathode materials. The previous section has demonstrated the need for ever increasing energy density in Li-ion cells and the benefits that switching to a Mg working ion could afford. As has been discussed the pyroborates are an unexplored family of polyanions that can offer very high capacities due to the light weight framework and high voltages through the inductive effect. With just one previous report that suggests Mg may be mobile. Here we assess the structural changes when varying both the transition metal and Mg to transition metal ratio and explore the electrochemical performance in a Mg-ion cell and when electrochemically exchanging Mg for Li in a Li-ion cell. To our knowledge the layered orthoborates have not previously been considered for Li- or Mg-ion cells, perhaps due to the lack of Li analogues, however their light weight framework and layered structure mean they may be of interest. As with the pyroborates, their structure and electrochemistry are explored in this thesis. The development of methods to reliably test Mg-ion cathodes and electrolytes is also discussed, and the new $Mg(PF_6)_2$ based inorganic salt electrolyte is tested.

Chapter 2. Experimental Techniques

2.1 Solid state synthesis

2.1.1 Overview

All the materials studied as cathodes were synthesised via the high temperature solid state method, also known as ceramic synthesis. The method involves the direct reaction of precursors, often metal oxides, acetates or oxalates, at high temperatures. The precursors are accurately weighed, mixed and ground before being pressed into pellets. Grinding and pellet formation are required to ensure homogenous mixing and good contact between precursors.[124,125]

Temperatures up to 1050 °C are required to overcome the lattice energy and induce sufficient ion mobility to form the desired phase. These elevated temperatures often lead to thermal decomposition of the precursors and therefore gaseous products are released. Multiple milling and calcination steps at increasing temperatures are therefore required to complete the reaction.[126]

Varying the temperature and starting materials used gives control over the products formed, and controlling the atmosphere during reaction provides control of the oxidation states. The use of a graphite crucible is to further reduce the O_2 partial pressure around the reactants, as O_2 will react with the carbon to form CO_2, which then flows away from the point of reaction. Pellets can also be sealed in evacuated silica tubes to give an inert atmosphere; in this case precursors that do not give off thermal decomposition products are required. Heating and cooling rates can also affect the reaction. By varying the heating rate or using intermediate heating and regrinding steps different pre-reactions can occur, leading to differences in reactivity when the final reaction temperature is reached. Cooling very slowly (<1 ˚C min^{-1}) aids formation of the thermodynamic product, but can lead to formation of low temperature impurities. Cooling very quickly, known as quenching, can "freeze" the high temperature structure, but can lead to more disordered structures.

Due to the sustained high temperatures required and reliance on diffusion to give homogeneity, solid state reactions require a large input of energy and long reaction times (days to weeks). Undesirable phases can be formed and impurities can be introduced from the milling process or synthesis vessel. Despite this, solid state synthesis remains a very useful and convenient method due to the low cost and availability of precursors, as well as the control of conditions

afforded.

An alternative route that often requires lower temperatures and leads to smaller particle sizes are reactions in molten salts (or fluxes). These involve the use of a low melting point salt which can behave as a solvent or a sacrificial reactant. This is relevant for the synthesis of borate polyanions as boric acid, and the B_2O_3 formed after pre-heating, have low melting points and so act as a pseudo-flux in these reactions. This allows reduced reaction times and ensures sufficient mixing of the materials, reducing impurities.

2.1.2 Solid state synthesis of borates

The general scheme of borate synthesis will now be discussed, with detailed individual synthetic routes for each material studied given at the beginning of the chapter in which the material is discussed.

Synthesis of both the orthoborates ($M_3(BO_3)_2$) and pyroborates ($M_2B_2O_5$) where *M* can be Mg, Mn, Co, Ni, Fe or V, require a source of Mg, transition metal (*TM)*, B and O. The precursor source for Mg was either MgO or $Mg(CH_3COO)_2{\cdot}4H_2O$ (magnesium acetate). The acetate is more reactive, therefore affording faster reactions and fewer impurities, however, the amount of hydration is variable therefore accurate weighing is more difficult. MgO was used in the majority of reactions with magnesium acetate used where impurities were observed when synthesised with MgO. Transition metals precursors were oxalates (C_2O_4), *e.g.* $MnC_2O_4{\cdot}2H_2O$ (manganese oxalate dihydrate) or $CoC_2O_4{\cdot}2H_2O$ (cobalt oxalate dihydrate) with 2+ oxidation states. These were preferred over the binary oxides as fewer impurities were observed and significantly shorter reaction times were required. This is thought to be due to the lower decomposition temperature, allowing formation of reactive intermediates after pre-heating at low temperatures. Initially B_2O_3 (boron trioxide) was used as a source of B, however its hygroscopic nature and hardness led to difficulties in accurate weighing, therefore H_3BO_3 (boric acid) was used instead.

A typical synthesis involves weighing and mixing the above precursors in the desired ratio. The resultant fine powder is placed in an alumina crucible and heated at 3 ˚C min^{-1} to 450 ˚C in a Carbolite or Vecstar tube furnace or Lenton box furnace, where it is held for 10 hours. Pelletising the powder is not required as the boric acid dehydrates to form B_2O_3 which in turn melts at 450 ˚C, aiding mixing. During heating, water and CO_2 are evolved, causing an amorphous borate melt containing Mg and the *TM* to be formed on cooling.

The powder is then re-ground and heating is repeated with increasing temperatures (*e.g.* 650 and 850 ˚C for 10 hours) leading to increasing crystallisation of the borate product, visible in

the X-ray diffraction. The final heat at 1050 ˚C affords the final crystalline product. An example heating schedule is given in Figure 2-1.

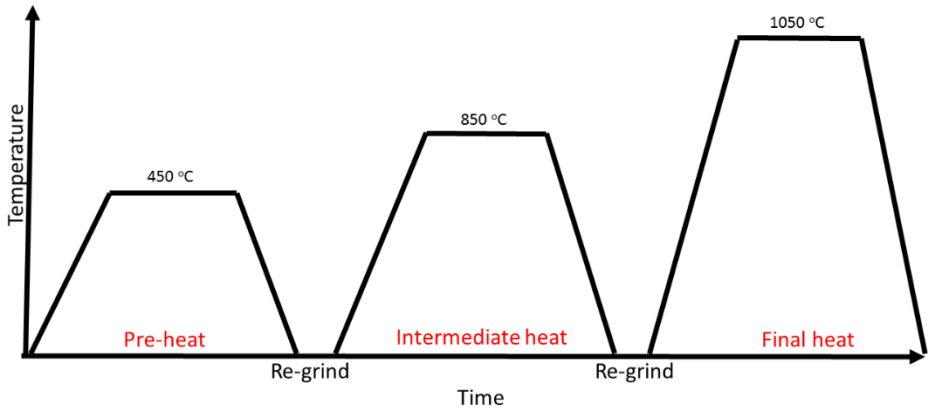

Figure 2-1. Example of a heating schedule for the synthesis of transition metal borates.

Where inert or reductive conditions were required, flowing argon or 5% H_2 in argon and/or a graphite crucible were used. A small piece of Mo metal was placed up-flow of the reactants to indicate if the furnace had remained free of O_2 throughout the reaction, and to ensure a sufficiently low O_2 partial pressure by removing O_2 from the gas (Mo metal will dull in the presence of O_2 at elevated temperatures).

2.2 Powder diffraction techniques

Diffraction experiments are used to gain insight into the bulk structure of crystals. They are used ubiquitously in the physical and biological sciences to aid structure determination of everything from proteins to unknown solids in geological samples.[127] The development of this technique, plus the introduction of the Rietveld method as a means for refining a model against diffraction data,[128] allows for accurate structural information to be obtained. Another important advantage of using powdered samples is that it is often the material's bulk properties that are of interest, and as diffraction data represents an average over the solid it is a powerful technique, especially when combined with other analytical tools.[129]

Both powder X-ray diffraction (PXRD) and powder neutron diffraction (PND) were used for this thesis and a description of the techniques and the refinement of collected data is given in the following sections.

2.2.1 Crystallography and diffraction

2.2.1.1 Crystals

Crystals are solids in which the atoms or molecules are regularly ordered. Each crystal is derived from a basic building block, known as the unit cell, which continuously repeats in three dimensions. To compare and contrast the myriad of different crystal structures it is necessary to categorize them. Auguste Bravais first did this in 1849 by showing that, so long as the unit cell was the simplest repeating unit and that they pack to fill all available space, there are only 7 possible unit cell shapes – known as the 7 crystal systems, detailed in Table 2-1. These are defined by their unit cell parameters; the distances a, b and c, and angles α, β and γ.[126,130]

As well as categorising unit cell shape, the distribution of points within the repeating units can also be defined, these are the four types of lattice:

- **Primitive (P)** Lattice point at each corner.
- **Body-centred (I)** Lattice point at each corner and one at the centre of the cell.
- **Face-centred (F)** Lattice point at each corner and one in the centre of each face.
- **Base-centred (A, B or C)** Lattice point at each corner and one in the centres of one pair of opposite faces (letter designation depends on which face is occupied, e.g. A-centred has lattice points on the *bc* face).

When these 7 permissible shapes are combined with the 4 types of lattice, 14 Bravais lattices are obtained, Table 2-1.

Table 2-1. The seven crystal systems and 4 lattice types combine to give 14 Bravais lattices. Listed with decreasing symmetry.

Crystal system	Unit cell	Lattice type
Cubic	$a = b = c$ $\alpha = \beta = \gamma = 90°$	P, I, F
Tetragonal	$a = b \neq c$ $\alpha = \beta = \gamma = 90°$	P, I
Orthorhombic	$a \neq b \neq c$ $\alpha = \beta = \gamma\ 90°$	P, C, I, F
Hexagonal	$a = b \neq c$ $\alpha = \beta = 90°, \gamma = 120°$	P
Trigonal	$a = b = c$ $\alpha = \beta, \gamma \neq 90° < 120°$	P
Monoclinic	$a \neq b \neq c$ $\alpha = \gamma = 90°, \beta > 90°$	P, C
Triclinic	$a \neq b \neq c$ $\alpha \neq \beta \neq \gamma \neq 90°$	P

The symmetry of a crystal is defined from a point at the centre of a perfect crystal. Only 32 point groups (geometric symmetries) are allowed, as the unit cells must stack exactly. When the 14 Bravais lattices are combined with the 32 internal crystal symmetries (point groups) 230 space groups are defined. These 230 crystal structures describe all the possible space filling patterns.

Within the lattices, families of parallel planes exist to which it is useful to refer. These are described by the 3 integers *h, k* and *l* and are termed Miller indices. The Miller indices are the reciprocal of the planes that intercept on the *a, b* or *c* axis. The perpendicular distance between these planes (interplanar spacing) is termed d_{hkl}.

2.2.2 Diffraction

Diffraction relies on the atomic planes in a crystal causing interference to incident radiation. The powdered sample is irradiated by an X-ray or neutron beam at varying angles using a goniometer. The beam penetrates the sample and is partially reflected by the lattice planes determined by their Miller indices, *hkl*. If the inter-atomic distance between two scattering points obeys Bragg's law (that is, when the difference in path length ($2d\sin\theta$) is equal to an integer number of wavelengths ($n\lambda$)) then constructive interference occurs, leading to intensity in the diffraction pattern, Equation 8.[131,132]

$$n\lambda = 2d_{hkl}\, sin\theta \qquad \text{Equation 8}$$

Where n is an integer, λ is the incident beam wavelength, d is the inter-atomic distance and θ is the angle between the incident beam and the scattering point on a crystallographic plane, Figure 2-2.[126]

Therefore, for a beam of constant λ, diffraction is only observed for the discrete angles that satisfy Bragg's law. The lattice parameters of a cell can be calculated by relation to the interplanar spacing, d_{hkl}. For example, in a cubic system d_{hkl} can be calculated by Equation 9. This relationship differs for each crystal system.

$$d_{hkl} = \frac{a}{\sqrt{(h^2+k^2+l^2)}} \qquad \text{Equation 9}$$

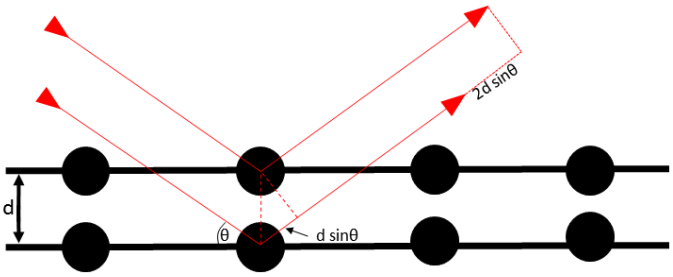

Figure 2-2. Depiction of Bragg's Law. The incident radiation reflects off lattice points, with the path length difference equalling $2d\sin\theta$. If the extra distance travelled by the lower beam is equal to an integer number of wavelengths, constructive interference occurs. This is Bragg's law, Equation 8.

The position of allowed peaks in the diffraction pattern are those that satisfy Bragg's law, however, not all allowed reflections will give rise to observed intensity. In cells more complex than primitive, where lattice points sit on sites other than the cell corners, destructive interference can occur between identical objects related by intra-cell translation, leading to out of phase scattering at certain Bragg angles. This results in some of the reflections predicted by Bragg's law not being observed in the diffraction pattern. The selection rules that define systematic absences for the different Bravais lattices are given in Table 2-2.

Table 2-2. Selection rules for the Bravais lattices.

Bravais lattice	**Allowed reflections**	**Forbidden reflections**
Primitive cubic	Any *h*, *k*, *l*	None
Body centred	$h + k + l$ = even	$h + k + l$ = odd
Face centred	*h*, *k*, *l* all odd or all even	*h*, *k*, *l* mixed odd and even
Hexagonal	All others	$h + 2k \neq 3n$

The position of peaks in the diffraction pattern are related to the size and symmetry of the unit cell, but their intensities relate to the type and distribution of the scattering matter, *i.e.* different atoms, ions or molecules. The intensity of each peak is described by Equation 10.

$$I_{hkl} = |F_{hkl}|^2 \times M_{hkl} \times LP(\theta) \qquad \text{Equation 10}$$

Where I_{hkl} is peak intensity, F_{hkl} is the structure factor, M_{hkl} is the multiplicity, $LP(\theta)$ is the Lorentz geometric correction and polarization factor.

The structure factor, F_{hkl}, Equation 11, is dependent on both the position of each atom, and its scattering factor. The scattering factor depends on the nature of incident radiation and will be discussed in detail in the relevant diffraction section.

$$F_{hkl} = \sum_j f_j e^{2\pi i(hx_j + ky_j + lz_j)} \times e^{(-B\ sin^2\theta/\lambda^2)}$$ Equation 11

Where f_j is the scattering factor of the j^{th} atom, h k and l are its Miller indices, x_j, y_j and z_j are its fractional coordinates and B is an isotropic temperature factor = $8\pi^2\mu^2$ (units of Å^2), where μ^2 (often called U) is the root mean square displacement of the atom from its average position.

Therefore, by careful analysis of the intensities observed at Bragg reflections and the positions of these reflections, it is possible to determine the crystal symmetry, cell parameters, the atoms present and the lattice sites they occupy.

2.2.3 Comparison of diffraction techniques

Both X-rays and neutrons have wavelengths comparable with interplanar distances and are therefore scattered by crystalline material. Table 2-3 compares the wavelength and major contributor to the scattering factor for both types of radiation.

Table 2-3: Comparison of X-rays and neutrons in their use as diffraction radiation.

Radiation	**Typical wavelength λ**	**Scattered by**	**Structure factor variation**	**$\frac{sin\theta}{\lambda}$ dependence**
X-rays	0.5-2.5 Å	Electrons	$f_j \propto$ atomic number	Marked decrease in F_{hkl} with increasing $\frac{sin\theta}{\lambda}$
Neutrons	0.5-3 Å	Nuclei	No systematic variation with atomic number	F_{hkl} is not angle dependent

2.2.3.1 Powder X-ray diffraction (PXRD)

PXRD requires a source of monochromatic X-rays at the appropriate wavelength (typically 0.5-2.5 Å, similar to lattice spacings). The primary source for laboratory X-rays is via accelerated electrons hitting a metal target. An electrically heated filament, often tungsten, ejects electrons which are then accelerated in an electric field. The electrons strike the atoms in a target metal anode, causing ejection of electrons from the core orbitals. When outer electrons fall back to this lower energy, electromagnetic radiation of a specific wavelength is emitted (fluorescence). The frequency of this intense emission is characteristic of the anode material. When an electron is ejected from the core K shell (n = 1), it can be filled by electrons from the L shell (n = 2) or M shell (n = 3), producing different wavelength radiation (L to K transition = Kα, M to K transition = $K\beta$). A smaller variation in wavelength also occurs due to transitions from orbitals with different angular momentum quantum numbers, hence Kα_1 and Kα_2 are observed for a change in angular moment of 1 and 0 respectively. The most commonly used target anode

is copper which gives X-rays of λ, $K\alpha_1 = 1.54184$ Å and $K\alpha_2 = 1.54439$ Å. As a monochromatic beam is normally required, and $K\alpha$ is the more intense, $K\beta$ lines can be removed by using a metal foil filter composed of the element adjacent to the target in the periodic table; in copper's case, nickel.

Powders should have sufficiently small crystallite size that a smooth distribution of crystal orientations are observed. If the crystallite size is too large (>10 μm) or the powder is preferentially aligned along a given axis, then not all Bragg reflections may be observed as not all crystallographic directions are probed, meaning complete structural refinement is not possible. The scattering factor mentioned in section 2.2.2 is a description of the effectiveness of a given atom to scatter radiation. For X-rays this is dependent on electrons; atoms with more electrons scatter more strongly. This is useful as it allows distinction between different atoms sitting on the same lattice point (they will have different scattering cross sections). However, this means that for crystals containing both heavy and lighter elements, the scattering from the lighter elements is obscured, and it therefore may not be possible to obtain complete information about their atomic positions or occupancy. For example, in this thesis PXRD was used to determine the site occupancy and positions of transition metals, but not of the lighter elements, B and O. For these PND was used.

The scattering factor also depends on the Bragg angle. Atoms and their distribution of electrons have a finite size, so as θ increases, scattered X-rays are increasingly out of phase with those scattered at different points, significantly reducing scattering intensity.

For this thesis, a Cu anode was used. Data was collected on a PANalytical EMPYREAN (Cu Kα, Bragg-Brentano geometry, 40 mA and 40 kV beam) instrument. The software X'Pert Data Collector was used to collect the data. Air sensitive samples were either packed in a 0.5mm silica capillary, sealed in an argon-filled glove box with wax, or sealed under Kapton film in a PANalytical rotating sample holder. Collections of PXRD patterns took between 10 minutes and 12 hours depending on the sample and were typically over a 2θ range of 10° to 120°.

2.2.3.2 Powder neutron diffraction (PND)

Neutron diffraction is less commonly used than PXRD due to the production of neutrons being expensive and hazardous. However, neutrons offer some significant advantages over X-rays in certain systems and PND is therefore a valuable tool in crystallography.

The main advantages are that they are non-destructive to the sample, have deep penetration lengths, quasi-random scattering factor, little $\frac{sin\theta}{\lambda}$ dependence, and are sensitive to magnetic moments. These are discussed in more detail below.

A beam of neutrons exhibit either particle or wave like properties according to the de Broglie relationship, Equation 12, and can therefore be used for diffraction.

$$\lambda = \frac{h}{p} \qquad \text{Equation 12}$$

Where λ is the wavelength, p is momentum of the particle ($p = mass \times velocity$) and h is Planck's constant.

High velocity, low wavelength, neutrons are produced in atomic fission reactions from a uranium source. Their wavelength can be increased to be useful for diffraction by using deuterated water to slow them. These neutrons are then reflected from a plane of a single-crystal monochromator to reduce the spread of wavelengths, thus creating a monochromatic beam of neutrons with a wavelength of ~1 Å.

Alternatively, a high intensity beam with a range of wavelengths can be produced in a spallation source. Here, protons are accelerated to high energies then released to strike a metal target, where spallation of neutrons occurs. The entire spallation beam with its varying wavelengths is used, so instead of varying the angle to probe each d spacing, the times of flight of the neutrons are measured at a fixed angle. The use of the entire beam results in greater intensity than reactor sources.

The scattering of neutrons is caused by their ½ spin interacting with the spin state of the nucleus of an atom in the sample. When a neutron interacts with a nucleus it can be absorbed, scattered coherently (leading to diffraction) or scattered incoherently (leading to background noise). The spin of the neutron is also affected by unpaired electrons, resulting in sensitivity to magnetic structure.

Unlike in PXRD where the scattering factor is proportional to the number of electrons, the scattering factor in PND is a property of the nucleus and does not vary in a systematic way. In fact, they can vary between isotopes of the same element, Figure 2-3. Therefore, lighter elements scatter as effectively as heavy elements, allowing them to be located in the structure. For example, in this thesis B is a principle component of the structures, but due to presence of transition metals such as Mn its position is hard to determine by PXRD. Whereas in PND the coherent length for ^{11}B is 6.65 fm and for Mn is -3.73 fm, giving good contrast and allowing determination of B positions.

It should also be noted that the nuclei act as point scatters (rather than the finite size of an electron cloud), therefore structure factor is independent of the scattering angle. Thus smaller *d* spacings can be probed with greater resolution.

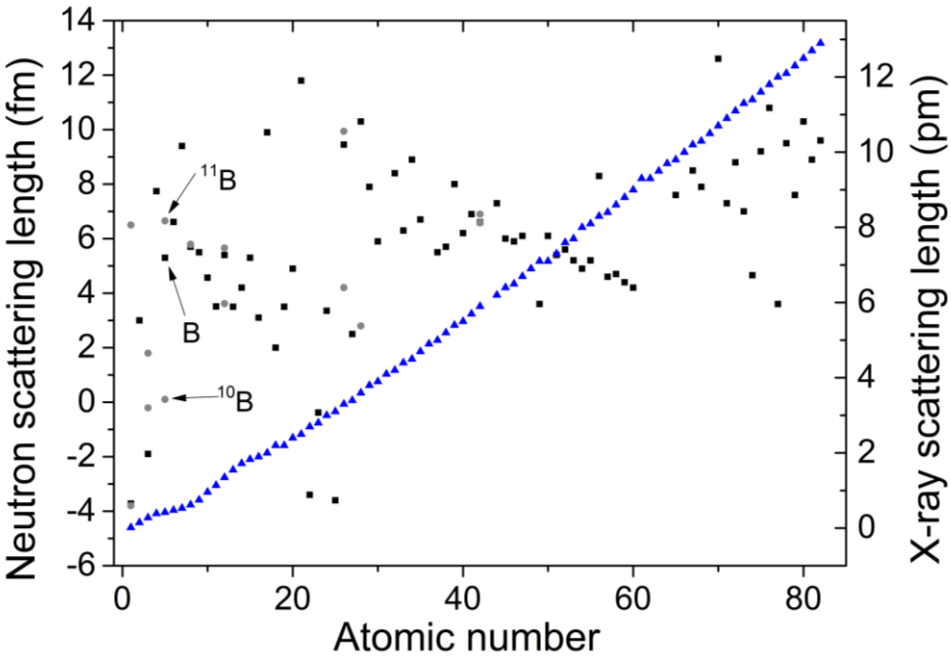

Figure 2-3. Comparison of the neutron and X-ray scattering lengths for elements and selected isotopes. Black squares represent the neutron scattering lengths for atoms with natural abundance of isotopes, with selected isotopes shown by grey circles (left hand axis). Blue triangles are the X-ray scattering lengths for a given atom (right hand axis).

For this thesis PND data were collected at the ILL in Grenoble, France on the D2B instrument. Neutrons are generated by a high-flux nuclear reactor. The reactor is powered by a single fuel rod that provides a neutron flux with a peak at λ = 1.2 Å. Detection of neutrons is via 128 individual, 2 dimensional, 30cm long ^{3}He detector tubes. Detection via these tubes allows the user to process data collected across the whole tube for maximum signal, or in the centre third only for increased resolution.

D2B uses a germanium (^{115}Ge) crystal to collimate the beam. Altering the crystal orientation allows the wavelength to be varied between 1.051 and 3.152 Å. For the experiments discussed in this thesis data was collected at λ = 1.596 Å over a 2θ range of 10°-160°, with a step size of 2θ = 0.050018°, the local contact was Emmanuelle Suard. Samples containing B were enriched with ^{11}B to avoid the high neutron absorption of ^{10}B. Samples were packed in 40 mm by 8mm vanadium canisters, in an argon filled glovebox where needed, and data was collected over a period of 4-12 hours depending on the mass of sample available.

2.2.4 Structure refinement

Structure refinement is an integral part of crystallography as it allows structural information to be gleaned from the collected data. Rietveld analysis involves refinement of a structural model against the collected data using a least-squares fit method.[128]

The Rietveld method requires a reasonably good initial model, then by refining parameters such as cell parameters, atom types and positions, thermal parameters, particle size and strain, and instrumental resolution parameters, a model that fits the data can be obtained.

If the model deviates significantly from the observed pattern it can be useful to start with profile matching, or Le Bail fitting, which does not require information on structure or sample composition.[133] This helps to determine peak shape functions, background points, and cell parameters before running the Rietveld method.

The calculated intensity at a given step (angle or energy in the diffraction pattern) for the model is given by Equation 13.[134]

$$y_i(calc) = y_i^b + s\sum_{hkl} L_{hkl}P_{hkl}A\,|F_{hkl}|^2\varphi(2\theta_i - 2\theta_{hkl}) \qquad \text{Equation 13}$$

Where y_i^b is the background intensity, s is the scale factor for a given phase, L_{hkl} and P_{hkl} are Lorentz and polarization factors seen in Equation 10, A is an absorption factor, primarily an instrumental parameter, $|F_{hkl}|$ is the structure factor of the proposed model at a given reflection and φ is the profile function which is 2θ dependent, this model's peak shape.

How well the calculated pattern fits the data can easily be observed by a difference plot, however it can also be described mathematically by the weighted R_{wp} value, Equation 14. R_{wp} takes into account the relative magnitude of the intensity, ensuring all peaks have equal significance in the refinement, so the value is not dominated by the most intense peaks.

$$R_{wp} = \left\{ \sum_i w_i [y_i(obs) - y_i(calc)]^2 / \sum_i w_i [y_i(obs)]^2 \right\}^{1/2} \quad \text{Equation 14}$$

Where $y_i(obs)$ is the observed intensity at step i, $y_i(calc)$ is the calculated intensity and $w_i = \frac{1}{y_i}$.

R_{wp} will be small for well collected data with a good fit and should be approaching the statistically expected value, R_{exp}, Equation 15 .

$$R_{exp} = [(N - P) / \sum_i^N w_i y_i(obs)^2]^{1/2} \quad \text{Equation 15}$$

Where N is the number of data points and P the number of parameters.

For a perfect fit $R_{wp} = R_{exp}$, the ratio of these gives the goodness of fit, χ^2, Equation 16. The refinement is optimised using the least squares method to reduce the value of χ^2.

$$\chi^2 = [\frac{R_{wp}}{R_{exp}}]^2 \quad \text{Equation 16}$$

A value of 1 indicts a perfect fit, values greater than 1 mean the structural model does not completely describe the data, and values less than 1 suggest the data have been over collected.

In practice Rietveld refinements often start by refining the non-structural parameters of zero-point error (sample deviation) and scaling factor. After this the lattice parameters are refined to improve matching of allowed Bragg reflections with observed intensity. Next the atomic positions, occupancy and thermal parameters can be refined to improve peak intensity matching. Refinement of the background and peak shape are also important to achieve a good fit.

Particle size can also be modelled by using Scherrer analysis. As particle size reduces peak width increases according to Equation 17.[135,136]

$$\epsilon(2\theta) = \frac{K\lambda}{b\ cos\theta} \quad \text{Equation 17}$$

Where ϵ is the crystalline size broadening at diffraction angle 2θ, K is the Scherrer constant which is symmetry dependent, λ is the wavelength and b is the additional line broadening due to size effects. As ϵ is inversely proportional to $\cos\theta$ broadening is most pronounced at large values of 2θ. The analysis uses a spherical harmonic expansion dependent on the crystal system of the crystal. Micro-particle size is then inferred by comparison with the peak widths of a crystalline silicon standard.

In this thesis Rietveld and Le Bail analysis was performed using the Fullprof suite of programs.[137] Backgrounds were fitted using a linear interpolation of data points. The peak shape was modelled using a pseudo-Voigt function with weighted Gaussian and Lorentzian components, and peak broadening was modelled using a symmetry dependent Scherrer analysis.[136] Instrumental broadening parameters were determined from a crystalline silicon standard.

2.3 Electrochemical testing

Throughout this thesis electrochemical tests are used to assess the viability of each material as a cathode in Li-ion or Mg-ion cells. Electrochemical tests are very sensitive techniques allowing calculation of the number of ions transferred and investigation into the mechanism occurring. Both coin cells and 3-electrode cells were used and both are described in detail below.

2.3.1 Electrolyte production

For Li-ion cells, commercially available 1M $LiPF_6$ in 1:1(v/v) ethylene carbonate (EC)/ dimethyl carbonate (DMC) (Merck) was used.

For Mg-ion cells, a variety of electrolytes have been tested and they will be discussed in detail in Chapter 6. The most studied in this thesis were: 0.5M – 2M $Mg(TFSI)_2$ (Solvionic – 99.5%) in tetrahydrofuran (THF) (Fisher Scientific) or acetonitrile (ACN) (Anhydrous, 99.8%, Sigma-Aldrich), 1M $Mg(ClO_4)_2$ (99% Sigma-Aldrich) in ACN, and 0.76 M $MgPF_6$ in THF/ACN. Before dissolving in the relevant solvent the solid salts of $Mg(ClO_4)_2$ and $Mg(TFSI)_2$ were dried under dynamic vacuum at 150˚C. $Mg(PF_6)_2$ was synthesised by Evan Keyzer in the Wright Group.[138]

2.3.2 Electrode production

2.3.2.1 Cathodes

Once synthesised, materials to be tested as cathodes were prepared into conductive films. First, the material was ground using a high-energy ball mill with a zirconia jar and 10 mm zirconia balls, to reduce the particle size. Particles sizes of ~100nm were achieved as determined by Rietveld refinement and Scherrer analysis. Grinding involved four stages of five-minute

milling, with five-minute rest periods in-between. The rest period is necessary to avoid degradation of the material due to heat. 20-50 wt% conductive carbon was then added to the ball mill jar (Super P, Alfa Aesar, 99%) and the mixture was further milled for two five minute stages with a 5-minute rest in-between.

To produce a film, 10 wt% polyvinylidene fluoride (PVDF) copolymer (Kyner Flex) was added to the active material/carbon mixture, and a few drops of N-methyl pyrrolidine (NMP, Sigma Aldrich) were then added to dissolve the polymer. Acetone was added to the mixture to allow casting onto a glass slide to create a film a few mm thick. The cast film was dried in air, then at 70˚C overnight. The dried film was cut into 7/16-inch diameter disks using a circular punch.

Some materials would not form a stable film via this method, so an alternative polytetrafluoroethylene (PTFE) method was used. 10% PTFE was added to the active material/carbon mixture and ground in a mortar and pestle until the material formed a paste (small amounts of ethanol were added to aid mixing where required). The paste was then firmly pressed using a glass rod to produce a film with a thickness of a few mm.

2.3.2.2 Anodes

For testing in Li-ion cells, a Li metal anode was used (Lithium ribbon, Sigma-Aldrich). The use of Li metal, although not commercially viable, allows direct measurement against the Li^+/Li^0 redox couple, which is far simpler than using more chemically complex commercial anodes such as graphite. It also ensures an excess of Li is present in the cell so that capacities are limited only by the cathode material being investigated. Before use, the metal was brushed clean and cut to size using a circular punch.

For Mg-ion ion cells Mg ribbon was used (99.5% Sigma-Aldrich). Prior to use the metal was polished using either a combination of 160 and 500 grit aluminium oxide sand paper, or by running a razor blade across the surface. 3 × 1 cm strips were cut from the ribbon and placed in each cell.

2.3.3 Cell set up

2.3.3.1 Coin cells

CR2032 coin cells were constructed to test both Li-ion and Mg-ion cells in a two-electrode configuration, and to produce material for ex-situ PXRD, Figure 2-4. All cells were constructed in an argon glove box (<0.1 ppm O_2, <0.1ppm H_2O). For Li-ion cells 316 grade stainless steel casings were used with stainless steel current collectors and Whatman borosilicate separators soaked in 7-8 drops of electrolyte.

Mg-ion cells were produced in the same way, but for some experiments Al coin cell casings and current collectors were used. This was to avoid corrosion of the stainless steel by some electrolytes.

Coin cells were tested on an Arbin BT2000 potentiostat with current ranges of ± 10 μA and ± 1 mA and ± 10 V voltage range. Cells tested at increased temperatures were placed in Memmert UF30 ovens and rested for 2 hours before cycling, to allow equilibration. Cells were connected to the Arbin via temperature-resistant cables threaded through an inlet in the oven.

To prepare ex-situ samples for PXRD or NMR, the coin cells were disassembled in an argon glove box (<0.1 ppm O_2, <0.1ppm H_2O), washed with DMC and dried under vacuum.

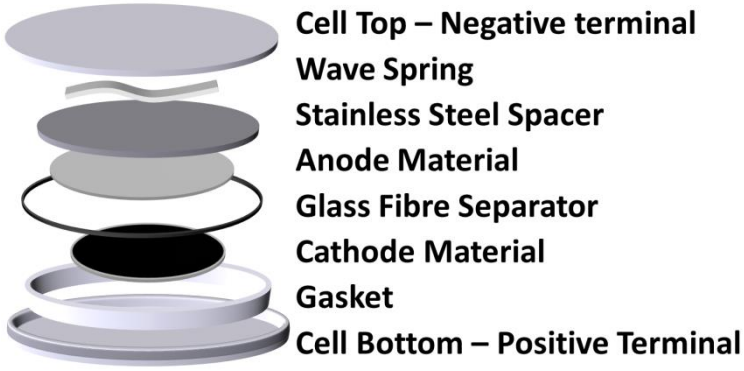

Figure 2-4 Schematic of a coin cell.

2.3.3.2 3-electrode flooded cell

As the current standard Mg-ion electrolytes have stability issues with the coin cell casing, a 3-electrode flooded cell set up was used to avoid these side reactions. A glass bowl with a small, flat bottomed section for electrolyte was cleaned with 35% nitric acid, rinsed with acetone and dried in a drying oven. The lid is sealable with a rubber O-ring and contains 5 ports for inserting electrodes or sealing with plastic plugs. Sealing the system limits solvent evaporation and allows measurements to be made over multiple days. Electrodes were pierced through rubber septums and connected to the potentiostat via crocodile clips.

The reference electrode used was Mg wire (Goodfellow, 0.5mm 99.9%). Counter electrodes used were Mg ribbon, Pt wire (Goodfellow, 0.5mm, 99.9%) or carbon coated polyethylene film (Goodfellow, 0.08mm). Pt wire was cleaned using 35% nitric acid and polished using 1200 grit silicon carbide abrasive. Working electrodes were the synthesised cathode materials cast into

films as described previously. The films were re-dissolved in ethanol and coated onto Pt wire. Typical loadings were ~1 mg.

Once the electrodes were in place, 3-4 ml of electrolyte was pipetted in to fill the base and cover the electrodes, and the cell was sealed.

The potentiostat used was an Ivium Vertex and all measurements were carried out in an argon filled glove box.

2.3.4 Electrochemical Techniques

The most commonly used technique in this thesis is galvanostatic cycling of coin cells which allows the capacity, working voltage, efficiency and cycle life to be assessed. A cell is rested for 3-6 hours and the open circuit voltage recorded (OCV). A constant current is then applied at rates varying from C/100 to 10C (charging in 100 hours and 6 minutes respectively) until a pre-set voltage limit is reached, at which point the current is reversed. A C/25 rate was used for most capacity determination and cycle life experiments, with slower rates used to investigate ion removal with reduced kinetic barriers (especially in Mg-ion cells) and high rates used to give an indication of cell performance at high power.

Galvanostatic intermittent titration technique (GITT) was used to complement galvanostatic cycling. GITT affords information on the energetics of the electrochemical reactions occurring. The measurement consists of a series of galvanostatic pulses each followed by a relaxation time where no current is applied, see Figure 2-5. The rest period is characterised by a short, sharp change in potential due to internal resistance (a drop after charge current is applied, and increase after discharge), followed by a gradual decrease as the material reaches equilibrium. Once the cell returns to its OCV the difference between this value and the voltage at the end of the galvanostatic step is observed, and is termed the overpotential. The overpotential is the extra energy required for the reaction to occur and therefore ideally will be minimal. Large overpotentials suggest either large electrical resistance in the cell (poor contacts or insulating active material not sufficiently mixed with conductive carbon), or large ionic resistance (high activation energies for ion movement).

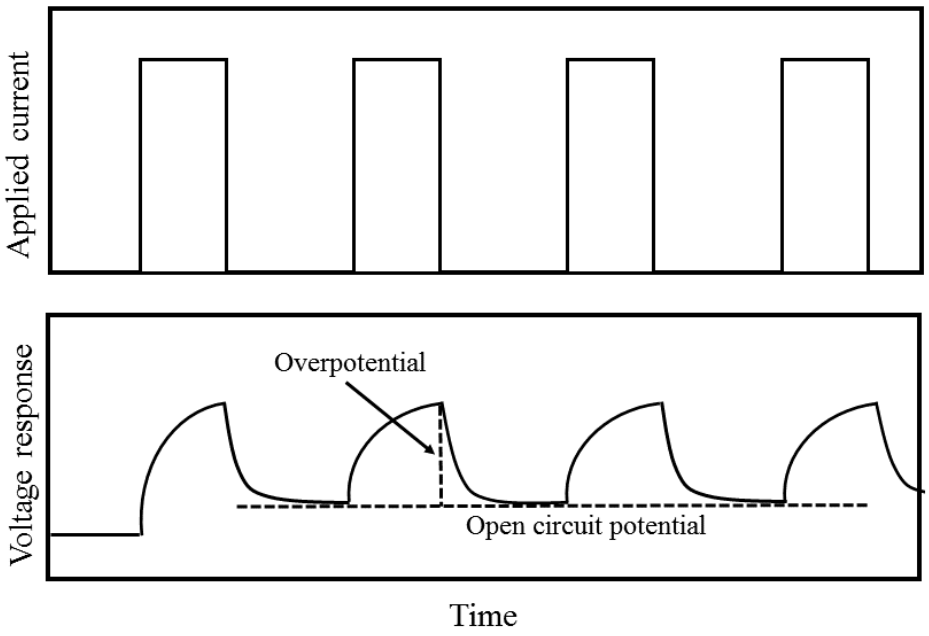

Figure 2-5 Principles of GITT. A current is applied and the voltage responses measured. After a given time the current is removed and the cell allowed to rest until the equilibrium voltage is reached, at which point current is re-applied.

Cyclic voltammetry (CV) was primarily used in the 3-electrode set up. For this method, the voltage is swept from OCV up to the desired oxidative limit, then back down to the reductive limit, while measuring the current between the working and counter electrodes. As when an oxidative/reductive process occurs (*e.g.* (de)intercalation of an ion from the active material) a positive/negative current is observed. This method allows determination of the voltage at which an electrochemical process occurs, allowing separation of the side reactions from the real processes, thus aiding interpretation of the electrochemical mechanisms. By cycling the voltage, information on the reversibility of the reactions can be obtained.

2.4 Magic angle spinning nuclear magnetic resonance

Solid-state magic angle spinning nuclear magnetic resonance (MAS NMR) is a valuable tool in studying the local environment, short-range order and ion-dynamics in battery materials. The chemical shift and relaxation behaviour of disordered materials contains information which cannot be analysed with diffraction methods, which rely on long range order. ^{6}Li and ^{7}Li MAS NMR has been used extensively to study cathodes,[139–141] anodes,[142] SEI[56] and electrolytes.[143,144] In this thesis, the ^{7}Li and ^{11}B environments of cycled $MgMnB_2O_5$ were studied at various points of charge vs. a Li anode. ^{7}Li and ^{11}B spectra were acquired by Zigeng Liu.

2.4.1 Acquiring a spectrum

When nuclei with spin quantum number $I \neq 0$ are placed in a magnetic field (B_0) the Zeeman effect causes the spin states to split into $2I+1$ levels, the difference in energy between these states is the Larmor frequency ω_0, Figure 2-6. The sensitivity of NMR to local environment occurs as the observed signal shift and line shape are determined by the local chemical environment causing perturbations to these distinct energy levels. Perturbations can be caused by dipolar coupling (nuclear-nuclear spins), shift interactions (nuclear-electron spin) and quadrupolar coupling. The intensity of a signal is determined by the isotope's natural abundance, the number of sites in the sample, sample size, temperature and magnetic field strength.

When acquiring an NMR spectrum, the sample is placed in a magnetic field of strength B_0 causing the nuclear spins to align leading to a net magnetic moment along the B_0 direction. Once the spins are aligned (i.e. have reached equilibrium in the field) they precess at the Larmor frequency. A radio frequency is then applied from a surrounding coil, to both remove the system from equilibrium and allow signal detection. An applied 90˚ pulse causes the spins to precess in the xy plane (*i.e.* 90˚ to B_0) resulting in a rotation of the magnetic moment in the coil, inducing a voltage. As the spins return to alignment in the B_0 direction, the voltage decays and voltage-time signal is acquired. The voltage-time signal is then translated to intensity-frequency via Fourier transformation, giving the NMR spectra. To improve the quality of signal acquired, a Hahn echo experiment was used, where the spin magnetization is refocused after a second, 180˚ pulse is applied, removing any dephasing that may occur due to inhomogeneous magnetic fields.

Magic angle spinning (MAS) is required for powder samples as the interaction with an applied field can vary for different crystal orientations (chemical shift anisotropy, CSA) therefore, as powdered samples have a broad distribution of crystal orientations a very broad signal is observed for static measurements. As the CSA is proportional to $(3\cos^2\theta)$, if a sample is spun at the "magic angle" $\theta = 54.7^\circ$ the chemical shielding is averaged to a single isotropic peak.[145] If the CSA is greater than the MAS frequency, spinning side bands are observed at multiples of the MAS frequency.

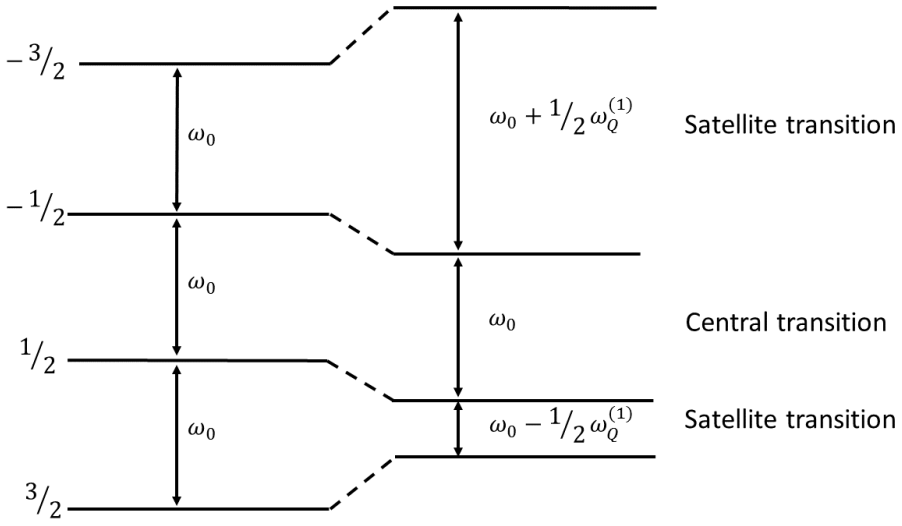

Figure 2-6: The Zeeman effect, resulting Larmor frequencies (ω_0) and first-order quadrupolar coupling for I = 3/2 nuclei. ω_Q^1 is the first order quadrupolar coupling constant. Adapted from Laws *et al.*.[145]

2.4.2 Considerations for analysis of NMR spectra

2.4.2.1 Relaxation

The relaxation parameters T_1 and T_2 can be used to determine if an ion is in a diamagnetic or paramagnetic environment. The time taken for the spins to return to the B_o direction after a pulse is applied is driven by spin-lattice relaxation processes (T_1). This is generally fast for paramagnetic materials, due to interactions with electron spins, and slower for diamagnetic materials. The spin-spin relaxation (T_2) is the time constant of the signal decay, again this is faster for paramagnetic samples than diamagnetic.

2.4.2.2 Paramagnetism

The magnetic moment of paramagnetic ions such as Mn^{2+}, Fe^{2+} or Co^{2+} can be many times greater than the nuclear magnetic moment of the nuclear spin being observed, therefore this hyperfine interaction dominates the observed NMR shift. Hyperfine interactions can be through space (dipolar) or through bond (Fermi contact) and can lead to large deviations in chemical shift and anisotropy.

2.4.2.3 Quadrupolar interactions

^{11}B and ^{7}Li have a spin of 3/2 and are therefore a quadrupolar nuclei (I >1/2). Interactions of the quadrupole moments with the surrounding electric field gradient cause satellite transitions in static spectra, Figure 2-6. The coupling only occurs in centres with non-cubic symmetry, so can provide information on the symmetry and distortions of local environments.

^{7}Li and ^{11}B NMR spectra of the cycled materials were acquired in a 1.3 mm probe head on a Bruker 500 MHz and 200 MHz spectrometer, with magic angle spinning (MAS) up to 60 kHz. Li_2CO_3 (99.99%, Aldrich) was used as a 0-ppm reference for ^{7}Li NMR and a 0.1M H_3BO_3 in H_2O solution was used as a 19.6 ppm reference for ^{11}B NMR. Data was analysed using Bruker TopSpin 3.5. All spectra were acquired with the help of Zigeng Liu or Paul Bayley.

2.5 SQUID Magnetometry

A Superconducting Quantum Interference Device (SQUID) consists of two Josephson junctions (two superconductors separated by a thin insulating layer) in a superconducting ring and can be used to detect and measure very small changes in magnetic fields. When a current is maintained across the device, quantum tunnelling of Cooper pairs can occur, therefore a voltage, which depends on the Josephson junction's phase, can be measured. An applied magnetic field induces a change in current within the ring, and therefore the measured voltage. This phenomenon is very sensitive to the magnetic flux strength and therefore to the magnetic moment of a sample.

To measure the moment of a sample a few mg of material is packed in cling film and pressed into a sample holder. This is inserted into the centre of a superconducting magnet which can generate large magnetic fields. The SQUID is shielded from the high fields in the sample space with the magnetic signal being detected by an additional superconducting coil, then transferred to the SQUID. Samples are then cooled to 2 K in the absence of a field. Once the temperature is stabilised a field is applied and a magnetisation measurement is taken by moving the sample within the detector coil. The temperature is then increased in regular increments and magnetisation measured at each point.

The data collected for a known mass of sample in a field, H, gives the molar magnetisation, M_m, which can be converted to the molar magnetic susceptibility, χ_m by Equation 18**.**

$$\chi_m = \frac{dM_m}{dH} \qquad \text{Equation 18}$$

In the low field regime where the change of magnetisation with the field is linear, this can be approximated to $\chi \cong \frac{M_m}{H}$.

Linear regions of the temperature-dependent data were fit using the Curie-Weiss law, Equation 19.

$$\chi_m = \frac{C_m}{T - \theta} \qquad \text{Equation 19}$$

Where C_m is the molar Curie constant and θ is the Weiss temperature. The experimentally derived Curie constant can be used to calculate μ_{eff}, Equation 20.

$$\mu_{eff}^2 = \frac{3k_B C_m}{N_A \mu_B^2} \sim 8C_m \qquad \text{Equation 20}$$

Where k_B is the Boltzmann constant, N_A is Avogadro's constant and μ_B is the Bohr magneton. It is possible to compare this value with calculated values which are directly related to the electronic configuration of the cations, Equation 21.

$$\mu_{eff} = g\sqrt{S(S+1)} \qquad \text{Equation 21}$$

Where g is the Lande g-factor and accounts for angular momentum, and S is the spin quantum number. For transition metal ions spin-orbit coupling can be assumed to be negligible and therefore the spin only form of the equation is used where g = 2.

As carbon and PTFE make up a significant portion of the cathode material there is a diamagnetic contribution to the measured magnetisation of ex-situ samples. This was accounted for by comparing the magnetisation of the pristine material with the uncycled cathode material and calculating a diamagnetic contribution per gram of carbon/PTFE, which was then applied to the ex-situ samples. The calculated diamagnetic contribution was 1.15×10^{-7} emu mol^{-1}, which is a reasonable value given the literature values for aromatic carbon and PTFE are 3.8×10^{-6} and -6×10^{-6} emu mol^{-1} respectively.

The measurements described in this thesis were carried out on a Quantum Design magnetic Properties Measurement System (MPMS3) superconducting quantum interference device (SQUID) magnetometer. The magnetization (M) was measured in a field of 1000 Oe as a function of temperature on warming from 2 to 300 K after cooling in zero field.

2.6 Bond valence sum maps

Bond valence sum (BVS) maps were used to investigate potential diffusion pathways and interstitial sites in Mg containing borates. BVS maps are produced by using the BVS method

to calculate the oxidation state of an imaginary mobile ion on a defined mesh in a unit cell. The oxidation state of a position in the cell is a function of the number of possible bonds, and the bond strength.[146] The strength of the bond (or its electrostatic valence) correlates with the length of the bond and the specific cation – anion interaction. Therefore, for a given interaction between a cation and anion in a cell, the valence can be calculated by Equation 22.

$$bond\ valence = s = \exp\left(\frac{R_0 - R}{B}\right) \qquad \text{Equation 22}$$

Where the bond valence is the number of electron pairs that form the bond, in valence units, R is the length of the bond between two given atoms, and R_0 and B are empirical parameters for the specific ion pair. Values of R_o and B that had been previously determined for the Mg^{2+} - O^{2-} interaction were used.[147] The sum of the bond valences for each bond around an atom is equal to its oxidation state, therefore the oxidation state of an ion with coordination number, CN, is calculated by Equation 23.

$$oxidation\ state = \sum_{CN} s \qquad \text{Equation 23}$$

A map is then produced that gives the absolute value of the difference between the ideal and calculated valence, the bond sum variance ($|\Delta s|$ in v.u), thus allowing investigation of accessible sites for an ion with the calculated valence.

This method has been successfully used in a number of Li- and Mg-ion battery cathode materials to give insight into potential diffusion pathways, with the magnitude of Δs giving an indication of the barrier to ion diffusion.[98,148]

The benefits of the BVS map method are that it is robust and computationally cheap, while providing a visual indication of likely conduction pathways. It can also handle partial occupancies without the need for supercells. However, as the method does not take into account ion dynamics, electrostatic repulsion between same charged species, or structural flexibility, actual diffusion pathways may differ significantly.

2.7 X-ray Absorption Near-Edge Structure (XANES) Spectroscopy

XANES spectroscopy provides details of the local coordination environment and oxidation state of the absorbing ion.[149,150] A synchrotron X-ray photon is absorbed causing an electron to be excited from the ground state to an excited state, if the photon energy exceeds the electron binding energy. The transitions obey the dipole selection rules, $\Delta l = \pm 1$, $\Delta j = \pm 1$, $\Delta s = 0$, with

the primary transition being from a core *s* orbital to an empty *p* orbital (K edge for a 1*s* electron, L for a 2*s* electron).

The region around the absorption edge contains fine structure caused by scattering of the excited electron wave by surrounding atoms, leading to interference dependent on the local environment of the absorbing atom. Typically, the region up to 50 eV above the edge is termed XANES and contains information on the absorbing ion's oxidation state and local environment, while the region after this is termed EXAFS (Extended X-ray Absorption Fine Structure) and contains information on each surrounding atom's placement, atomic number and thermal motion.[151] The inflection point of the absorption edge corresponds to the binding energy of the core shell electron and is therefore indicative of the atom's atomic number and oxidation state, with the edge shifting to higher energy with increasing oxidation state. Absorption edges can have multiple components caused by orbital hybridization, giving rise to transitions with slightly differing energies. For transition metals a weaker, pre-edge feature, is sometimes observed corresponding to the forbidden 1*s* → 3*d* transition ($\Delta l = 2$) caused by mixing with 4*p* orbitals. For a centro-symmetric, undistorted, octahedra no *p*-*d* orbital mixing occurs therefore the pre-edge feature is not observed, whereas for distorted octahedra the intensity of this feature increases with increasing distortion of the local environment. A tetrahedral environment will have the strongest intensity pre-edge feature as the coordination causes the most 3*d*-4*p* orbital hybridization.[152]

Pellets for XANES measurement were formed by mixing the material with Polytetrafluoroethylene (PTFE) polymer to give a total mass of ~60 mg, the mixture was then pressed into 8 mm pellets. Ex-situ samples were prepared in the glove box and sealed in foil bags. XANES spectroscopy data were collected by Michael Gaultois and Giannantonio Cibin on beamline B18 at the Diamond Light Source (Proposal number SP15303).

Chapter 3. Structural and electrochemical investigation of the orthoborates, $M_3(BO_3)_2$

3.1 Introduction

Anhydrous borates have gained considerable attention recently due to their use as battery cathodes,[46,48,153,154] second harmonic generation materials[155] and piezoelectrics.[156] There are two anionic borate groups that form the basis of the wide variety of borate crystal structures, these are the trigonal planar BO_3^{3-} and tetrahedral BO_4^{5-} groups. These building blocks can coordinate to metal cations individually, for example in the orthoborates ($M_3^{2+}(BO_3)_2$) where each oxygen atom on a planar BO_3 coordinates to the cation, or they can form polymeric chains sharing 1, 2, 3 or (for the tetrahedral unit) up to 4 oxygen atoms with an adjacent borate unit. Common examples of these polyanions include the metaborates ($M^{1+}BO_2$) which consists of 2 dimensionally linked BO_3^{3-} units[157] and the pyroborates ($M_2^{2+}B_2O_5$) where each BO_3 unit is linked to one other neighbour forming short, linear, chains.[158]

The orthoborates are a class of orthorhombic (*Pnnm*) borate which contain isolated BO_3^{3-} units. The stoichiometry and colour of the crystals were first described in the late 18th century[159,160] and their crystal structure has since been described in detail in the naturally occurring $Mg_3(BO_3)_2$ (kotoite),[161,162] $Mn_3(BO_3)_2$ (jimboite),[163,164] $Mg_3(BO_3)_2$ (takedaite)[165] and synthetic Ca, Ni, Mn, Co, Sr, Ba and Mg samples.[157,166–168] Mixed metal orthoborates such as cobalt dinickel orthoborate $CoNi_2(BO_3)_3$[169] also crystallise in the orthorhombic structure exemplifying the versatility of this crystal structure.

The defining characteristic of the metal orthoborates is discrete, near equilateral, trigonal planar BO_3^{3-} groups that form layers through the cell, Figure 3-1. Evidence for the existence of discrete BO_3^{3-} units is seen in the short B-O bond distances (~1.35 Å) within the triangles.[164] Therefore, the structure is best described as $M_3(BO_3)_2$. Between the borate layers sit two distorted octahedral *M*1 and *M*2 sites, which the divalent metals occupy in a 1:2 ratio, Figure 3-2. Although both octahedra are distorted, the nature of the distortion differs based on their bonds to the BO_3 triangle. *M*1 bonds to BO_3 units by sharing an edge, forcing a shorter O-*M*-O bond angle along that edge, and subsequently a large O-*M*-O angle for the other equatorial bonds. The axial angle is 180° and the axial bonds are normal to the equatorial plane, so although there is a large overall bond angle variance ($\sigma^2 = 220°$, where σ is the mean square deviation from average bond angle),[170] the site retains high symmetry (2*a*). *M*2 has a smaller overall bond angle

variance (69°) but every bond is distorted, leading to lower symmetry (4*f*). Each oxygen has one boron and three M^{2+} nearest neighbours.

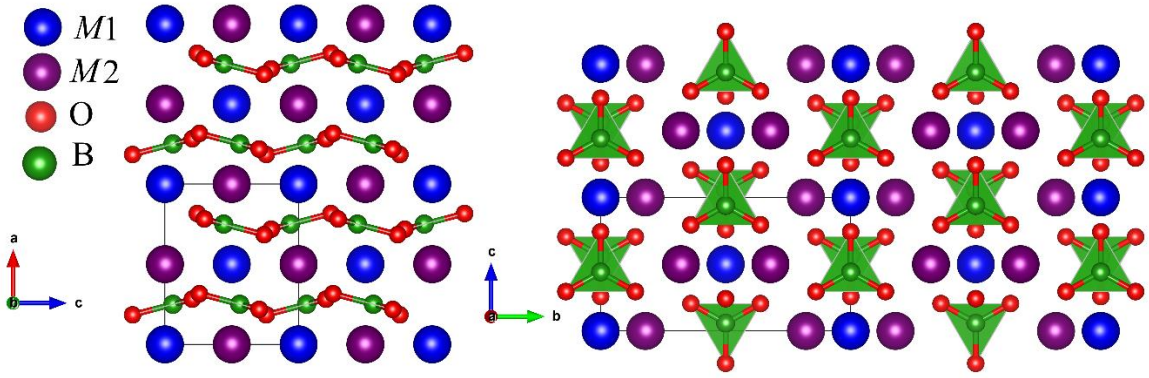

Figure 3-1. Structure of the $M_3(BO_3)_2$ orthoborates viewed along the *b* (left) and *a* (right) axis.

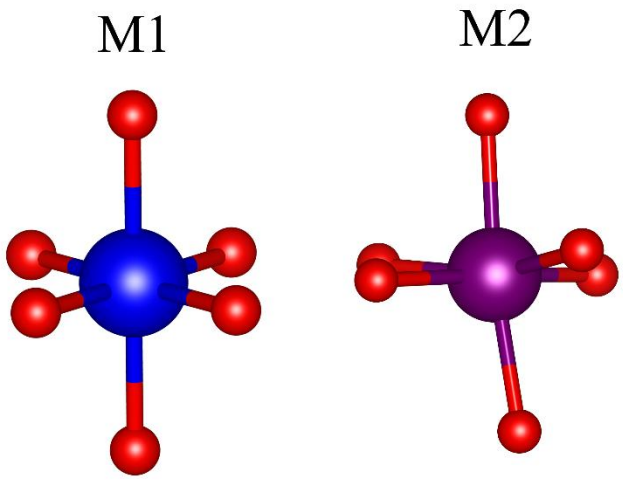

Figure 3-2. Octahedral arrangement of O around site *M*1 and *M*2. *M*1 is a higher symmetry site (2a) than *M*2 (4f).

3.1.1 Interest for battery cathodes

As discussed in Chapter 1, borate polyanion based cathodes exhibit high voltages and large theoretical capacities as Li-ion cathodes. The Li*M*BO_3 (*M* = Fe, Mn, Co) family has been extensively studied and with careful preparation of the cathode and using mixed metal phases, capacities of ~200 mAh g^{-1} at over 4 V have been achieved.[45,48,153,171] The use of each transition metal brings both advantages and disadvantages: $LiFeBO_3$ exhibits good reversibility but low voltage; $LiMnBO_3$ has a higher voltage but poor Li diffusivity due to antisite defects;[172] and $LiCoBO_3$ gives high voltages but a capacity of <30 mAh g^{-1}.

Compared to LiMBO$_3$ the orthoborates have a higher M to B ratio, meaning their theoretical capacities are significantly greater, while the voltages are likely to be similar due to utilising the same BO$_3$ connectivity. A theoretical study in 2015 suggested Li$_4M^{2+}$(BO$_3$)$_2$ as a candidate for Li-ion batteries, utilising both the 2+/3+ and 3+/4+ redox couple to form Li$_2M^{4+}$(BO$_3$)$_2$ at highest oxidation. However, although the stoichiometry is similar, the crystal structure is more comparable with LiMBO$_3$ than the M_3(BO$_3$)$_2$ orthoborates described previously (M and Li occupy different sites and form channels rather than layers).[29] Also, only recently has a Li$_4M$(BO$_3$)$_2$ compound been synthesised, and here M was the redox inactive Ca ion.[173] As direct synthesis of Li containing orthoborates with the layered structure is not currently possible, we investigate Mg containing orthoborates with the aim of removing the Mg and replacing it with Li electrochemically. The ability to form mixed transition metal structures was crucial to achieving high capacities in previously studied polyanions, so the flexibility of these materials may allow optimisation of structural and electrochemical properties.

Although the orthoborate crystal structure has been well described, detailed analysis of M^{2+} site occupancies and how the structure is affected by mixed metal systems has not previously been studied. Here we show the mixed metal orthoborates Mg$_x M^{2+}_{3-x}$(BO$_3$)$_2$, (where M = Mn, Co, Ni and x = 2/3 or 4/3), and show that a solid solution is formed for each compound. We demonstrate that preferential occupancy of the Mg and transition metal on the M1 and M2 sites occurs. This ordering is dependent on the transition metal, with Mn exhibiting the least ordering and Co the most. The Ni based compounds are also shown to be hygroscopic, forming a distorted phase on hydration.

We use bond valence sum calculations to show that a percolating pathway exists for both Mg and Li in the structure, with the Mg requiring a greater variance in valance and therefore likely to display more sluggish diffusion. Electrochemical measurements vs. a Li anode show that up to 86% of the Mg can be removed from the Mg$_2$Mn(BO$_3$)$_2$ and be replaced by Li, in a roughly 1:1 ratio. This utilises both the $Mn^{2+/3+}$ and $Mn^{3+/4+}$ redox couples and two distinct voltage regions are observed. In MgMn$_2$(BO$_3$)$_2$ and Mg$_2$Co(BO$_3$)$_2$, where less Mg occupies site M1, lower capacities are achieved, however Li is still found to replace the removed Mg in a roughly 1:1 ratio. Ex-situ PXRD shows the orthoborate structure is retained and that the unit cell contracts on removal of Mg^{2+} from the structure.

3.2 Experimental

The orthoborates were synthesised by grinding stoichiometric amounts of transition metal oxalate $MnC_2O_4.2H_2O$ (Alfa Aesar 30% Mn min), $NiC_2O_4.2H_2O$ (Puratronic, 99.998%), or $CoC_2O_4.2H_2O$ (Aldrich, >99%) with MgO (Alfa Aesar 99.998%) and H_3BO_3 (Alfa Aesar 99.99%) into a fine powder. The mixtures were heated to 400 °C at 3 °C min^{-1} and held for 10 hours. Samples were then cooled, reground and heated to 650 °C and held for 24 hours. Cooling and regrinding was repeated followed by a 24-hour heat at 800 °C. The final synthesis step was heating to 1050 °C at 3 °C min^{-1}, samples were held at this temperature for 24 hours before being furnace cooled. The inclusion of intermediate heating steps reduced the presence of metal oxide and other borate impurities. If impurities were present (indicated by PXRD or visual assessment of colour), the final heating step was repeated until the impurity was removed or the amount present no longer decreased. For Mn containing materials all synthesis steps were performed under flowing argon. All other materials were synthesised in air, though to avoid hydration Ni containing orthoborates were stored under argon. ^{11}B enriched samples prepared for neutron powder diffraction were synthesised from ^{11}B-Boric acid (Aldrich 99%).

PXRD experiments were carried out on a PANalytical Empyrean Series 2 Diffractometer System with CuKα radiation (λ = 1.540598 Å, 1.544340 Å). Rietveld analysis was performed using the FullProf suite of programs over a 2θ range of 10°-70°, with step size of 2θ = 0.0167°. Backgrounds were fitted using a linear interpolation of data points.

Constant wavelength PND data were collected over a 2θ range of 10°-160°, with step size of 2θ = 0.050018° on the D2B instrument (λ = 1.596 Å) at Institut Laue-Langevin (ILL, Grenoble). Samples were packed under inert conditions in sealed vanadium canisters and measured for 12 hours. Rietveld analysis[128] was performed using the FullProf suite of programs[137] over a 2θ range of 10°-150°, with step size of 2θ = 0.050018°. Backgrounds were fitted using a linear interpolation of data points. The peak shape was modelled using a pseudo-Voigt function.

3.3 Results

3.3.1 Synthesis of $Mg_xCo_{3-x}(BO_3)_2$ and description of the structure

Two members of the $Mg_xCo_{3-x}(BO_3)_2$ series were prepared with x = 1 and 2. $Mg_2Co(BO_3)_2$ synthesis resulted in a phase pure light purple powder, while the deep purple $MgCo_2(BO_3)_2$ phase contains a 3% CoO impurity, even after multiple re-heats at 1050 °C. Table 3-1 gives the refined structural information for the $Mg_xCo_{3-x}(BO_3)_2$ system, including refined stoichiometries of $Mg_{2.08(6)}Co_{0.92(6)}(BO_3)_2$ and $Mg_{1.01(4)}Co_{1.99(4)}(BO_3)_2$ for $Mg_2Co(BO_3)_2$ and $MgCo_2(BO_3)_2$ respectively, as determined by Rietveld refinement of powder neutron and X-ray diffraction, Figure 3-3. For ease, only the nominal compositions will be referred to from here on. The refined crystal structures show that these new phases display the BO_3 layers characteristic of the orthoborates and show little deviation in structure from the end members. This is exemplified by the unit cell volume change shown in Figure 3-4a, demonstrating that a solid solution is formed in the $Mg_xCo_{3-x}(BO_3)_2$ system, with just a 2.1% change across the whole series. The small volume change is due to the similar ionic radii of the two divalent metals (high spin Co^{2+} has an ionic radius of 0.745 Å and Mg^{2+} 0.72 Å). The volume and cell parameter change is not entirely linear with the mixed phases having larger than expected parameters (i.e. closer to $Co_3(BO_3)_2$ than $Mg_3(BO_3)_2$ than an ideal solid solution would suggest). The non-linear variation of the lattice parameters with composition is consistent with the partial ordering of the Mg and Co ions. There is a greater reduction in *a* than in *b* or *c*, associated with reducing the distance between BO_3 planes on addition of Mg, Figure 3-4b.

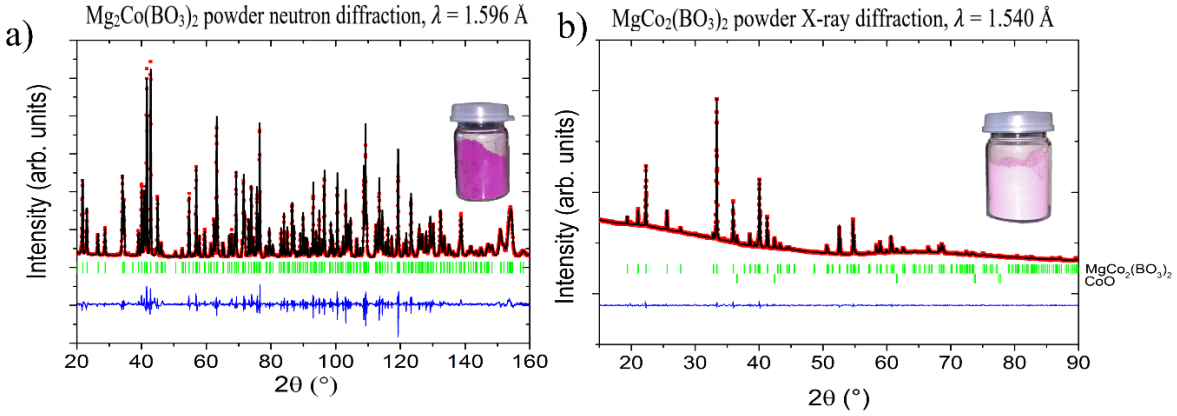

Figure 3-3: a) Neutron diffraction pattern (red dots) and Rietveld fit (black line) of $Mg_2Co(BO_3)_2$. Allowed Bragg reflections are shown as green tick marks and the difference pattern in blue. b) Powder X-ray diffraction pattern (red dots) and fit (black line) of $MgCo_2(BO_3)_2$ and CoO impurity (3.09%). Allowed Bragg reflections are shown as green tick marks and the difference pattern in blue.

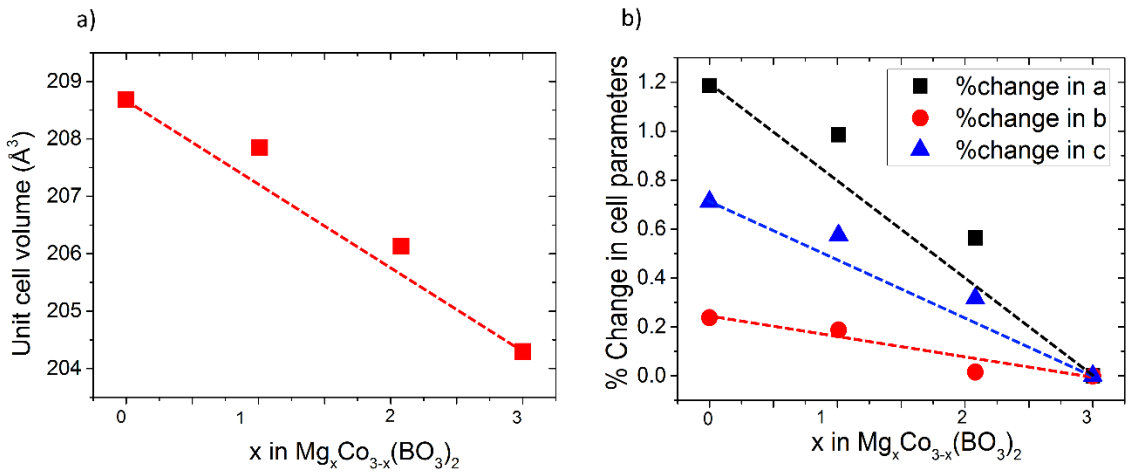

Figure 3-4. a) The change in volume across the $Mg_xCo_{3-x}(BO_3)_2$ series and b) the % change in lattice parameters across the series. Lines connecting the end members show how parameters would vary if the change was completely linear.

Both the $Mg_2Co(BO_3)_2$ and $MgCo_2(BO_3)_2$ phases display significant cation ordering, with the Co preferring the *M*1 site. In $MgCo_2(BO_3)_2$ *M*1 is almost entirely occupied by Co (94%), with the *M*2 site 53% occupied by Co. In $Mg_2Co(BO_3)_2$ *M1* is 68% Co compared to 24% on *M*2 per formula unit (complete disorder would be 33% on each). If the $Mg_2Co(BO_3)_2$ system was completely ordered Co would occupy all the *M*1 site as it does in $MgCo_2(BO_3)_2$, however this is not observed. This is not entirely unexpected as Mg is well known to occupy the same sites as transition metals. An explanation for the cation order is that *M*1 is the higher symmetry site (*M*1 = 2/m, *M*2 = 2) and therefore is more accommodating of the directional *d* orbitals found on Co. *M*1 is also slightly smaller than *M*2 though due to the similarity in ionic radii, this is unlikely to be the main driving force behind the preferential occupation of sites.

Table 3-1. Refined structural parameters for the $Mg_xCo_{3-x}(BO_3)_2$ system in the *Pnmn* space group. Errors are given in brackets for refined values. A combined PND and PXRD refinement was used for the $Mg_2Co(BO_3)_2$ phase while PXRD only was used for $MgCo_2(BO_3)_2$, using B and O positions from $Mg_2Co(BO_3)_2$.

		$Mg_3(BO_3)_2$[164]	**$Mg_2Co(BO_3)_2$**	**$MgCo_2(BO_3)_2$**	**$Co_3(BO_3)_2$**[164]
χ^2			4.21	2.31	
R_{wp}			3.58	1.01	
a (Å)		5.398	5.42843(3)	5.45115 (6)	5.462
b (Å)		8.416	8.41730(5)	8.43178(9)	8.436
c (Å)		4.497	4.51123(3)	4.52286(4)	4.529
Vol (Å^3)		204.297	206.013(2)	207.884(4)	208.685
M1	Occ (Mg/Co)	1/0	0.32/0.68(5)	0.06/0.94(1)	0/1
(2a)	B_{iso} (Å^2)	1	0.5(1)	1.5(1)	1
(0,0,0)					
M2	y	0.321	0.3126(3)	0.3129(2)	0.321
(4f)	Occ (Mg/Co)	1/0	0.881/0.119(6)	0.476/0.527(3)	0/1
$(0,y,\frac{1}{2})$	B_{iso} (Å^2)	1	0.44(5)	2.7(1)	1
Refined Mg/Co ratio		n/a	$Mg_{2.08(6)}Co_{0.92(6)}$	$Mg_{1.01(4)}Co_{1.99(4)}$	n/a
B	x	0.25	0.2559(3)	0.2559	0.25
4g	z	0.56	0.5434(4)	0.5434	0.56
(x,0,z)	B_{iso} (Å^2)	1	0.19(3)	0.19	1
O1	x	0.316	0.3223(4)	0.3223	0.316
4g	z	0.258	0.2491(5)	0.2491	0.258
(x,0,z)	B_{iso} (Å^2)	1	0.31(3)	0.31	1
O2	x	0.218	0.2064(3)	0.2064	0.218
8h	y	0.139	0.1393(2)	0.1393	0.139
(x,y,z)	z	0.705	0.6980(3)	0.6980	0.705
	B_{iso} (Å^2)	1	0.35(4)	0.35	1
wt% of CoO		n/a	0	3.09	n/a

3.3.2 Synthesis of $Mg_xMn_{3-x}(BO_3)_2$ and description of the structure

Synthesis of $Mg_xMn_{3-x}(BO_3)_2$ where x = 1 and 2 resulted in phase pure brown powders with refined stoichiometries determined from Rietveld analysis of neutron diffraction of $Mg_{2.06(3)}Mn_{0.94(3)}(BO_3)_2$ and $Mg_{0.9(04)}Mn_{1.1(04)}(BO_3)_2$, Figure 3-5 and Table 3-2. For ease, only the nominal compositions will be referred to from here.

As with in the Mg/Co system a solid solution is formed and a linear change in volume is observed across the series, Figure 3-6. However, the change in volume is much greater, an 11.4% increase from Mg_3 to Mn_3, attributed to a greater difference in ionic radii (0.72 Å and 0.83 Å for Mg^{2+} and Mn^{2+} respectively).[174] The increase in volume is subtly anisotropic, with *a* changing the most and *c* the least. The anisotropy is significantly less than that observed in the $Mg_xCo_{3-x}(BO_3)_2$ system. This may be due to decreased cation ordering of Mg and Mn over the two sites leading to more consistent changes in the cell. Preferential occupation of sites is again observed, however to a lesser extent than in the $Mg_xCo_{3-x}(BO_3)_2$ system and for opposite sites. Here the Mg has a preference for site *M*1 with the transition metal preferentially occupying *M2*. In $Mg_2Mn(BO_3)_2$, where disorder would have 66% Mg on each site the refined occupancies are 82% for *M*1 and 62% for *M*2 showing a clear preference for *M*1. This is thought to be driven by *M*2 being the larger site and therefore more easily occupied by the larger Mn^{2+} ion. As the Mn^{2+} is high spin d^5 the symmetry of the site has less effect on ordering.

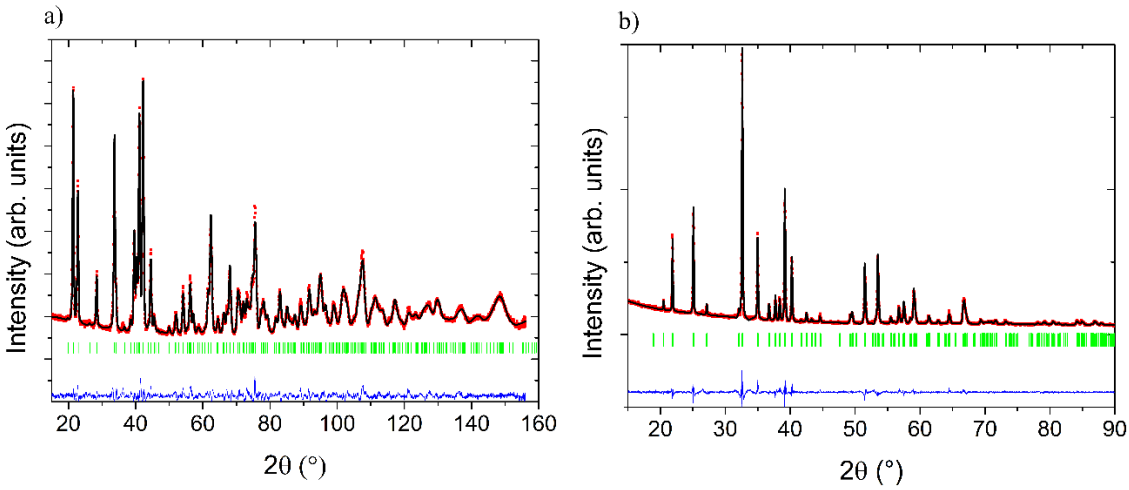

Figure 3-5. Rietveld refinement (black line) of a) PND data for $Mg_2Mn(BO_3)_2$ (red dots) and b) PXRD data for $MgMn_2(BO_3)_2$ (red dots). Allowed Bragg reflections for the phase are shown with green ticks, and difference between data and refinement with blue line.

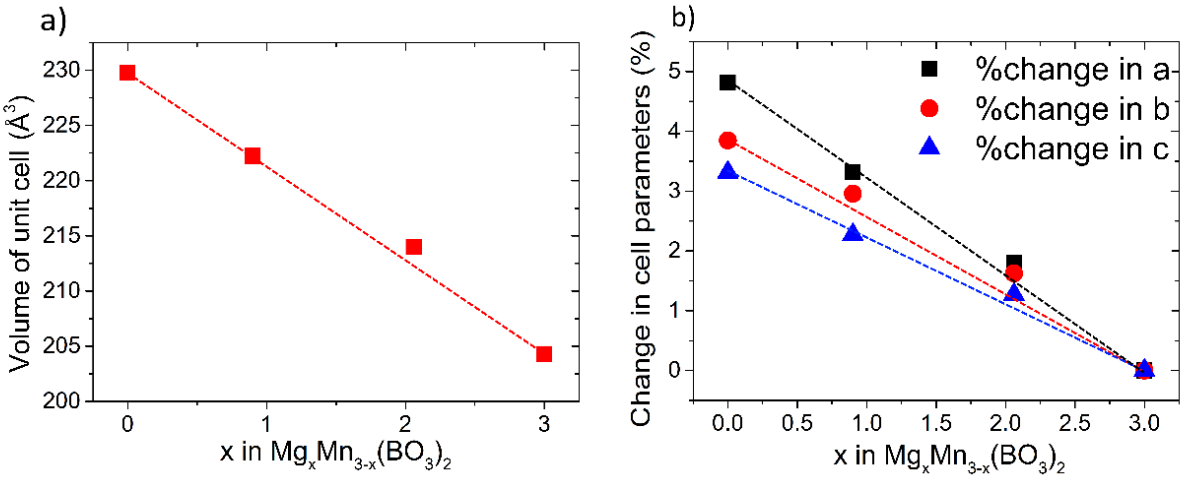

Figure 3-6. a) The change in volume across the $Mg_xMn_{3-x}(BO_3)_2$ series and b) the % change in lattice parameters across the series. Lines connecting the end members show how parameters would vary if the change was completely linear.

Table 3-2. Refined structural parameters for the $Mg_xMn_{3-x}(BO_3)_2$ system in the *Pnmn* space group. Errors are given in brackets for refined values. A combined PND and PXRD refinement was used for the $Mg_2Mn(BO_3)_2$ phase while PXRD only was used for $MgMn_2(BO_3)_2$, using B and O positions from $Mg_2Mn(BO_3)_2$.

		$Mg_3(BO_3)_2$[164]	**$Mg_2Mn(BO_3)_2$**	**$MgMn_2(BO_3)_2$**	**$Mn_3(BO_3)_2$**[162]
χ^2			1.45	2.87	
R_{wp}			5.91	5.63	
a (Å)		5.398	5.4947(2)	5.57697(8)	5.638
b (Å)		8.416	8.5526(0.3)	8.6650(1)	8.714
c (Å)		4.497	4.5542(2)	4.59915(2)	4.633
Vol ($Å^3$)		204.297	214.017(4)	222.252(6)	227.617
M1	Occ (Mg/Mn)	1/0	0.816/0.184(1)	0.579/0.421(1)	0/1
(2a)	B_{iso} ($Å^2$)	1	0.7(1)	1.8(1)	1.5
(0,0,0)					
M2	y	1	0.8(2)	0.97(7)	0.8
(4f)	Occ (Mg/Mn)	1/0	0.623/0.377(2)	0.224/0.776(3)	0/1
$(0,y,\frac{1}{2})$	B_{iso} ($Å^2$)	0.321	0.3123(7)	0.3119(2)	0.3116
Refined Mg/Mn ratio		n/a	$Mg_{2.06(3)}Mn_{0.94(3)}$	$Mg_{1.03(04)}Mn_{1.98(4)}$	n/a
B	x	0.25	0.2548(5)	0.2548	0.258
4g	z	0.56	0.5458(5)	0.5458	0.475
(x,0,z)	B_{iso} ($Å^2$)	1	0.60(5)	0.60	1
O1	x	0.316	0.3173(5)	0.3173	0.299
4g	z	0.258	0.2522(6)	0.2522	0.760
(x,0,z)	B_{iso} ($Å^2$)	1	1.10(5)	1.10	0.8
O2	x	0.218	0.2050(4)	0.2050	0.216
8h	y	0.139	0.1373(2)	0.1373	0.13
(x,y,z)	z	0.705	0.6996(4)	0.6996	0.302
	B_{iso} ($Å^2$)	1	0.77(3)	0.77	1

3.3.3 Synthesis of $Mg_xNi_{3-x}(BO_3)_2$ and description of the structure

The $Mg_xNi_{3-x}(BO_3)_2$ system is bright green and pure phases of both $Mg_2Ni(BO_3)_2$ and $MgNi_2(BO_3)_2$ have been synthesised and characterised by PXRD, Figure 3-7. However, the larger batch of Mg_2Ni synthesised with enriched boric acid for PND contained ~12% $MgNiB_2O_5$ impurity. So, it should be noted that although pure phase $Mg_2Ni(BO_3)_2$ can be synthesised, the characterization below was performed for a sample containing a pyroborate impurity. The refined stoichiometry of the impurity is very close to that of the main phase so its presence should not affect the results significantly. As with the other orthoborates a solid solution is formed with a small change in cell volume from $Mg_3(BO_3)_2$ to $Ni_3(BO_3)_2$, however due to the smaller ionic radii of Ni^{2+} here there is a decrease of 2.3% across the series, Figure 3-8. Significant cation ordering is observed and as with the $Mg_xCo_{3-x}(BO_3)_2$ system the transition metal occupies *M*1 preferentially, Table 3-3. Again, this is thought to be driven by the transition metal directional *d* orbitals leading to a preference for the higher symmetry site. The smaller ionic radius of Ni may also drive ordering as *M*1 is the lower volume site. In $MgNi_2(BO_3)_2$ site *M*1 is completely occupied by Ni with the rest of the Ni the occupying *M*2 with the Mg, and in the lower Ni content $Mg_2Ni(BO_3)_2$ *M*1 is 62% Ni (disorder would be 33%). These values are very similar to those observed in the $Mg_xCo_{3-x}(BO_3)_2$ systems (94% and 68%) suggesting that the phenomenon driving the cation ordering is the same.

Although the cation ordering behaviour and formation of a solid solution is similar to the $Mg_xCo_{3-x}(BO_3)_2$ system, the change in individual lattice parameters is quite different. Here there is very little change in *a* across the series, whereas in $Mg_xCo_{3-x}(BO_3)_2$ and $Mg_xMn_{3-x}(BO_3)_2$ *a* saw the greatest change. There is a reduction in both *b* and *c* associated with contracting the channels the B occupy rather than the distances between BO_3. The reasons for the differences in cell parameter changes between Co, Mn and Ni based systems are unclear.

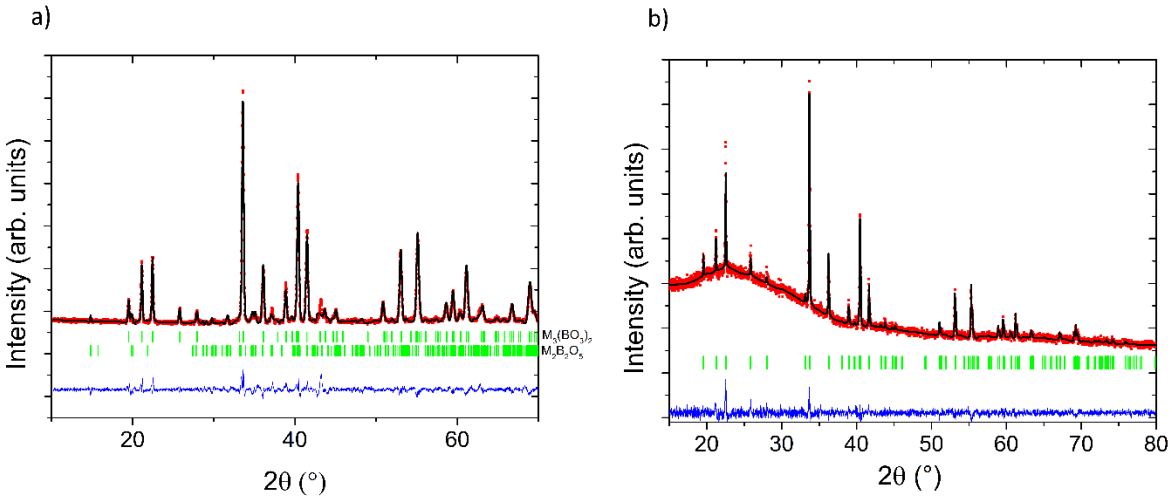

Figure 3-7. Rietveld refinement (black line) of a) PND data for $Mg_2Ni(BO_3)_2$ (red dots) and b) PXRD data for $MgNi_2(BO_3)_2$ (red dots). Allowed Bragg reflections for the phase are shown with green ticks, and difference between data and refinement with blue line.

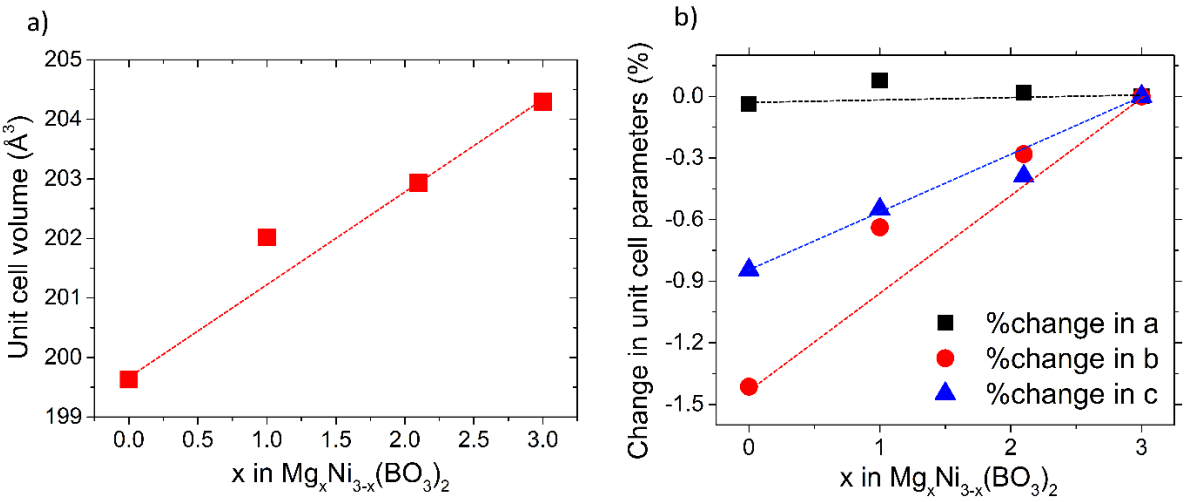

Figure 3-8. a) The change in volume across the $Mg_xNi_{3-x}(BO_3)_2$ series and b) the % change in lattice parameters across the series. Lines connecting the end members show how parameters would vary if the change was completely linear.

Table 3-3. Refined structural parameters for the $Mg_xNi_{3-x}(BO_3)_2$ system in the *Pnmn* space group. Errors are given in brackets for refined values. A combined PND and PXRD refinement was used for the $Mg_2Ni(BO_3)_2$ phase while PXRD only was used for $MgNi_2(BO_3)_2$, using B and O positions from $Mg_2Ni(BO_3)_2$.

		$Mg_3(BO_3)_2$[164]	**$Mg_2Ni(BO_3)_2$**	**$MgNi_2(BO_3)_2$**	**$Ni_3(BO_3)_2$**[168]
χ^2			4.88	1.33	
R_{wp}			5.14	4.56	
a (Å)		5.398	5.3989(6)	5.4021(1)	5.396
b (Å)		8.416	8.39233(9)	8.3623(3)	8.297
c (Å)		4.497	4.47952(5)	4.4723(1)	4.459
Vol ($Å^3$)		204.297	202.934(4)	202.02(1)	199.63
M1	Occ (Mg/Ni)	1/0	0.376/0.624(3)	0/1	0/1
(2a)	B_{iso} ($Å^2$)	1	0.26(4)	0.8	1.38
(0,0,0)					
M2	y	1	0.51(3)	0.8	1.23
(4f)	Occ (Mg/Ni)	1/0	0.874/0.126(3)	0.524/0.476(7)	0/1
$0,y,\frac{1}{2}$	B_{iso} ($Å^2$)	0.321	0.3130(2)	0.3138(6)	0.1846
Refined Mg/Ni ratio		n/a	$Mg_{2.1(06)}Ni_{0.9(06)}$	$Mg_{0.95(08)}Ni_{1.95(08)}$	n/a
B	x	0.25	0.2563(3)	0.2563	0.256
4g	z	0.56	0.5435(3)	0.5435	0.548
(x,0,z)	B_{iso} ($Å^2$)	1	0.31(3)	0.31	1.3
O1	x	0.316	0.3235(3)	0.3235	0.325
4g	z	0.258	0.2498(4)	0.2498	0.246
(x,0,z)	B_{iso} ($Å^2$)	1	0.366(3)	0.366	0.1
O2	x	0.218	0.2040(2)	0.2040	0.202
8h	y	0.139	0.1390(1)	0.1390	0.140
(x,y,z)	z	0.705	0.7018(3)	0.7018	0.700
	B_{iso} ($Å^2$)	1	0.355(2)	0.355	0.3

When exposed to air a subtle structural change occurs which leads to anisotropy in the PXRD peaks. This is thought to be due to hydration of the structure causing a distortion, as heating to 100 °C in a vacuum oven or storing under argon reverses the change. A comparison of PXRD data for a sample held in air and a sample held in a vacuum oven can be seen in Figure 3-9.

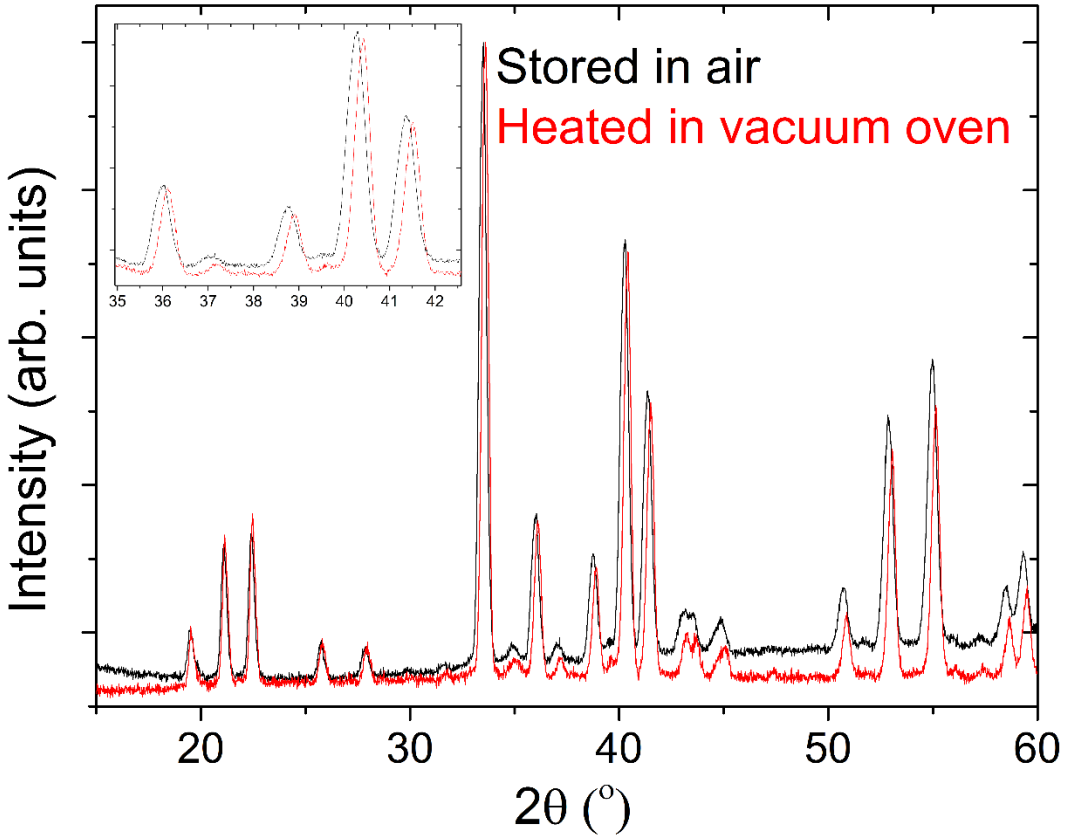

Figure 3-9. Comparison of PXRD collected for $Mg_2Ni(BO_3)_2$ stored in air at room temperature and stored in a vacuum oven at 100 °C. Inset shows a blow up of the 35 – 43° 2θ region.

3.3.4 Synthesis of $Mg_2Co_{0.5}Ni_{0.5}(BO_3)_2$ and description of the structure

It has been shown that two divalent metals can occupy the *M*1 and *M*2 sites and successful synthesis of $Mg_2Co_{0.5}Ni_{0.5}(BO_3)_2$ shows that the structure can also accommodate 3 different ions. This stoichiometry was chosen as Co and Ni have shown a preference for site *M*1, which when fully occupied supplies one ion to the formula unit. Therefore, if the material displays complete cation ordering the Co and Ni will occupy *M*1 only, with *M2* being fully occupied by Mg.

The PXRD analysis shows that the synthesis was successful, though a small $CoAl_2O_4$ impurity is present (0.65%) due to reaction with the alumina crucible, Figure 3-10. Even though a Co containing impurity is present, both the pink colour of the material and the PXRD refinement indicate the presence of Co in the final compound. The lack of peak splitting indicates that a single phase containing Mg, Co and Ni has been formed, rather than separation into Mg,Co and Mg,Ni materials. The refinement used the $Mg_2Co(BO_3)_2$ combined PND and PXRD determined structure as a starting point with refined parameters given in Table 3-4. As Co and

Ni have similar atomic numbers PXRD is not sensitive to refining their relative occupancies, therefore their occupancies were tied together during the refinement. Consequently cation ordering is discussed in terms of Mg vs. (Co,Ni).

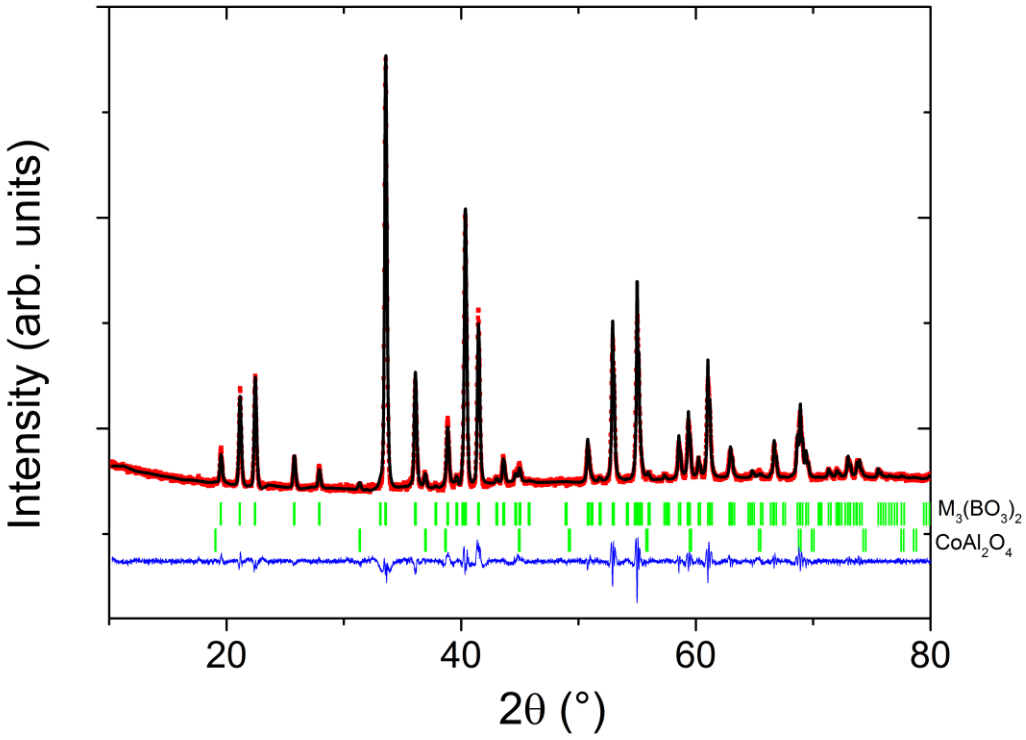

Figure 3-10. Rietveld refinement (black line) for $Mg_2Co_{0.5}Ni_{0.5}(BO_3)_2$ PXRD data (red dots) with allowed Bragg reflections for the orthoborate and spinel impurity (green tick marks) and difference pattern (blue line).

Table 3-4. Structural data for $Mg_2Co_{0.5}Ni_{0.5}(BO_3)_2$ from PXRD. The Co and Ni occupancies were linked as they are indistinguishable in PXRD. O and B positions and thermal parameters from $Mg_2Co(BO_3)_2$ PND refinement were used.

		$Mg_2Co_{0.5}Ni_{0.5}(BO_3)_2$
χ^2		5.25
R_{wp}		1.79
a (Å)		5.4149(3)
b (Å)		8.4134(4)
c (Å)		4.4975(2)
Vol (Å^3)		204.90(1)
M1 (2a) (0,0,0)	Occ (Mg/(Co,Ni)	0.384(1)/0.616(1)
	B_{iso} (Å^2)	0.2(1)
M2 (4f) 0,y,$\frac{1}{2}$	y	0.5(1)
	Occ (Mg/(Co,Ni)	0.808(1)/0.192(1)
	B_{iso} (Å^2)	0.7(1)
B 4g (x,0,z)	x	0.2559
	z	0.5434
	B_{iso} (Å^2)	0.19
O1 4g (x,0,z)	x	0.3223
	z	0.2491
	B_{iso} (Å^2)	0.31
O2 8h (x,y,z)	x	0.2064
	y	0.1393
	z	0.6980
	B_{iso} (Å^2)	0.35
wt% of $CoAl_2O_4$		0.65(3)

Co and Ni display a clear preference to occupy *M*1, with 61.6% of transition metals present on this site. This is consistent with the cation ordering observed for $Mg_2Ni(BO_3)_2$ and $Mg_2Co(BO_3)_2$ in which 62% and 68% of the ion sit in this site respectively. The unit cell volume of $Mg_2Co_{0.5}Ni_{0.5}(BO_3)_2$ is 205.108 Å^3, which is between the volumes of $Mg_2Co(BO_3)_2$ (206.8 Å^3) and $Mg_2Ni(BO_3)_2$ (202.93 Å^3), as would be expected for a solid solution, Figure 3-11.

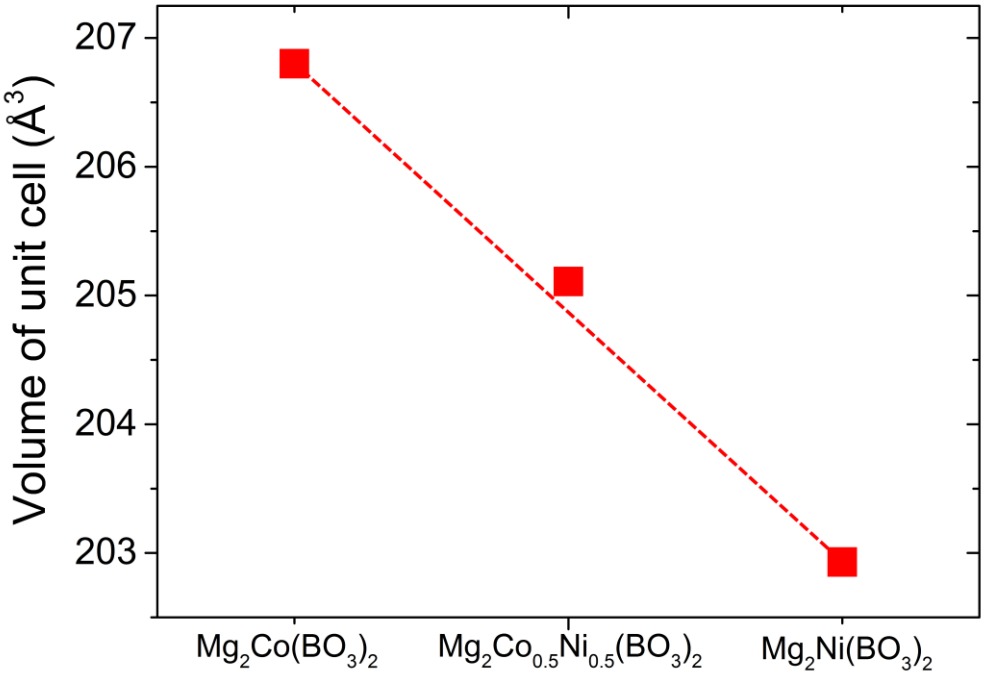

Figure 3-11. Unit cell volume with varying Co and Ni content in $Mg_2(Co,Ni)(BO_3)_2$. Line connecting the end members show how parameters would vary if the change was completely linear.

3.4 Bond valence sum (BVS) calculations

BVS calculations were used to assess the potential for Mg- and Li-ion diffusion in the orthoborates. The value at which a percolating network is formed can give an indication as to the likely kinetic barrier to diffusion, as well as details of the diffusion pathway. For comparison, in the pyroborate a percolating network is formed with a valance variance of 0.2 v.u., $FePO_4$ at 0.1 v.u. and $MgMnSiO_4$ at 0.3 v.u..[98] Calculations were carried out for a Li^+ ion and a Mg^{2+} ion on crystallographic information files (CIFs) containing only the anion structure.

BVS calculations for orthoborates with an Mg^{2+} ion with valence variance of $\pm$0.2 v.u (where a percolating network is formed in the pyroborates, see Chapter 4),[98] show only small isolated sections of the cell are accessible, and no clear diffusion pathway is formed, Figure 3-12. An interstitial site in the centre of a triangle formed of 2*M*2 and 1*M*1 is observed, however it does

not link to either site directly. Increasing the variance to $\pm$0.7 v.u. leads to the formation of a percolating network for a Mg^{2+} ion, Figure 3-12. The network links the two *M* sites by extending the interstitial site observed at $\pm$0.2 v.u and forming a continuous layered network in the *c* direction. An ion diffusing through this pathway must pass through one of the *M* sites, therefore cation disorder may severely hinder diffusion by blocking the pathway. There is a difference in pathway for the two *M* sites, where an ion on site *M*1 does not have to pass through *M*2, so cation ordering where Mg occupies site *M*1 could be advantageous. If Mg preferentially occupies *M*2, diffusion could be hindered as movement from this site must involve passing through *M*1. This is in contrast with the pyroborates where the percolating network is through interstitial sites, therefore diffusion is not blocked by ions occupying the *M* sites. Further increasing the variance to $\pm$1.2 v.u. links the layers to form a 3d network, however the barrier for an ion moving between the layers is likely to be too high to be utilised during cycling of a battery.

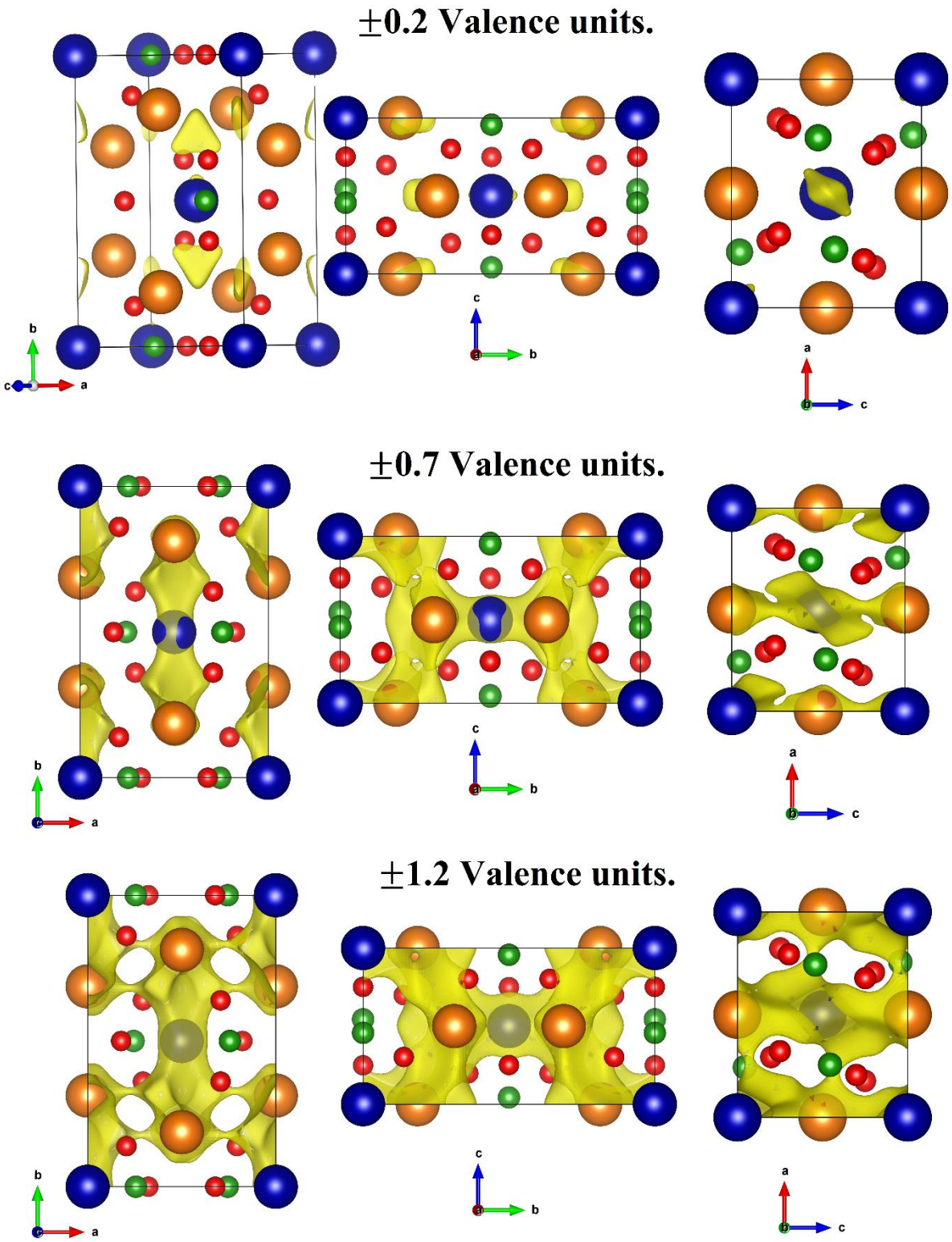

Figure 3-12. Bond valence sum maps for a Mg^{2+} ion in the orthoborate cell with a variance in valence unit of 0.2, 0.7 and 1.2 v.u. The isosurface for a given value is shown in yellow. Blue spheres in the cell represent *M*1, orange spheres are *M*2, green spheres are boron and red spheres are oxygen.

When cycled vs. a Li anode, a cathode formed of an orthoborate would have the Mg^{2+} ions removed and replaced with Li^{+} ions, therefore it may be informative to compare the BVS isosurfaces of Li^{+} to Mg^{2+}. The univalent Li ion forms a percolating network at a lower valance variance than that observed for Mg^{2+} (0.45 v.u. compared to 0.7 v.u.), Figure 3-13. This suggests that if Li can be inserted into the structure it will be more mobile than the Mg it replaces. Li^{+} is known to have a lower kinetic barrier to diffusion than Mg^{2+} in many materials,[72,80,87] so this result fits with the existing literature. With a variance of 0.7 v.u. a full 3d percolating network is formed, whereas this requires a variance of 1.2 v.u. in the Mg^{2+} calculations, again suggesting Li^{+} diffusion in the orthoborates will be easier than Mg^{2+}.

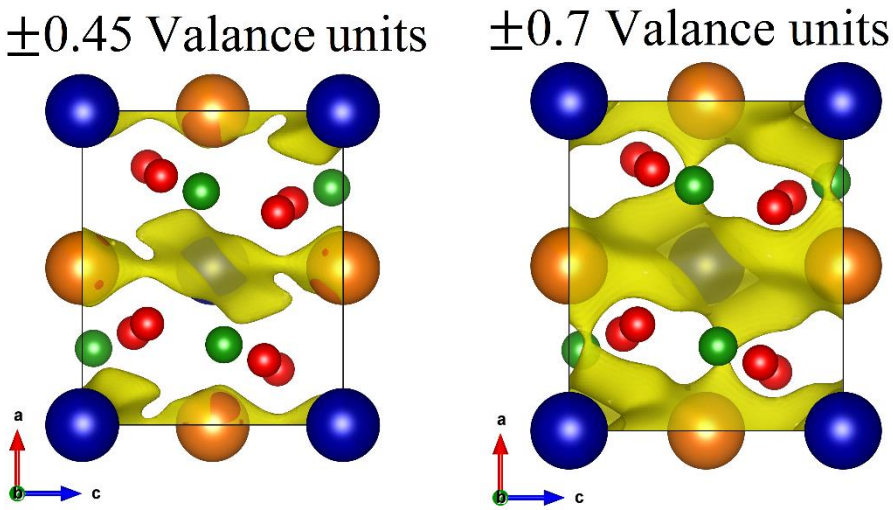

Figure 3-13. BVS maps for a Li^{+} ion in the orthoborate structure. A percolating layer is formed in the *c* direction with 0.45 v.u. variance (left) while the layered networks join to form a 3d percolating network at with a variance of 0.7 v.u. (left).

The BVS maps suggest that Mg diffusion is possible and that cation ordering, with Mg occupying *M*1, would be beneficial to this diffusion. Unfortunately, both Co and Ni display a preference for site *M*1 which may block the diffusion channels. Mn however shows little cation order so a greater proportion of Mg occupies *M*1. The high valance variance required to form a percolating network suggests removal will be more sluggish than in the pyroborates (Chapter 4), and so may require slow rates or high temperatures to achieve significant capacities.

3.5 Electrochemistry

In the Mg rich compounds, $Mg_2M(BO_3)_2$, removal of 1 Mg to form $MgM^{4+}(BO_3)_2$ would give a capacity of ~240 mAh g^{-1} (depending on the transition metal). Full Mg removal would require oxidation of the transition metal to M^{6+}, which is improbable. Li insertion into the oxidised material to form $Li_2MgM^{2+}(BO_3)_2$ gives a theoretical capacity of ~265 mAh g^{-1}.

In the lower Mg content materials, $MgM_2(BO_3)_2$, full extraction of the Mg would lead to the transition metal having a 3+ oxidation state ($M_2(BO_3)_2$ with a theoretical capacity of ~210 mAh g^{-1}. Insertion of 2 Li into the oxidised material to fully reduce the transition metals back to their original oxidation states gives capacities ~235 mAh g^{-1}.

In terms of capacity, the ideal stoichiometry is $Mg_{1.5}M_{1.5}(BO_3)_2$ as this represents the highest Mg content that could be removed while maintaining reasonable transition metal oxidation states. Full extraction of Mg to form a material with 4+ oxidation ($M_{1.5}(BO_3)_2$) state gives theoretical capacities of ~340 mAh g^{-1}. Insertion of 3 Li^+ to reduce the transition metal to its original state would yield capacities of ~400 mAh g^{-1}.

3.5.1 $MgMn_2(BO_3)_2$ electrochemistry

Full removal of the Mg from the structure to form $Mn_2^{3+}(BO_3)_2$ has a theoretical capacity of 212.87 mAh g^{-1}. Insertion of 2 Li to form $Li_2Mn_2^{3+}(BO_3)_2$ would give 235.6 mAh g^{-1}.

Charging $MgMn_2(BO_3)_2$ vs. a Li anode gives a capacity of 16 mAh g^{-1}, meaning 0.075 Mg^{2+} are removed from the cell (7.5% of the theoretical capacity), Figure 3-14. The low capacity indicates that the material is electrochemically active, but diffusion is hindered, as suggested by the BVS calculations. The material is also expected to be electronically insulating which could further hinder performance. Two clear plateaus are observed, the first starting at 4.0 V and the second above 4.3 V. As these two processes are relatively close in potential, it is likely they are due to Mg removal from *M*1 and *M*2, which due to differing environments will have different free energies. A difference in voltage could also be attributed to further Mn redox reactions ($Mn^{2+/3+}$ and $Mn^{3+/4+}$), however as full extraction of Mg yields a wholly 3+ material this is unlikely, even though Mg removal requires a 2-electron process. Oxidation from Mn^{2+} to Mn^{3+} and Mn^{4+} would also be expected to have a much larger difference in potential than is observed here.

Subsequent discharge results in the insertion of 0.09 Li^+ ions into the structure (11 mAh g^{-1}), which is just over 1 Li ion for each Mg removed. The theoretical capacity was calculated assuming 2:1 Li:Mg replacement as this retains the same number of electrons transferred, however the insertion of Li may be limited by the number of crystallographic sites available. This occurs over a predominantly sloping voltage profile, with a small shoulder at 2.2 V. This process is fully reversible on charge, however, on continued cycling the capacity fades to 7.3 mAh g^{-1} and the shoulder becomes less apparent. After 120 cycles the capacity is stabilised to a fully reversible 7 mAh g^{-1}. Comparing this to the Mn based pyroborates discussed in Chapter 4, the orthoborate does not have the excess capacity on charge or the gradual increase in

capacity on extended cycling. This could be due to less structural change occurring on cycling, either caused by inherent stability of the material, or simply because fewer ions are being removed/inserted, exerting less strain on the structure.

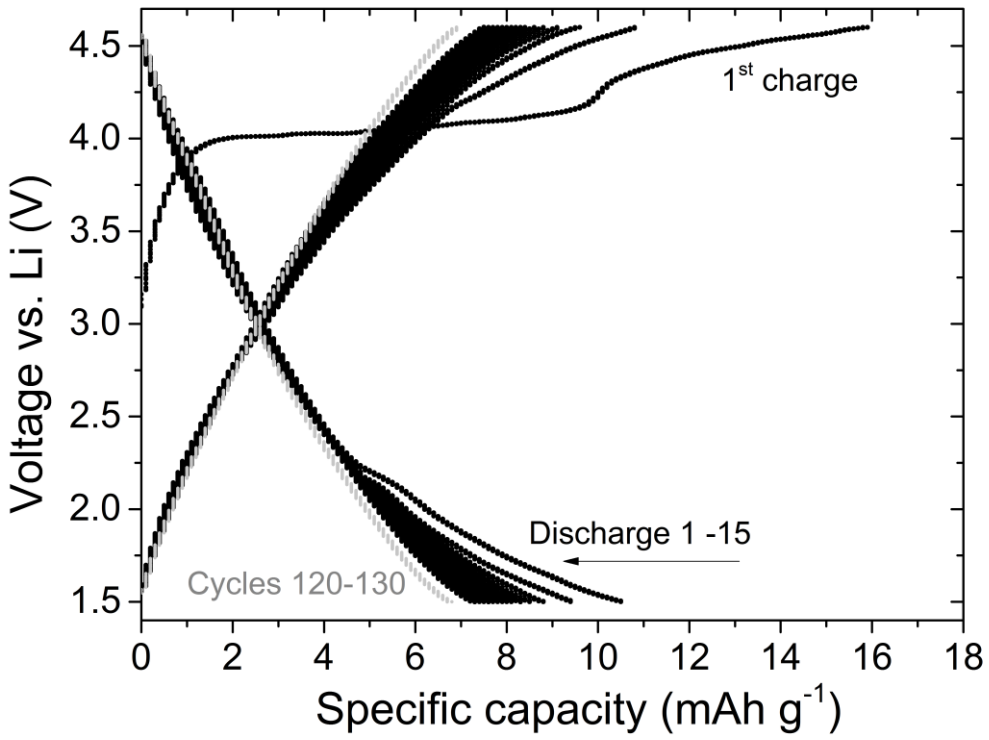

Figure 3-14. Cycling behaviour of $MgMn_2(BO_3)_2$ at C/25 vs. a Li anode at room temperature. The first charge involves Mg removal from the structure while later cycles involve Li (de)intercalation. The 1st 15 cycles are in black, with cycles 120-130 shown in grey.

With the aim to overcome the sluggish kinetics of Mg removal, cells were cycled at the slower rate of C/100, Figure 3-15. The first charge (Mg removal) capacity is improved, with 29.6 mAh g^{-1} or 0.14 Mg^{2+}, achieved, double that observed at C/25 and 14.0% of the theoretical capacity. The voltage profile shows 4 electrochemical regions, including two at lower voltage than those observed at the higher rate (3.3 V and 3.5 V). These may be the same process observed at C/25 with reduced overpotential, while the two higher voltage processes may have been above the voltage limit at C/25. The presence of regions not observed at higher rates suggests these processes are severely diffusion rate limited and so can only progress at slow rates.

On Li insertion, a similar voltage profile to C/25 is observed, with a shoulder at ~2.3 V, but here a capacity of 26.0 mAh g^{-1} is achieved, equating to 0.2 Li^+ ions. This is not fully reversible with 24 mAh g^{-1} removed on 2nd charge, and capacity fade is again observed over subsequent cycles. The improved capacity at slower rates indicates that reversible intercalation is possible in the material, but it is hindered by poor electronic or ionic conductivity. Previous studies have shown that these issues can be mitigated by optimising cathode construction and material synthesis, therefore improved performance could come from further study.

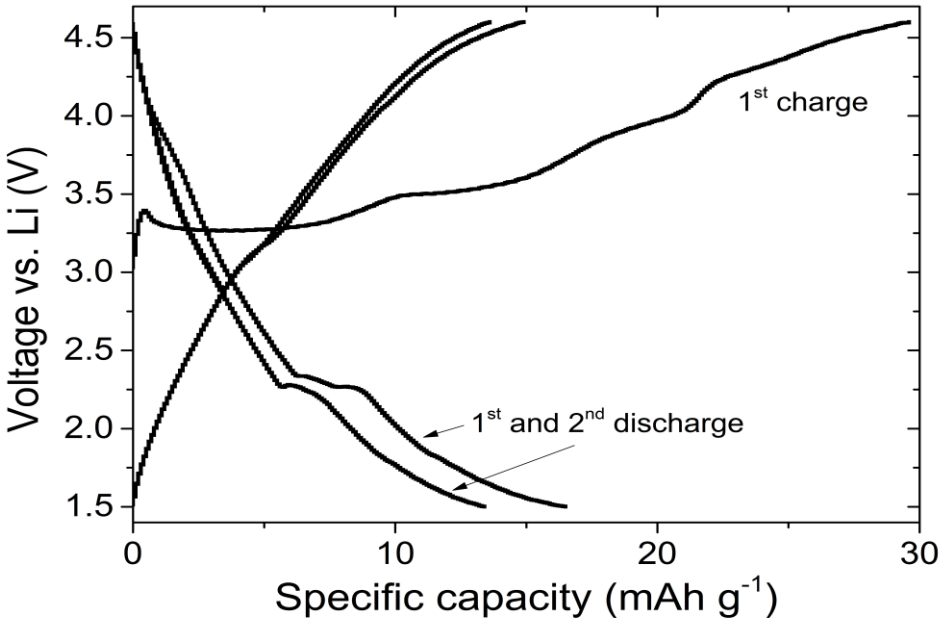

Figure 3-15. Cycling behaviour of $MgMn_2(BO_3)_2$ at a rate of C/100 vs. a Li anode.

Cells were also cycled at 55 °C at C/25 to try and improve diffusion kinetics, and greater reversible capacity was achieved, Figure 3-16. On charge 44.5 mAh g^{-1} or 0.2 Mg were removed from the cell, more than at both C/25 and C/100 at room temperature. The voltage profile is more similar to C/25 at room temperature than C/100, with two clear plateaus after an initially high polarisation. The overpotential of both regions are reduced but the first more significantly, with the lower voltage plateaus starting at 3.4 V rather than 4.0 V, and the higher voltage region occurring above 4.0 V instead of 4.2 V. This reduction of overpotential accounts for the increased capacity achieved.

On discharge (Li insertion) a higher capacity is also achieved (26.1 mAh g^{-1}, 0.22 Li^+), again roughly replacing each Mg^{2+} ion removed with 1 Li^+. A shoulder at 2.4 V is observed, with a 0.2 V reduction in overpotential, and here it is much more pronounced than at room temperature.

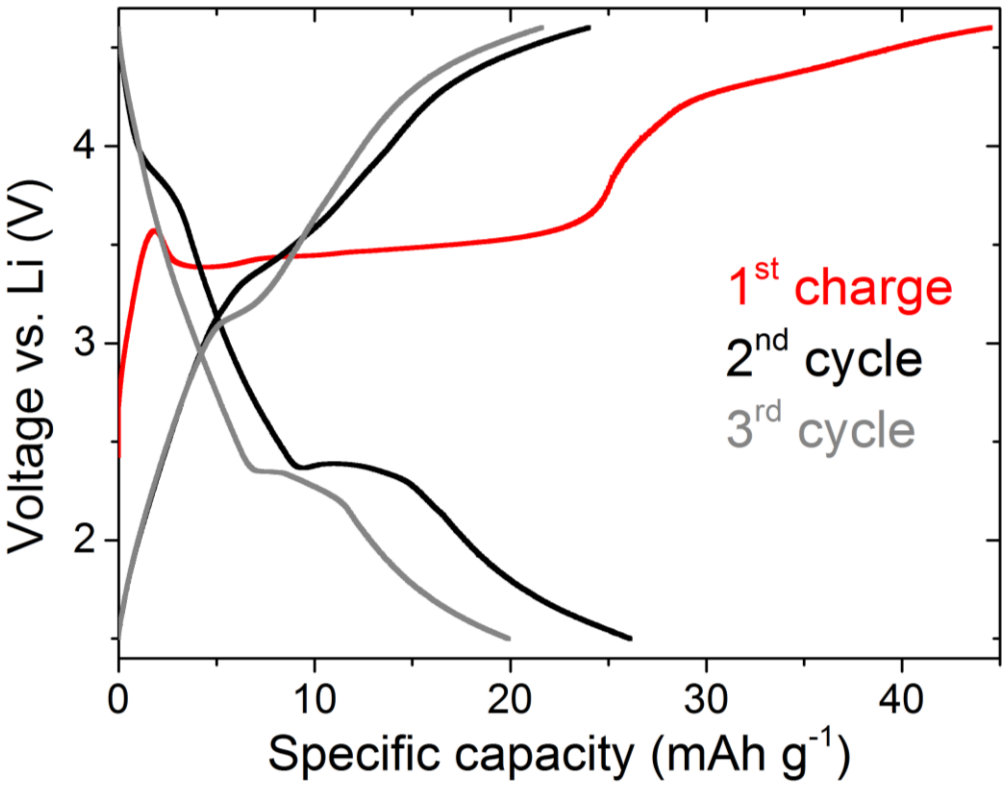

Figure 3-16. Cycling behaviour of $MgMn_2(BO_3)_2$ vs. a Li anode at 55 °C at a rate of C/25.

3.5.2 $Mg_2Mn(BO_3)_2$ electrochemistry

In the Mg rich $Mg_2Mn(BO_3)_2$ phase the more mobile site *M*1 is predominantly occupied by Mg (0.816 Mg, 0.184 Mn), which may aid diffusion as fewer immobile Mn are present to block the diffusion pathway. Removal of 1 Mg^{2+} to form $MgMn^{4+}(BO_3)_2$ gives a theoretical capacity of 243.2 mAh g^{-1}, with subsequent insertion of 2 Li^+ resulting in a theoretical capacity of 272.3 mAh g^{-1}.

On first charge vs. a Li anode a capacity of 99.4 mAh g^{-1} is achieved, equivalent to the removal of 0.4 Mg^{2+} per formula unit to form $Mg_{1.6}Mn(BO_3)_2$, Figure 3-17. Mg^{2+} removal occurs over two distinct electrochemical processes, the first is a plateau at 3.5 V which accounts for ~60 mAh g^{-1} of the capacity, followed by a second, more sloping process above 4.2 V. These may be attributed to either removal from the two differing *M* sites or oxidation of the Mn^{2+} to Mn^{3+} then Mn^{4+}. The voltage of the electrochemical regions is similar to the high temperature cycling in the $MgMn_2(BO_3)_2$ material; this and the higher capacities achieved suggest Mg^{2+} diffusion is easier in the Mg rich material.

On discharge a capacity of 46.7 mAh g^{-1} is achieved (0.34 Li^+ per unit cell), which equates to 85% replacement of the number of Mg^{2+} ions removed, and less than half the number of

electrons. Therefore, as with the $MgMn_2(BO_3)_2$ material, it seems that Li insertion is limited by the number of crystallographic sites available, rather than the oxidation state of Mn. The insertion of Li^+ is reversible, with 45.5 mAh g^{-1} achieved on the subsequent charge, however gradual capacity fade is observed over the following cycles.

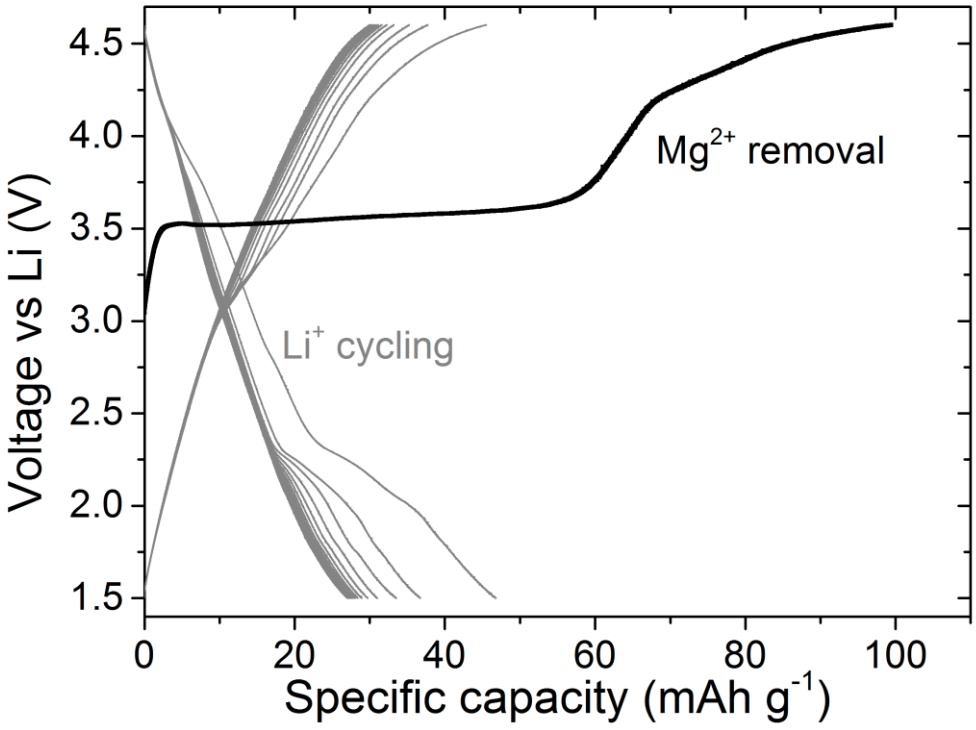

Figure 3-17. Cycling behaviour of $Mg_2Mn(BO_3)_2$ in a Li-ion cell cycled at room temperature at a rate of C/25.

Cycling at increased temperatures (55 °C) results in improved Mg^{2+} removal capacity, 209.9 mAh g^{-1} or 0.86 Mg^{2+}, Figure 3-18. This is roughly equal to the amount of Mg present on site *M*1 as calculated by Rietveld analysis (0.81). As with the room temperature cycling this occurs over two voltage regions, here the first plateau is at 3.25 V with the second process above ~4.2 V. The relatively large difference in voltage, and the fact that removal of 0.86 Mg^{2+} requires oxidation of at least some of the Mn^{2+} to Mn^{4+} suggests these two process may be due to $Mn^{2+/3+}$ and $Mn^{3+/4+}$ oxidation. These values are similar to those observed for 2-electron, Mn containing, cathode $Na_3MnPO_4CO_3$ (3.4 V and 4.0 V).[175]

On discharge 83.5 mAh g^{-1} is achieved meaning 0.61 Li^+ have been inserted into the cell. This is a greater capacity than achieved at room temperature but is still less than 1 Li^+ inserted for each Mg^{2+} removed. Excess capacity is observed on charge, presumably caused by electrolyte breakdown induced by the increased temperatures.

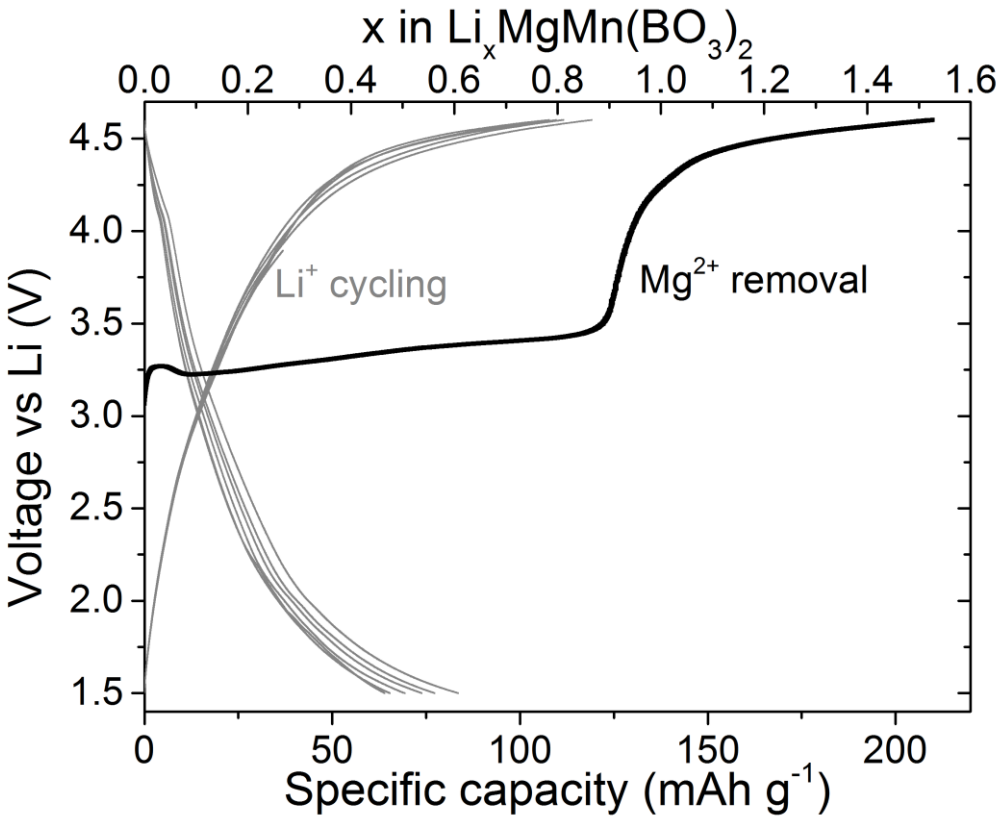

Figure 3-18. Cycling behaviour of $Mg_2Mn(BO_3)_2$ in a Li ion cell cycled at 55 °C at a rate of C/25.

3.5.3 $Mg_2Co(BO_3)_2$ electrochemistry

Removal of 1 Mg would lead to oxidation of the Co^{2+} to Co^{4+}, with a theoretical capacity of 238.1 mAh g^{-1}. Formation of a 4+ oxidation state is in contrast with the previous section where full Mg removal forms a M^{3+} compound. Insertion of 2 Li to form $Li_2MgCo^{2+}(BO_3)_2$ would give 266.9 mAh g^{-1}.

On first charge at a rate of C/25 vs. a Li anode 31.4 mAh g^{-1} is achieved, meaning 0.13 Mg have been removed from the structure (13% of theoretical capacity), Figure 3-19. As in the $Mg_xMn_{3-x}(BO_3)_2$ system there are two clear plateaus on charge, however in this system they are at a lower voltage. The first has an average voltage of ~3.3 V and the second starts ~3.7 V with each contributing roughly equal capacity. At increased voltages there may also be a third process starting as the cell hits its voltage limit. Discharging results in insertion of 0.09 Li^+ ions with a capacity of 11.8 mAh g^{-1}, slightly less than 1 Li inserted for each Mg removed. A shoulder comparable to that observed in $MgMn_2(BO_3)_2$ is observed at 2.2 V, however, it is only obvious in the 1st cycle and fades quickly to a sloping profile. After 10 cycles the capacity is stable and fully reversible at 9.4 mAh g^{-1}.

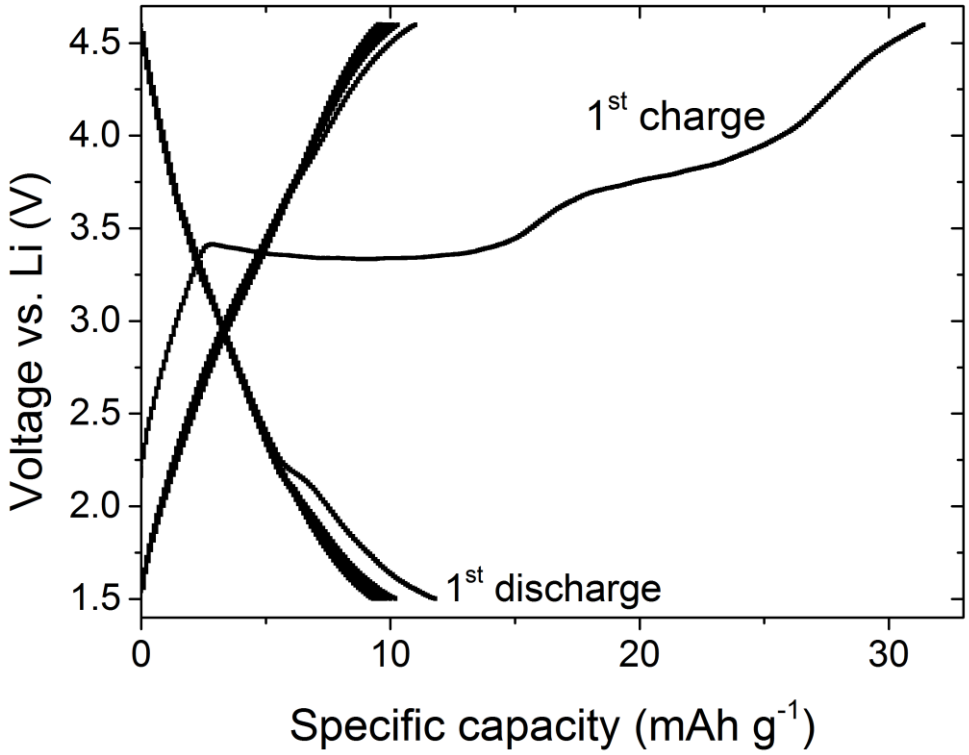

Figure 3-19. Cycling behaviour of $Mg_2Co(BO_3)_2$ vs. a Li anode at a rate of C/25.

Cycling at the slower rate of C/100, Figure 3-20 sees very little improvement in the 1st charge capacity (32.3 mAh g^{-1}), which contrasts with the behaviour of the other orthoborates studied. This suggests that removal of more than 0.13 Mg is hindered by the voltage applied rather than the kinetics of diffusion. This may be due to the cation ordering observed, with Co preferentially occupying the more mobile *M*1 site and blocking transport of Mg. However, with the excess Mg in the structure there is still significant amounts of Mg occupying *M*1 (0.32 Mg occupy *M*1 according to the Rietveld refinement). Co is also known to form very insulating borates, which renders the material electrochemically inactive, for example in thin films of $LiCoBO_3$ where <1 mAh g^{-1} was achieved.[153]

The Li insertion capacities however, are significantly improved with a first discharge capacity of 17.7 mAh g^{-1}, or 0.13 Li inserted. The discharge capacity then fades over the next 5 cycles until stabilising at a fully reversible 13 mAh g^{-1}.

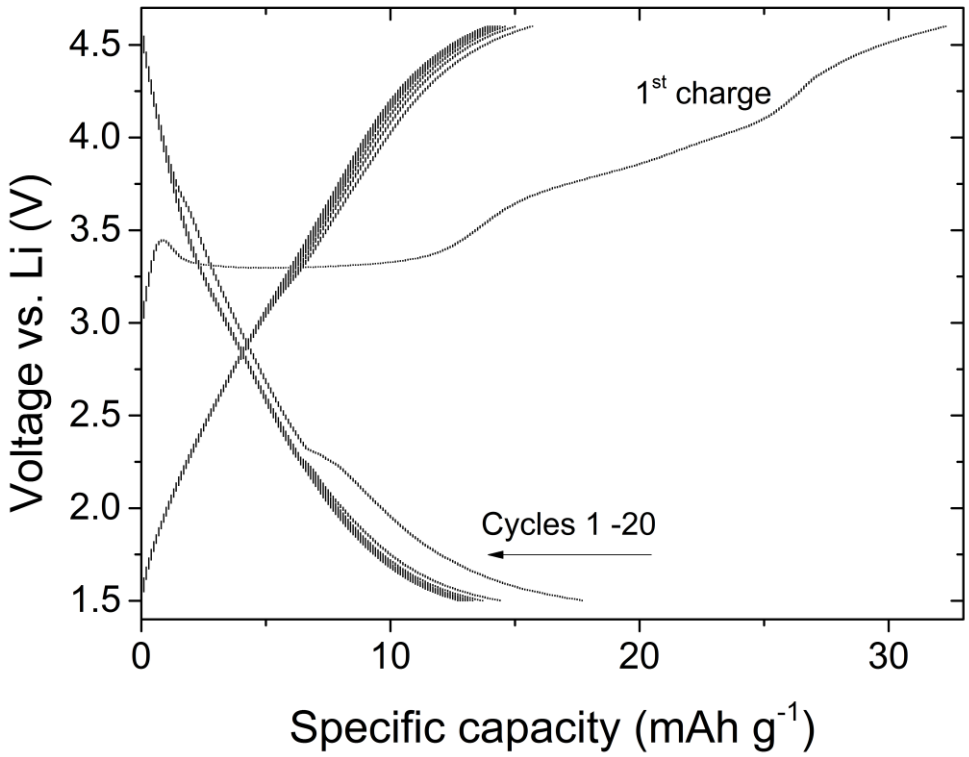

Figure 3-20. Cycling behaviour of $Mg_2Co(BO_3)_2$ vs. a Li anode at a rate of C/100.

Cycling at a higher temperature at a rate of C/25 again leads to very little change in the 1st charge capacity, Figure 3-21. Here 34.7 mAh g^{-1} was achieved, only marginally higher than the 31.4 and 32.3 mAh g^{-1} achieved at room temperature for C/25 and C/100 respectively. However, the voltage profile does differ, with the lower voltage plateau no longer being clearly visible, while the 2nd plateau is still evident. There is also a region of high polarisation at the beginning of charge, usually associated with nucleation of a new (demagnesiated) phase. The 3rd feature that looked to be starting at very high voltages at room temperature is seen to start around 4.25 V at 55 °C and contributes a large proportion of the capacity. This supports the assertion that Mg removal is limited by voltage rather than diffusion in this material.

The Li insertion capacity on discharge is further improved upon over the cells cycled at C/100, with 25.0 mAh g^{-1} or 0.19 Li inserted. The charge capacity is also increased with >20 mAh g^{-1} reversible capacity on 2nd charge. As with the previous cells the capacity fades quickly, with a reversible capacity of 19.1 mAh g^{-1} reached after 3 cycles.

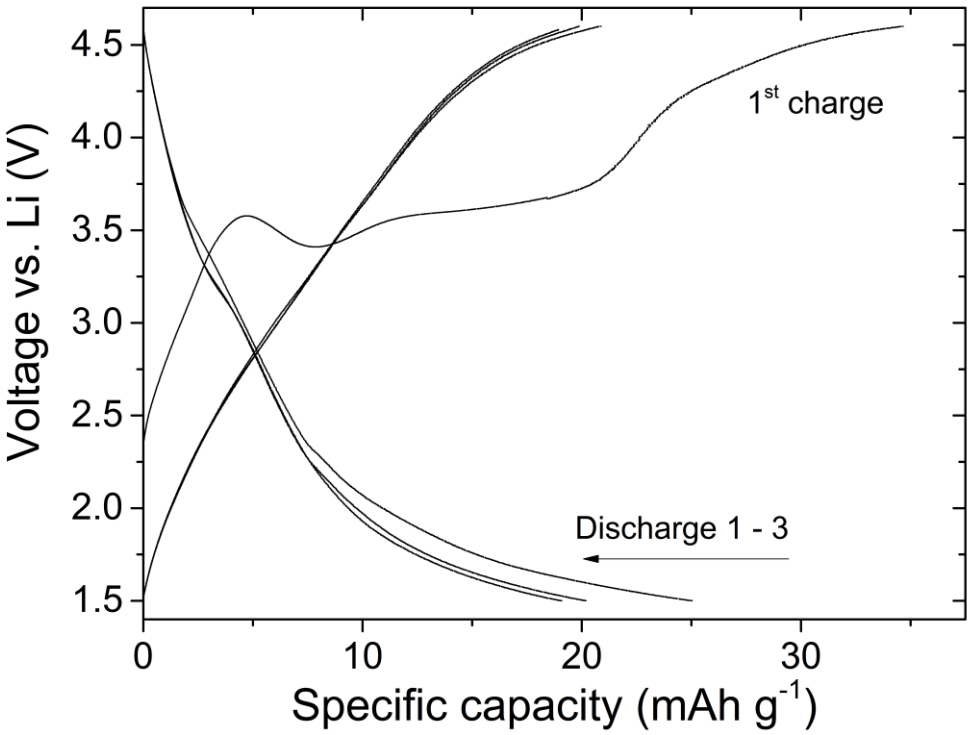

Figure 3-21. Cycling behaviour of $Mg_2Co(BO_3)_2$ vs. a Li anode at 55 °C and a rate of C/25.

3.5.4 Ex-situ diffraction

Charging $MgMn_2(BO_3)_2$ vs. Li leads to a 0.7% reduction in the volume of the unit cell relative to the uncycled material, as determined by Le Bail refinement of ex-situ material, Figure 3-22. This is a small but significant change associated with the removal of limited amounts of Mg from the cell. Unlike in the pyroborates discussed in subsequent chapters, no change in the unit cell symmetry is observed.

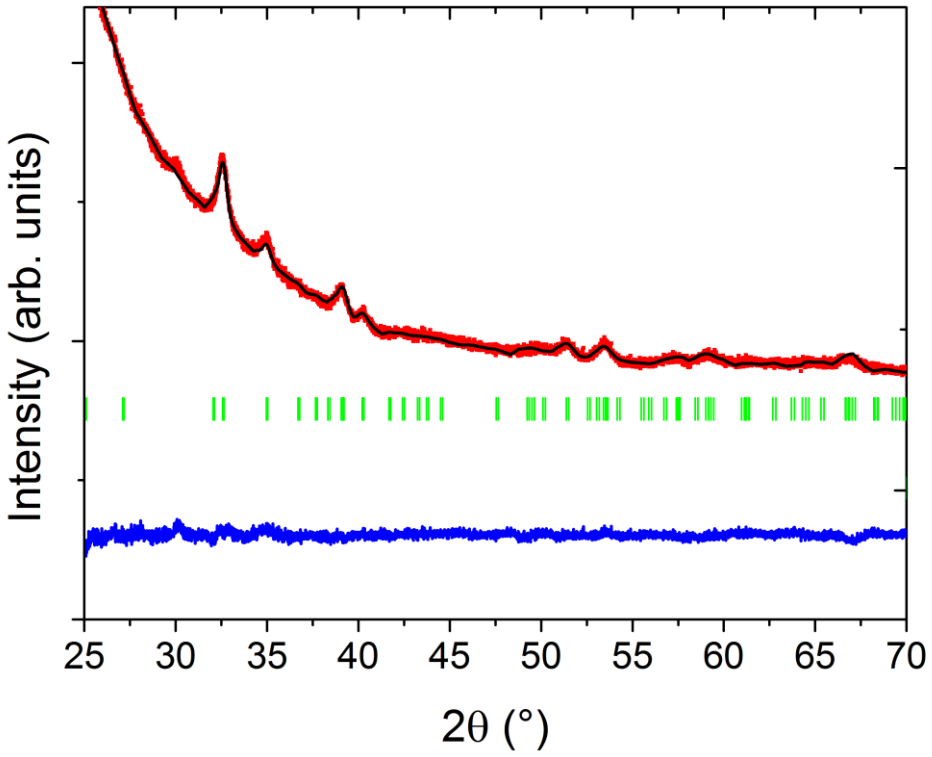

Figure 3-22. Le Bail refinement (black line) on ex-situ PXRD of $MgMn_2(BO_3)_2$ charged vs. a Li anode (red dots). Allowed Bragg reflections are in green with the difference pattern shown in blue.

On removal of ~0.9 Mg from $Mg_2Mn(BO_3)_2$ the orthoborate unit cell contracts to a volume of 208.03(3) $Å^3$, a 2.8% decrease from the pristine (214.017(4) $Å^3$). Unfortunately the broad peak shape and low intensities hinder more in-depth analysis of the changes in crystal structure, Figure 3-23. If data with an improved signal to noise ratio and more crystalline peaks (perhaps by shorter ball milling times and slower cycling) any preferential removal of Mg^{2+} from one site other another should be detectable.

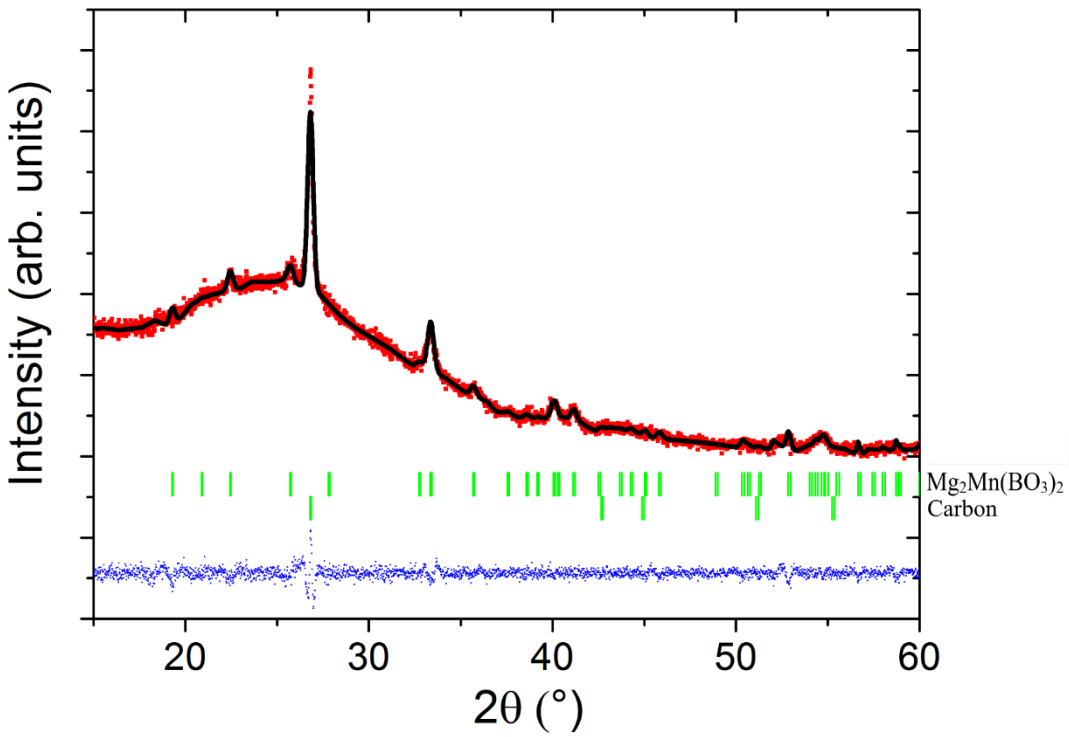

Figure 3-23. Ex-situ PXRD of $Mg_2Mn(BO_3)_2$ after charge in a Li-ion cell. The Le Bail refinement is shown in black, the PXRD data in red, the allowed Bragg reflections are in green (upper ticks are the orthoborate and lower ticks are for the carbon used in the cathode film) with the difference pattern shown in blue.

Ex-situ PXRD of $Mg_2Co(BO_3)_2$, Figure 3-24, shows that the reflections in the cycled sample's pattern appear to be shifted slightly to higher angle, indicating a reduction in unit cell volume, though the change is not definitive. Le Bail fits also suggest a reduction in unit cell volume of 2.3% (201.2(1) $Å^3$ compared to 206.013(2) $Å^3$ in the pristine material), though again this is inconclusive as there is very little change in the R_{wp} between a volume of 200 and 206 $Å^3$. However, the R_{wp} does increase significantly with unit cell volumes greater than 206 $Å^3$.

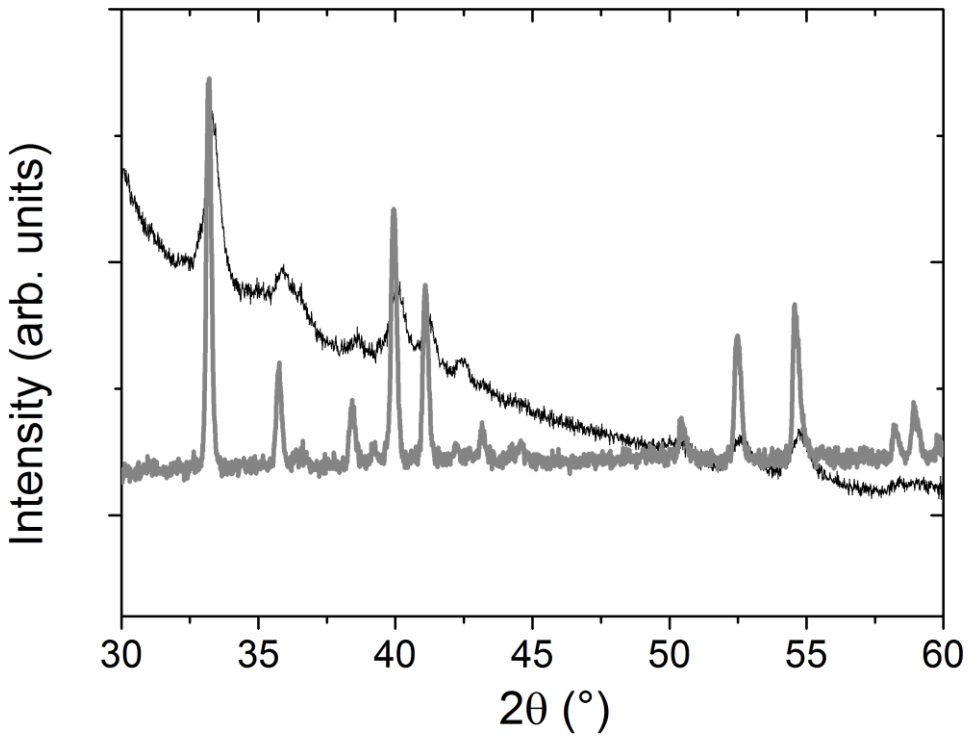

Figure 3-24. Comparison of PXRD for $Mg_2Co(BO_3)_2$ charged vs. Li (black line) and pristine $Mg_2Co(BO_3)_2$ (grey line).

3.6 Conclusions

Three series of di-cation mixed metal orthoborates have been successfully synthesised and shown to form solid solutions, these are $(Mg_xCo_{3-x}(BO_3)_2$, $(Mg_xMn_{3-x}(BO_3)_2$ and $(Mg_xNi_{3-x}(BO_3)_2$. The orthoborate structures contain two metal sites, *M*1 and *M*2 in a 1:2 ratio. Both *M* sites are distorted octahedra, but differ in the nature of their distortion. These site differences lead to cation ordering with the transition metals with directional *d* orbitals (Co, Ni) preferring to occupy the higher symmetry site *M*1, except with Mn^{2+}, which has the high spin d^5 electronic configuration and preferentially occupies the larger *M*2 site.

The higher Ni and Co content samples $MgNi_2(BO_3)_2$ and $MgCo_2(BO_3)_2$ both have *M*1 almost wholly occupied by the transition metal (100% and 94% respectively), with the excess residing on *M*2 with the Mg. In the lower Ni and Co content samples, $Mg_2Ni(BO_3)_2$ and $Mg_2Co(BO_3)_2$, ordering is still observed but to a lesser extent (62% and 68% of the ions sit in the site respectively, compared to expected values for a randomised distribution of 33%). The similarity of these values suggests the ordering mechanism is similar. Some ordering is still observed in the $(Mg_xMn_{3-x}(BO_3)_2$ however in this case the transition metal preferentially occupies site *M*2. This ordering is thought to be driven by cation size differences, with Mn being significantly

larger than Mg, and therefore being more readily accommodated in the larger site, *M*2. In reality, the cation ordering of all the phases analysed is likely a combination of the two types of driving force.

We have also shown that the 3-metal orthoborate $Mg_2Co_{0.5}Ni_{0.5}(BO_3)_2$ can be synthesised, exemplifying the flexibility and variability possible in these structures. As with the 2-metal samples Co and Ni show a strong preference for the *M*1 site. The ability to tune the composition and therefore the structure and structure-related properties of these materials means that voltage, stability and capacity could potentially be improved and optimised.

Bond valence sum calculations show that a Mg^{2+} percolating network is formed within the *M* layers with a valance variance of $\pm$0.7 v.u., suggesting diffusion may be hindered without structural changes to the cell. The diffusion pathway also requires ions to move through sites occupied by immobile transition metals, therefore cation ordering to form channels containing Mg only is preferable to disorder. Li^+ ions are expected to be more mobile as a percolating network is formed at $\pm$0.45 v.u..

When $MgMn_2(BO_3)_2$ is cycled vs. a Li anode at 55 °C 44.5 mAh g^{-1} capacity is achieved, which equates to the removal of 0.2 Mg from the structure. This occurs over two high voltage plateaus at 3.4 V and 4.0 V vs. Li. The observation that cycling at slower rates or higher temperatures gives an increase in performance indicates that Mg diffusion is the limiting factor in these experiments, as suggested by the BVS calculations. Up to 0.22 Li^+ ions can be reversibly inserted into the oxidised material (26.1 mAh g^{-1}), roughly a 1:1 swap of Mg^{2+} for Li^+ ions.

In the Mg rich $Mg_2Mn(BO_3)_2$ up to 0.86 Mg^{2+} is removed the cell at 55 °C, giving a capacity of 209.9 mAh g^{-1}. This is significantly larger than that observed in the $MgMn_2(BO_3)_2$ material and is roughly equal to the amount of Mg residing on site *M*1. Two voltage regions are observed, a plateau at 3.25 V and a more sloping process above 4.2 V, attributed to $Mn^{2+/3+}$ and $Mn^{3+/4+}$ oxidation respectively. On discharge, just under 1 Li^+ is inserted for each Mg^{2+} removed, giving a capacity of 83.5 mAh g^{-1} (0.61 Li^+). On subsequent cycles gradual capacity fade is observed, with excess capacity on charge due to electrolyte breakdown induced by the elevated temperatures.

Charge of $Mg_2Co(BO_3)_2$ sees 0.15 Mg removed from the structure, with 31.4, 32.3 and 34.7 mAh g^{-1} achieved at a rate of C/25, C/100 and C/25 at 55 °C respectively. The lack of improvement with slower rates or at increased temperatures suggests a phenomenon other than slow diffusion is hindering performance. This may be caused by immobile Co blocking the diffusions channels as Co preferentially occupies the *M*1 site (whereas Mn preferentially

occupies the *M*2 site). 3 electrochemical regions are observed at 3.3 V, 3.7 V and >4.0 V, with the high voltage region being more pronounced at increased temperatures. As with the $MgMn_2(BO_3)_2$, around 1 Li is inserted for each Mg removed, with a maximum of 25.0 mAh g^{-1} (0.19 Li^+) achieved on discharge. All cells experienced capacity fade on extended cycling with the capacity stabilising after ~10 cycles at a lower capacity than achieved on 1st discharge.

Ex-situ PXRD shows that the orthoborates undergo unit cell contractions on removal of Mg on first charge while retaining the orthoborate structure. A 2.8% contraction is observed on removal of 0.9 Mg^{2+} from $Mg_2Mn(BO_3)_2$. This is a relatively small change for removal of ~1/3 of the cations, which may aid stability of the material over many cycles. Relatively small amounts of Mg have been removed from the $MgMn_2(BO_3)_2$ and $Mg_2Co(BO_3)_2$ structures, therefore, observing only small changes in the PXRD pattern is unsurprising.

The demonstration of electrochemical processes in this new class of cathode material is exciting as although capacities are currently small compared to commercialised cells, if the improvements seen in the PO_4 and BO_3 systems could be translated to this system, then very high capacity and high voltage cathodes could be produced. The variability of stoichiometry, both in terms of transition metal and Mg content, also allows for further optimisation. A Mg to transition metal ratio of 1.5:1.5 offers the highest capacities, though as this study was looking for cation ordering and the sites are in a 2:1 ratio these materials were not synthesised. However, as a solid solution has been demonstrated to form, it is likely that these would be stable.

Chapter 4. Synthesis and electrochemical investigation of the pyroborate $Mg_xMn_{2-x}B_2O_5$

4.1 Introduction

4.1.1 Crystal structure

The crystal structure of the pyroborates ($M_2B_2O_5$, M = divalent ion) has been investigated and described by various groups, some characterised naturally occurring minerals from mines (for example in the North Korean Suan mine, giving rise to name Suanite for $Mg_2B_2O_5$ and the Fuka mine in Okayama Prefecture, Japan.) and others from synthetic samples.[176–178] The MB_2O_5 (M = Mg, Mn, Fe, Co, Sc etc.) system produces heteromorphous monoclinic ($P2_1/c$) and triclinic ($P\bar{1}$) crystals, which differ only in slight deviations from 90˚ angles and a smaller unit cell for the triclinic polymorph, Figure 4-1.[179] The larger monoclinic cell results from a doubling of the c direction (for $P\bar{1}$ – setting 1). The polyanion framework is formed of $B_2O_5^{4-}$ units (two corner-sharing BO_3 triangles), which link ribbons of edge-sharing MO_6 octahedra. The ribbons extend over four MO_6 units, creating M_4O_{18} tetramers which share edges to form chains which extend infinitely along the a axis, Figure 4-2. Within the ribbons there are two crystallographically distinct sites, $M1$ and $M2$, present in a 1:1 ratio. The $M1$ site (blue octahedra) is more distorted and larger than $M2$ (purple octahedra) with larger bond angle variance. Due to the differing environments of $M1$ and $M2$ there is the possibility of cation ordering over the sites when two different M cations are used (as observed in the orthoborates, Chapter 3).

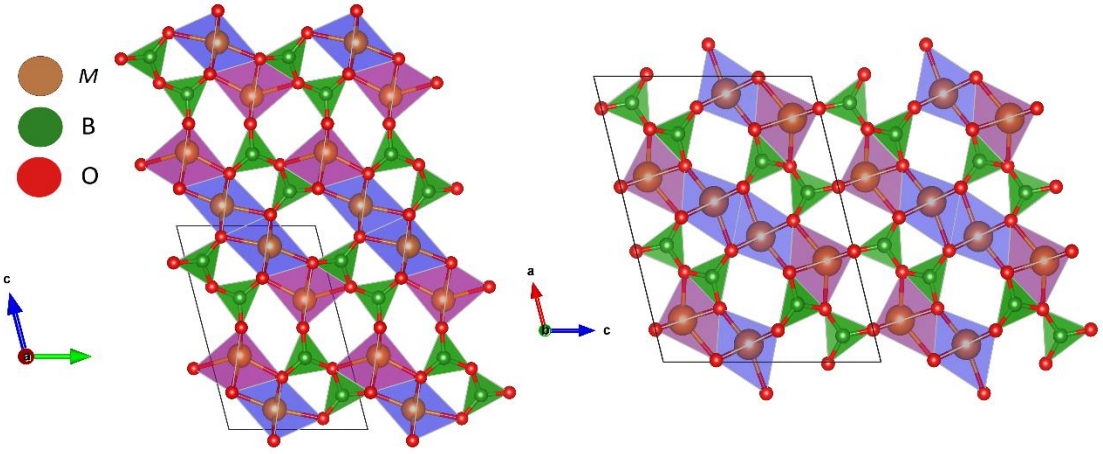

Figure 4-1. Comparison of the triclinic (left, $P\bar{1}$) and monoclinic (right, $P2_1/c$) crystal structures for $M_2B_2O_5$. M is a 2+ cation and $M1O_6$, $M2O_6$ and BO_3 polyhedra are shown in purple, blue and green respectively.

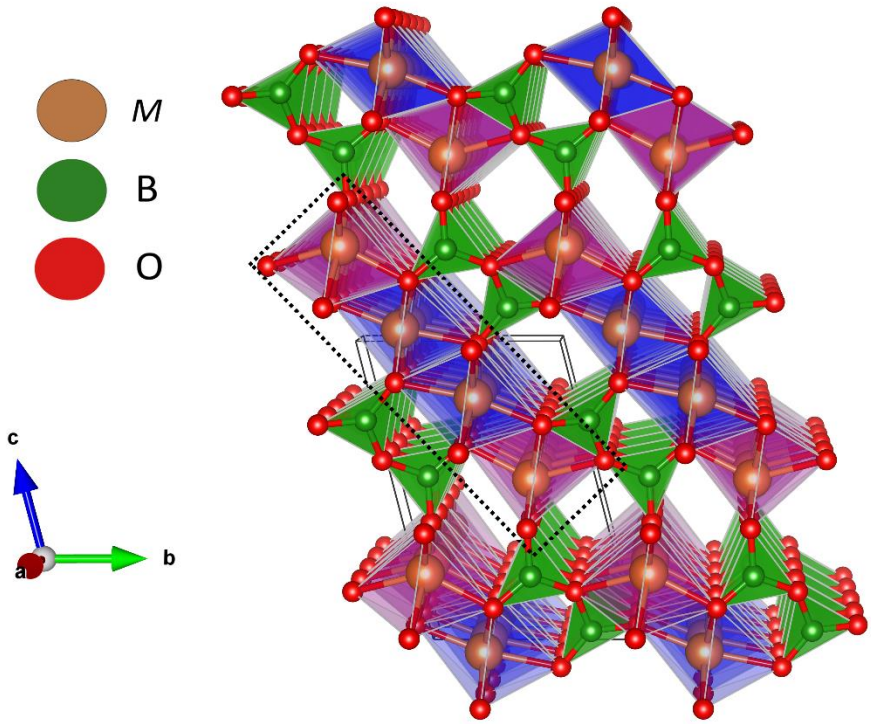

Figure 4-2. Crystal structure of tetragonal $M B_2O_5$ with the dashed rectangle indicating the M_4O_{18} ribbon, which extends infinitely in the *a* direction.

The majority of the early work on pyroborates was on materials where *M* was a single cation, *e.g.* $Mg_2B_2O_5$, $Fe_2B_2O_5$, $Co_2B_2O_5$ or $Mn_2B_2O_5$,[158,177,179,180] however a later study by Utzolino and Bluhm on $MgMnB_2O_5$ and $MnCoB_2O_5$ showed that two different metals could occupy the *M* octahedra in the same structure.[181] Mixed metal structures are common in other borates (with different *M*:B:O ratios), for example in the M_2BO_5 system Mg, $Mn^{2+,3+,4+}$, $Fe^{2+,3+}$, Al and Ti have all been found to form stable, mixed metal species.[182] This flexibility in metal occupancies is relatively unexplored in the pyroborates, therefore there is scope to investigate the formation of mixed metal pyroborates and use crystallography to study cation ordering that may occur due to the different environment of *M*1 and *M*2.

In this chapter the ability to synthesise mixed metal pyroborates which contain Mg and the redox active transition metal Mn is investigated, with characterisation of the resulting crystals by PXRD and PND. It is shown that a solid solution is formed and we find that the Mn and Mg are disordered over the two metal sites, with partial cation ordering where Mn preferentially occupies the larger, more distorted, site *M*1.

4.1.2 Interest for battery cathodes

It is the aim of this chapter to explore the use of the pyroborates, which may offer advantages over the BO_3^{3-} polyanion, as Li-ion cathode materials. One of the main advantages may be in stability. A theoretical study by Ceder *et al.*[29] where they investigated the relationship between delithiation voltage and stability to O_2 loss, showed that the $B_2O_5^{4-}$ polyanion offers higher voltages for a given redox couple than other borates, while not compromising on the stability of the framework to O_2 loss. In comparison, the BO_3^{3-} polyanion voltages are around the average for borates, with a significant decrease in stability. In the analogous phosphates, the high oxygen content polyanion PO_4^{3-} is less stable than the pyrophosphate, $P_2O_7^{4-}$, and decomposes via loss of O_2 to form a lower O:P ratio phase.[183] The borates may exhibit similar behaviour, explaining the stability calculation results, however to our knowledge this has not been investigated. The same computational study proposed $LiVB_2O_5$ as a high voltage, stable, Li-ion cathode, which is of interest as Li pyroborates have not previously been synthesised (there are no entries in the inorganic crystal structure database except for $LiAlB_2O_5$, which has a different structure), which may explain why this family of materials is as yet unexplored.

The crystal structure of the pyroborates may also lend itself to good electrochemical performance. A study by Bo *et al.*[98] using bond valence sum calculations suggested that the Mg^{2+} ions may be mobile in the pyroborate $Mg_xFe_{2-x}B_2O_5$ and therefore may be of interest for Mg-ion batteries. They also showed that on thermal oxidation above 200 °C Mg is removed from the structure. If the Mg^{2+} ions are mobile and can be removed from the structure it is expected that Li^+ ions could be inserted into the oxidised host. The Mg diffusion pathway was found to be via interstitial sites, avoiding the need to diffuse down the infinite chains of *M* which may be blocked by immobile transition metal ions. Only the *M*2 site forms this percolating network therefore the mobility of an ion may differ depending on which site it occupies, hence characterisation of the distribution of cations over these sites is important. As the two *M* sites have different environments, there is the possibility of complete cation ordering, which would lead to channels containing only Mg through the system, and greater ionic diffusivity if occupying the site *M2*.

A further advantage of the lightweight pyroborate unit is that unlike pyrophosphates, where the heavier $P_2O_7^{4-}$ group compromises the overall capacity,[39] the lighter boron atom (and fewer oxygen atoms) means that a move from borates to pyroborates does not compromise the theoretical capacity.

Although the Mg diffusion properties and formation of high voltage Li-intercalated structures have been proposed for the pyroborate family, the properties have not been explored experimentally. Here we explore the ability to remove Mg from the structure while retaining the polyanion framework, and the ability to reversibly intercalate Li into the host structure.

4.2 Synthesis

The Mn pyroborate was synthesised by grinding stoichiometric amounts of the transition metal oxalate $MnC_2O_4.2H_2O$ (Alfa Aesar, 30% Mn min), with MgO (Alfa Aesar, 99.998%) and H_3BO_3 (Alfa Aesar, >99.99%) into a fine powder. The mixtures were heated to 400 °C at 3 °C min^{-1} and held for 10 hours. This step decomposes the oxalate and melts the boric acid to form an amorphous borate glass. Samples were then cooled and reground to ensure homogenous distribution of metals, and heated to 600 °C at 3 °C min^{-1}, then to 1050 °C at 1 °C min^{-1} where samples were held for 24 hours before being furnace cooled. If impurities were present (indicated by colour or PXRD), the final heating step was repeated until the impurity was removed or the amount present no longer decreased as determined by PXRD. To avoid oxidation of the Mn on heating, all synthesis steps were carried out under flowing argon. ^{11}B enriched samples prepared for neutron powder diffraction were synthesised from ^{11}B-Boric acid (Aldrich 99%).

4.3 Results

4.3.1 Structure

Although the $x = 1$ compound has been previously synthesised it is unknown if other ratios are stable, or if a solid solution can be formed. The extent of order (or disorder) of the Mg and Mn over the two metal sites has also not previously been investigated, and could be instrumental in achieving ionic diffusion through the channels.

PXRD and PND analysis of $Mg_xMn_{2-x}B_2O_5$ (x = 2/3, 1, 4/3) indicated the formation of phase pure products. Rietveld refinement showed that all three materials adopt the triclinic phase rather the monoclinic structure found for $Mn_2B_2O_5$.[177,181] This fits with previous reports of furnace cooled $Mg_2B_2O_5$ and $Mn_2B_2O_5$ samples forming the triclinic polymorph.[179,184] For x = 1 and x = 4/3, combined neutron and X-ray diffraction refinements were carried out to determine the crystal structure. This allowed for B and O positions to be determined from the neutron data and Mg and Mn positions and occupancies from PXRD. For x = 2/3, only PXRD data was available so B and O positions from the x = 1 combined neutron refinement were used, with other parameters refined against the PXRD data. A representative PND refinement for x = 4/3 is shown in Figure 4-3.

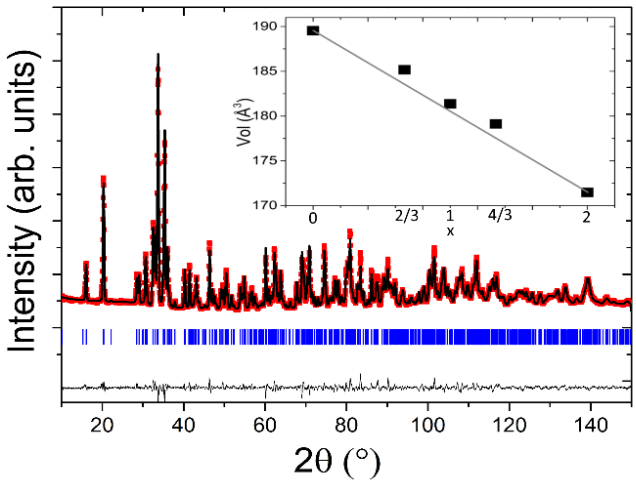

Figure 4-3. Neutron diffraction pattern (red dots) and fit (black line) of $Mg_{4/3}Mn_{2/3}B_2O_5$. Allowed Bragg reflections are shown as blue tick marks. Inset shows the change in cell volume in $Mg_xMn_{2-x}B_2O_5$ as a function of x determined from neutron and X-ray powder diffraction. Error bars are smaller than the symbols.

The refined volumes shown in the inset of Figure 4-3 vary with composition, with higher Mn content increasing the unit cell volume. The deviation from wholly linear volume change is consistent with the partial ordering of the Mg and Mn ions. The volume of *M*1 and *M*2 polyhedra and average *M*-O bond distances also change systematically with increasing Mn content, Table 4-1.

Table 4-1. Summary of refined crystal structure parameters determined from PXRD and PND at room temperature for the solid solution $Mg_xMn_{2-x}B_2O_5$, formed between $Mg_2B_2O_5$ and $Mn_2B_2O_5$

$Mg_xMn_{2-x}B_2O_5$	**$x = 0$[177]**	**$x = \frac{2}{3}$**	**$x = 1$**	**$x = \frac{4}{3}$**	**$x = 2$[158,177]**
Space group	$P\bar{1}$	$P\bar{1}$	$P\bar{1}$	$P\bar{1}$	$P\bar{1}$
χ^2		2.15	3.33	11.7	
R_{wp}		20.1	19.7	9.88	
Vol (Å^3)	189.53	185.172(9)	181.365(10)	179.131(6)	171.48/171.33
M1 occ (Mn/Mg)	1/0	0.73/0.28(10)	0.647/0.353(8)	0.403/0.597(6)	0/1
M2 occ (Mn/Mg)	1/0	0.61/0.39(10)	0.353/0.647(8)	0.264/0.736(6)	0/1
Average M1-O (Å)	N/A	2.196(10)	2.173(5)	2.131(7)	2.1292(15)
Average M2-O (Å)	N/A	2.160(10)	2.142(5)	2.139(7)	2.0946(15)

In all cases, the Mg and Mn ions are disordered over the *M*1 and *M*2 sites, Table 4-1. Full structural details are given in appendix tables A4-1, A4-2 and A4-3.This is in agreement with previous analysis by Utzolino and Bluhm,[181] however, a slight preference for Mn to occupy the more distorted, but larger, *M*1 site is observed for all the mixed-metal samples. This is exemplified by $MgMnB_2O_5$, where total disorder would give occupancies of 0.5 in each site whereas a 0.65/0.35 split is observed. However, higher Mg content on *M*2 may aid Mg removal and Li insertion as bond valence sum calculations carried out by Bo *et al.* suggest that the Mg ion diffusion pathway occurs via interstitial sites linked with the *M*2 site.[98] Bond valence sum (BVS) calculations were carried out for $MgMnB_2O_5$ and a similar percolation pathway involving interstitial sites was found to form at the same valence variance (0.2 v.u.) as $Mg_{2/3}Fe_{4/3}B_2O_5$, Figure 4-4. This is unsurprising as the calculation is based on the anion framework, which differs only slightly, meaning the percolating 2+ cation network as calculated by BVS should be a feature of all the pyroborates.

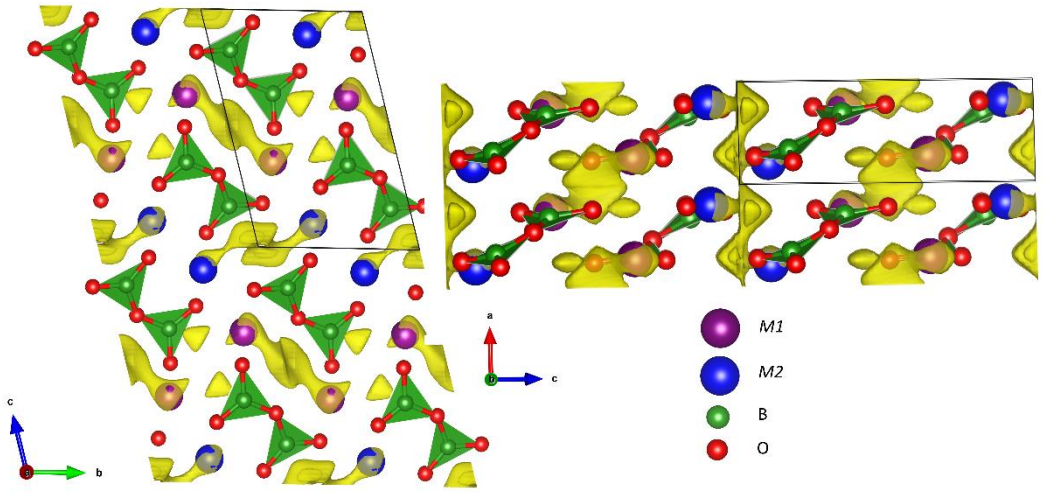

Figure 4-4. Bond valence sum map for a 2+ cation in $MgMnB_2O_5$ with a variance of ± 0.2 v.u. A percolating network is formed along the *a* axis, linking M2. Mg preferentially occupies M2 which may lead to ionic diffusion in the material.

4.3.2 Theoretical capacities of $Mg_xMn_{2-x}B_2O_5$

For each phase manganese has an oxidation state of 2+ in the pristine material, and the total theoretical capacity of the three materials is then a function of both the total Mn content and the Mg available for extraction as we now illustrate: for x = 4/3 ($Mg_{4/3}Mn_{2/3}B_2O_5$) the capacity obtained on oxidising all the Mn^{2+} to Mn^{4+} forming $Mg_{2/3}Mn_{2/3}B_2O_5$ corresponds to 207.9 mAh g^{-1}. Since the mass of the lithiated sample is lower, a slightly higher theoretical capacity is obtained on full lithiation (231.6 mAh g^{-1}), where we have assumed reduction back to Mn^{2+} and the insertion of 2 Li ions per Mg removed to form $Li_{4/3}Mg_{2/3}Mn^{2+}_{2/3}B_2O_5$. For x = 1 the

Mg:Mn ratio is optimal and demagnesiation to form $Mn^{4+}B_2O_5$ gives the highest theoretical capacity of 296.6 mAh g^{-1} and 342.5 mAh g^{-1} for lithiation to form $Li_2Mn^{2+}B_2O_5$. For x = 4/3, there is insufficient Mg in the material to oxidise all the Mn^{2+} to Mn^{4+} and a Mn^{3+} compound in theory results ($Mn^{3+}_{4/3}B_2O_5$), with a lower associated capacity of 187.3 mAh g^{-1}. Lithiation to form $Li_{4/3}Mn^{2+}_{4/3}B_2O_5$ has a theoretical capacity of 204.1 mAh g^{-1}. In the subsequent text all reported cycle rates are based on Mg removal capacities.

4.3.3 $MgMnB_2O_5$ electrochemistry and ex-situ characterisation

$MgMnB_2O_5$ was investigated as a Li-ion cathode material in the most detail due to it having the highest theoretical capacity of the series. Also in the previously discussed Li*M*BO_3 system, Mn provided moderate rate capability and high capacity. The Mn ion can, in principle, cycle utilizing two electron couples (between Mn^{2+} and Mn^{4+}). On first charge vs. Li^+, a capacity of 330 mAh g^{-1} was achieved at a rate of C/25, suggesting complete removal of Mg from the structure (theoretical capacity of 296.6 mAh g^{-1}), Figure 4-5. The labile nature of Mg differs from previous Mg containing Li-ion cathodes, such as Mg doped $LiCoO_2$ or $LiFePO_4$[185,186], where Mg is thought to be electrochemically inactive, providing structural stability only. The slight excess of capacity on 1st charge varies with each cell and is therefore attributed to side reactions with the electrolyte rather than a deviation from a 1:1 Mg/Mn stoichiometry.

The subsequent discharge process consists of Li^+ ion insertion into the demagnesiated Mn^{4+} framework. On 1st discharge, 220 mAh g^{-1} of Li^+ were inserted equating to 1.2 Li ions per unit cell, which is smaller than the theoretical capacity calculated by assuming insertion of 2 Li^+ ions for each Mg^{2+} ion (342.5 mAh g^{-1}). The sloping nature of the electrochemical profile can be attributed to Mg/Mn site disorder and the different local environments of Li.[187]

The Li ions are then fully removed on 2nd charge (221 mAh g^{-1}). Over subsequent cycles the capacity is gradually increased reaching a maximum of 1.47 Li ions, 252 mAh g^{-1} after 12 cycles. The increase in capacity is accompanied by a change in voltage profile. The initially lower capacity is attributed to deintercalated Mg^{2+} ions being present in high enough concentration near the cathode to continue to be involved in cycling, and their sluggish reinsertion into the framework resulting in larger overpotential. As the cycle number increases, the Mg ions diffuse into the bulk electrolyte leaving a significant excess of Li ions as the main electro-active species. This hypothesis is supported by Figure 4-6, which shows that no change in voltage profile occurs over the first 10 cycles when a new coin cell is assembled with a washed demagnesiated cathode and fresh Li electrolyte, as the residual Mg ions were removed. The reduced capacity is attributed to film degradation during coin cell disassembly and washing.

After 100 cycles the capacity and slope of the charge and discharge processes stabilised at a reversible capacity of 194 mAh g^{-1}. Discharge to 1.5 V results in formation of $Li_{1.1}Mn^{(+2.9)}B_2O_5$. Two subtle changes in slope are observed in the d*Q*/d*V* vs. V plots at ~2.8 V and 4.2 V on charge, and at 2.5 V and 4.0 V on discharge (Figure 4-7), which may correspond to the $Mn^{2+} \leftrightarrow Mn^{3+}$ and $Mn^{3+} \leftrightarrow Mn^{4+}$ processes. This suggests relatively low overpotential for the high voltage process, consistent with galvanostatic intermittent titration technique (GITT) experiments, Figure 4-8. The 300 mV overpotential on Li removal and 200 mV overpotential for Li insertion are comparable to overpotentials in the early stages of *m*-$LiMnBO_3$ cycling.[172] However, the large increases in overpotential at deep charge and discharge seen in other borates, which limit capacity, are not observed here.

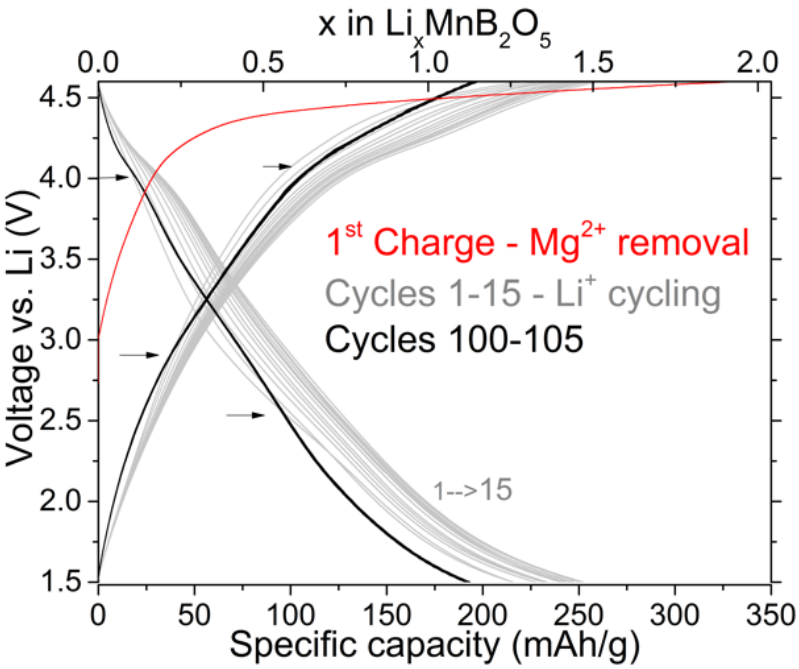

Figure 4-5. Cycling of $MgMnB_2O_5$ at C/25. Initial charge (Mg removal) - red line. Subsequent cycling vs. Li for 10 cycles - grey lines. Cycling vs. Li after 100 cycles - black line. Arrows indicate changes in slope, with values extracted from d*Q*/d*V* plots, Figure 4-7.

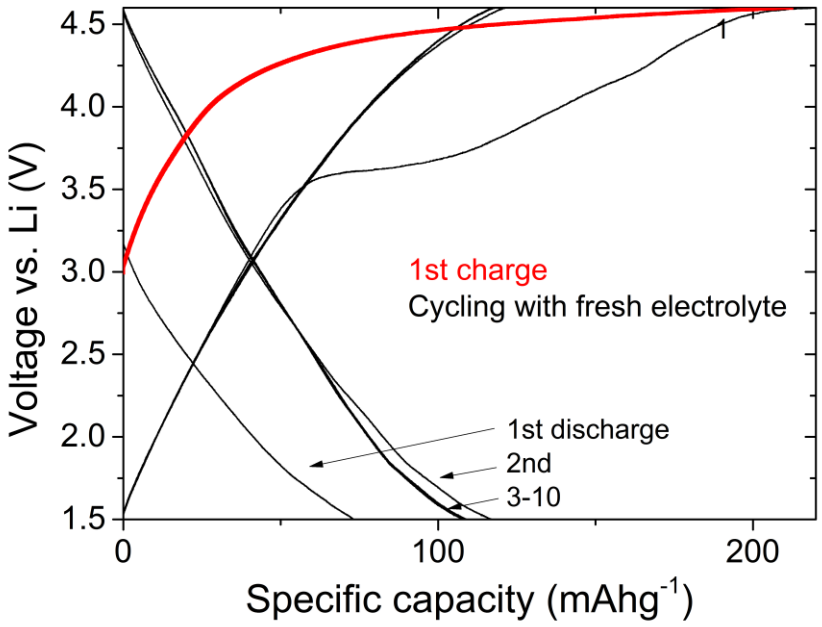

Figure 4-6. Cycling $MgMnB_2O_5$ at C/25 vs. Li. After 1st charge material is removed, washed in EC/DMC and a new coin cell constructed for subsequent cycling. The reduced capacity compared to initial cycling can be attributed to cathode film degradation leading to some material becoming electrochemically inaccessible in the new cell, and self-discharge of the material prior to coin cell disassembly.

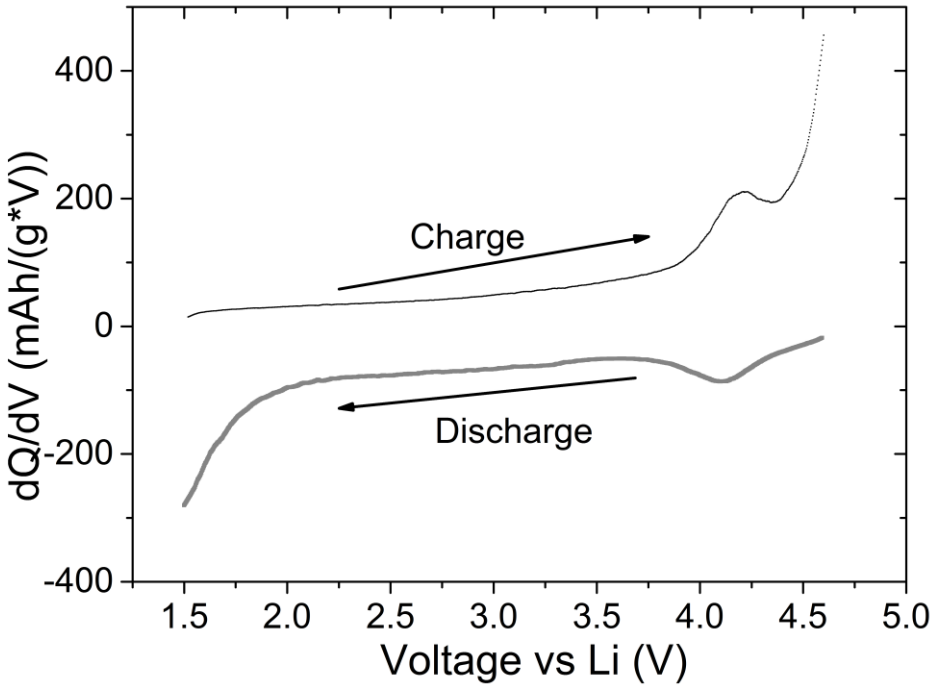

Figure 4-7. d*Q*/d*V* plot for 10th cycle of $MgMnB_2O_5$ vs. Li see in Figure 4-6.

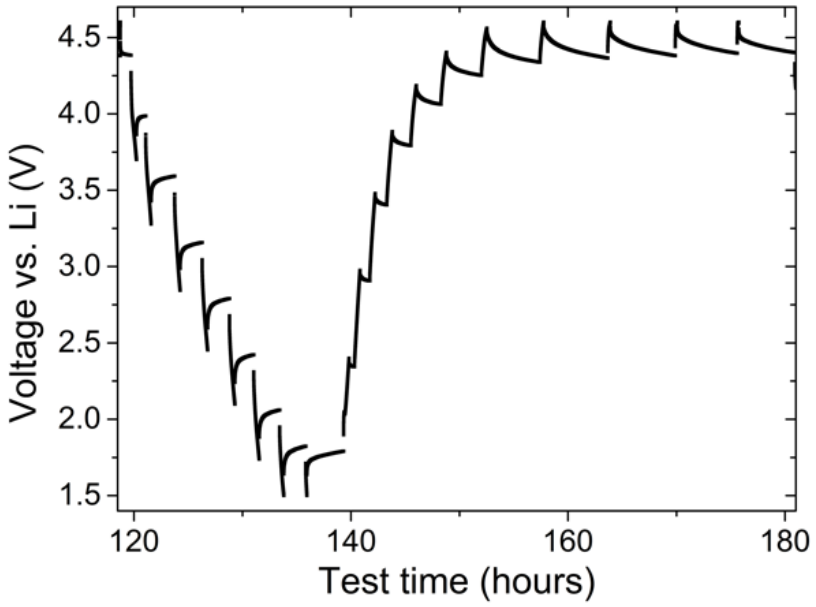

Figure 4-8. Third cycle of a GITT experiment of $MgMnB_2O_5$ vs. Li showing the equilibrium voltage for Li insertion and removal. Cycled at C/25 with up to 100 h rest period.

At the higher rate of C/5, the Mg removal capacity is reduced to 177 mAh g^{-1}, 0.6 Mg^{2+} ions per formula unit, as shown in Figure 4-9. This is followed by lithium insertion of 125 mAh g^{-1}, 56.8% of the capacity achieved at C/25. Continued cycling at C/5 for 1000 cycles shows a gradual increase in capacity up to 314 mAh g^{-1}. This equates to reversible insertion of 1.82 Li^+ per formula unit with a specific energy of 802 Wh kg^{-1}, assuming all the Mg^{2+} is removed during the 1000 cycles. Increased capacity with extended cycling is often ascribed to electrochemical grinding reducing the particle size and improving diffusion kinetics, however as full Mg^{2+} removal was possible on first charge, this seems doubtful. It is more likely that amorphisation or other structural rearrangements occur which allow the material to host the increased number of ions (1.82 Li^+ for each Mg^{2+} removed).

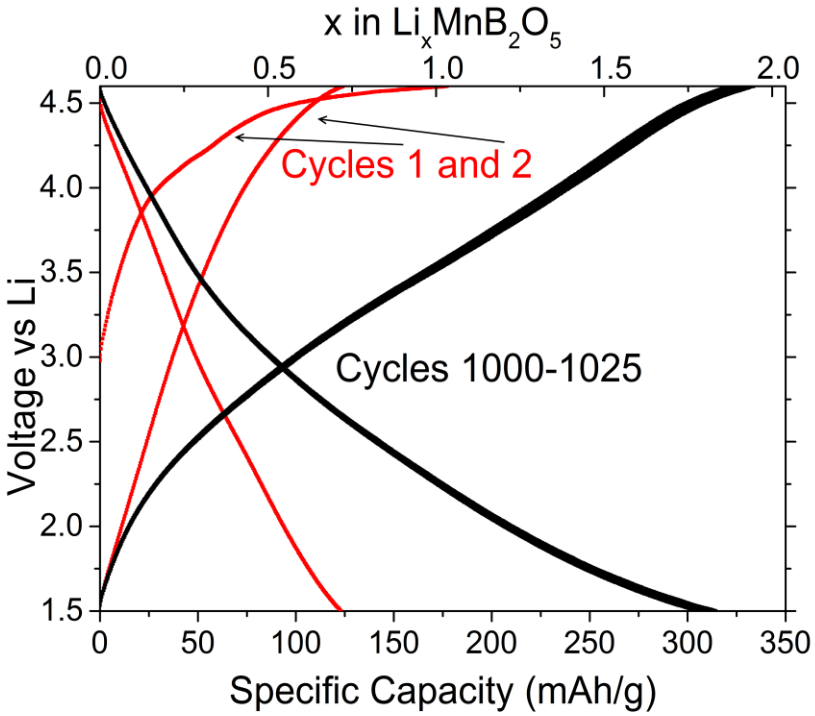

Figure 4-9. Cycling of $MgMnB_2O_5$ vs. Li at C/5 between 1.5 and 4.6 V. Initial charge and subsequent discharge and 2nd charge - red line. Cycles 1000-1025 - black lines.

The rate capability of $MgMnB_2O_5$ over the first 180 cycles is shown in Figure 4-10. The initial cycles at C/5 likely still involve Mg^{2+}. After 6 cycles the capacity settles at ~111 mAh g^{-1} and increasing the charge rate to 2C leads to a 12% reduction in capacity, 97.4 mAh g^{-1}.

Electrochemical tests were also carried out to investigate Li intercalation into the as prepared $MgMnB_2O_5$ cathode, into which 0.3 Li^+ (47.1 mAh g^{-1}) can be inserted at C/25 (inset Figure 4-13). This occurs before demagnesiation (*i.e.* discharging the cell first), which suggests the presence of Mn^{3+} in the pristine material caused by small deviations from ideal stoichiometry. The capacity may also arise from Li intercalation into carbon. However, it is believed to involve at least some intercalation into $MgMnB_2O_5$ as ex-situ diffraction (discussed in the following section) shows a change in unit cell volume and an additional peak associated with doubling the unit cell.

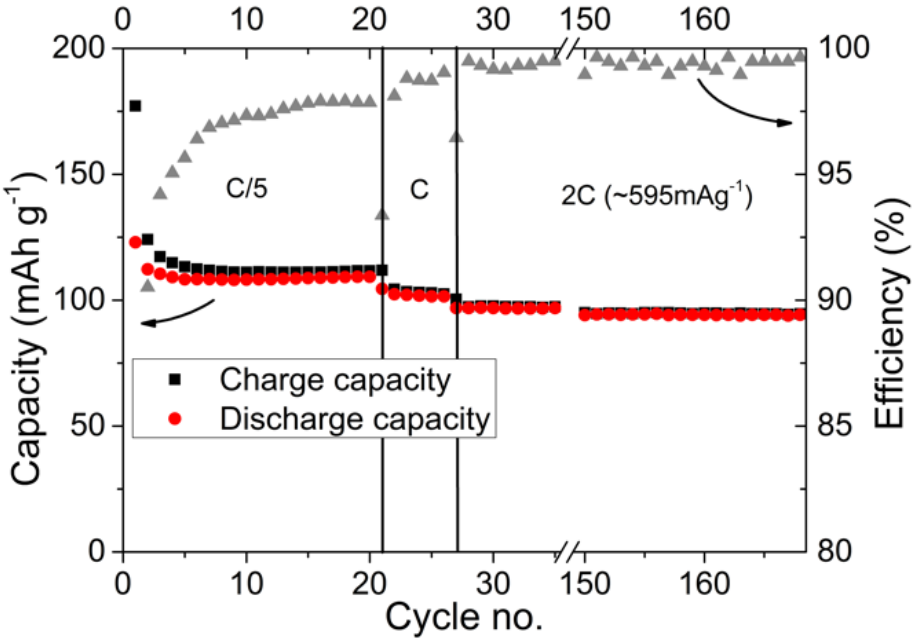

Figure 4-10. Rate study at C/5, C and 2C for $MgMnB_2O_5$ over the first 180 cycles. Left axis, charge and discharge capacity. Right axis, efficiency on expanded scale.

Extending the cycling region to below 1.5 V leads to significantly greater capacities, Figure 4-11. A discharge capacity of ~345 mAh g^{-1} is reached by 0.88 V at which point a change in slope is observed. This equates to full theoretical capacity for Li intercalation, therefore it appears to be possible to insert 2 Li for each Mg removed, however a large polarisation is required. Ex-situ PXRD, Figure 4-14, shows that the orthoborate framework is retained. Further reducing the voltage leads to a high capacity process between 0.6 and 0.3 V, giving a total capacity of 1045 mAh g^{-1}, or 6 Li per formula unit. It is unlikely that all this capacity is due to an electrochemical reaction of the pyroborate as the intercalation of just 4 Li would lead to formation of a Mn^0 compound. The capacity observed could be due to a combination of a conversion reaction to form a Mn^0 borate glass, similar to that observed for $Cu_3B_2O_6$,[65,188] and other reactions such as Li intercalation into the carbon or Li plating onto the current collector. However, the voltage profile does not indicate multiple processes are occurring below 0.88 V. On charge, ~900 mAh g^{-1}, or ~5.2 Li were removed from the electrode, with a very large polarisation, characteristic of a conversion reaction which requires significant energy to force a change in crystal structure. Although conversion reactions permit high capacities, the large overpotentials and significant capacity fade render their commercial use impracticable. For example, the discharge plateau for $Cu_3B_2O_6$ is at 2 V vs. Li but very large (1 and 2 V) overpotentials are observed on charge.[188] It also exhibits significant capacity fade, with 1/3 of the initial capacity retained after 30 cycles, even after electrode optimisation.

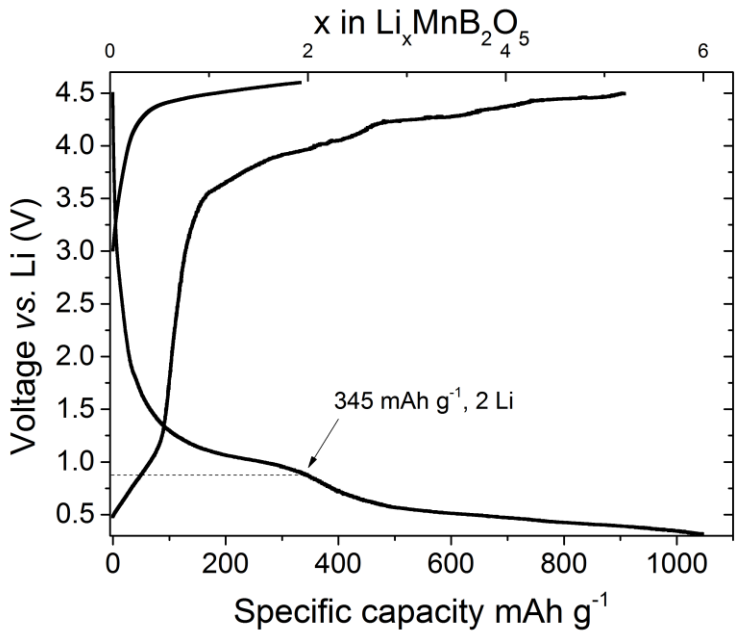

Figure 4-11. Electrochemical cycling of $MgMnB_2O_5$ to low voltages vs. Li. The initial charge to 4.6 V has the same characteristics as those previously described. This is followed by two low voltage, high capacity processes at ~1 V and 0.5 V on discharge which are almost fully reversible up to 4.6 V. The dashed line indicates the voltage at which full Li intercalation occurs, equivalent to replacement of 2 Li for 1 Mg per formula unit.

4.3.3.1 Ex-situ diffraction

Ex-situ powder X-ray and neutron diffraction were carried out to assess structural changes on demagnesiation and lithium insertion. Figure 4-12 shows a typical neutron diffraction data fitted with a profileless pattern matching refinement of the demagnesiated material $Mg_xMnB_2O_5$ (charged), $Li_xMnB_2O_5$ (lithium inserted after demagnesiation, charge-discharged) and $Li_xMgMnB_2O_5$ (lithium insertion into $MgMnB_2O_5$, discharge only). All 3 patterns have a peak at ~18.5° which is not observed in the pristine material. This is characteristic of a doubling of the unit cell in the *c* direction. Further characterisation of the change in structure is not possible due to the quality of the pattern and the small size of the active material particles in the electrode.

The change in volume per unit cell associated with each cycling stage is given in Figure 4-13. Volumes are given per 2 formula units (or a single triclinic unit cell) to allow comparison between the standard and doubled unit cells. With the removal of Mg to form MnB_2O_5 there is a 4.2% reduction in volume. Subsequent Li insertion increases the volume by just 1%. This is a small volume change for a relatively high capacity electrode material. It is also worth noting that the polyanion framework is retained even after removing 50% of the cations. The small volume change on Li cycling means that electrochemical grinding is unlikely to be the cause of the gradual increase in capacity over extended cycling. An alternative mechanism could be a

change in cation environment caused by mobility in the disordered metal sites or structural rearrangement that offers more Li sites. A gradual increase in capacity has been observed the $LiFeBO_3$ system over the first ~50 cycles, which was explained by structural changes induced at low voltages (<1.8 V).[46,171] Detailed structural analysis of the cycled material to determine the sites for Li was hindered by small particle size and amorphisation, as seen in the ex-situ diffraction patterns (Figure 4-12). The ^{7}Li MAS NMR spectra of the material acquired after one charge-discharge cycle do not contain sufficient resolution to determine where the Li ions are located. Detailed NMR discussion can be found in the following section.

Inserting Li into the pristine $MgMnB_2O_5$ results in a 5% volume decrease, supporting the observation that some Li is inserted into the active material, rather than into carbon or reaction with the electrolyte to form an SEI layer. This suggests the presence of a small amount of Mn^{3+} in the starting material. The reduction in volume on insertion of ions may be counter intuitive, but it can be rationalised by changes in electrostatic repulsion between polyanion blocks. Insertion of Li^+ shields the negative charges on the oxygens and attracts the polyanions closer together, reducing the cell volume. This mechanism has previously been observed for Li insertion into CoO_2, where increasing the amount of Li^+ between the layers causes a contraction of unit cell by ~2%.[189]

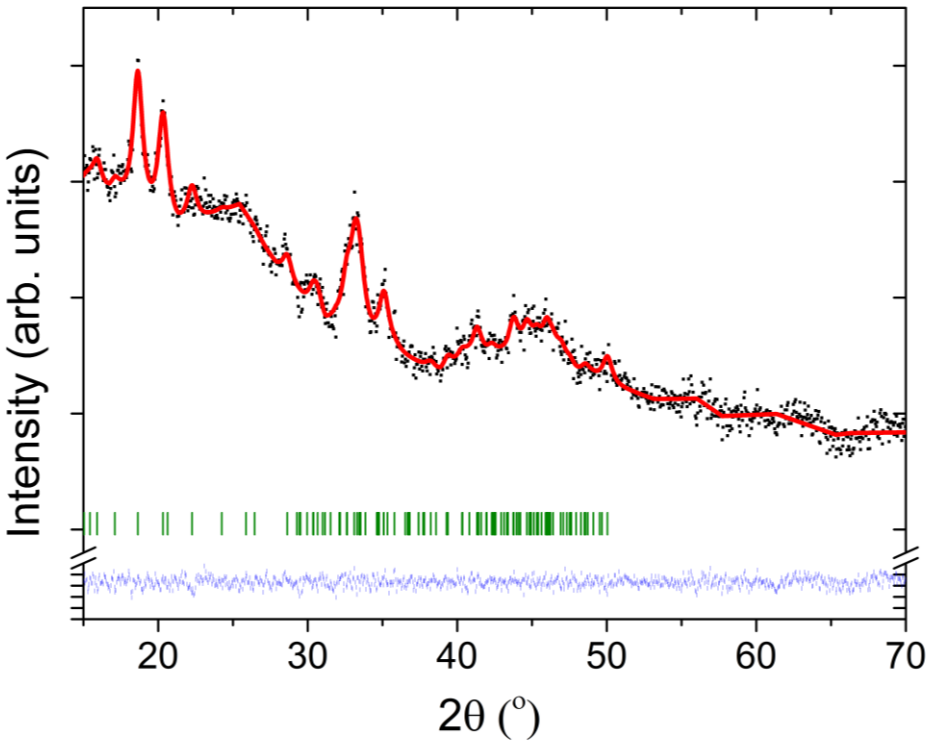

Figure 4-12. Neutron powder diffraction (black dots) of demagnesiated $MgMnB_2O_5$ fitted with a Le Bail refinement (red line). Allowed Bragg reflections are shown with green tick marks, and the difference pattern is in blue. The pattern and fit are representative of all the ex-situ PND data collected.

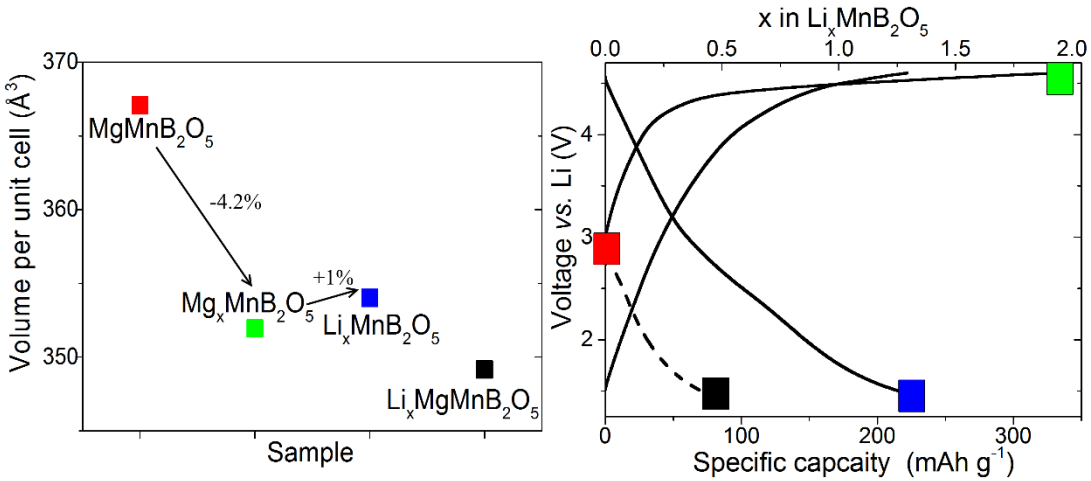

Figure 4-13. Right) Volume change for $MgMnB_2O_5$ on cycling at C/25 between 1.5 V and 4.6 V, determined by pattern fitting of neutron diffraction data. Left) The point of cycle each sample was taken from. The dotted line represents discharge only from open circuit potential.

Ex-situ PXD of material discharged to 0.8 V vs. Li (400 mAh g^{-1}, ~2.2 Li per unit cell) which is the end of the 1st discharge process observed in Figure 4-11, shows a retention of the pyroborate polyanion framework with a unit cell volume of 366.3 $Å^3$, Figure 4-14. This is significantly greater than that observed on discharge to 1.5 V (354.0 $Å^3$), and approaching that

of the fully Mg occupied pristine material (367.1 $Å^3$). This suggests that below 1.5 V more Li can be inserted into the framework, further reducing Mn back to its initial 2+ oxidation state. As the voltage is decreased further and the amount of Li inserted becomes greater than can be accommodated by a $Mn^{4+/2+}$ change. As no additional peaks are observed it is likely that a conversion reaction is occurring to form amorphous or nanoparticulate products containing Mn^0.

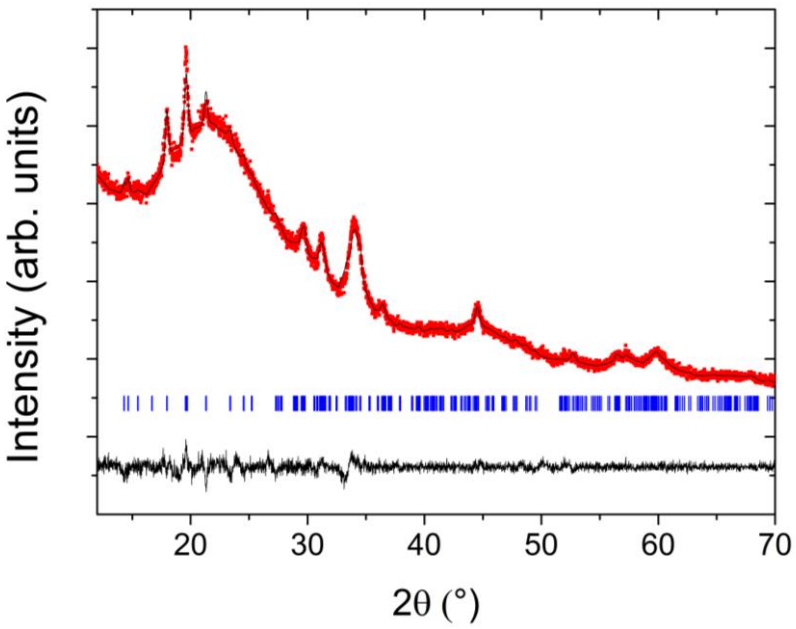

Figure 4-14. Le Bail refinement for $MgMnB_2O_5$ discharged to 0.8 V, giving a capacity of 400 mAh g^{-1}. The polyanion framework is retained and no new peaks associated with new phases are visible.

4.3.3.2 ^{7}Li NMR

The assertion that Li is inserted into the framework on cycling is further supported by ^{7}Li MAS NMR spectra, Figure 4-15. The intensity of the Li resonance from the charged-discharged material is significantly greater than that seen in the charged sample, meaning a large amount of Li has been inserted into the structure. The charged sample contains just 3% of the Li inserted during discharge. The Li present in the charged sample may be due to small amount of self-discharge or formation of an SEI with the lithium containing electrolyte. The resonance of the discharged sample appears to have two components both with short spin-lattice (T_1) and spin-spin (T_2) relaxation times (T_1 = 1.63 s and 20ms, and T_2 = 519 ms and 804 μs), characteristic of Li interacting with a paramagnetic centre. The majority of this intercalation is reversible, demonstrated by the decrease in Li signal on 2nd charge to almost that of the 1st charge. This agrees well with the electrochemistry where 2nd charge has 100% coulombic efficiency.

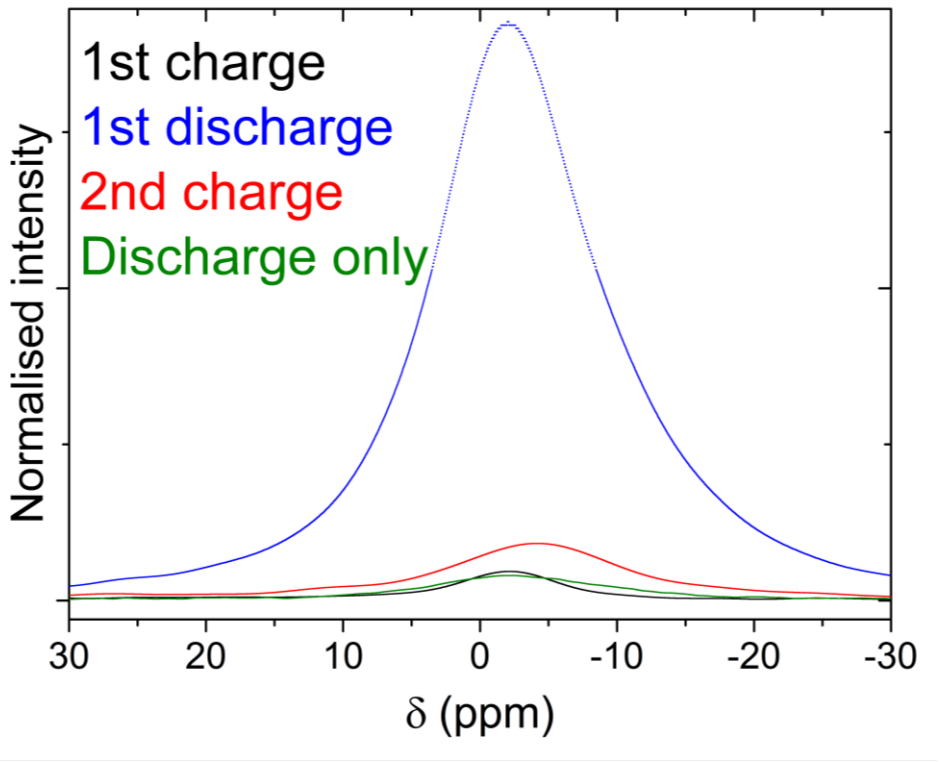

Figure 4-15. ^{7}Li NMR spectra of $Li_xMnB_2O_5$ sample at different states of charge with 50 kHz spinning rate.

Compared to the large paramagnetic shift observed in $LiMnBO_3$ (-201 ppm),[190] $LiMnB_2O_5$ displays only a small shift, and in fact the resonance of around -2 ppm is similar to many diamagnetic Li environments. However, the short relaxation times suggest a paramagnetic environment and the quantity of Li inserted is more consistent with insertion into the Mn containing material, rather than formation of diamagnetic products. Jeongjae Lee carried out a series of calculations to help elucidate these conflicting results. The VASP code was used to give a crude ionic relaxation of the structure before CRYSTAL was used to refine the structure and calculate pNMR shifts. As these codes cannot handle partial occupancy, a cell with composition $LiMn_2B_2O_5$ was constructed by the following method. From the initial structure of $Mn_4B_4O_{10}$, 2 Mn were removed from *M*2, the site predicted to have greatest ion diffusivity, and the remaining Mn given an oxidation state of 4+ to form $(Mn^{4+})_2B_4O_{10}$. The structure was relaxed and 1 Li ion placed on a vacant *M*2 site (while leaving the other vacant), resulting in reduction of a nearby Mn^{4+} to Mn^{3+}. This structure was again relaxed, then the spin density at the nuclear position was calculated, giving the pNMR shifts, Equation 24.

$$\delta_{iso} \propto \frac{\psi_N^2}{T - \theta}$$ Equation 24

Where δ_{iso} is the shift, ψ_N^2 is the nuclear spin density, T is temperature and θ is the Weiss constant calculated from SQUID magnetometry. The calculated spin density for the ^{7}Li is much smaller than in other paramagnetic cases, and yields a shift of 26.37 ppm, suggesting some diamagnetic contribution may also play a role. The low spin density and associated small paramagnetic shift from this model supports the assertion that the resonance at around -2 ppm is due to Li in the pyroborate material. The explanation for the low spin density (and therefore minimal paramagnetic shift) can be observed in the spin density map, Figure 4-16, which shows a high concentration of spin polarisation above and below the BO_3 plane, utilising the π bonded BO_3 framework. This is likely due to the highly electronegative borate polarising the framework, and limiting the spin density transferred to the Li nuclei which sits on the borate π-plane. The spin density around boron is calculated to be 20 times that of Li.

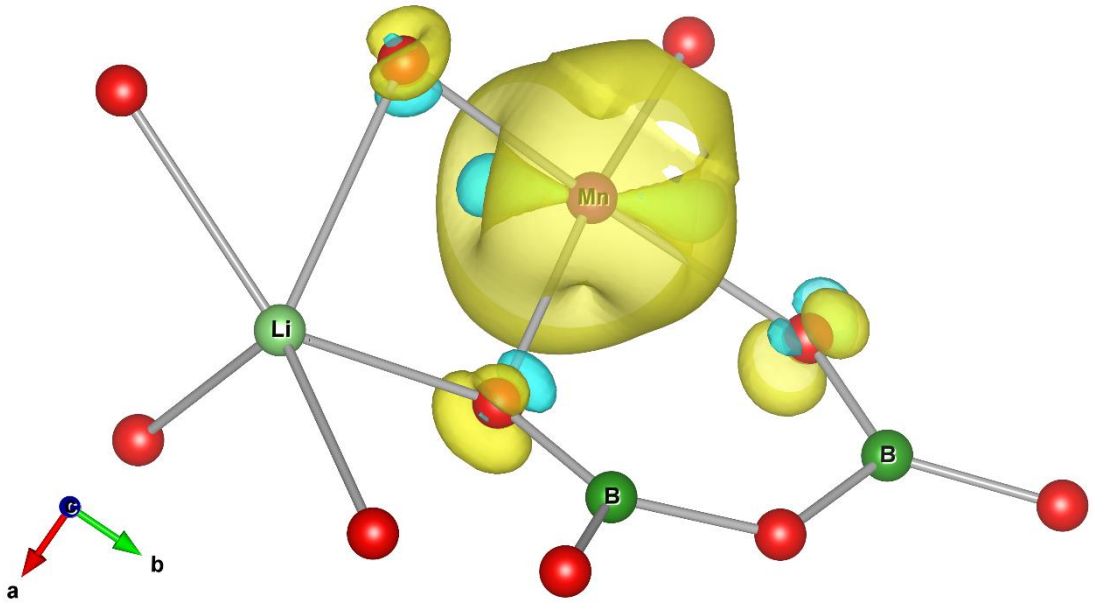

Figure 4-16. Calculated spin density map for $LiMn_2B_2O_5$ where Li occupies the M2 site. Spin density is concentrated in the π-framework of the borate anion, with little transferred to the out of plane Li.

The spectra obtained for the discharged first sample (i.e. before Mg removal) shows a low intensity peak with similar resonance to that seen in the cycled samples, which is ascribed to a small amount of Li insertion, further supporting the presence of Mn^{3+} in the pristine material, as indicated by electrochemistry and diffraction.

A comparison of the 1st discharge with the 100th discharge (Figure 4-17) shows that in later cycles Li insertion quantities are ~80% of those achieved on 1st discharge. This agrees with the electrochemistry measurement where capacities were greater for initial discharges than those after 100 cycles. The value obtained from the capacity change between 1st discharge and 100th is ~88%, and the difference in these values can be attributed to variation among different electrochemical cells.

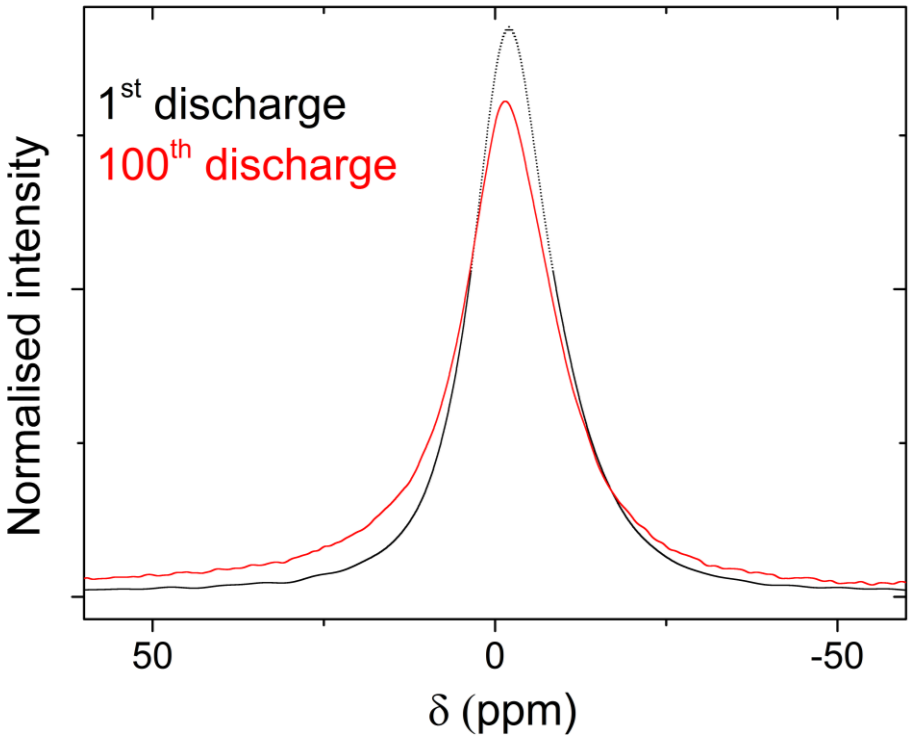

Figure 4-17. ^{7}Li spectra of 1st and 100th discharged $Li_xMnB_2O_5$ (x = 1) material with a spinning rate up to 50 kHz.

4.3.3.3 SQUID magnetometry

If Mg is removed from the structure, the remaining Mn should undergo oxidation to balance the loss of the 2+ ion. On Li insertion there should be a corresponding Mn reduction. Therefore, measurement of the Mn magnetic moment will give some indication of the redox reaction occurring during cycling.[191] The expected magnetic moments for high spin Mn^{2+}, Mn^{3+}, and Mn^{4+} are 5.9 μ_B, 4.9 μ_B and 3.9 μ_B respectively, assuming no spin orbit coupling ($\mu_{so} = g\sqrt{s(s+1)}$).

Figure 4-18 shows the inverse magnetic susceptibility, χ^{-1}, for the uncycled x = 1 cathode material, 1st charge, subsequently discharged and 2nd charge ex-situ samples. The calculated effective moment for the uncycled material is 6.0 μ_B, equating to Mn^{2+}, as expected. On charge (Mg removal) Mn oxidation occurs to between Mn^{3+} and Mn^{4+} (a calculated magnetic moment of 4.5 μ_B). On 1st discharge (Li insertion) the oxidised Mn is reduced to between Mn^{2+} and Mn^{3+} (5.5 μ_B). The fact that Mn is not fully reduced back to Mn^{2+} is consistent with the electrochemical data, where 1st charge has a greater capacity than 1st discharge. On 2nd charge the Mn is oxidised back to between Mn^{3+} and Mn^{4+}, further demonstrating reversible intercalation.

The calculated moment for the discharged only sample is 6.2 μ_B, greater than the 6.0 μ_B of the pristine material. This suggests that some reduction of Mn may be occurring and that calculated values for all samples are slightly overestimated. This may be due to residual magnetic interactions meaning fits were not in a regime where the Curie-Weiss analysis is valid. This has previously been observed in other Mn systems with large Weiss temperatures.[192] Therefore, although the calculated value for the uncycled material is 6.0 μ_B, it is possible that it contains a small amount of Mn^{3+}.

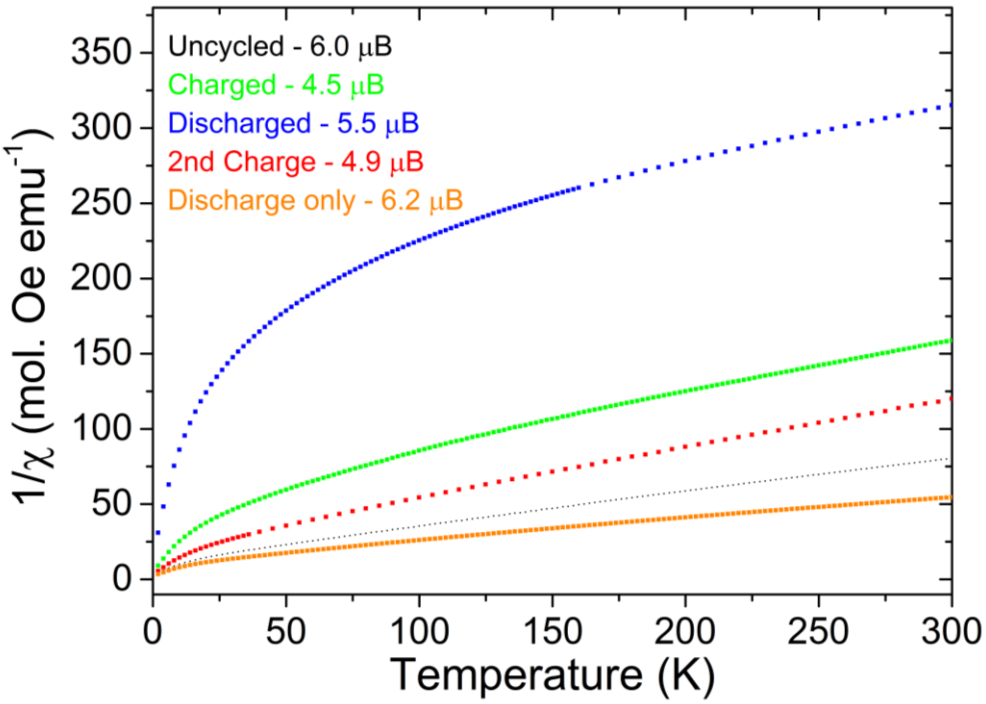

Figure 4-18. Magnetic moments for x = 1 material ex-situ samples and the data they are calculated from. Magnetisation measured from 2-300 K in a 1000 Oe field.

4.3.3.4 XANES

X-ray absorption structure spectra measured for the Mn K edge in ex-situ samples show a shift to higher energy on charge and increase in white line energy, indicative of oxidation, and a shift to lower energy on discharge, indicative of reduction, Figure 4-19. The shift from pristine to 1st charge is less than 1 eV, significantly smaller than would be expected from the electrochemistry and comparison with the standards, Figure 4-20. On discharge a shift to lower energy is observed which does not fully reach that of the pristine, as expected from the electrochemistry.

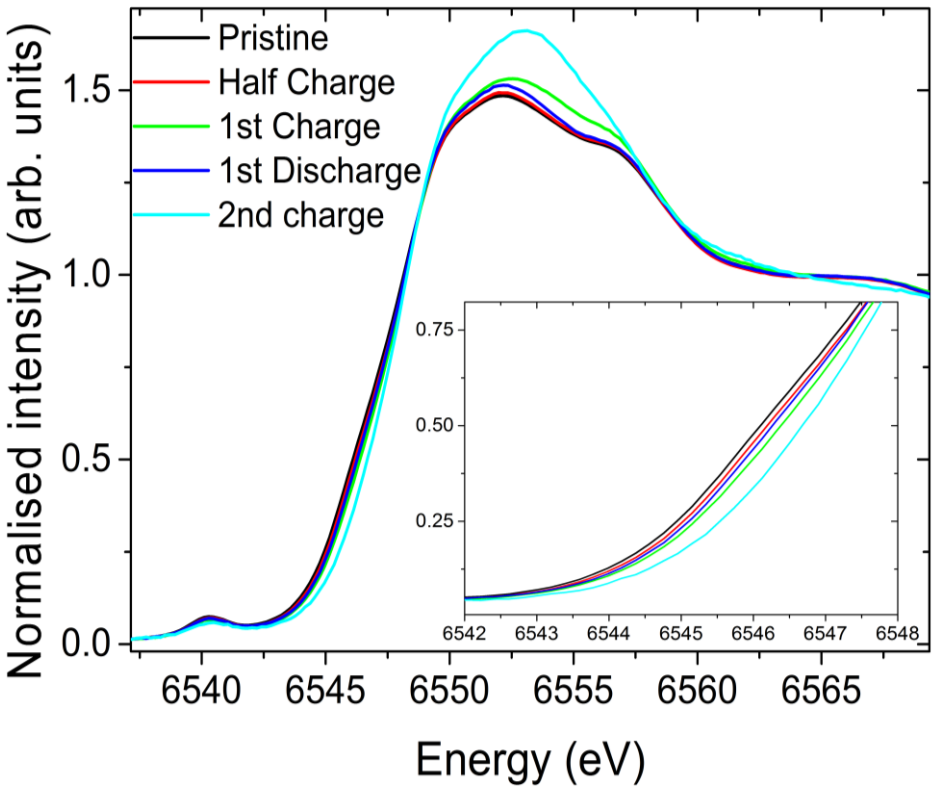

Figure 4-19. XANES spectra for ex-situ cycled $MgMnB_2O_5$ samples at the Mn K edge. A blow up of the edge onset is shown in the inset.

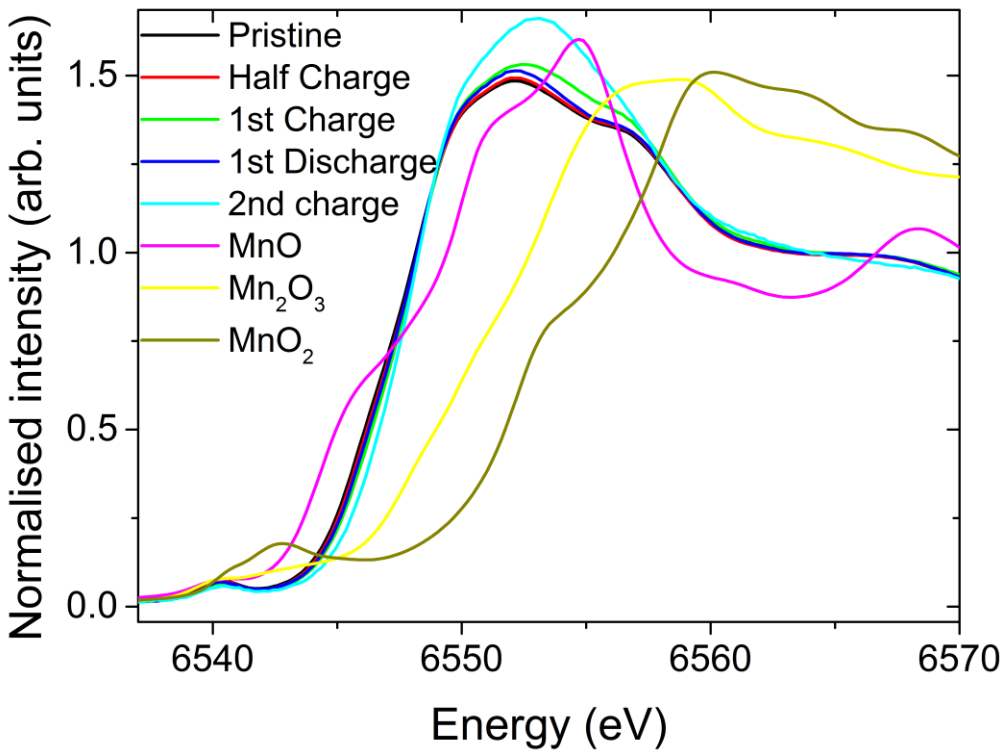

Figure 4-20. XANES spectra for ex-situ cycled $MgMnB_2O_5$ samples and Mn^{2+}, Mn^{3+} and Mn^{4+} standards at the Mn K edge.

The electrochemistry for 2nd charge suggests the Mn oxidation state should be the same as the end of 1st change, however an even greater shift is observed and the white line peak intensity is further increased suggesting a higher Mn oxidation state is formed. XANES is also sensitive to changes in environment so this difference could be due to slight structural changes on replacing Mg with Li. As well as the small shift in edge energy there is a change in peak shape which may indicate growth and consumption of different oxidation states. This is most clear in the 1st derivative plot, Figure 4-21, where a peak at 6545.5 eV associated with Mn^{2+} diminishes on charge, and reforms on discharge, while a peak at 6548.5 eV associated with a higher oxidation state grows on charge and is consumed on discharge. The oxidation state of the high-energy peak cannot be determined due to overlap of features in the Mn^{3+} and Mn^{4+} standards, Figure 4-22.

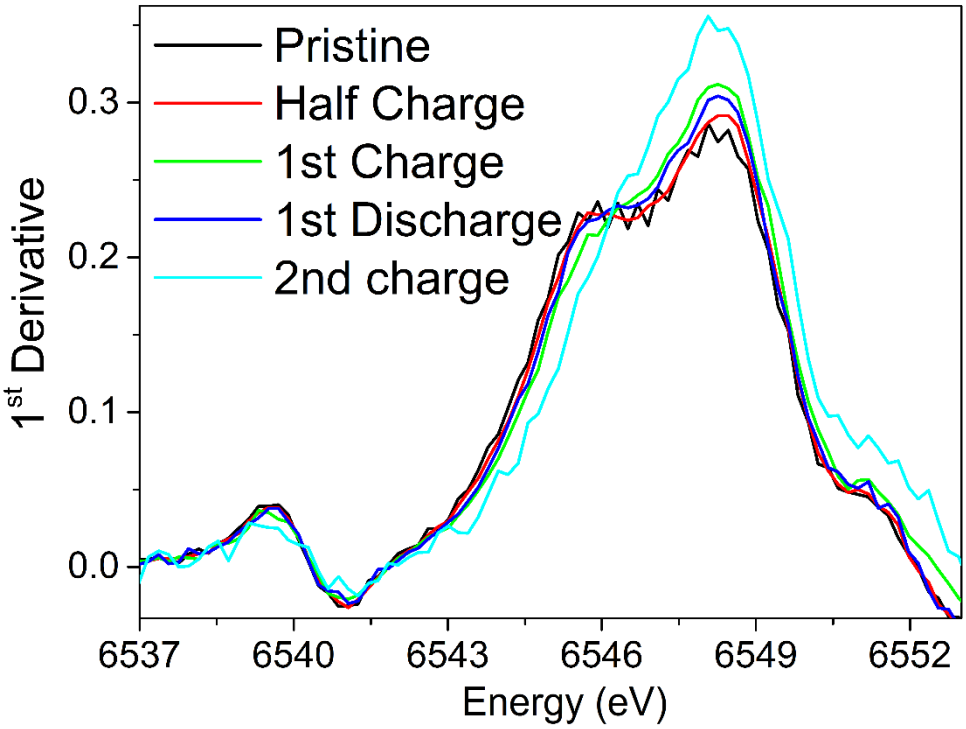

Figure 4-21. 1st derivative of the XANES spectra shown in Figure 4-19.

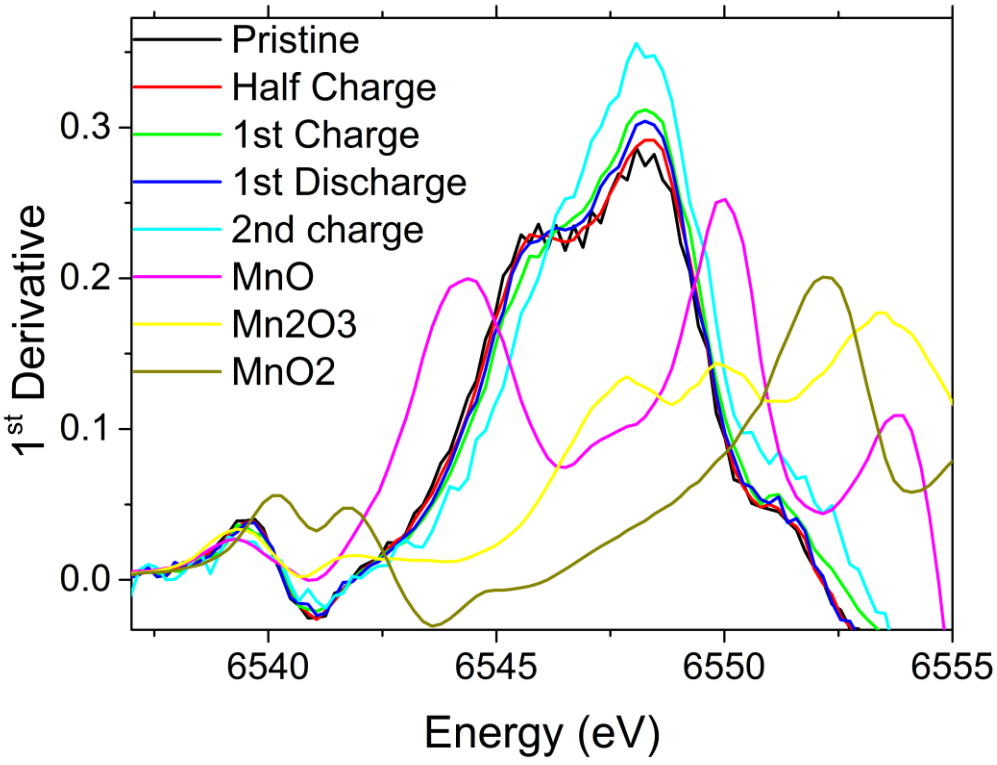

Figure 4-22. 1st derivative of the XANES spectra shown in Figure 4-20.

Although the spectra clearly show a systematic shift on cycling, the extent of the shift is less dramatic than would be expected for the complete $Mn^{2+/4+}$ oxidation suggested by the electrochemistry. This is not a unique finding and indeed there is a theme of Mn XANES showing remarkably little shift in a number of Li-ion cathode materials, including Li*M*BO_3, Li*M*PO_4 and the Li excess layered oxides.[193–195] A possible explanation for this behaviour is the hybridization of O 2*p* states and Mn 3*d* states leading to predominantly O 2*p* character below the Fermi level in these materials. Density of state calculations in $Li(Mn_xFe_{1-x})BO_3$ showed that Fe has 3*d* states isolated below the Fermi level meaning oxidation is localized on the Fe atom. While Mn displays no localized 3*d* states and instead hybridized O 2*p* sites sit below the Fermi level, therefore a much larger contribution to oxidation is expected to come from O^{2-} to O^- than $Mn^{2+/3+}$ or $Mn^{3+/4+}$. In the Li excess layered oxides, where full Li removal capacity is greater than can be balanced transition metal redox, it has been shown that oxygen redox plays a large role.[195] The formation of localized electron holes on oxygen can account for the charge compensation required for Li^+ removal and they show that the loss of O_2 is avoided by coordination of the peroxo-like species to high oxidation state transition metals. Mn in particular is shown to promote electron-hole localization and therefore stable oxygen redox chemistry. A separate study showed this anion redox chemistry can proceed in two steps, firstly formation of the peroxo-like species via $2O^{2-} \rightarrow O_2^{2-} + 2e^-$, which coordinates to the transition metal and requires a structural reorganization.[196] The further oxidation of O_2^{2-} forms O_2 which is evolved from the structure and leads to cathode degradation.

The presence of oxygen redox chemistry as well as Mn redox could explain the small spectroscopic shift observed.

4.3.4 $Mg_{4/3}Mn_{2/3}B_2O_5$ electrochemistry

$Mg_{4/3}Mn_{2/3}B_2O_5$ has a Mg removal theoretical capacity of 207.9 mAh g^{-1} (assuming removal of 2/3 Mg), with subsequent insertion of 4/3 Li giving a theoretical capacity of 231.6 mAh g^{-1}.

Cycling $Mg_{4/3}Mn_{2/3}B_2O_5$ at C/25 (Figure 4-23) gives a Mg removal capacity of 161.4 mAh g^{-1} (0.51 Mg), which is 78% of the theoretical capacity. Subsequently 130.0 mAh g^{-1} of Li is inserted into the structure, which equates to 0.74 Li assuming $Mg_{2/3}Mn_{2/3}B_2O_5$ or 0.76 Li assuming $Mg_{0.8}Mn_{2/3}B_2O_5$ as calculated from 1st charge capacity. This is fully reversible with the same sloping charge and discharge slopes seen in $MgMnB_2O_5$. As for $MgMnB_2O_5$, the capacity increases reaching a discharge capacity of 145 mAh g^{-1} after 10 cycles.

By running at the slower rate of C/100 a slightly higher Mg removal capacity of 169.3 mAh g^{-1} (0.54 Mg) is obtained, 81% of theoretical capacity. As with $MgMnB_2O_5$, the majority of the Mg

removal capacity is above 4.0 V, with just 30 mAh g^{-1} (~20%) below 4.0 V. Li insertion capacities are also increased significantly on cycling, with 166.1 mAh g^{-1} (0.95 Li assuming $Mg_{2/3}$ or 0.97 Li assuming $Mg_{0.8}$) on first discharge, further increasing to 194.8 mAh g^{-1} (1.11 Li assuming $Mg_{2/3}$ or 1.15 Li assuming $Mg_{0.8}$) at the end of the 10th discharge. Therefore, for each Mg removed from the structure, 2 Li are inserted. Li insertion on the 10th discharge occurs with a shoulder at 4.1 V and a change in slope at 3 V, higher voltages than those observed for $MgMnB_2O_5$ (4.0 and 2.5 V respectively). On charge there is continuous capacity from 1.5 V with no obvious changes in slope until around 4.0 V, with a shoulder in dQ/dV at 4.25 V, Figure 4-24. The higher voltage discharge and lower voltage charge is explained by the lower overpotential (150 mV) observed in the GITT curve, Figure 4-25. As with $MgMnB_2O_5$ 50% of the Li insertion capacity is realised above 4.0 V.

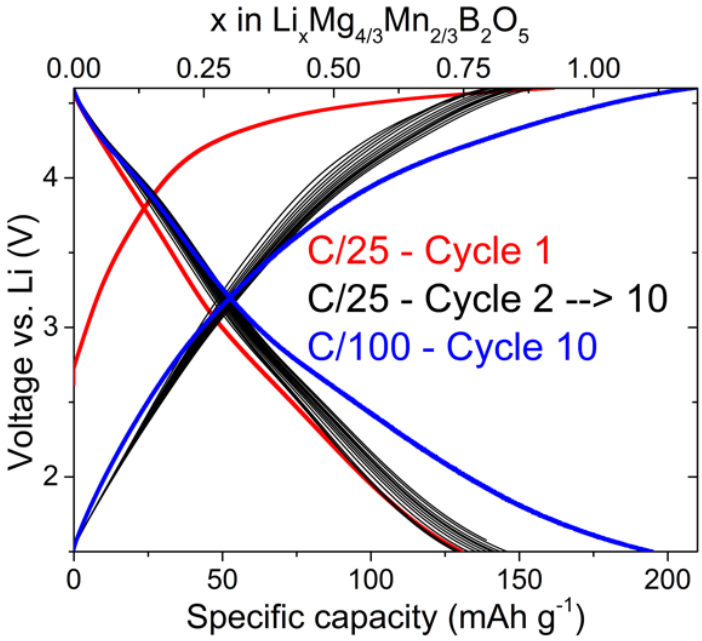

Figure 4-23. Cycling of $Mg_{4/3}Mn_{2/3}B_2O_5$ at a rate of C/25 and C/100 vs. Li. 1st cycle of Mg removal and initial Li insertion at C/25 in red, subsequent C/25 cycles in black, 10th cycle at C/100 in blue.

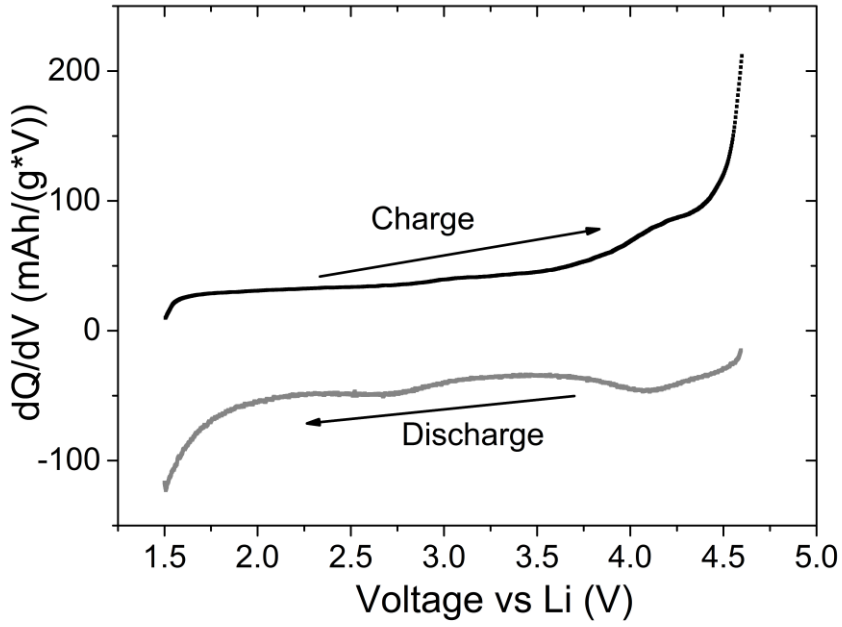

Figure 4-24. d*Q*/d*V* plot for the 10th cycle in a $Mg_{4/3}Mn_{2/3}B_2O_5$ vs. Li cell.

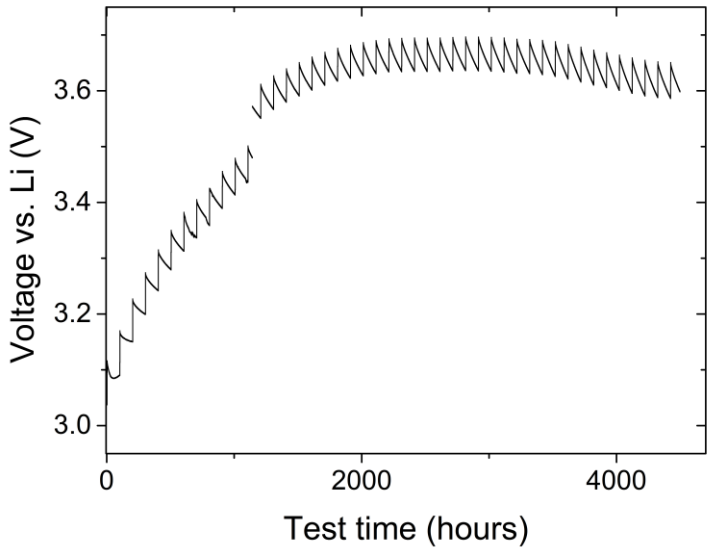

Figure 4-25. GITT on first charge of $Mg_{4/3}Mn_{2/3}B_2O_5$.

4.3.5 $Mg_{2/3}Mn_{4/3}B_2O_5$ electrochemistry

The Mn rich pyroborate $Mg_{2/3}Mn_{4/3}B_2O_5$ has a Mg removal theoretical capacity of 187.3 mAh g^{-1} and insertion of 1.33 Li into $Mn_{4/3}B_2O_5$ would give 204.05 mAh g^{-1}.

$Mg_{2/3}Mn_{4/3}B_2O_5$ has significantly lower reversible capacity than $MgMnB_2O_5$, achieving just 17.6 mAh g^{-1} after 10 cycles (0.11 Li^+), even at a slower rate of C/50, Figure 4-26. Though there

is little capacity, the discharge curves still show two processes similar to those seen in the Mg rich compounds. This suggests there are real and reversible electrochemical reactions occurring, but that they are significantly hindered. GITT experiments show a very large overpotential (>1V) associated with both Mg removal and Li insertion, Figure 4-27. This is significantly higher than the Mg rich compounds and indicates poor ionic and/or electronic conductivity. Mg and Li diffusion could be limited to the surface of the particles due to the excess of Mn blocking the Li/Mg diffusion pathways in the structure.[98] In addition, the change in structure that leads to a doubling of the unit cell on cycling may vary the interstitial site potentials, resulting in diffusion being unfavourable.

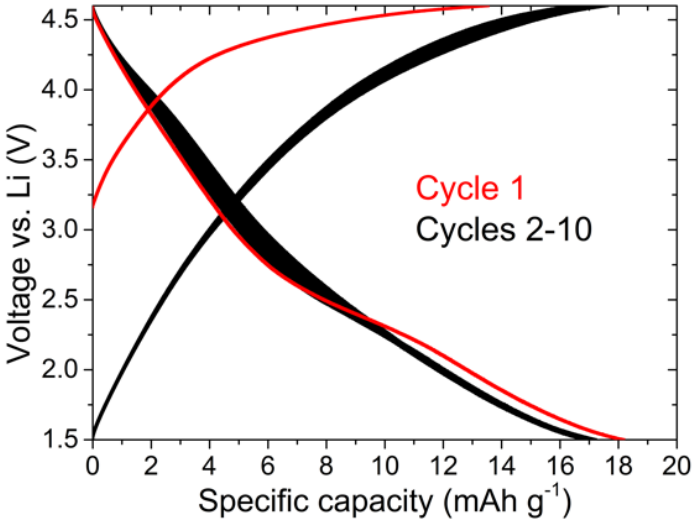

Figure 4-26. Cycling behaviour of $Mg_{2/3}Mn_{4/3}B_2O_5$ at a C/50 rate. Cycle 1 is Mg^{2+} removal and subsequent Li insertion – red curve, Cycles 2-10 are subsequent cycles vs. Li – black curve.

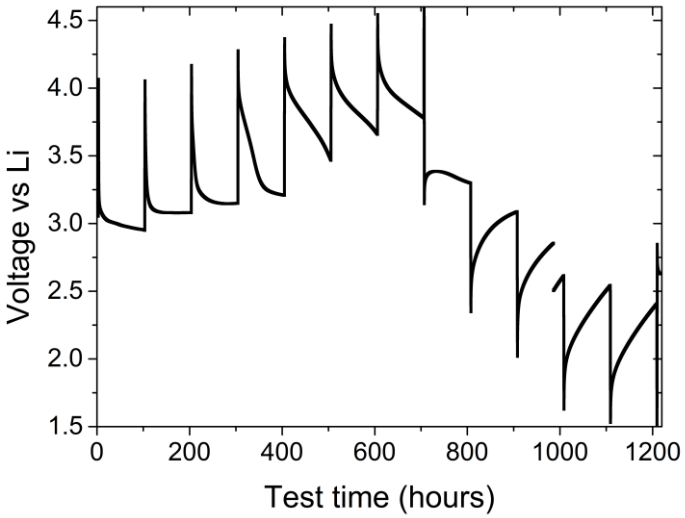

Figure 4-27. Galvanostatic intermittent titration experiment on $Mg_{2/3}Mn_{4/3}B_2O_5$ on 1st charge and discharge vs. Li. Over 1V of overpotential is observed on both 1st charge and discharge.

4.4 Conclusions

Three points of the solid solution formed between $Mg_2B_2O_5$ and $Mn_2B_2O_5$ ($Mg_xMn_{2-x}B_2O_5$ where x = 2/3, 1 and 4/3) have been synthesised and shown to crystallise in the triclinic structure consisting of interconnected ribbons of MO_6. Mn shows a preference to occupy the site $M1$ which is the more distorted and larger octahedral site, due to its large ionic radius. However, the difference is not great enough to cause complete ordering, so Mg and Mn are still distributed across the two sites. The increased Mg content on site $M2$ may aid diffusion as this site is calculated to have greater ion mobility than site $M1$.

The three phases display varying electrochemical activities when cycled vs. a Li anode. Increasing the Mg content reduces the overpotential for Mg removal and Li insertion, improving Li cycling capacities. The low Mg content, x = 2/3 has very little Mg removal or Li insertion capacity above 1.5 V.

$MgMnB_2O_5$ has the highest theoretical capacity of the three phases and on charge full Mg removal from the structure is observed (330 mAh g^{-1}). Further cycling vs. a Li^+ anode achieves a Li discharge capacity of 240 mAh g^{-1} (1.4 Li^+), with 193 mAh g^{-1} retained after 100 cycles. This is equivalent to reversible intercalation of 1.1 Li^+ ions per unit cell after 100 cycles. The electrochemical process occurs over a sloping profile down to 1.5 V with two features observed at 2.5 V and 4.0 V on discharge. Capacities >100 mAh g^{-1} are retained at the increased rate of C/5, with a gradual increase in capacity to >300 mAh g^{-1} after 1000 cycles, which is approaching full theoretical capacity (insertion of 2 Li^+ ions). The cause of the increase is unknown though similar phenomena have been observed previously and attributed to electrochemical grinding, change in crystallinity or Mn site migration. The combination of high capacity and moderate rate capability makes this material of interest for high power cells.

A small volume change on Mg removal and Li insertion in $MgMnB_2O_5$ was observed by PND and PXRD structural analysis. The volume change on Li cycling is just 1%, similar to that observed for $LiMBO_3$, which is advantageous for cycle lifetimes. ^{7}Li NMR of x = 1 charged and discharged samples shows reversible insertion of Li into the structure. This, along with the oxidation and reduction of Mn calculated from the SQUID Magnetometry demonstrates that Mg is removed from the structure on charge, and replaced by Li on discharge.

Discharging $MgMnB_2O_5$ to below 1.5 V sees the full theoretical capacity of 342.5 mAh g^{-1} achieved by 0.88 V, meaning that for each Mg removed, 2 Li have been inserted. A further decrease in voltage leads to a very high capacity of >1045 mAh g^{-1} which is thought to consist

of a combination of a conversion reaction to a Mn^0 compound and side reactions. This process is not fully reversible and proceeds with a very large polarisation.

0.51 Mg (78% of theoretical) can be removed from the $x = 4/3$ material at C/25, this is increased to 0.54 Mg (169.3 mAh g^{-1}, 81% of theoretical capacity) at the slower rate of C/100. Subsequently reversible insertion of 0.75 Li per unit cell at C/25 is achieved, increased to 1.1 Li at the slower rate of C/100, with a discharge capacity of 194.8 mAh g^{-1} (84% of theoretical). For each Mg removed from the structure 2 Li are inserted, suggesting that if full demagnesiation could be achieved then full Li capacity would follow. The $x = 2/3$ material achieves 17.6 mAh g^{-1} at a rate C/50, with the lower capacity caused by a much greater overpotential than in the $x = 1$ or 4/3 systems. However, similar features in the voltage profile are observed suggesting the material is electrochemically active.

This initial study of a new class of Li intercalating polyanion material demonstrates facile Mg removal and Li insertion. The quantity of Li inserted is much greater than that achieved in the initial studies of Li*M*BO_3 (~0.2 Li)[44] which have since been optimised to reach full capacity, suggesting with further study improvements in capacity, voltage and stability could be made.

4.5 Appendix

Table A4-1. Refined cell parameters determined from combined powder neutron and X-ray diffraction at room temperature for $MgMnB_2O_5$. Errors given in brackets.

$MgMnB_2O_5$	**Atom**	***x***	***y***	***z***	**B**	**Occ.**
Triclinic $P\bar{1}$ Volume = 181.376(9) Å^3 *a* = 3.20758(9) Å *b* = 6.2134(2) Å *c* = 9.4127(4) Å α = 104.623(2) Å β = 90.511(2) Å γ = 92.012(3) Å χ^2 = 3.33 R_{wp} = 19.7	Mn/Mg1 (2*i*)	0.725(2)	0.218(7)	0.361(6)	3.0(3)	0.647/0.353 (8)
	Mn/Mg2 (2*i*)	0.201(3)	0.377(1)	0.099(73)	1.5(4)	0.353/0.647(8)
	B1 (2*i*)	0.619(4)	0.679(2)	0.352(1)	0.8	1
	B2 (2*i*)	0.333(4)	0.878(3)	0.170(1)	0.8	1
	O1 (2*i*)	0.266(5)	0.698(4)	0.054(2)	0.8	1
	O2 (2*i*)	0.216(5)	0.090(4)	0.182(2)	0.8	1
	O3 (2*i*)	0.739(6)	0.478(3)	0.256(2)	0.8	1
	O4 (2*i*)	0.550(5)	0.859(3)	0.299(1)	0.8	1
	O5 (2*i*)	0.762(5)	0.722(3)	0.499(2)	0.8	1

Table A4-2. Refined cell parameters determined from X-ray diffraction at room temperature for $Mg_{2/3}Mn_{4/3}B_2O_5$. Errors given in brackets.

$Mg_{2/3}Mn_{4/3}B_2O_5$	**Atom**	***x***	***y***	***z***	**B**	**Occ.**
Triclinic $P\bar{1}$ Volume = 185.172(9) Å^3 *a* = 3.23915(7) Å *b* = 6.2347(2) Å *c* = 9.4884(3) Å α = 104.735(1) Å β = 90.624(1) Å γ = 92.943(3) Å χ^2 = 2.15 R_{wp} = 20.1	Mn/Mg1 (2*i*)	0.741(2)	0.2161(6)	0.3670(6)	2.8(3)	0.73/0.28 (1)
	Mn/Mg2 (2*i*)	0.2317(2)	0.3636(7)	0.1005(6)	3.7(3)	0.61/0.39 (1)
	B1 (2*i*)	0.6910	0.6793	0.3523	0.8	1
	B2 (2*i*)	0.3327	0.8784	0.1699	0.8	1
	O1 (2*i*)	0.2658	0.6975	0.0543	0.8	1
	O2 (2*i*)	0.2164	0.0899	0.1821	0.8	1
	O3 (2*i*)	0.7393	0.4777	0.2562	0.8	1
	O4 (2*i*)	0.5504	0.8591	0.2992	0.8	1
	O5 (2*i*)	0.7624	0.7222	0.4994	0.8	1

Table A4-3. Refined cell parameters determined from combined powder neutron and X-ray diffraction at room temperature for $Mg_{4/3}Mn_{2/3}B_2O_5$. Errors given in brackets.

$Mg_{4/3}Mn_{2/3}B_2O_5$	**Atom**	***x***	***y***	***z***	**B**	**Occ.**
Triclinic $P\bar{1}$ Volume = 179.131(6) Å^3 *a* = 3.18809(7) Å *b* = 6.2021(1) Å *c* = 9.3675(2) Å α = 104.556(1) Å β = 90.534(1) Å γ = 92.029(1) Å χ^2 = 11.7 R_{wp} = 9.88	Mn/Mg1 (2*i*)	0.704 (6)	0.185 (4)	0.347 (2)	1.9 (2)	0.403/0 .597(6)
	Mn/Mg2 (2*i*)	0.215(4)	0.369 (4)	0.107 (1)	1.9 (2)	0.264/0.736 (6)
	B1 (2*i*)	0.692 (1)	0.679 (7)	0.353 (5)	0.24(9)	1
	B2 (2*i*)	0.337 (1)	0.8784 (9)	0.1699 (5)	0.06(9)	1
	O1 (2*i*)	0.256 (1)	0.6958 (8)	0.0550 (5)	0.01(1)	1
	O2 (2*i*)	0.207 (2)	0.0930(9)	0.1831(5)	0.3(1)	1
	O3 (2*i*)	0.749 (2)	0.4794(9)	0.2558 (5)	0.2(1)	1
	O4 (2*i*)	0.551 (1)	0.8597(8)	0.2973(6)	0.43(9)	1
	O5 (2*i*)	0.754(2)	0.7211(9)	0.5034 (5)	1.0(1)	1

Chapter 5. Synthesis and electrochemical investigation of $Mg\mathit{M}B_2O_5$ (M = Co, Fe, Ni)

5.1 Introduction

In the previous chapter, it was shown that replacement of the Mg in $Mg_xMn_{2-x}B_2O_5$ with Li in an electrochemical cell leads to high capacities which are maintained over 100's of cycles. By altering the transition metal in the structure the voltage, capacity, structural stability and electrical conductivity can be changed. This is exemplified in the $Li\mathit{M}BO_3$ system where when M = Mn a high capacity can be achieved but with high polarisation, whereas when M = Fe reversibility is improved but structural stability is an issue and when M = Co very little capacity is achieved due to poor electronic conductivity. Ni is also often used to raise the voltage of the system. Therefore, the electrochemical properties of pyroborates containing Co, Fe and Ni are investigated.

5.2 Synthesis

The Ni and Co pyroborates were synthesised by grinding stoichiometric amounts of the transition metal oxalate $NiC_2O_4.2H_2O$ (Puratronic, 99.998%), or $CoC_2O_4.2H_2O$ (Aldrich, >99%), with MgO (Alfa Aesar, 99.998%) and H_3BO_3 (Alfa Aesar, >99.99%) into a fine powder. The powders were then reacted with the same heating schedule as $Mg_xMn_{2-x}B_2O_5$, however due to the stability of Co^{2+} and Ni^{2+}, reactions were carried out in air. The Ni containing orthoborates were stored under argon to avoid hydration. ^{11}B enriched samples prepared for neutron powder diffraction were synthesised from ^{11}B-Boric acid (Aldrich 99%).

Compounds in the $Mg_xFe_{2-x}B_2O_5$ series were found to be more sensitive to synthesis conditions than Mn, Co, or Ni based pyroborates. This is not wholly unsurprising as synthesis requires stabilising Fe^{2+} over the more stable d^5 Fe^{3+}, and previous studies showed that $LiFeBO_3$ is air sensitive.[46] Initial synthesis attempts, using the published method,[98] involving flowing 5% H_2 and a graphite crucible at 1050 °C were unsuccessful with large amounts of Fe metal present, indicating these conditions were too reducing. Subsequent alterations to the conditions to give a less reducing atmosphere (using argon as the flowing gas and an alumina crucible) were successful for x = 2/3 but not for x = 1 or 4/3. Using these conditions for x = 1 or 4/3 produced a variety of impure products. In the least reducing conditions (argon flow and alumina crucible) Fe^{3+} oxidation products were observed ($(Mg,Fe)_2OBO_3$), and in intermediate conditions (5% H_2 and alumina crucible or argon and graphite crucible) other Fe^{2+} borates ($(Mg,Fe)_3(BO_3)_2$) were

observed alongside the desired product. Therefore, an alternative synthesis route was attempted.

$MgFeB_2O_5$ was synthesised in sealed, evacuated, silica tubes. To avoid degassing during synthesis, a reaction with constant stoichiometry was required, therefore FeO, MgO and B_2O_3 starting materials were used. Stoichiometric amounts were weighed, ground and formed into a dense pellet before being sealed in an evacuated silica tube. The reaction mixture was heated to 600 °C at 3 °C min^{-1} then to 1050 °C at 1 °C where it was held for 24 hours before being furnace cooled. Exposure to air was minimised after synthesis to avoid degradation. This synthesis route was unsuccessful for $Mg_{4/3}Fe_{2/3}B_2O_5$, with a variety of impurities observed such as $(Mg,Fe)_2BO_4$, $(Mg,Fe)_3(BO_3)_2$ and Fe_2O_3.

5.3 Results

5.3.1 $Mg_xCo_{2-x}B_2O_5$

5.3.1.1 Structure

The new mixed metal structures with x = 2/3, 1 and 4/3 were synthesised as phase pure purple powders in the triclinic form, as indicated by PXRD, Figure 5-1a. Rietveld analysis was used to confirm the purity and calculate the unit cell volumes and *M* site occupancies, Table 5-1. As PXRD is not sensitive to O or B, only the *M* site positions and occupancies were refined, a representative refinement for x = 2/3 is shown in. The change in cell volume with x is linear, meaning a solid solution has been formed between $Mg_2B_2O_5$ and $Co_2B_2O_5$, as was observed for the Mn pyroborate, Figure 5-1b.

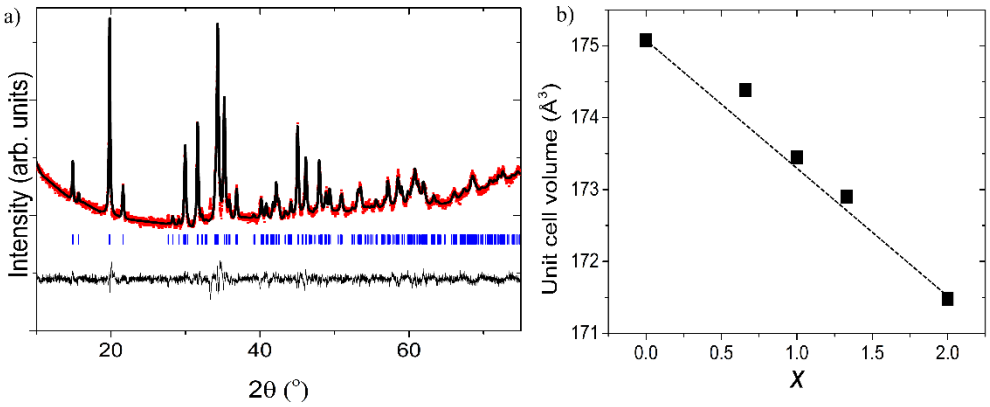

Figure 5-1. a) X-ray powder diffraction pattern (red dots) and fit (black line) of $Mg_{4/3}Co_{2/3}B_2O_5$. Allowed Bragg reflections are shown as blue tick marks. b) Unit cell volume as a function of x in $Mg_xCo_{2-x}B_2O_5$.

Table 5-1. Summary of the refined crystal structure parameters determined from PXRD and PND at room temperature for the solid solution $Mg_xCo_{2-x}B_2O_5$, formed between $Mg_2B_2O_5$ and $Co_2B_2O_5$.

$Mg_xCo_{2-x}B_2O_5$	**$x = 0$[195]**	**$x = \frac{2}{3}$**	**$x = 1$**	**$x = \frac{4}{3}$**	**$x = 2$[157,175]**
Space group	$P\bar{1}$	$P\bar{1}$	$P\bar{1}$	$P\bar{1}$	$P\bar{1}$
χ^2	n/a	4.08	2.52	4.77	n/a
R_{wp}	n/a	21.1	5.04	5.32	n/a
Vol (Å^3)	175.08	174.380(8)	173.45(1)	172.90(1)	171.48/171.33
M1 occ (Co/Mg)	1/0	0.653/347(7)	0.44/0.56(2)	0.33/0.67(1)	0/1
M2 occ (Co/Mg)	1/0	0.680/0.320(6)	0.51/0.49(2)	0.34/0.66(1)	0/1
Average M1-O (Å)	2.13	2.127(1)	2.13(1)	2.13(1)	2.1292(15)
Average M2-O (Å)	2.11	2.113(8)	2.11(1)	2.11(1)	2.0946(15)

As with the Mn version, Co and Mg occupy both sites, however here they are completely disordered. In each phase there is a very slight tendency for Co to occupy site *M*2 over *M*1, but the deviation from disorder is so small as to be negligible. The lack of ordering may be due to the similar size of Co and Mg, high spin Co^{2+} has an ionic radius of 74.5 pm and the radius of Mg^{2+} is 72 pm. The cell volumes of the parent compounds ($x = 2$ and $x = 0$) are also more similar than in the Mn system (171.48 and 175.08 Å^3 in the Co system, and 171.48 and 189.53 Å^3 in the Mn system). The lack of ordering between Co and Mg is in stark contrast to that seen in the orthoborates, where almost full cation ordering was observed, Chapter 3. In the orthoborates the two sites have different symmetries (2*a* and 4*f*), leading to a driving force other than site size, whereas in the pyroborates the two sites have the same symmetry (2*i*). The lack of ordering may hinder Mg-ion diffusion (and subsequent Li intercalation) as there are more immobile Co on the *M*2 site.

This series of materials has the same structure as the Mn pyroborates, therefore the BVS calculated diffusion pathway is the same. However, as Co has a higher redox potential than Mn, and the cation ordering differs, electrochemical properties may differ.

5.3.1.2 Theoretical capacities of $Mg_xCo_{2-x}B_2O_5$

As demonstrated for the Mn series, the theoretical capacity of each phase is dependent on both the total Co content and the amount of extractable Mg while also maintaining a reasonable Co oxidation state. Therefore, x = 2/3, where if all the Mg is removed a compound with average oxidation state of Co^{3+} is formed, has a Mg removal theoretical capacity of 180.45 mAh g^{-1}. Insertion of 2 Li for each Mg removed (*i.e.* 1.33 Li per formula unit) into $Co_{4/3}B_2O_5$ to fully reduce back to Co^{2+} gives a theoretical capacity of 207.5 mAh g^{-1}. For both the x = 1 and x = 4/3 the higher Mg content means high capacities are possible, but this relies on oxidation to Co^{4+}. For x =1, complete removal of Mg leads to $Co^{4+}B_2O_5$ with a theoretical capacity of 289.9 mAh g^{-1}. Insertion of 2 Li to form $Li_2Co^{2+}B_2O_5$ has a higher capacity due to the decreased mass of the demagnesiated phase, 333.8 mAh g^{-1}. For x = 4/3 not all the Mg can be removed without oxidising Co above Co^{4+}, therefore Mg removal is limited to forming $Mg_{2/3}Co_{2/3}B_2O_5$ with a capacity of 206 mAh g^{-1}. Full lithiation of this compound would form $Li_{4/3}Mg_{2/3}Co_{2/3}B_2O_5$, 226.9 mAh g^{-1}. As before all charge rates are based on the Mg removal capacity.

5.3.1.3 $Mg_{2/3}Co_{4/3}B_2O_5$ electrochemistry

The initial charge vs. a Li anode at a rate of C/50 yields a capacity of 20.0 mAh g^{-1}, 0.075 Mg^{2+} per formula unit, similar to that observed for $Mg_{2/3}Mn_{4/3}B_2O_5$, Figure 5-2. However, unlike the Mn version 2 clear plateaus are evident. After an initial overpotential associated with nucleation, the reaction proceeds at a voltage of ~3.9 V vs. Li, followed by a second process form 4.35 V to 4.6 V. The two processes may be Mg removal from the two *M* sites, which have different environments and therefore differing free energies. Subsequent discharge into the partially demagnesiated structure involved insertion of 0.09 Li^+ (15 mAh g^{-1}) with a sloping voltage profile. The shoulder at 2.35 V indicates an electrochemical process is occurring, however over subsequent cycles this disappears, and the discharge capacity reduces. On charge to 4.6 V the process is fully reversible. The limiting charge voltage was then increased to 4.8 V with the aim of increasing the reversible capacity by de-intercalating more ions. This was partially successful, increasing the discharge capacity back up to 15.5 mAh g^{-1} (from a minimum of 12.4 mAh g^{-1}), however the efficiency was reduced with greater capacity on charge than discharge, presumably due to electrolyte break down.

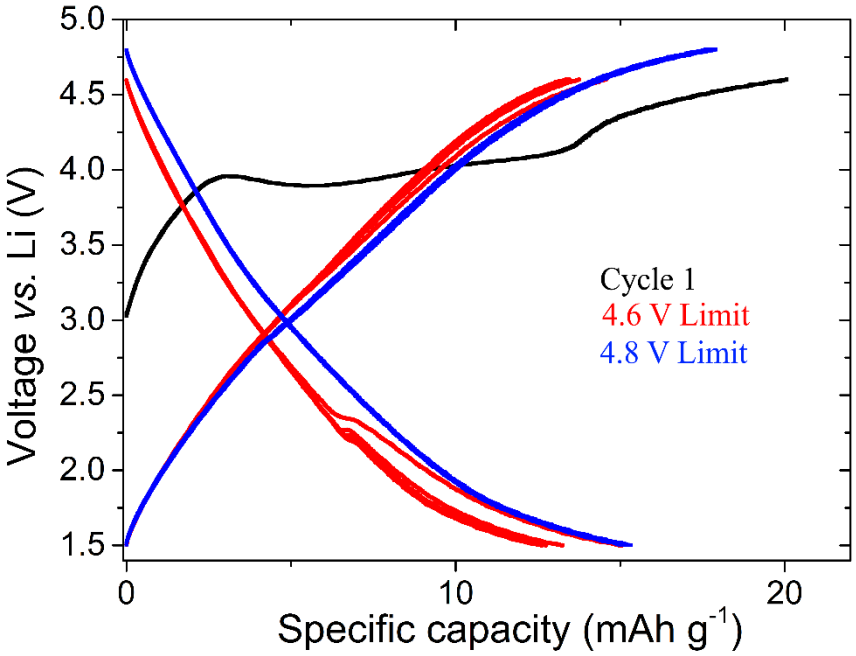

Figure 5-2. Cycling behaviour of $Mg_{2/3}Co_{4/3}$ at a rate of C/50. 1st charge removal of Mg – black curve. Li cycling between 4.6 V and 1.5 V vs. Li – red curve. Li cycling between 4.8 V and 1.5 V – blue curve.

Two further methods were employed to try and improve the reversible capacity of the material: a) increasing the temperature at which the cells were cycled which improves the kinetics and may aid ion diffusion, and b) reducing the discharge voltage which may allow further intercalation to occur with higher overpotentials.

Cycling at 55 °C increases the 1st charge capacity to 93.7 mAh g^{-1}, 0.34 Mg and 52% of the theoretical capacity, significantly more than is achieved at room temperature (20.0 mAh g^{-1}), Figure 5-3. The low voltage process occurs at 3.25 V compared to the 3.9 V observed at room temperature, suggesting that cycling at higher temperature has reduced the overpotential, therefore affording greater capacity within the same voltage window. Li insertion capacities are also increased with a 1st discharge of 43.8 mAh g^{-1} equating to intercalation of 0.27 Li ions (20% of theoretical capacity). After cycling at 55 °C for >100 cycles the reversible capacity has increased significantly, with a discharge capacity of 264.4 mAh g^{-1}, 1.5 Li which is almost fully reversible, with a slight excess in capacity on charge. The increase in capacity is accompanied by the loss of plateaus on both charge and discharge, though a change in slope is still observed at around 2.8 V and 3.5 V. It is possible that the increase in reversible capacity is due to a combination of improved intercalation with increasing cycle number due to electrochemical grinding and structural rearrangements while retaining the basic pyroborate structure.

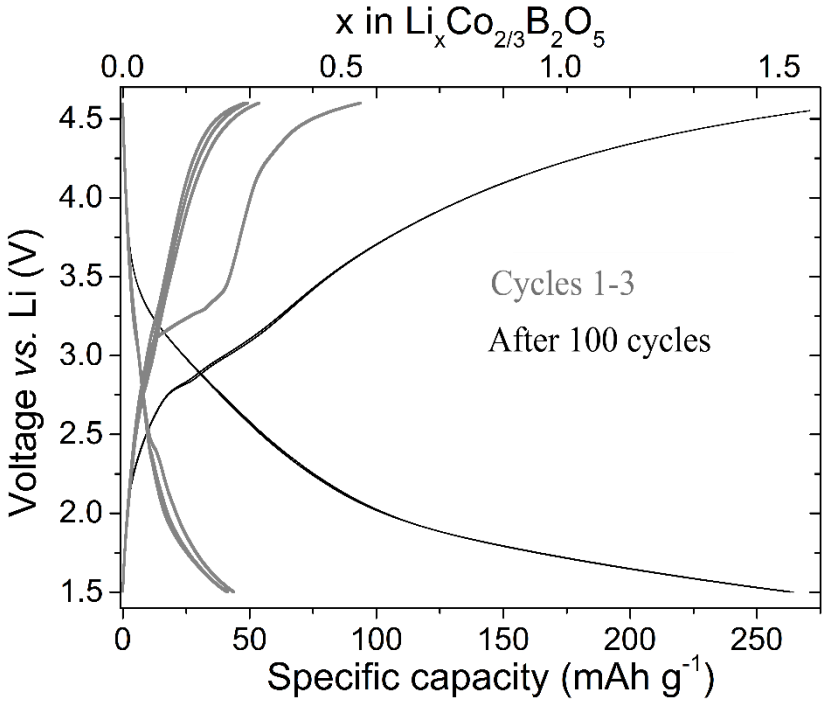

Figure 5-3. Cycling behaviour at 55 °C of $Mg_{2/3}Co_{4/3}B_2O_5$ at a rate of C/50 vs. Li. Cycles 1-3 – grey curve. Representative cycle after >100 cycles – black curve.

Discharging to 1 V gives a capacity far greater than the theoretical Li intercalation capacity (569 mAh g^{-1} compared to 207.5 mAh g^{-1}) which suggests the formation of a $Li_{3.3}Mg_xCo_{4/3}B_2O_5$ phase, Figure 5-4. To compensate for the insertion of 3.3 Li, Co must be reduced to below 2+, and in fact, assuming the presence of some residual Mg in the structure, Co would need to be around Co^0. This likely proceeds via a conversion reaction to form a Co^0 compound. A large portion of the discharge capacity is irreversible, with removal of 220 mAh g^{-1}, ~1.3 Li, achieved up to 4.6 V. The voltage profile is sloping with 2 processes visible, a low voltage process below 2.5 V and a high voltage process above 4 V. Subsequent discharging shows significantly less capacity than the 1st discharge, however it is still greater than on charge (340.2 and 260.0 mAh g^{-1} on 2nd and 3rd discharge respectively). The cycling occurs with a very large overpotential.

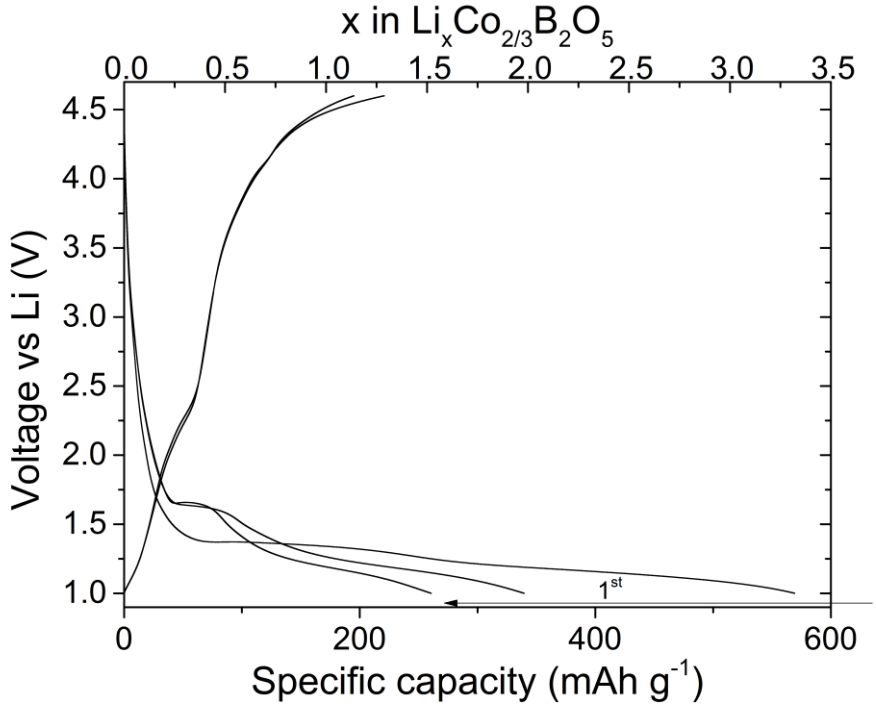

Figure 5-4. Cycling behaviour of $Mg_{2/3}Co_{4/3}B_2O_5$ with extended voltage window. 1st charge (Mg removal) has been removed. 1st discharge to 1 V has a capacity of 569 mAh g^{-1}, far greater than the theoretical capacity for Li intercalation of 226.9 mAh g^{-1}.

5.3.1.3.1 Ex-situ diffraction

Ex-situ PXRD diffraction of $Mg_{2/3}Co_{4/3}B_2O_5$ discharge to 1 V shows reflections that can be assigned to the pyroborate structure, indicating that not all the material has undergone a conversion reaction, Figure 5-5. It is worth noting that the peak ~2θ = 18° due to a doubling of the unit cell, present in the Mn system, is not observed here. This suggests that the original triclinic crystal structure is retained on cycling. No Co metal or other new phases are observed meaning any conversion reaction, or side reactions that may account for the extra capacity over theoretical, form amorphous products or very small nanoparticles. This has previously be observed in the VS_4 cathode where elemental V is formed and observed in the pair distribution function of X-ray data, but not in the PXRD.[197]

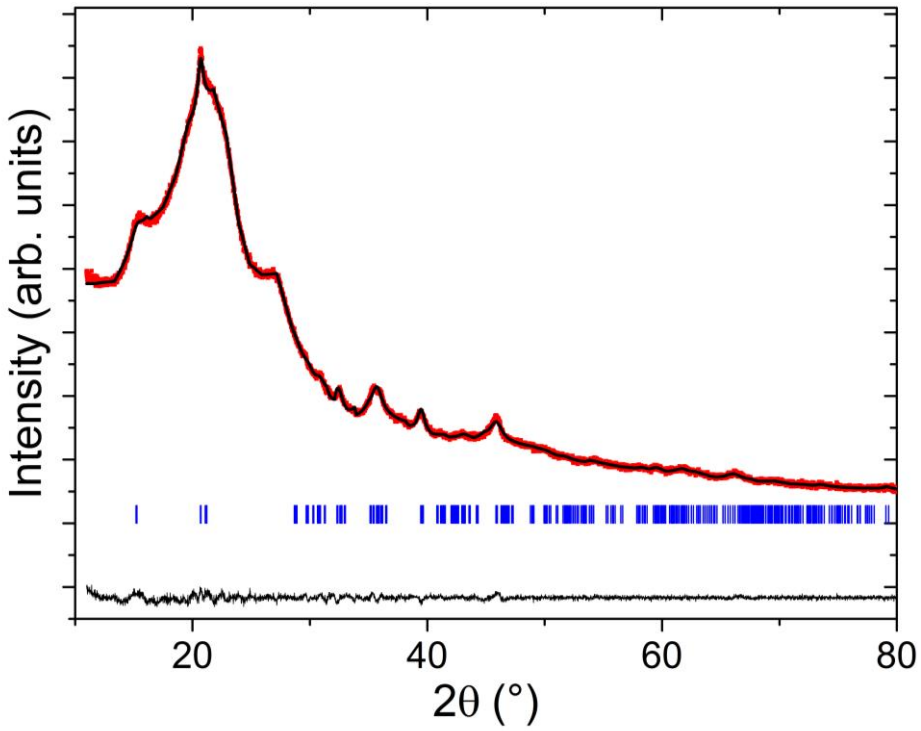

Figure 5-5. Ex-situ powder X-ray diffraction of $Mg_{2/3}Co_{4/3}B_2O_5$ discharged to 1 V vs. Li. Diffraction pattern (red dots). Le Bail fit of the triclinic structure (black curve). Allowed Bragg reflections (Blue tick marks).

5.3.1.4 $MgCoB_2O_5$ electrochemistry

$MgCoB_2O_5$ has the highest of theoretical capacities of the Mg,Co series, with oxidation to Co^{4+} and full Mg removal giving 290.0 mAh g^{-1} and insertion of 2 Li into the demagnesiated structure giving 333.9 mAh g^{-1}.

Cycling vs. Li at a rate of C/25 realises no appreciable capacity (<2 mAh g^{-1}, not shown) therefore the rate was reduced to C/100 to investigate if the material is completely inactive, or if the reaction is hindered by a large activation barrier (arising from poor electronic or ionic conductivity). At a rate of C/100, 6.3 mAh g^{-1} of Mg is removed (0.02 Mg), significantly less than that achieved in $Mg_{2/3}Co_{4/3}B_2O_5$ or the analogous $MgMnB_2O_5$, but more than at C/25, Figure 5-6. Li insertion capacities are also low (5.3 mAh g^{-1}, 0.03Li, on first discharge), presumably as the lack of Mg removal leaves few vacancies to occupy. The small Li quantity that is inserted is fully reversible with 5.2 mAh g^{-1} observed on 2nd charge. The Mg removal occurs with a plateau at 3.7 V, slightly lower than in the $Mg_{2/3}Co_{4/3}B_2O_5$ material (3.9 V), with a second process starting above ~4.3 V. Two features are also observed on Li insertion, one at 2.3 V similar to that observed in $Mg_{2/3}Co_{4/3}B_2O_5$, and a second at 1.9 V that is unique to the material, followed by a shallow slope to 1.5 V. The Li removal voltage profile is more sloping, consistent with previous studies.

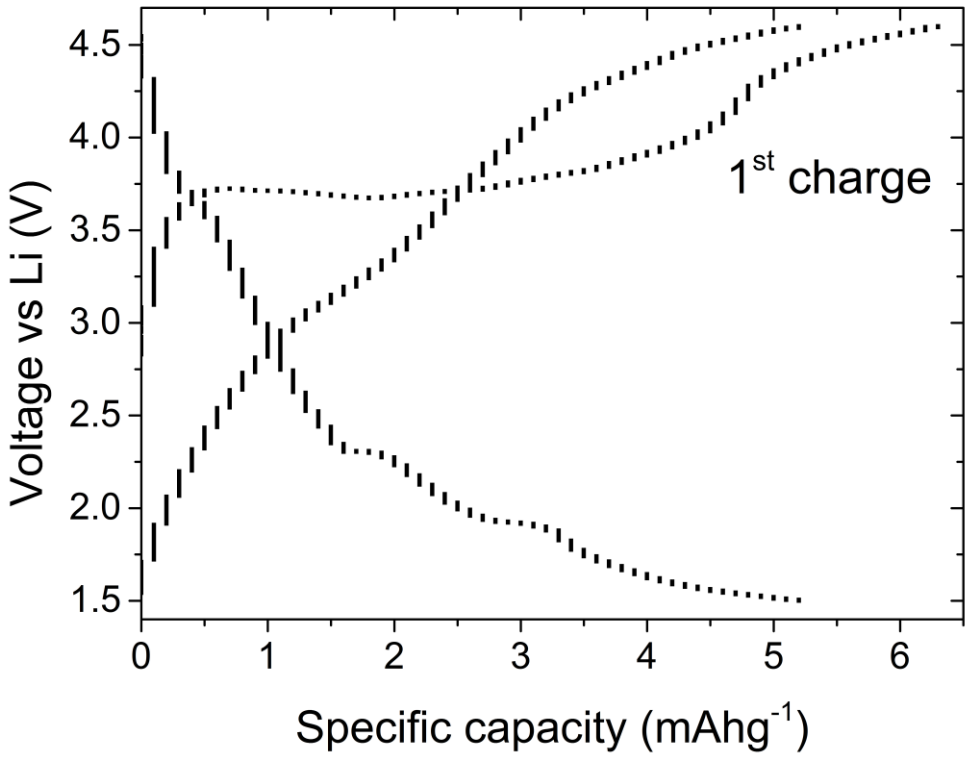

Figure 5-6. Cycling behaviour of $MgCoB_2O_5$ at a rate of C/100 at room temperature vs. Li. 1^{sr} charge involves Mg removal, subsequent cycling involves Li cycling.

By charging at the slower rate of C/100 and the elevated temperature of 55 °C the first charge capacity is increased to 61.8 mAh g^{-1}, 0.21 Mg, Figure 5-7. This is 10 times greater than that achieved at room temperature, indicating electrochemical reactions in the material are possible, but are severely hindered by electronic or ionic conductivity. As with the room temperature data, two plateaus are present, though the overpotential is now reduced; they occur at 3.3 V and 4.5 V. The Li insertion capacity is also increased, though the improvement is less dramatic, with <14 mAh g^{-1} (0.8 Li^+) achieved in the first 15 cycles. The discharge voltage profile is smoothed out compared to the room temperature cycles, with only a shoulder at 2.3 V remaining on 1st discharge, and no discernible features on subsequent cycles. The charge capacity remains larger than the discharge for ~5 cycles, though the lower voltage plateau is no longer observed, being replaced by a sloping profile. This excess charge capacity could be due to continued removal of Mg which is not replaced by Li, however it is more likely a combination of side reactions caused by the increased temperatures. After 5 cycles the difference between charge and discharge capacities is small, however continued capacity fade is observed.

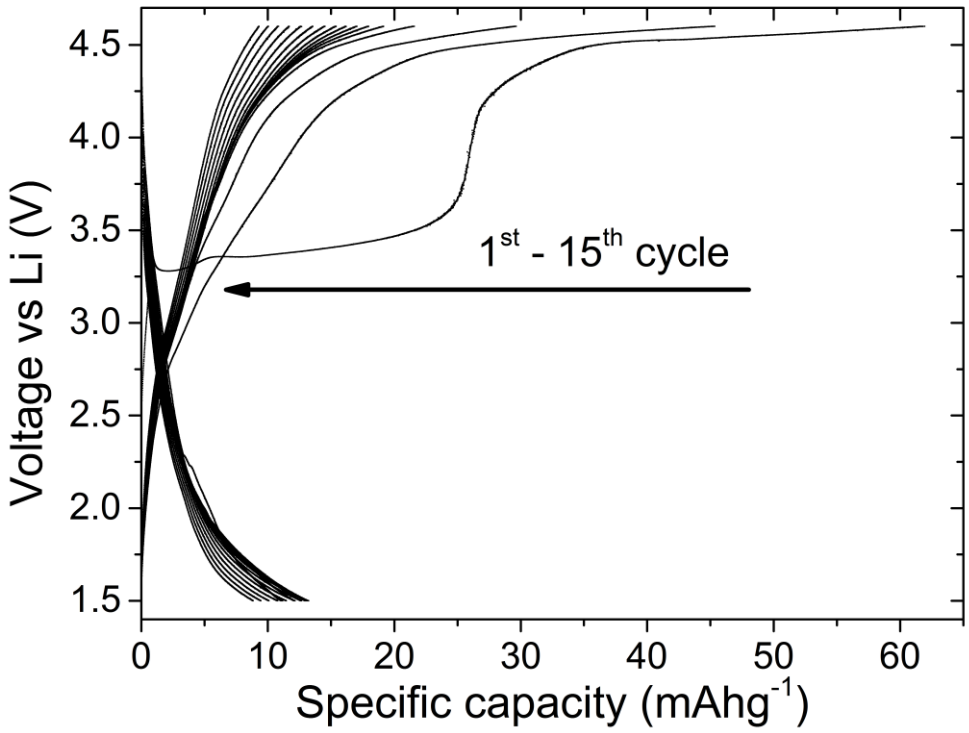

Figure 5-7. Cycling behaviour at 55 °C of $MgCoB_2O_5$ at a rate of C/100 vs. a Li anode.

5.3.1.5 Conclusions

$Mg_{2/3}Co_{4/3}B_2O_5$, $MgCoB_2O_5$ and $Mg_{4/3}Co_{2/3}B_2O_5$ were synthesised and shown to crystallise in the same $P\bar{1}$ space group as the Mn series. Whereas the Mn series displayed some propensity for cation ordering, here the Co and Mg are completely disordered over the two sites. This is due to the similarity in ionic radii of the cations, which also leads to minimal unit cell volume changes across the series.

Cycling of $Mg_{2/3}Co_{4/3}B_2O_5$ at room temperature gives a low Mg removal capacity (25 mAh g^{-1}), however two clear plateaus are observed at 3.9 V and 4.35 V, indicating Mg is being removed but diffusion is hindered. The Li insertion capacity is also limited, though it is fully reversible between 1.5 V and 4.6 V. Extending the charge voltage limit to 4.8 V increases the reversible capacity slightly, hinting that higher capacities could be achieved if the overpotential could be reduced. Cycling at 55 °C improved the Mg removal capacity to 93.7 mAh g^{-1} (52% of theoretical capacity, 0.34 Mg^{2+}) over two processes, the first at 3.25 V and the second above 4.2 V. Li insertion capacities were also improved, with 1st discharge achieving 20% of theoretical capacity, which then increases to just over full theoretical capacity (264.4 mAh g^{-1}, 1.5 Li) after 100 cycles. Discharge to 1 V sees a partially irreversible conversion reaction occur

where a Co^0 compound is likely formed to balance the insertion of 3.3 Li (569 mAh g^{-1}). Only 220 mAh g^{-1} or 1.3 Li is reversible, and this quickly fades over the first 3 cycles. Ex-situ PXRD of material discharged to 1.0 V showed a retention of the polyanion framework, and no new phases, meaning either the 3.3 Li are inserted into the framework, or the conversion reaction products are amorphous and the observed peaks are due to residual orthoborate material.

Cycling of $MgCoB_2O_5$ at C/100 and elevated temperatures gives a Mg removal capacity of 61.8 mAh g^{-1} over two voltage plateaus at 3.3 V and 4.5 V. This is 10 times greater than achieved at room temperature and indicates that a reaction with a high activation barrier is occurring. 1st discharge see insertion of 0.04 Li^+ (13.2 mAh g^{-1}), which fades to 8.8 mAh g^{-1} after 15 cycles. The first 5 charge process see substantial excess capacity which decreases with increasing cycle number.

5.3.2 $Mg_xNi_{2-x}B_2O_5$

5.3.2.1 Structure

Ni is often used as a redox ion to raise the voltage of a system (e.g. in NMC), however its use in polyanion battery electrodes is limited. Synthesising $LiNiPO_4$ proved challenging and its reversible capacity is low due to poor electrical conductivity and instability of electrolytes at high voltages,[198] and to our knowledge $LiNiBO_3$ has not been studied. $MgNiB_2O_5$ was synthesised to assess the use of Ni as the transition metal in the pyroborates, though it is more likely to be used as a co-ion in a mixed transition-metal-structure. Unlike the previous systems discussed the transition metal only structure (*i.e.* $Ni_2B_2O_5$) has not previously been synthesised, however other Ni borates are known, and they behave in a similar manner to Mn and Co borates. The $x = 1$ structure was chosen as it demonstrated the best electrochemical properties in the Mn system.

Initial synthesis attempts formed a mixture of the desired product and Ni_2AlBO_5, an impurity formed by reaction with the alumina crucible. Subsequently a sacrificial layer of starting material was used to line the crucible before a pellet of reactants was placed on top. This improved the purity significantly however small amounts of Ni_2AlBO_5 remained, even after sanding the surface (the impurity is green, main product yellow).

Rietveld refinement using the PXRD data shows that the main phase crystallises in the familiar triclinic structure with 1.9% of the impurity present by weight, Figure 5-8. The modelled peak shape does not fit the data well, even with a large asymmetry parameter, and suggests a slight distortion from the triclinic model. This is similar to that seen in the $(Mg,Ni)_3(BO_3)_2$ orthoborate system where distortion was caused by hydration of the compound, Chapter 3. As the peak

shape is not well modelled, the occupancies of the metal ions are constrained to 1:1 so the exact composition cannot be extracted. A summary of the structural parameters and comparison to $Mg_2B_2O_5$ is given in Table 5-2. The $MgNiB_2O_5$ unit cell and M site average bond lengths are reduced compared to $Mg_2B_2O_5$, this is in contrast to the Co and Mn systems where introduction of the transition metal expands the cell. This is due to the smaller radius of the Ni^{2+} ion, 6.9 pm compared to Mg^{2+}, 7.2 pm. The difference in radii also leads to partial cation ordering, with Ni displaying a clear preference to occupy M2, the smaller octahedral site. This is the site thought to form a percolating cation network so the reduced Mg occupancy may hinder ion diffusion.

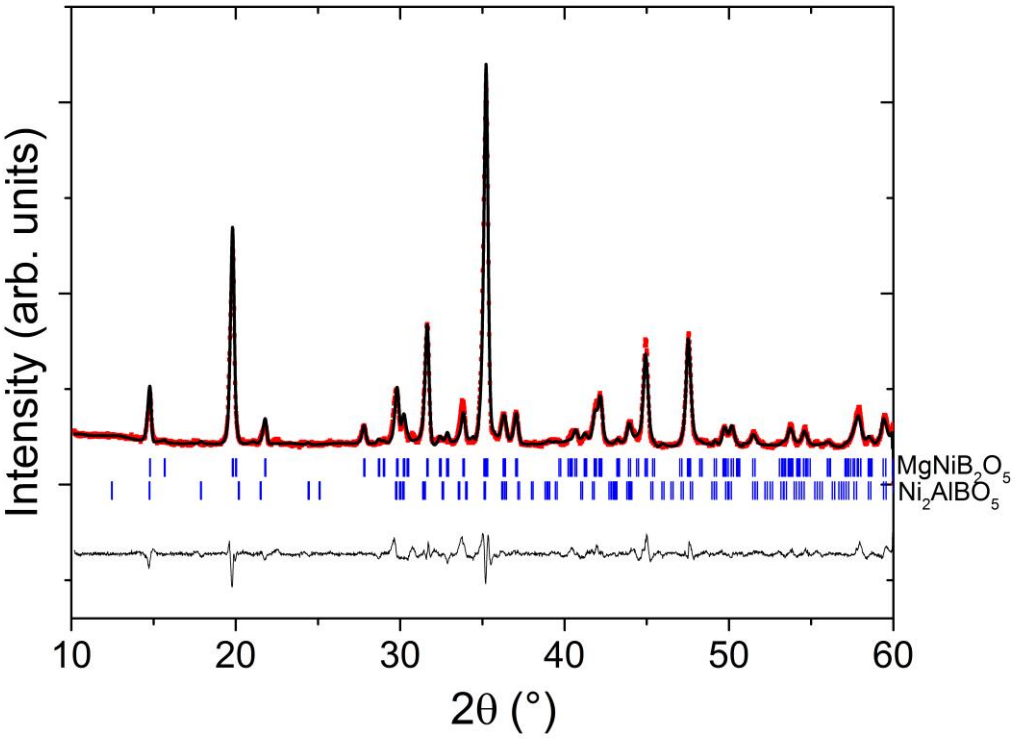

Figure 5-8. PXRD data of $MgNiB_2O_5$ – red dots. Rietveld refinement – black line. Allowed Bragg reflections for the main phase and impurity – blue tick marks. Difference pattern – grey line.

Table 5-2. Summary of refined crystal structure parameters determined from PXRD at room temperature for $MgNiB_2O_5$.

$\mathbf{Mg_xNi_{2-x}B_2O_5}$	$x = 1$	$x = 2$[158,177]
Space group	$P\bar{1}$	$P\bar{1}$
χ^2	8.41	
R_{wp}	5.47	
Vol ($Å^3$)	170.63(4)	171.48/171.33
M1 occ (Ni/Mg)	0.38/0.62(5)	0/1
M2 occ (Ni/Mg)	0.62/0.38(5)	0/1
Average M1-O (Å)	2.1098(8)	2.1292(15)
Average M2-O (Å)	2.0931(8)	2.0946(15)

5.3.2.2 $MgNiB_2O_5$ electrochemistry

The theoretical capacity for full Mg removal from $MgNi^{2+}B_2O_5$ to form $Ni^{4+}B_2O_5$ is 290.3 mAh g^{-1}. Subsequent insertion of 2 Li^+ ions to form $Li_2Ni^{2+}B_2O_5$ would yield 334.3 mAh g^{-1}. Mg removal from the structure by cycling vs. Li at a rate of C/25 achieved a capacity of just 10.6 mAh g^{-1}, or 0.07 Mg^{2+} ions, Figure 5-9. Although the capacity is significantly smaller than in previous systems, here there is a clear, high voltage plateau, which is preferable to the more sloping profile observed in $MgMnB_2O_5$. The Mg extraction occurs at between 4.0 V and 4.3V with a peak in the dQ/dV at 4.15 V, Figure 5-10.

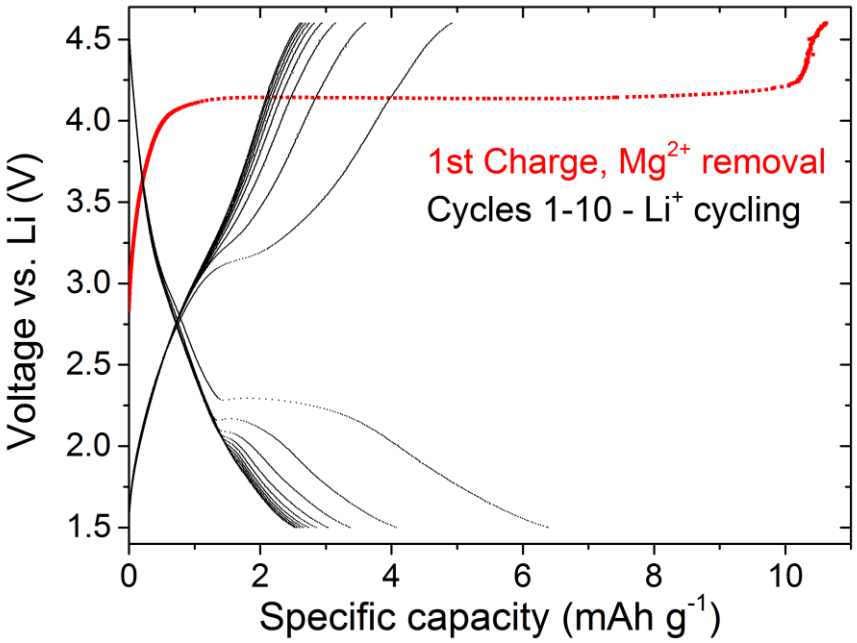

Figure 5-9. Cycling behaviour of $MgNiB_2O_5$ at C/25. 1st charge involving Mg removal – red curve. Subsequent cycling vs. Li – black curve.

The Li insertion capacity achieved on discharge is also limited (6.4 mAh g^{-1}, 0.04 Li^+), however, a clear plateau develops at 2.3 V again in contrast to the subtle changes in slope observed in the Mn system. Incomplete removal of Li on 2nd charge occurs with a feature at 3.1 V. The amount of Li removed matches that inserted over the discharge plateau at 2.3 V, suggesting Li inserted during this process is reversible, while that at lower potentials is irreversible up to 4.6 V. The d*Q*/d*V* plots show 1 clear process on charge and discharge associated with the $Ni^{2+/3+}$ redox couple and removal of Mg from just one of the *M* sites. Figure 5-11 shows that on Li removal 2nd charge) a second, higher voltage process may be starting ~4.5 V, which could be associated with the $Ni^{3+/4+}$ redox couple.

The presence of electrochemical plateaus suggests that both Mg and Li are mobile in the structure, but the low capacity and high polarisation indicate that diffusion is severely limited. This is exemplified by the large polarisation between Li insertion and removal (0.99 V, Figure 5-11) and the fact that polarisation increases in subsequent cycles.

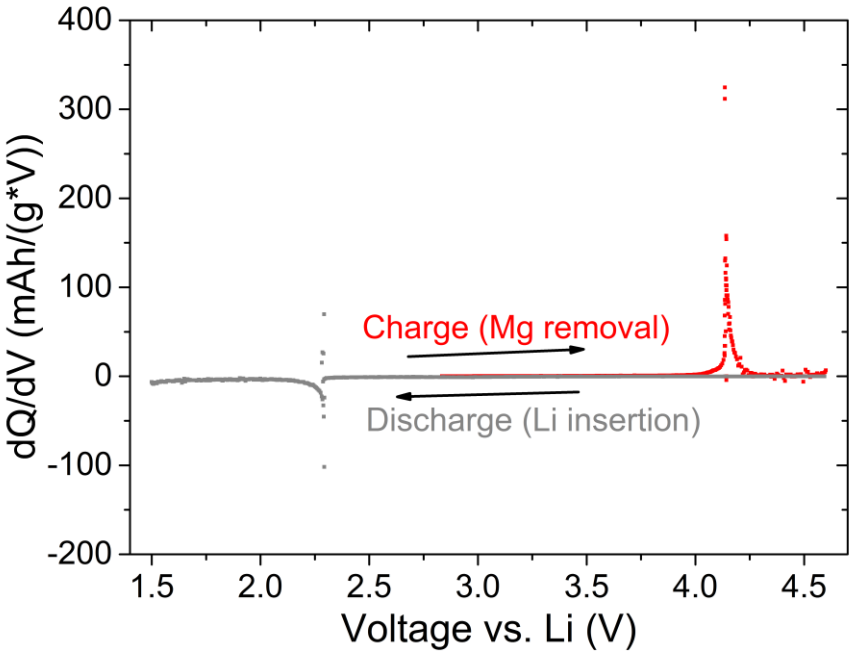

Figure 5-10. d*Q*/d*V* plot for 1st charge and discharge of $MgNiB_2O_5$ vs. Li at a rate of C/25

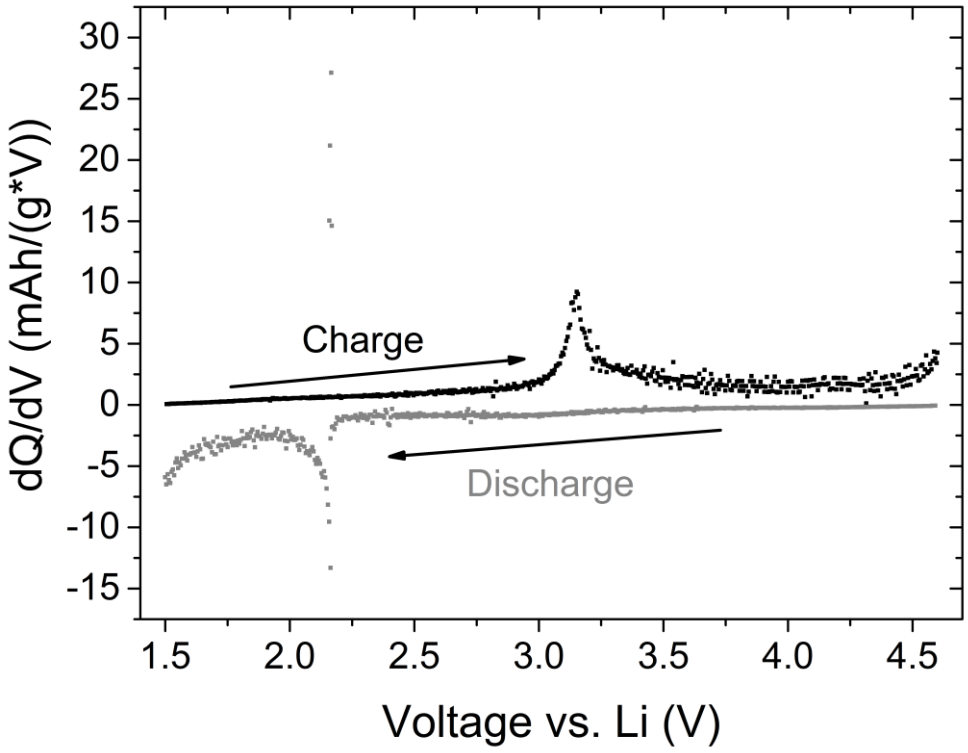

Figure 5-11. d*Q*/d*V* plot for 2nd charge and discharge of $MgNiB_2O_5$ vs. Li at a rate of C/25.

Cells were cycled at 55 °C with the aim of improving the cation diffusion kinetics and therefore the reversible capacity. Figure 5-12 compares the 1st charge (Mg removal) and 1st discharge (Li insertion) for cells cycled at 21 °C and 55 °C. The high temperature cell has a 2.8 times greater Mg removal capacity (29.2 mAh g^{-1}) and two plateaus are observed. The first plateau between 3.3 V and 3.5 V accounts for the majority of the capacity achieved and is thought to be the same process leading to the 4.15 V plateau at 21 °C. The presence of a second plateau, not observed in the low temperature cell, indicates that further Mg removal is possible, but is currently limited by poor ionic or electronic conductivity. Li insertion also occurs with reduced overpotential (~0.1 V), however the difference is less pronounced than on Mg removal (~0.8 V). On first discharge a Li insertion capacity of 13 mAh g^{-1} is achieved. As with the low temperature cell, the capacity achieved on 2nd charge (Li removal) matches that inserted during the ~2.3 V plateau, with the lower voltage process being irreversible up to 4.6 V. The start of a higher voltage process ~4.5 V is also more apparent in the high temperature cell. In contrast to previous systems, discharge to 1 V achieved no appreciable increase in capacity or evidence of a conversion reaction.

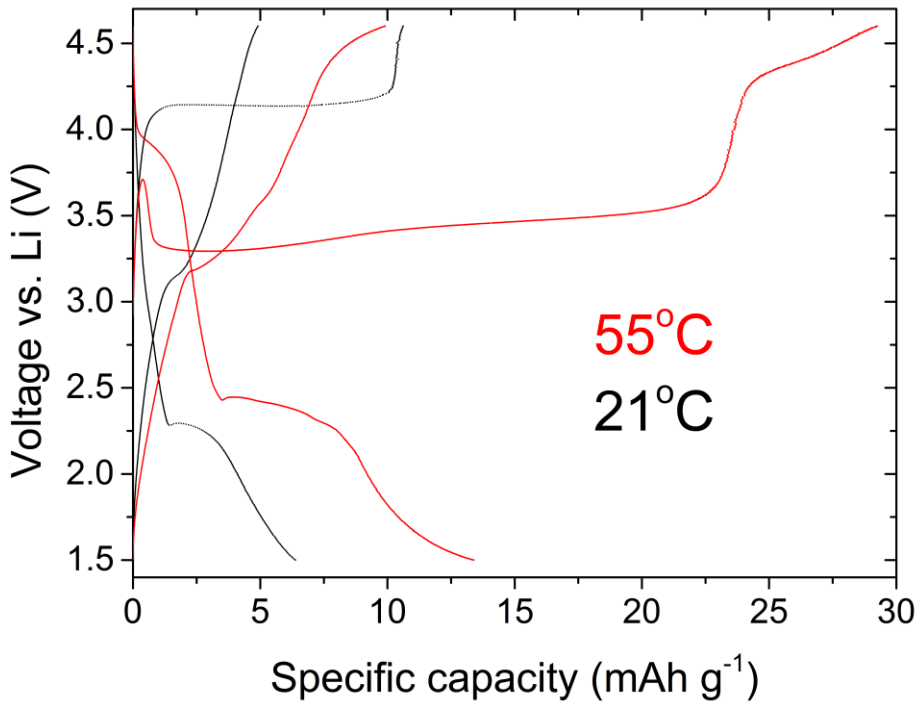

Figure 5-12. 1st and 2nd charge and 1st discharge of $MgNiB_2O_5$ at 21 °C (black curve) and 55 °C (red curve) vs. Li at a rate of C/25.

5.3.2.3 Conclusions

$MgNiB_2O_5$ was synthesised and PXRD analysis showed that it crystallises in the same triclinic structure as previous examples. The Ni^{2+} cation radius is smaller than Mg^{2+}, leading to preferential occupation with Ni displaying a preference for the smaller *M*2 site, the opposite to that observed for the larger Mn ion. Full refinement of the PXRD data was hindered by distortions in the unit cell which could not be properly modelled, and are likely due to hydration of the material, as seen in $Mg_xNi_{3-x}(BO_3)_2$.

On first charge in a Li-ion cell a plateau corresponding to Mg removal is observed at 4.15 V, though just 10.6 mAh g^{-1} capacity is achieved (0.07 Mg^{2+}, 7% of theoretical). The plateau does not contain any other features, unlike in Mn and Co systems, suggesting Mg is only being removed from one site. A plateau at 2.6 V occurs on discharge where a Li insertion capacity of 6.4 mAh g^{-1} is observed. Increasing the cycling temperature to 55 °C improves the capacity achieved on both Mg removal (29.3 mAh g^{-1}, 0.1 Mg^{2+}) and Li insertion (13 mAh g^{-1}, 0.08 Li^+). The charging voltage is reduced to 3.3 V and a second electrochemical process appears to start at ~4.5 V. In both the room temperature and high temperature data, Li insertion is not fully reversible, with only the capacity achieved during the 2.6 V discharge process appearing to be reversible.

5.3.3 $Mg_xFe_{2-x}B_2O_5$

5.3.3.1 Structure

Both $Mg_{2/3}Fe_{4/3}B_2O_5$ and $MgFeB_2O_5$ were synthesised in the triclinic crystal structure, with $Mg_{2/3}Fe_{4/3}B_2O_5$ being a phase pure sample while $MgFeB_2O_5$ contains ~15% (Mg,Fe)OBO_3, a mixed $M^{2+/3+}$ compound, Figure 5-13. The impurity was present in all stages of synthesis for both the standard method (under flowing gas) and in evacuated quartz tubes suggesting Fe oxidation occurs very early on in the reaction mechanisms whether using iron oxalate or iron oxide starting materials.

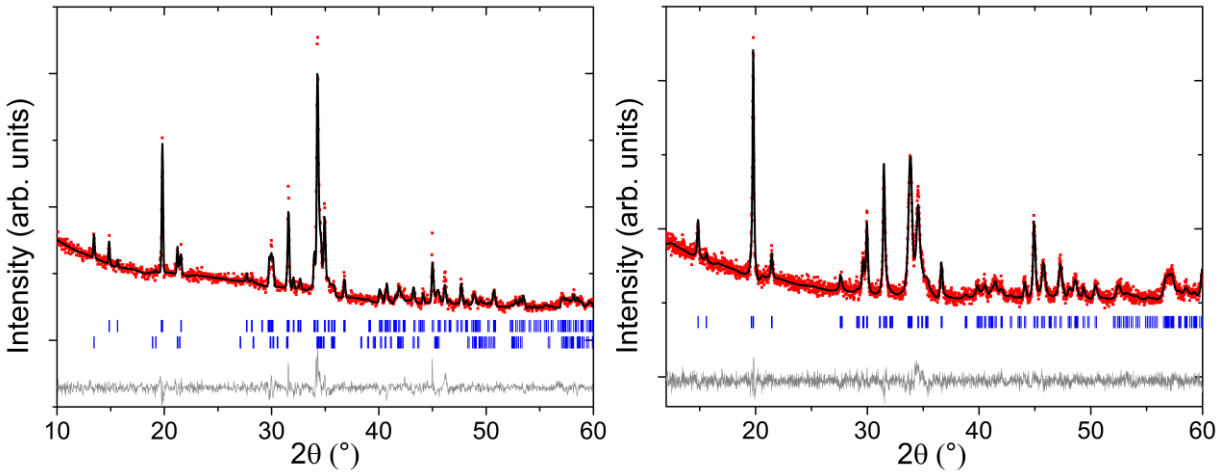

Figure 5-13. PXRD data of $MgFeB_2O_5$ (left) and $Mg_{2/3}Fe_{4/3}B_2O_5$ (right) – red dots. Rietveld refinement – black line. Allowed Bragg reflections for the main phase (upper tick marks) and $MgFeBO_4$ impurity (lower tick marks) – blue tick marks. Difference pattern – grey line.

Refinement of the *M*1 and *M*2 occupancies for $Mg_{2/3}Fe_{4/3}B_2O_5$ showed little deviation from complete disorder, consistent with previous results.[98] Refinement of occupancies for $MgFeB_2O_5$ was not possible due to overlap of the main phase and impurity peaks. The change in volume across the series is consistent with an increase in cation size, Figure 5-14.

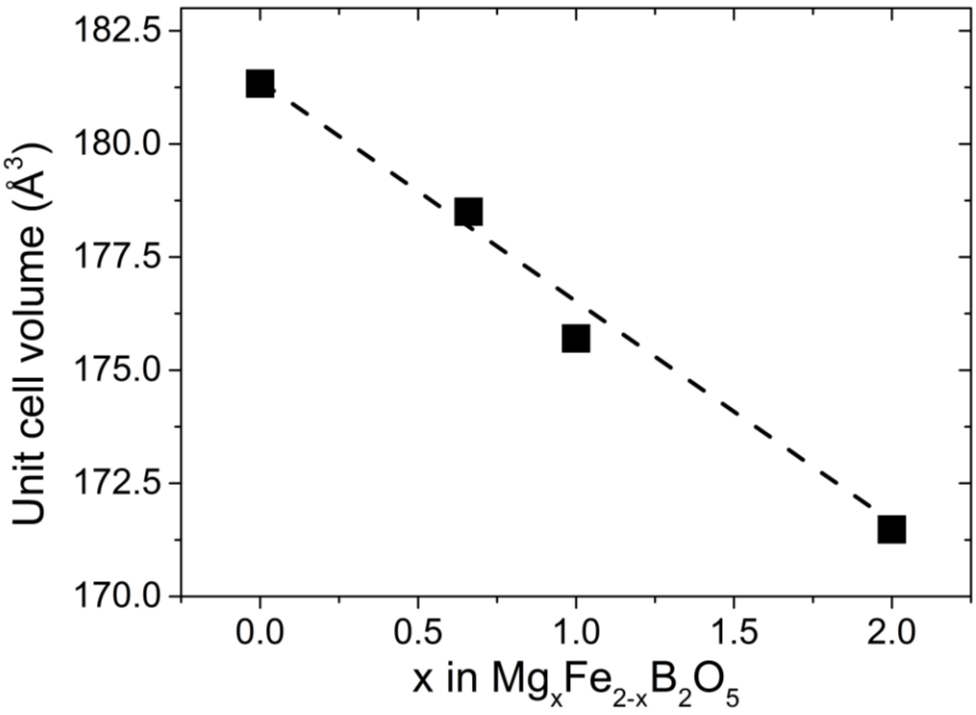

Figure 5-14. Unit cell volume change with varying *x* in $Mg_xFe_{2-x}B_2O_5$.

5.3.3.2 $Mg_{2/3}Fe_{4/3}B_2O_5$ electrochemistry and ex-situ characterisation

Full removal of the Mg to form $Fe_{4/3}B_2O_5$ would involve oxidation of Fe^{2+} to Fe^{3+} with a capacity of 180.3 mAh g^{-1}. This stoichiometry may be preferable to the higher Mg content materials, as oxidation to Fe^{4+}, which in most materials leads to a voltage exceeding current electrolyte stability windows, is not required for full Mg removal to occur. Reduction back to the Fe^{2+} to form $Li_{4/3}Fe_{4/3}B_2O_5$ would yield a capacity of 201.3 mAh g^{-1}.

The first charge of cycling vs. a Li anode at C/25 involves removal of Mg from the structure and a capacity of 134.0 mAh g^{-1}, or 0.5 Mg was achieved which is 76% of the theoretical capacity and significantly greater than that achieved in the Mn or Co analogues (17.6 and 20.0 mAh g^{-1} respectively), Figure 5-15. The oxidation of the structure occurs over two plateaus with onset voltages of 3.7 V and 4.0 V vs. Li, attributed to Mg removal from the two *M* sites. There is a raised voltage section between the two plateaus (which is reproducible) that could be due to an activation barrier, however this usually results in a bump rather than a flat region. Therefore, the change in voltage may be due to a structural rearrangement occurring as Mg is removed from the cell, such as migration of the Fe ions. Discharge to 1.5 V sees the insertion of 0.22 Li^+ ions into the structure, with a capacity of 32.6 mAh g^{-1}. This is clearly far less than the capacity achieved on charge and supports the idea that a structural change occurs on Mg removal, resulting in a less active phase. The 2nd charge capacity is greater than 1st discharge (43.4 mAh g^{-1}) and is therefore likely a combination of removing the inserted Li and residual Mg. Two distinct features are still observed, however they are less defined than on 1st charge. Subsequent cycling sees further reduction of capacity to a minimum of 24.4 mAh g^{-1} on discharge and continued smoothing of the charge curve. On continued cycling a gradual increase in capacity is observed, similar to that seen in the Mn system, however the change in capacity is less dramatic here. After 100 cycles the capacity settles to a reversible 39.4 mAh g^{-1} (0.26 Li) with a slight excess on charge, Figure 5-16. A plateau between ~3.4 and 3.0 V on discharge accounts for ~50% of the capacity, with the rest achieved during a sloping region down to ~1.6 V where a plateau begins to develop before hitting the 1.5 V limit.

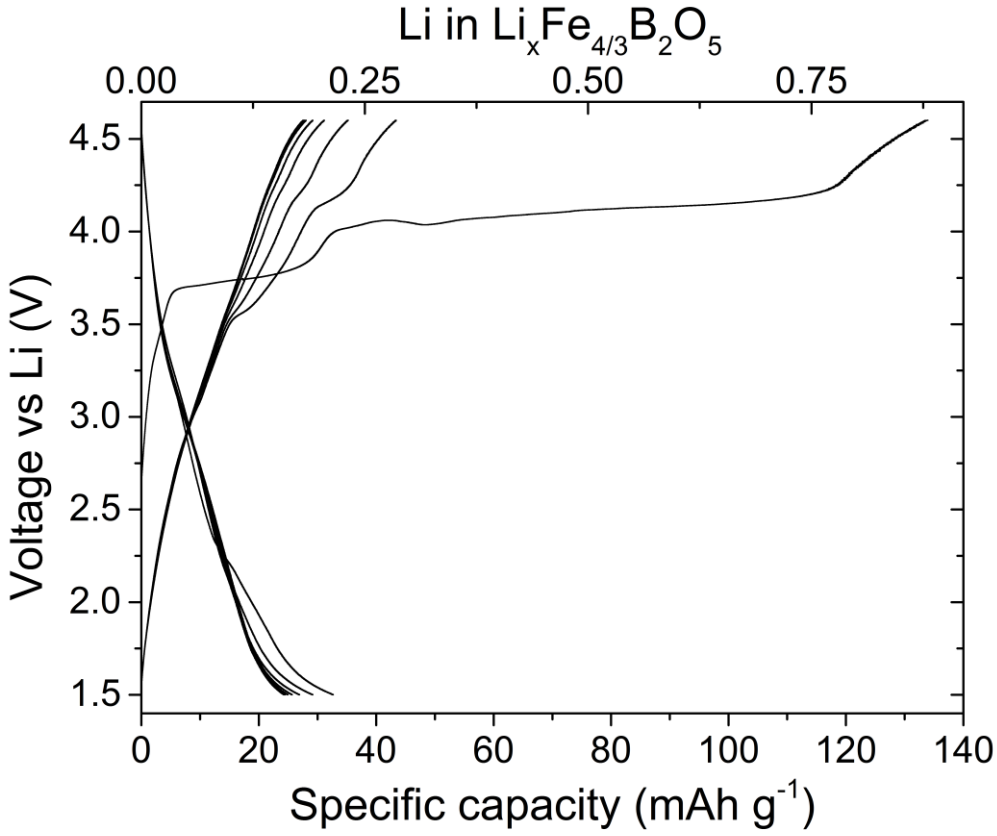

Figure 5-15. Cycling behaviour for the 1st 10 cycles of $Mg_{2/3}Fe_{4/3}B_2O_5$ in a Li-ion cell at a rate of C/25. The 1st charge (Mg removal) reaches 134 mAh g^{-1}, 75% of theoretical capacity.

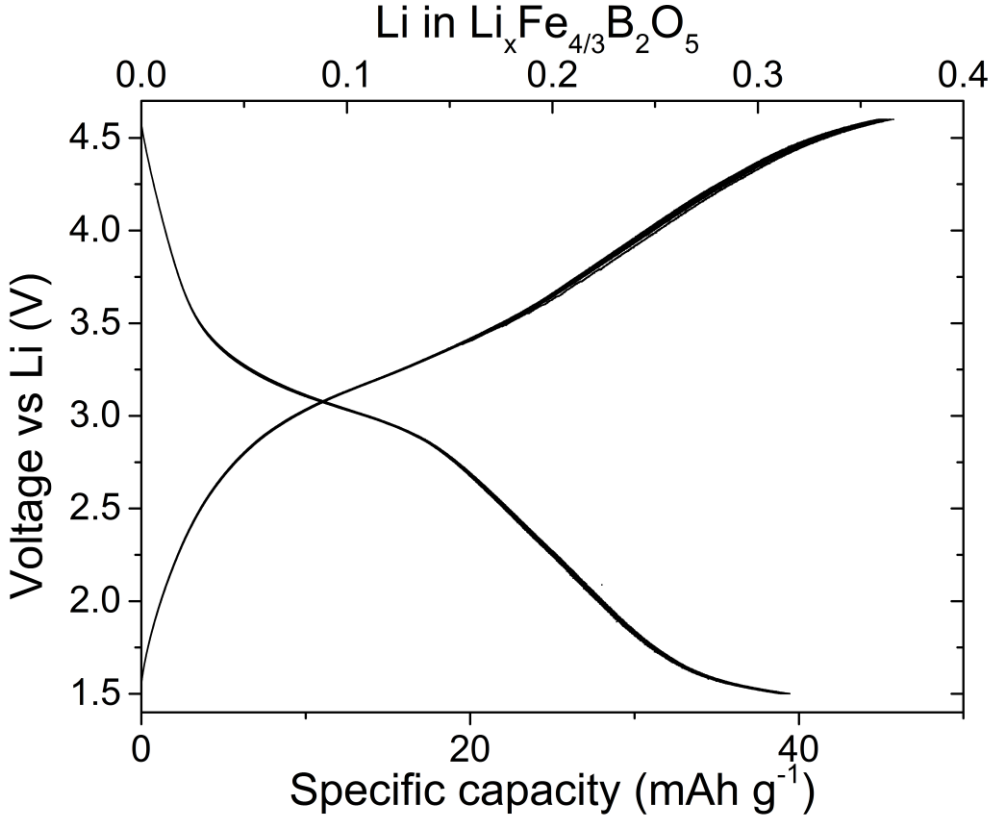

Figure 5-16. Cycling behaviour of $Mg_{2/3}Fe_{4/3}B_2O_5$ after 100 cycles at a rate of C/25.

Increasing the cycling temperature to 55 °C causes charge capacities to increase to over theoretical capacity, suggesting side reactions or material degradation is occurring, Figure 5-17. These extended charge processes are followed by discharge capacities of ~70 mAh g^{-1} (0.46 Li^+ ions), greater than those achieved at room temperature, indicating that at least some of the charge capacity is due to Mg removal and that increasing the temperature improves the diffusion kinetics of Li insertion into the material. As cycle number increases, the charge capacity decreases while discharge capacity increases until they converge to give a fully reversible reaction with capacity of 204.4 mAh g^{-1} after 16 cycles. This is full theoretical capacity for cycling between $Li_{4/3}Fe^{2+}_{4/3}B_2O_5$ and $Fe^{3+}_{4/3}B_2O_5$.

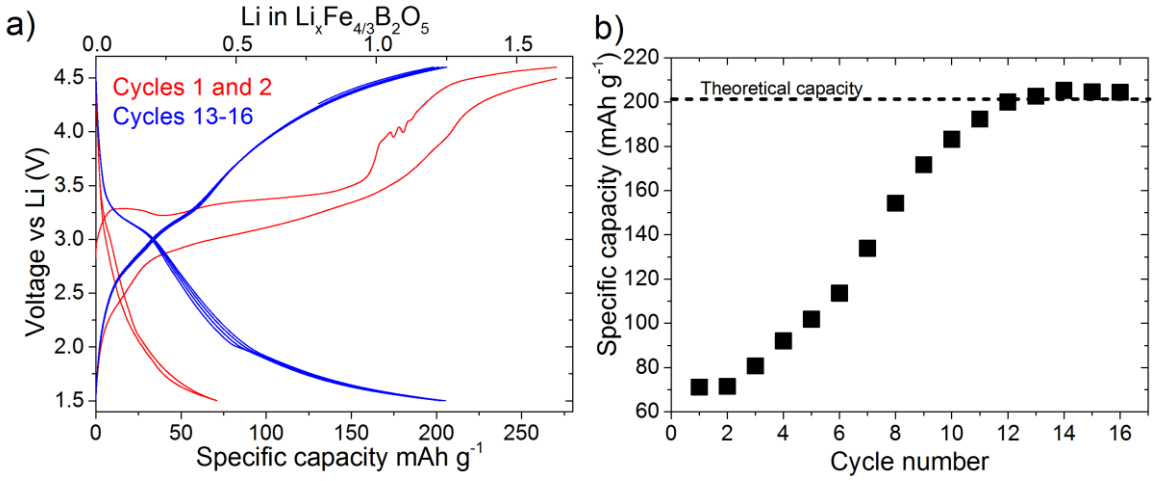

Figure 5-17. a) Cycling of $Mg_{2/3}Fe_{4/3}B_2O_5$ at 55 °C. Initial cycles (red) show large variations in charge and discharge capacity. Cycles 3-10 (black) show a gradual increase in discharge capacity and decrease in charge capacity. Cycles 16-20 (blue) show fully reversible insertion of 1.33 Li which is full theoretical capacity. b) Achieved capacity vs cycle number for the high temperature cycling. The dotted line indicates the theoretical capacity.

Extending the voltage window down to 1V sees this feature extend into a very high capacity region, and indeed a further plateau is observed, starting ~1.25 V, Figure 5-18. On 1st discharge after Mg removal (124.7 mAh g^{-1}), 3.4 Li (525.6 mAh g^{-1}) are inserted per unit cell, far exceeding the theoretical capacity. To compensate for insertion of 3.4 Li^+ a reduction of Fe to well below 2+ is required. It seems likely that a combination of Li insertion into the framework, followed by a conversion reaction to form an Fe^0 compound is occurring, however further analysis of the products is required to confirm this hypothesis. Unlike the other materials studied, this large capacity is completely reversible.

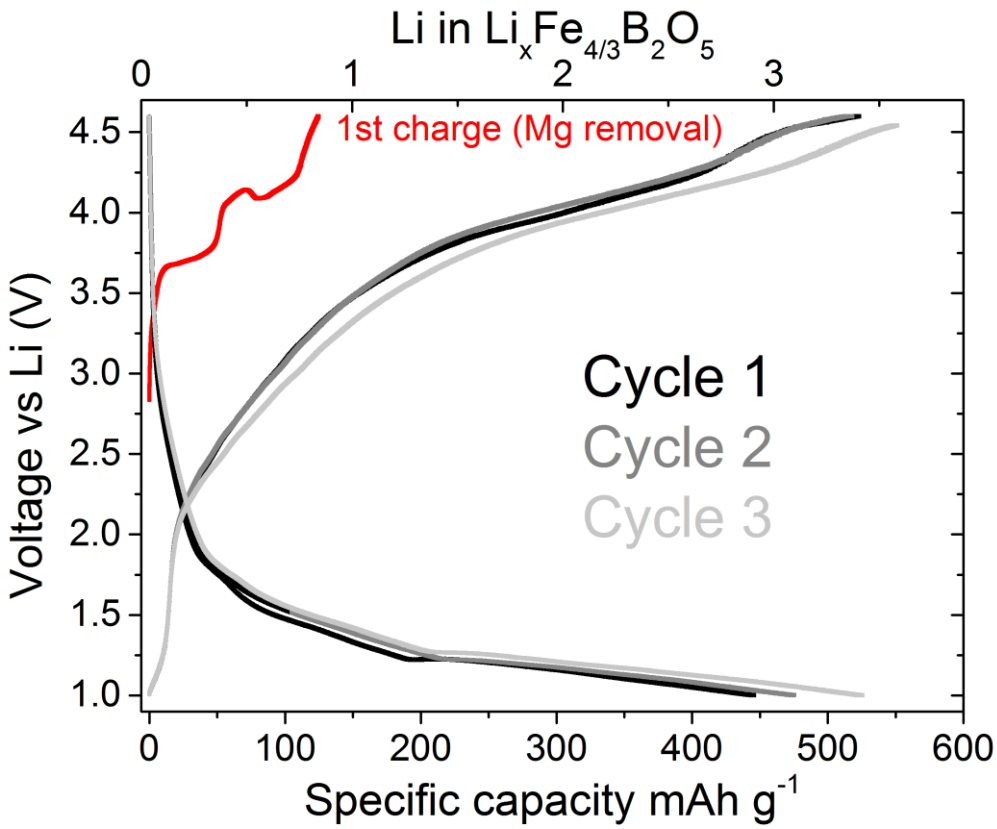

Figure 5-18. Cycling of $Mg_{2/3}Fe_{4/3}B_2O_5$ with an extended voltage range showing large capacities indicative of a conversion reaction.

5.3.3.2.1 Ex-situ diffraction

After charging and discharging between 4.6 V and 1.5 V for 16 cycles, the pyroborate structure is retained, Figure 5-19. The comparison to the ball milled but uncycled cathode material shows no significant broadening, though the intensity is reduced due to the low quantity of material available for the ex-situ sample. The large and broad background peak in the ex-situ pattern is due to the capillary used to keep the sample in inert conditions.

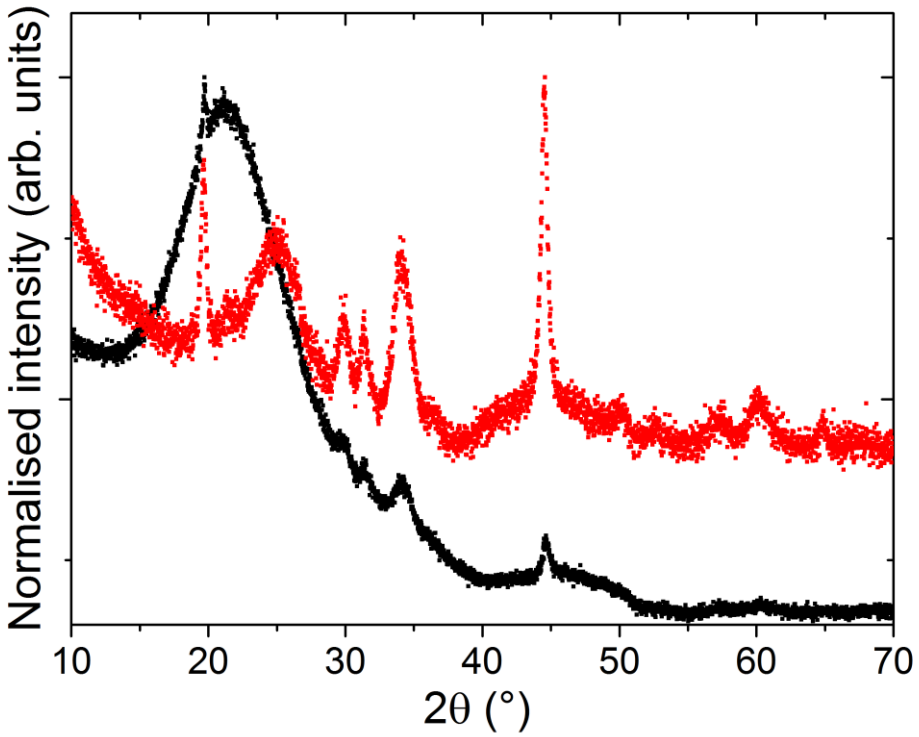

Figure 5-19. Comparison of PXRD collected for ex-situ cycled $Mg_{2/3}Fe_{4/3}B_2O_5$ (black dots) and the uncycled cathode (red dots).

5.3.3.3 $MgFeB_2O_5$

Removal of Mg from the structure to form $Fe^{4+}B_2O_5$ gives a theoretical capacity of 294.9 mAh g^{-1}, however the 3+/4+ couple often occurs at a voltage above the oxidation stability of standard electrolytes, therefore oxidation may be limited to 2+/3+ forming $Mg_{0.5}Fe^{3+}B_2O_5$ and limiting the capacity to 147.4 mAh g^{-1}. Li insertion to form $Li_2FeB_2O_5$ (i.e. insertion into the fully oxidised material) would give a capacity of 340.4 mAh g^{-1}, while insertion of 1 Li into $Mg_{0.5}Fe^{3+}B_2O_5$ to form $LiMg_{0.5}Fe^{3+}B_2O_5$ yields a capacity of 158.0 mAh g^{-1}.

The specific capacities achieved during electrochemical cycling are based on the mass of active material, which due to containing a large fraction of impurity, is not an entirely accurate measure of amounts of ions (de)intercalated. Accounting for the percentage of impurity is unreliable due to the overlap of peaks in the PXRD causing significant errors in the weight % fraction calculation.

On first charge (Mg removal) just 0.07 Mg^{2+} (10 mAh g^{-1}) are removed from the structure, and on subsequent discharge negligible amounts of Li were inserted (<5 mAh g^{-1}). The GITT for 1st charge, Figure 5-20 shows overpotentials in excess of 0.7 V at the beginning of the process, increasing to ~1.7 V as the electrochemical reaction progresses. The overpotential on discharge

is smaller, but still large enough to hinder electrochemical activity, and as little Mg is removed there are few vacancies for Li to occupy. During the relaxation stages, the system reaches an equilibrium voltage of ~2.1 V on charge, with a more sloping feature on discharge, similar to the plateau seen on charge and the sloping profile of discharge in $Mg_{2/3}Fe_{4/3}B_2O_5$.

The lack of electrochemical activity may be due to the presence of oxidised impurity (Fe^{3+}) which was shown to severely hinder the electrochemistry of $LiFeBO_3$.[46] When $LiFeBO_3$ material was synthesised and handled to ensure no Fe^{3+} impurity, capacities improved dramatically. Therefore, improved synthesis of $MgFeB_2O_5$ may also yield improved results.

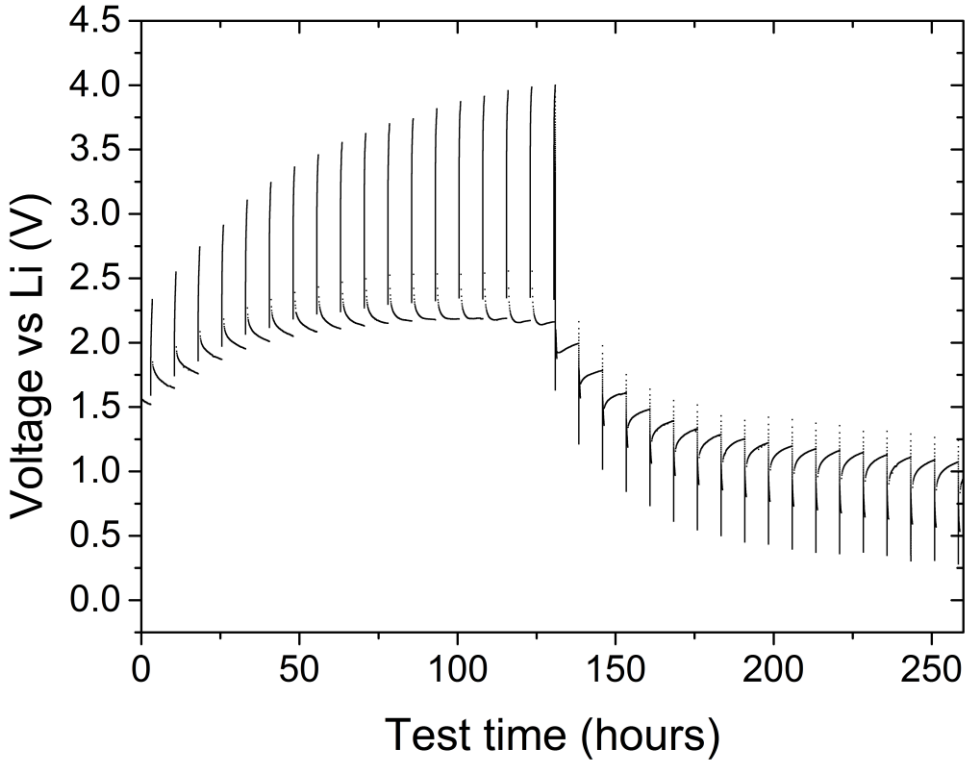

Figure 5-20. GITT on 1st charge and discharge of $MgFeB_2O_5$. A very large overpotential limits the achievable capacity.

5.3.3.4 Conclusions

Synthesis of $Mg_xFe_{2-x}B_2O_5$ proved more challenging than the other systems, with stabilisation of Fe^{2+} being the main issue (reaction conditions were either too reducing or too oxidising). Only the x = 2/3 material was synthesised as a pure phase, which again crystallises in the $P\bar{1}$ space group. The x = 1 material was found to contain an oxidised borate impurity which accounts for ~15% of the material by mass.

Cycling of the impure $MgFeB_2O_5$ gave very low capacities, 10 mAh g^{-1} on Mg removal and <5 mAh g^{-1} on Li insertion due to large overpotentials. The presence of an Fe^{3+} impurity was shown to render $LiFeBO_3$ electrochemically inactive and a similar mechanism could be occurring here. Improved synthesis and cathode formation may improve the electrochemical performance.

The first charge of x = 2/3 at a rate of C/25 yields a Mg removal capacity of 134.0 mAh g^{-1}, or 0.5 Mg, ~76% of theoretical capacity. This is significantly higher than that observed in the Mn or Co systems for x = 2/3 which may be due to the lower voltage offered by $Fe^{2+/3+}$. The reaction proceeds over two voltage plateaus at 3.7 V and 4.0 V vs. Li, attributed to Mg removal from the two distinct *M* sites. On discharge, Li insertion capacities of 32.6 mAh g^{-1} occurs, which increases to 39.4 mAh g^{-1} (0.26 Li^+, ~19.6% of theoretical) as cycle number increases. For the first few cycles charge capacities are greater than discharge suggesting continued Mg removal along with the inserted Li on charge. ~50% of the discharge capacity is achieved between 3.2 and 3.0 V. Ex-situ PXRD shows retention of the pyroborate structure after cycling.

Cycling at 55 °C leads to large charge capacities with variable voltage profiles, suggesting a combination of side reactions along with Mg removal. Initial Li insertion capacities are increased to ~70 mAh g^{-1} (34.5% of theoretical capacity). With continued high temperature cycling the capacity stabilises to 204.4 mAh g^{-1}, which is 100% of the theoretical capacity for cycling between $Li_{4/3}Fe^{2+}_{4/3}B_2O_5$ and $Fe^{3+}_{4/3}B_2O_5$.

As with previous systems, discharge to below 1.5 V leads to insertion of increased amounts of Li, requiring further reduction of Fe to compensate, with 3.4 Li (525.6 mAh g^{-1}) inserted on 1st discharge. The reaction is fully reversible, in contrast to the other transition metal systems. This is likely a conversion reaction however ex-situ PXRD shows no new phases present, so further investigation is required for confirmation.

5.4 Summary of Pyroborates in Li-ion cells

The use of polyanion structures where Li can replace labile Mg, without disrupting crystal structure, opens up a new avenue for novel Li-ion cathode materials with high energy densities. Facile Mg removal in $Mg_xM_{2-x}B_2O_5$ (*M* = Mn, Co, Fe or Ni) means that these materials may also be of interest for Mg-ion battery systems.

The Mn systems have been shown to have high capacities at moderate rates, especially the $x = 1$ compound where full theoretical capacities are achieved (>300 mAh g^{-1}). The assertion that Mg is removed from the structure and Li inserted was corroborated by ex-situ diffraction, ^{7}Li NMR and SQUID magnetometry.

In $Mg_{2/3}Co_{4/3}B_2O_5$ low capacities were achieved at room temperature, but by increasing the cycling temperature to 55 °C full and reversible theoretical capacity was achieved. The need for increased temperatures indicates that ion mobility is kinetically hindered compared to the Mn based materials, so cathode optimisation could improve the room temperature cycling and reduce the overpotential. A high capacity but low efficiency conversion reaction is evident at low voltages.

$MgNiB_2O_5$ displays high voltage deintercalation of Mg and Li from the structure, but again with limited capacity at room temperature. The voltage profile suggests ion diffusion from just one of the *M* sites, in contrast to the other systems. The Li inserted at low voltages appears to be irreversible up to 4.6 V, again differing from the other systems. At 55 °C the capacity is increased, overpotential reduced and a second, higher voltage process appears to be starting at ~4.5 V.

In $Mg_{2/3}Fe_{4/3}B_2O_5$ 75% of the Mg can be removed from the structure at room temperature, while Li insertion capacities are significantly lower for the first few cycles, but gradually increase with increasing cycle number. At 55 °C this gradual increase in capacity leads to full theoretical capacity being achieved after 16 cycles. The improved performance of the Fe system over Co and Ni is attributed to the lower redox potential of the $Fe^{2+/3+}$ couple. As with the Mn based system full capacity can be achieved, however here the ideal stoichiometry, $MgFeB_2O_5$, displays little reversible capacity, perhaps due to the presence of Fe^{3+} impurity rendering the surface inactive.

This study shows the pyroborates are a promising family of materials for high capacity, high rate, Li-ion cathodes. The replacement of 2 Li^+ for each Mg^{2+} removed in the Mn, Co and Fe systems and the lightweight borate framework leads to significantly higher gravimetric

capacities than those observed for the pyrophospate polyanions. Further improvements could be made by understanding the origin of the capacity increases over 1000 cycles of the $MgMnB_2O_5$ material, by forming mixed transition metal phases to tune the voltage and capacity, as has been successfully demonstrated in Li*M*BO_3,[48] or by improving the ionic and/or electronic conductivity via optimised composite and film construction.

Chapter 6. $Mg_xMn_{2-x}B_2O_5$ as a Mg-ion cathode

6.1 Introduction

The results shown in previous chapters have demonstrated that Mg^{2+} can be removed from both pyroborate and orthoborate structures, while retaining the basic framework of the material. The mobility of the Mg-ion means these structures may be of use in Mg-ion batteries, where Mg^{2+} is the working ion instead of Li^+. The main benefit of using Mg^{2+} is that its divalency causes two electrons to be forced through the circuit for each ion transferred, compared to one for Li, therefore increasing the energy density of a cell significantly. Although Li-ion research has progressed significantly since the 1980's, leading to an in-depth understanding of Li intercalation chemistry, Mg-ion battery research is still in its infancy, with sporadic improvements in understanding and performance over the last 20 years. Some of the major discoveries include showing reversible Mg intercalation into the Chevrel phase,[69] reversible intercalation into higher voltage V_2O_5 and $MgMSiO_4$ (M = Fe, Mn),[78,97,199] and the discovery of non-Grignard based electrolytes with higher voltage windows.[200] A more detailed description of potential benefits of Mg-ion batteries and the background literature is given in Chapter 1.

Although improvements in Mg-ion electrochemistry have been made, many challenges remain. A major issue is the reactivity of electrolytes with various cell components, leading to passivation of the Mg metal anode, uncontrolled side reactions with current collectors, dissolution of the cathode or a combination of these effects. Previous studies demonstrated that stainless steel, used as current collectors in coin cells, is readily corroded by many Mg-ion electrolytes, further limiting their already narrow stability window.[201,202] Aluminium was proposed as a more stable alternative, therefore all coin cells discussed here use aluminium coated stainless steel coin cell components (Cambridge Energy Solutions).

The issues with the electrolyte renders testing of new cathodes problematic as reproducible electrochemistry is difficult to achieve. One of the main barriers to reliable testing of cathodes is having an electrolyte with a large enough stability window to allow charge at reasonable voltages, without significant breakdown. This breakdown can lead to passivation of the anode, rendering the cell electrochemically inactive, or give continuous capacity due to electrolyte break down at a voltage below the cathode reaction, meaning higher voltages cannot be reached. Any side reaction consumes the electrolyte and will eventually lead to failure of the cell. There is currently no standard cell set up for investigating cathode materials, therefore an evaluation

of electrolytes and cell configurations was required before full electrochemical tests could be run.

There were two main goals to this work: firstly, to produce a test system that can reliably reproduce previous experiments and allow for assessment of both electrolytes and cathode materials, then secondly, apply these methods to our materials.

To assess the electrolyte window and reversibility of Mg plating of various electrolytes a 3-electrode cell was devised. This could be set up to use: a Pt, Mg, or cathode material working electrode; Mg pseudo-reference electrode; and carbon, Pt or Mg counter electrode. Here we show the 3-electrode cell allows for the testing of electrolytes and cathodes, demonstrated by Mg stripping and plating from 3 established electrolytes (Grignard based, $Mg(ClO_4)_2$ and $Mg(TFSI)_2$), and reversible Mg^{2+} into the Chevrel phase. A new electrolyte ($Mg(PF_6)_2$ is also tested and shown to support reversible Mg deposition with a wide voltage window as well as reversible cycling of the Chevrel phase in a full Mg-ion coin cell.

$MgMnB_2O_5$ is the object of Mg-ion electrochemical testing in this study; chosen as it demonstrated full Mg removal and structural stability when cycled vs. a Li anode. In a Li-ion cell Mg removal occurs >4.0 V which equates to ~3.3 V vs. Mg^{2+}, which, combined with the high theoretical capacity (296.6 mAh g^{-1}) could lead to much greater energy densities than those achieved so far. The expected reaction voltage is approaching the upper limit of electrolyte stability therefore various electrolytes and cell configurations were used to assess the use of $MgMnB_2O_5$ as a Mg-ion cathode material.

Reversible Mg^{2+} cycling is demonstrated in $MgMnB_2O_5$, with capacities ~150 mAh g^{-1} (cycling of 0.5 Mg^{2+}) achieved in the $Mg(TFSI)_2$/ACN electrolyte. 3-electrode cycling voltammetry on the cathode material show reversible redox process ~3 V, which is around where intercalation would be expected given the results in a Li-ion cell in Chapter 4. Ex-situ PXRD shows a volume change on charge consistent with Mg^{2+} removal, while SQUID magnetometry and XANES were used to explore Mn oxidation state changes.

6.2 Methods

6.2.1 Electrode preparation

Before use the working, reference and counter electrodes were cleaned to ensure impurities did not affect the results. For Pt this involved submersion in nitric acid which was then washed off with ethanol followed by drying in a vacuum oven at 100 °C. The purity of the Pt was ensured electrochemically with the Pt wire submerged in the electrolyte to be studied, and held at a positive voltage, to oxidise any impurities off the surface, until the current had stabilised. Fresh electrolyte was then used for the test. Mg was cleaned by sanding with fine grit (P1200) silicon carbide sand paper or a razor blade.

6.2.2 Electrolyte synthesis

The Grignard based $Mg(AlCl_2EtBu)_2$ was produced as a 0.25 M solution of in dry THF which has been stored over activate molecular sieves by Evan Keyzer following the literature method.[113] The method involves combing stoichiometric amounts of $MgBu_2$ and $AlCl_2Et$ in hexane under an inert atmosphere. After continuous stirring for 48 hours the hexane is evaporated leaving a white precipitate, which is then dissolved in the dry THF.

$Mg(TFSI)_2$ (>99.5%, Solvionic) and $Mg(ClO_4)\cdot 6H_2O$ (99% Sigma) powders were dried at 130 °C under vacuum prior to dissolution in solvent to form the electrolyte. Anhydrous acetonitrile was purchased from Sigma and further purified by distillation over CaH_2. This step was necessary to remove electrochemically active impurities which were observed on cyclic voltammetry, Figure 6-1. The purified solvent does not display the peaks observed in the as-purchased solvent which are associated with stripping and plating of impurities, however a capacitive response to the voltage sweep is still observed.

To synthesise the Chevrel phase, Mo_6S_8, stoichiometric amounts of MoS_2, Cu, and Mo powders were combined, ground and formed into a pellet. The pellet was placed in a graphite crucible and heated to 1100 °C under flowing 5% H_2 in Argon. The resultant $Cu_xMo_3S_4$ with 2 wt% Mo impurity was then stirred in a 6M HCl solution for 24 hours. This removes the Cu from the structure to form copper chloride (indicated by green colouration of the solution) and dissolves the Mo. The new pure product was washed with deionised water and successful synthesis was confirmed by PXRD.

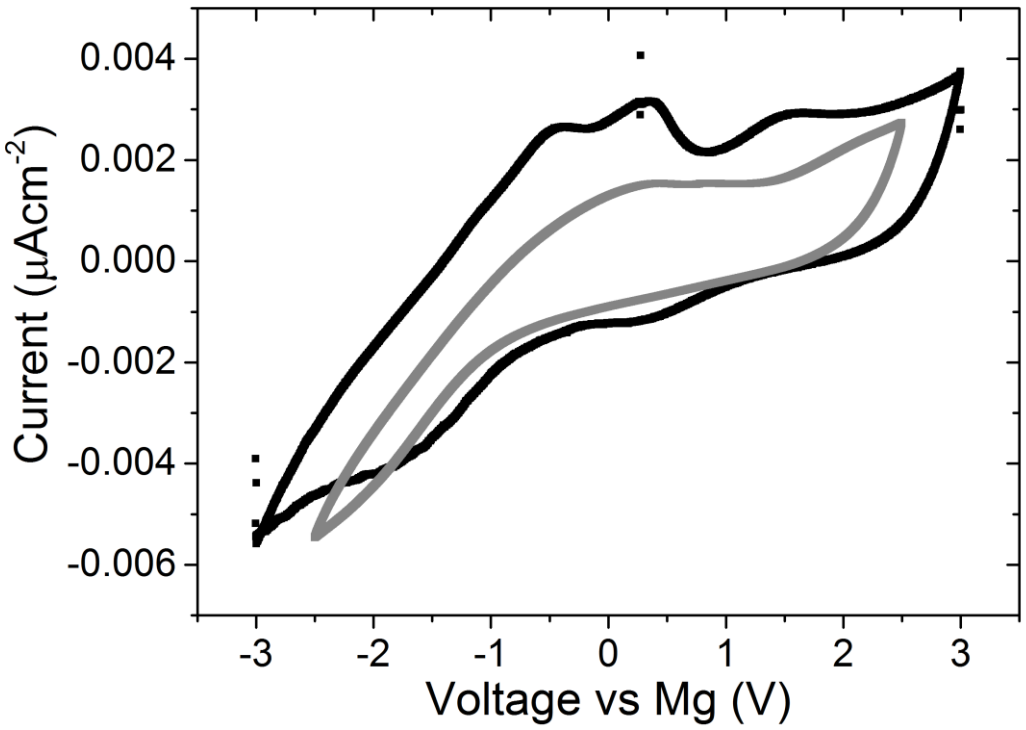

Figure 6-1. Comparison of cyclic voltammetry on a Pt working electrode on as purchased (black line) and purified and dried acetonitrile (grey line).

6.2.3 3-electrode cell

To avoid detrimental reactions between the cell components (notably the stainless steel current collectors) and the electrolyte previous experiments elsewhere have been conducted in 2 or 3 electrode flooded cells.[78,80,94,115] These are typically glass vials with Mg, Ag or Pt wire electrodes submerged in electrolyte. To replicate these studies and to assess our own electrolytes and cathodes a 3-electrode cell was devised based on a Metrohm electrolyte measuring vessel, Figure 6-2. Here the glass bowl has a small (1.5 cm) flat bottom section that can be used for experiments with small volumes of electrolyte, and septum caps can be inserted into the holes in the lid allowing insertion of the electrodes while maintaining an air tight seal.

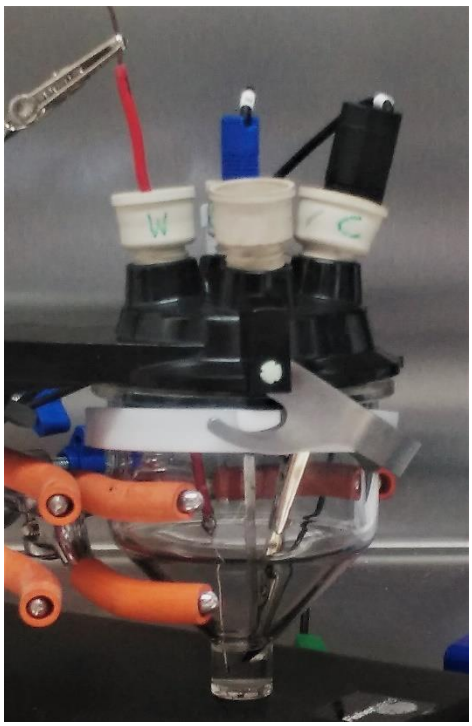

Figure 6-2. 3-electrode cell set up using a Metrohm vessel and rubber septums to hold the electrodes in place.

6.3 Electrolyte test

$Mg(ClO_4)_2$, $Mg(TFSI)_2$ (TFSI = Bis(trifluoromethanesulfonyl)imide), $Mg(AlCl_2EtBu)_2$ (Grignard based) and $Mg(PF_6)_2$ were tested in the 3-electrode flooded cell set up (Pt working electrode, Mg reference and Pt counter) to ascertain their voltage stability windows and whether they support Mg stripping and plating.

6.3.1 Grignard based

Although the stability window is not large enough to test polyanion cathodes, cyclic voltammetry of the Grignard based $Mg(AlCl_2EtBu)_2$ in dry tetrahydrofuran (THF) is included to give a reference of the response expected for an electrolyte system known to support reversible plating of Mg. Figure 6-3 shows cyclic voltammetry of the Grignard based electrolyte between -0.5 and 0.5 V vs. Mg. The voltage was initially swept from 0 V down to -0.5 V in order to plate Mg on the Pt electrode. A clear reductive peak is observed, starting at -0.22 V, and peaking at -0.47 V vs. Mg with a current of -0.12 $mAcm^{-2}$. The voltage reaches -0.4 V before the curve turns towards a reductive current, meaning that starting the plating process has a large initial overpotential, but once initiated the overpotential reduces, with plating continuing to around -0.15 V. The overpotential of ~0.4 V is greater than that observed for Li plating from $LiPF_6$ (<0.2 V).[203] On the oxidative sweep a large stripping peak is observed at 0.28 V vs. Mg, with a current of -0.12 $mAcm^{-2}$. This shows that in the Grignard based electrolyte Mg plating

is reversible with low overpotentials, however the peak currents reduce with extended cycling. Previous studies, discussed in Chapter 1, have produced a range of Grignard type electrolytes that have extended cycle life but all have small stability windows (typically <2.5 V) and this, along with the large overpotential for plating, mean they are unlikely to be used with high voltage cathodes.

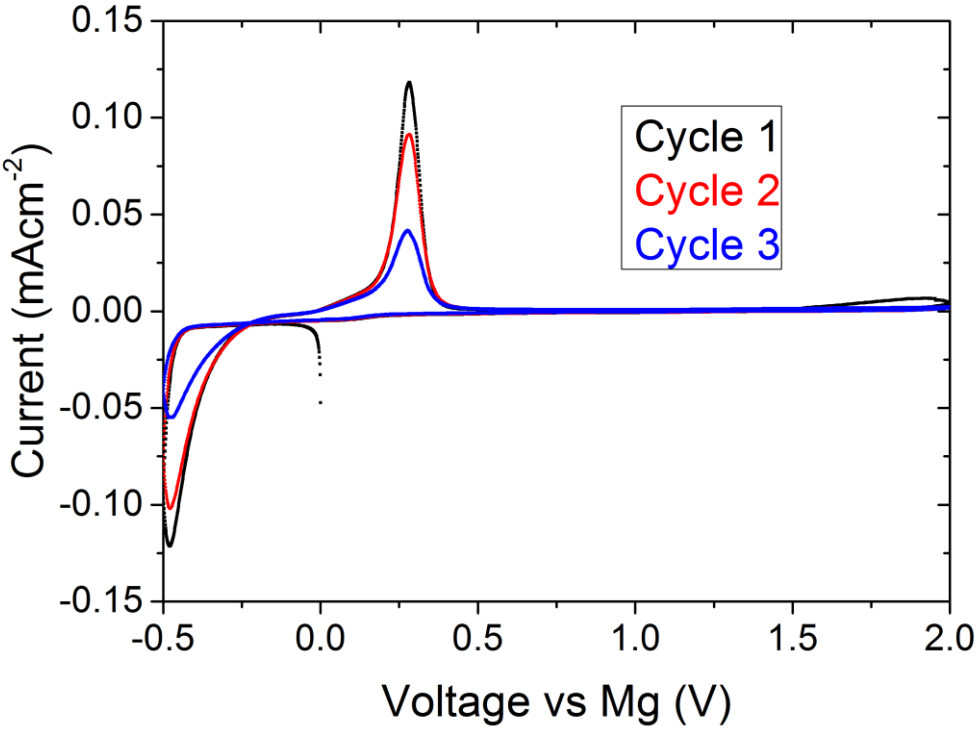

Figure 6-3. Cyclic voltammetry of the Grignard based $Mg(AlCl_2EtBu)_2$ electrolyte in dry THF with a scan rate of 10 mV s^{-1} displaying clear plating and stripping peaks.

The next step in assessing the cell design was to test a cathode in a known system. For this a film of the Chevrel phase was submerged in the Grignard based electrolyte with a Pt counter and Mg reference and the voltage was swept at 1 mV s^{-1}, Figure 6-4. Sweeping down from the open circuit voltage of 0.88 V vs. Mg sees insertion occur continuously down to 0 V. When the voltage is swept to more positive values two clear features are observed, attributed to Mg removal from sites A and B in the Chevrel phase structure. These features peak around 1.1 and 1.3 V vs. Mg, similar to the plateaus observed in galvanostatic measurements in the literature.[69] The ability to reversibly cycle the Chevrel phase indicates the 3 electrode flooded cell is suitable for testing new cathode materials.

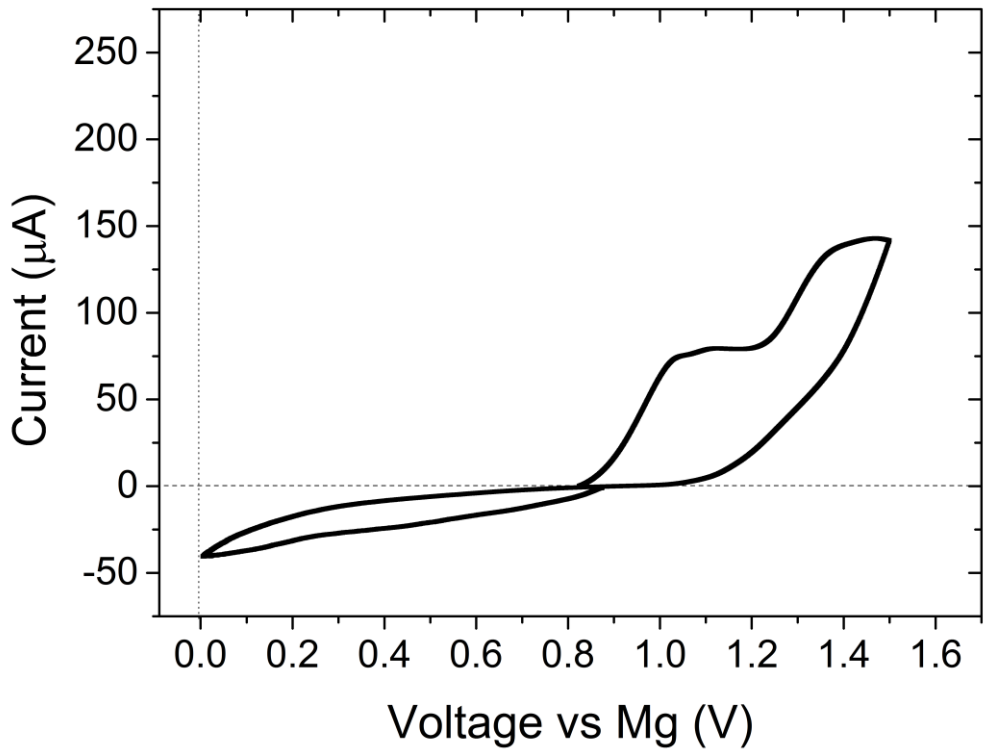

Figure 6-4. Cyclic voltammetry of a Chevrel phase cathode vs. a Pt counter electrode with Mg reference. Current below 0 V vs. Mg is associated with Mg insertion into the material, and current >0 μA with Mg removal.

6.3.2 Magnesium perchlorate

Cycling of 1M $Mg(ClO_4)_2$ in acetonitrile (ACN) between -1.0 and 1.0 V vs. Mg gives a negative current associated with Mg plating on the Pt electrode below 0 V, and a peak on the oxidative sweep at 0.87 V associated with Mg stripping, Figure 6-5. Both the stripping and plating currents are lower than those observed in the Grignard system meaning the reaction is slower in the perchlorate, as well as having a higher stripping overpotential. The plating current is also much greater than the stripping, suggesting this reaction (or a side reaction) is at least partially irreversible. The open nature of the curve (rather than retracing the same path) indicates a capacitive process is also occurring, this is thought to be due to the solvent as similar curves are seen when cycling dry acetonitrile only (Figure 6-1). Both the reductive and oxidative peak currents diminish over the first 6 cycles meaning the electrolyte no longer supports reversible Mg plating. The inset of Figure 6-5 shows that the electrolyte remains stable up to ~3.6 V vs. Mg, at which point significant current from electrolyte breakdown is observed. These results suggest the use of a $Mg(ClO_4)_2$ in ACN electrolyte may give reversible electrochemistry up to 3.6 V, however the cycle life will be limited and a large overpotential is likely.

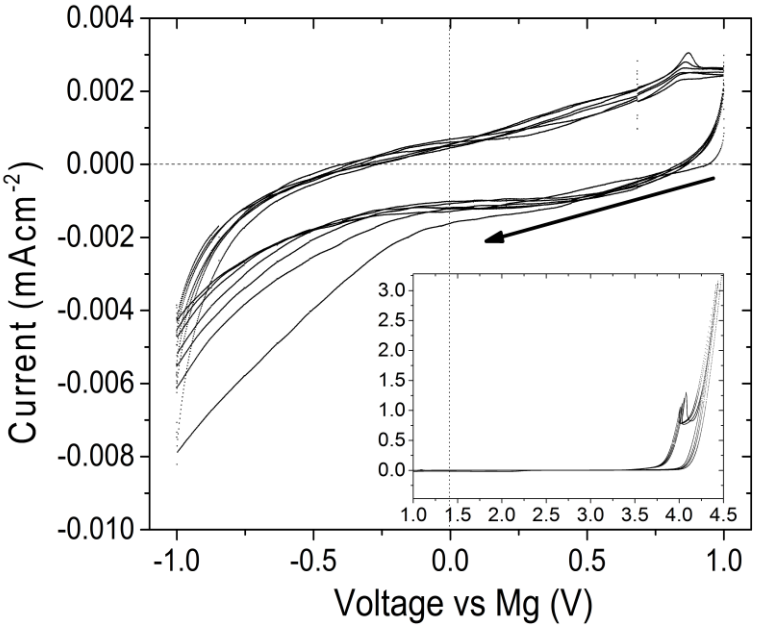

Figure 6-5. Cyclic voltammetry of $Mg(ClO_4)_2$ in ACN on a Pt working electrode with Mg pseudo-reference, at a scan rate of 10 mV s^{-1}. Inset: high voltage sweep showing electrolyte breakdown above 3.6 V. Axes labels are the same as the main plot.

6.3.3 Magnesium bis(trifluoromethane)sulfonimide

Mangesium bis(trifluoromethane)sulfonimide ($Mg(TFSI)_2$) in ACN is an established Mg-ion electrolyte, having been used to demonstrate reversible intercalation into a variety of cathodes, such as $MgFeSiO_4$, $MgFePO_4F$, MnO_2 and $MgMn_2O_4$.[88,95,110,204] $Mg(TFSI)_2$ is often used as it supports reversible de(solvation) of Mg^{2+} with a low overpotential and reasonable electrolyte window; typically being stable to ~3.5 V vs. Mg.[83] It is also safer than $Mg(ClO_4)_2$, although significant capacity fade is observed due to formation of a passivating layer. Typically, ACN is used as the solvent, however recently the use of coordination glymes has gained interest as they provide improved cycling efficiency and stability window at the expense of greater overpotential.[123]

Cyclic voltammetry of 0.5M $Mg(TFSI)_2$ in dry ACN (6ppm H_2O) was run by Zigeng Liu and the electrolyte was shown to support Mg^{2+} stripping and plating with low overpotential on a Pt working electrode with Mg counter and Mg pseudo-reference, Figure 6-6. Both the anodic and cathodic features are broad which suggests a surface reaction occurs before Mg^{2+} stripping or plating (e.g. adsorption of the electrolyte complex followed by deposition of Mg^{2+}), this would also explain the underpotential on the cathodic sweep where current associated with Mg^{2+} plating are observed above 0 V.

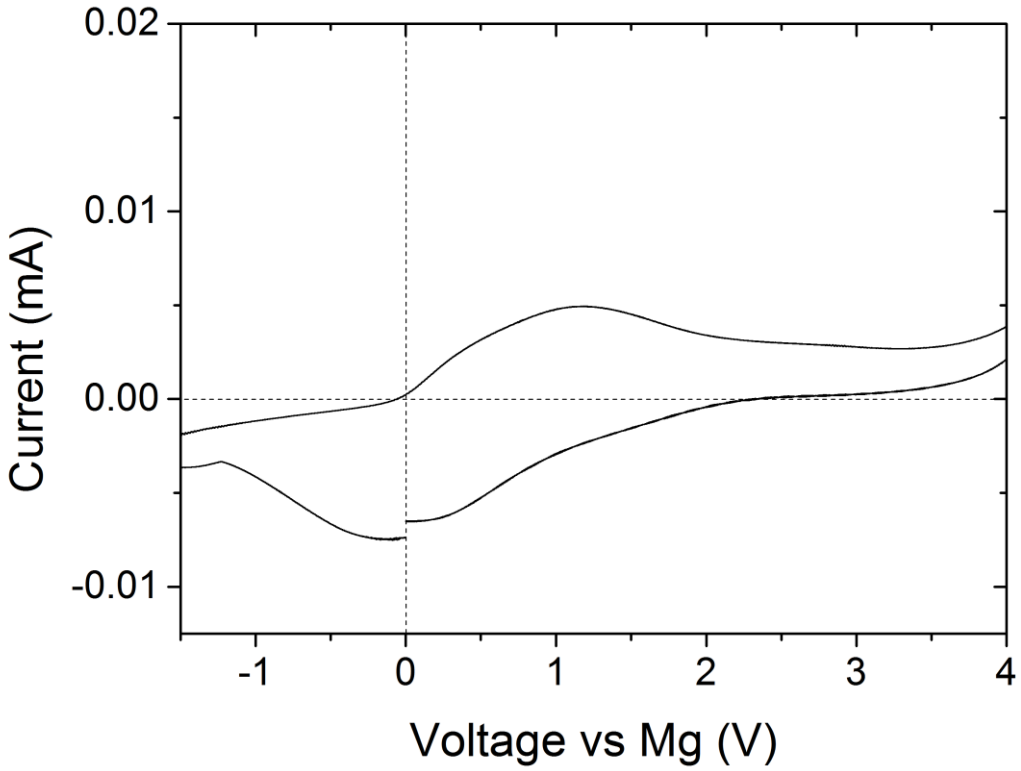

Figure 6-6. Cyclic voltammetry of 0.5M $Mg(TFS)_2$ in ACN with a Pt working electrode and Mg counter and reference.

Cycling at high voltages with fresh electrodes shows that $Mg(TFSI)_2$ in ACN begins to decompose ~3.5 V, consistent with the literature values, Figure 6-7. These results indicate $Mg(TFSI)_2$ in ACN may be a suitable electrolyte to test the borate polyanion-based cathodes as the electrolyte stability window is large enough to allow Mg removal from the lower voltage process seen vs. Li (assuming the voltages occur at the Li voltage -0.73 V – the difference in Li^+ and Mg^{2+} redox potential, with no overpotential).

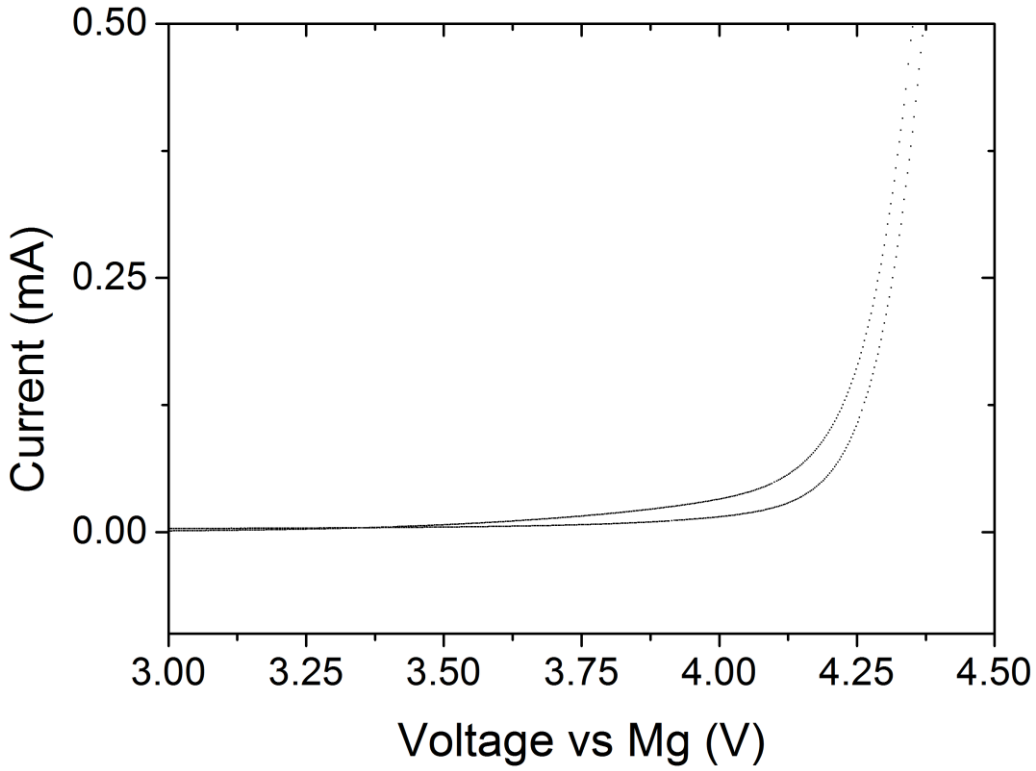

Figure 6-7. High voltage cyclic voltammetry of $Mg(TFSI)_2$ in ACN on Pt with Mg counter and reference electrodes. Oxidative breakdown of the electrolyte begins ~3.5 V.

6.3.4 Magnesium hexafluorophosphate

The inorganic salt $Mg(PF_6)_2$ is analogous to the $LiPF_6$ used in commercial Li-ion cells, however its use a Mg-ion electrolyte has not been widely discussed. An early review article on Mg-ion batteries stated that $Mg(PF_6)_2$ was unsuitable as an electrolyte as it was thought to decompose on Mg metal to form a passivating MgF_2 layer.[115] However, no detailed study of the electrochemistry to support this claim is available in the literature. To this end $Mg(PF_6)_2(CH_3CN)_6$ (an acetonitrile complex) was synthesised by Evan Keyzer in the Wright Group by reaction of Mg metal with stoichiometric amounts of $NOPF_6$, and its electrochemistry is explored by cyclic and linear voltammetry, symmetrical Mg cells, and cycling of the Chevel phase in a full coin cell.[138]

Cyclic voltammetry on a glassy carbon working electrode demonstrated plating and stripping of Mg in 0.71 M $Mg(PF_6)_2$ in ACN/THF electrolyte, with a stripping overpotential ~0.5 V, Figure 6-8a. When cycled on a Mg working electrode stripping and plating was again observed, with no appreciable decrease in electrochemical activity on extended cycling, suggesting no formation of a passivating MgF_2 layer at these voltages.

Linear sweep voltammetry on Pt, stainless steel (ss-316), glassy carbon and aluminium working electrodes show the electrochemical stability window is affected by the material used, Figure 6-8b. The use of stainless steel (a major component of coin cell parts) induces electrolyte oxidation at ~1.5 V vs. Mg, leading to a high anodic current. Further linear sweeps results in reduced anodic current suggesting the formation of a passivating layer. For Pt and Glassy carbon electrolyte oxidation begins ~ 2 V with a large increase in current at 2.5 V and 3.0 V respectively. Using Al as working electrode results in no significant current out to 4.0 V vs. Mg, though a small anodic current is observed ~1.8 V vs. Mg, suggesting the surface is passivated against further electrolyte breakdown. This is similar to that observed in the $LiPF_6$ system.

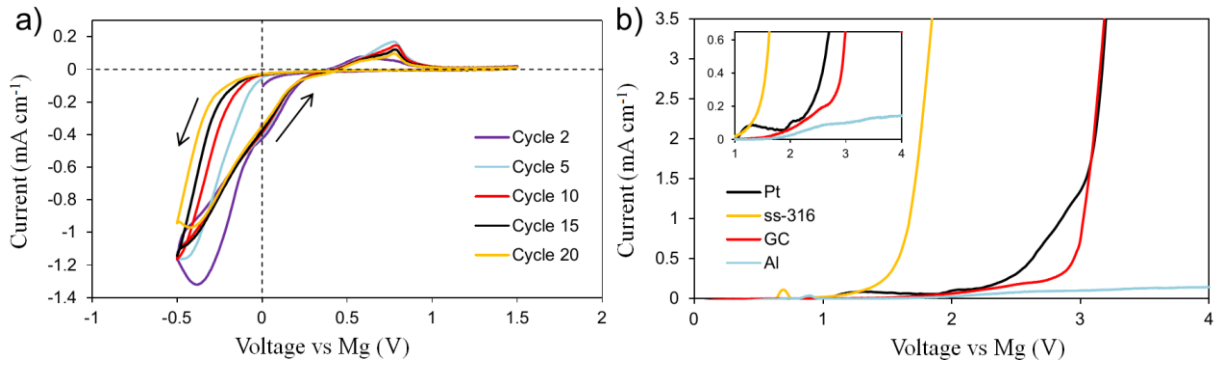

Figure 6-8. a) Cyclic voltammetry of $Mg(PF_6)_2$ in THF/ACN electrolyte with a scan rate of 25 mV s^{-1}. The working electrode was glassy carbon, with a Mg metal counter and reference. b) Linear sweep voltammetry on Pt, stainless steel-316, glassy carbon and Al working electrodes, at a scan rate of 25 mV s^{-1}. The inset shows an expansion of the low current density arising from the Al electrode. Figure reproduced from Keyzer et al.[138]

Cycling of a symmetric coin cell (Mg working and counter electrodes) using Al coated casings and current collectors shows Mg stripping and plating occurs with an overpotential of 0.5 V and efficiency of >99.96% over 250 hours of cycling, Figure 6-9. The relatively low and stable overpotential on continued cycling is consistent with reversible Mg electrochemistry rather than electrolyte breakdown and formation of a passivating layer. This is further supported by SEM/EDX (carried out with Evan Keyzer and Zigeng Liu) of the current collectors after cycling which showed clear Mg deposits on both aluminium and stainless steel, and contained only small amounts of F on the metal surface, Figure 6-10.

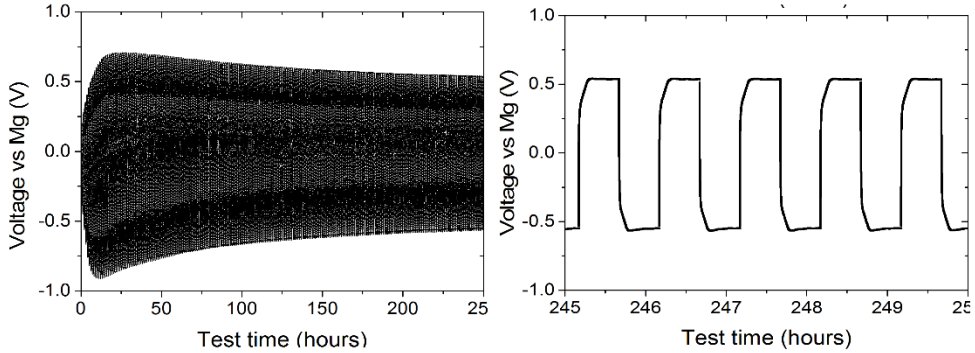

Figure 6-9. a) Cycling of a Mg symmetric cell with Al coin cell components and 0.71 M $Mg(PF_6)_2$ in ACN/THF electrolyte. A current density of 5 mA cm^{-2} was applied for 30-minute charge/discharge steps for ~250 cycles. b) Expanded section of cycling after 245 hours showing the 0.5 V overpotential. Figure reproduced from Keyzer et al..[138]

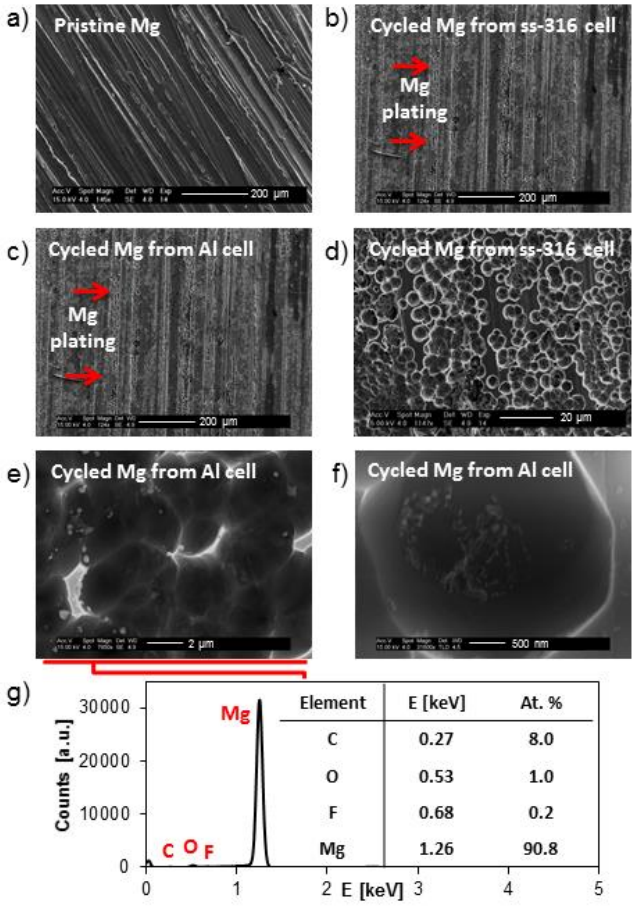

Figure 6-10. Surface analysis of pristine and Mg electrodes in 0.71 M 1 in 1:1 THF/CH_3CN. (a) SEM of an as prepared Mg electrode. SEM of Mg electrodes taken from cycled cells containing (b) ss-316 and (c) Al current collectors, showing large areas of Mg deposition. SEM of a cycled Mg electrode taken from a cell containing (d) ss-316 and (e) Al current collectors, highlighting the globular Mg plating morphology. (f) SEM of a single Mg bead deposited on the surface of a Mg electrode cycled with Al current collectors. (g) EDX analysis of the deposited Mg beads shown in (e). Reproduced from Keyzer *et al*.[138]

Having shown the electrolyte supports stripping and plating of Mg on a metal surface, reversible intercalation of Mg into the Chevrel phase (Mo_6S_8) was then tested. In a full Mg-ion coin cell using Al casings and current collectors, with a Mg metal anode and 0.71 M $Mg(PF_6)_2$ in ACN/THF electrolyte, 0.8 Mg^{2+} were inserted into the Chevrel phase on 1st discharge (96.5 mAh g^{-1}, 80% of the theoretical capacity), Figure 6-11. On subsequent cycles ~54 mAh g^{-1} is achieved, showing that $Mg(PF_6)_2$ supports reversible Mg^{2+} intercalation. The cycling of ~½ theoretical capacity is consistent with the literature where charge trapping limits the achievable capacity.

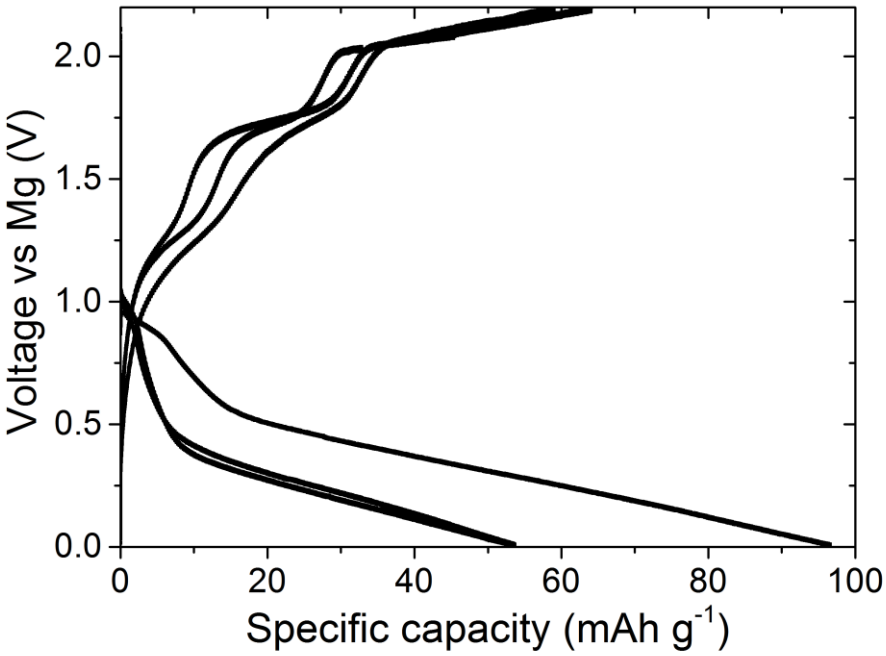

Figure 6-11. Cycling of Mo_6S_8 in a Mg-ion coin cell using the 0.71 M $Mg(PF_6)_2$ in ACN/THF electrolyte at a rate of C/100.

6.4 $MgMnB_2O_5$ electrochemistry

Figure 6-12 compares the 1st charge (Mg removal) for all the cathodes investigated in Li-ion cells. The ability to remove a significant amount of Mg from the structure clearly makes these families of materials interesting for Mg-ion batteries, however as subsequent cycling previously used a Li based electrolyte, the Mg intercalation characteristics were not assessed.

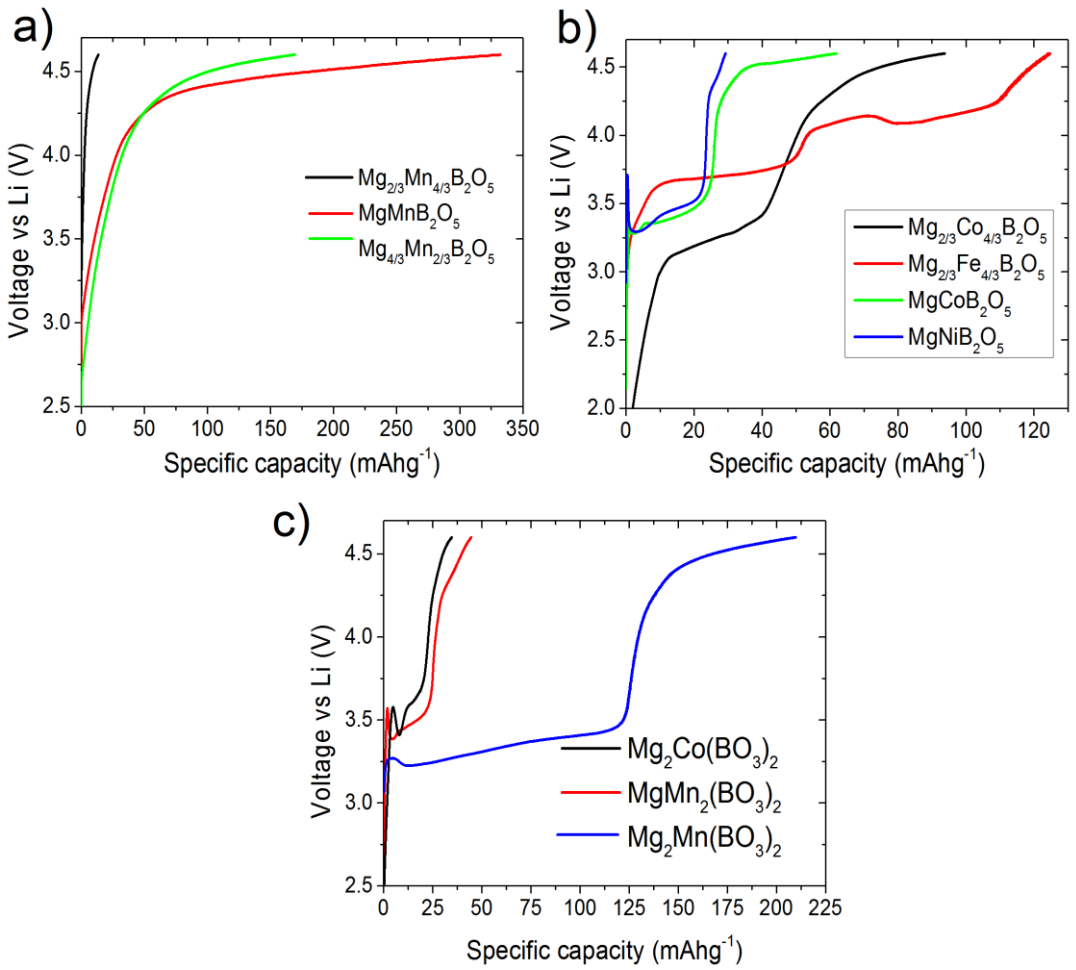

Figure 6-12. 1st charge (Mg removal) vs a Li anode with $LiPF_6$ in EC/DMC electrolyte in the a) pyroborates $Mg_xMn_{2-x}B_2O_5$, b) $Mg_xM_{2-x}B_2O_5$ where *M* = Co, Fe or Ni and c) the orthoborates $Mg_2Co(BO_3)_2$, $Mg_2Mn(BO_3)_2$ and $MgMn_2(BO_3)_2$.

As $MgMnB_2O_5$ gave the greatest Mg^{2+} removal capacity (for which the theoretical capacity is 296.6 mAh g^{-1}) and demonstrated that re-intercalation of ions was possible in a Li-ion cell, this material was chosen to test in a Mg-ion system. As the redox potential of Mg is 0.73 V higher than Li, the electrochemical process that occurs from 4.0 V vs. Li (Figure 6-13) would be expected to occur ~3.3 V. This is far above the stability threshold of the Grignard family of electrolytes, but may be achievable in $Mg(ClO_4)_2$ or $Mg(TFSI)_2$ based electrolytes.

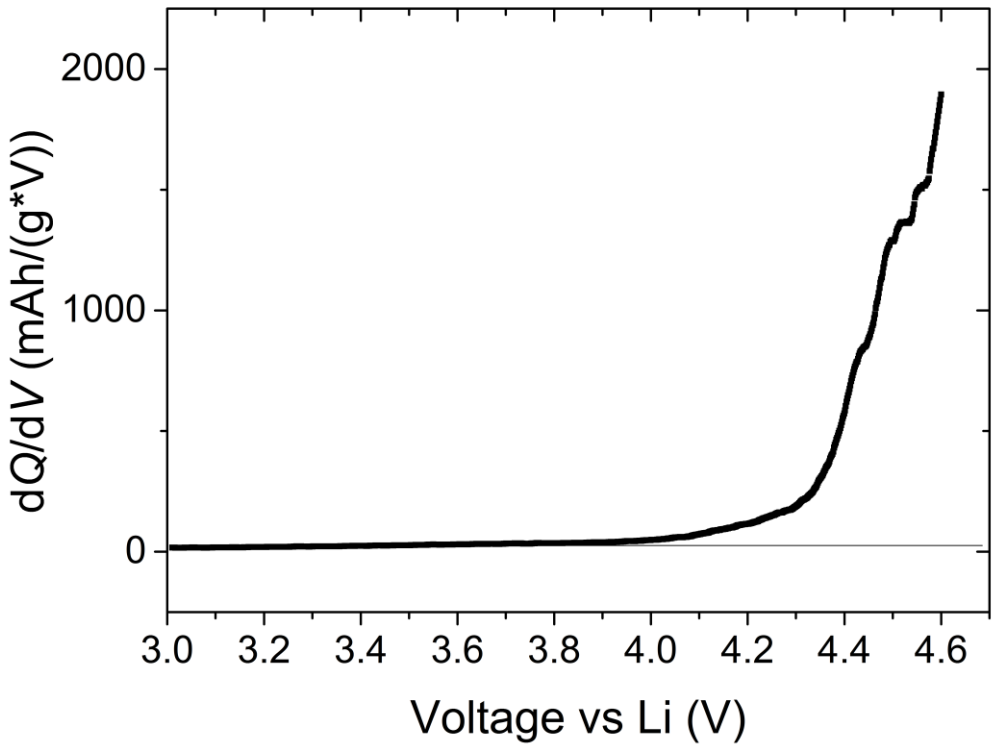

Figure 6-13. d*Q*/d*V* of the first charge of $MgMnB_2O_5$ in a Li-ion cell showing the onset of the Mg removal process at ~4.0 V.

6.4.1 $MgMnB_2O_5$ in full Mg-ion coin cells

Charge of $MgMnB_2O_5$ in a coin cell using 1M $Mg(ClO_4)_2$ in ACN electrolyte achieves a capacity of 36.1 mAh g^{-1} equating to 0.12 Mg^{2+} being removed from the cell, Figure 6-14. The majority of this capacity occurs over a sloping profile starting at the open circuit voltage of 1.8 V, though as 4.0 V is approached a plateau begins to emerge. On discharge 27.4 mAh g^{-1} is achieved down to 0.1 V equating to intercalation of 0.09 Mg^{2+} ions. Again, the capacity occurs over a sloping region with the redox process starting at ~2.1 V. The excess capacity on charge is likely due to electrolyte breakdown as 4.0 V is pushing the stability limits of the electrolyte, as demonstrated in Figure 6-5. The (de)intercalation of Mg^{2+} continues to be reversible over 10 cycles, though capacity fade is observed. By increasing the cycling temperature to 55 °C the charge capacity is increased to 93.8 mAh g^{-1}, however a significant proportion of this capacity is irreversible with 43.8 mAh g^{-1} achieved on discharge, equating to insertion of 0.14 Mg^{2+} per unit cell. The excess capacity is likely due to increased electrolyte breakdown caused by the increased temperature. As well as increased capacity, the overpotential on charge and discharge is reduced. This is especially evident on discharge where the process starts at ~2.4 V rather than 2.1 V at room temperature and the voltage takes longer to equilibrate after initial overpotential

(inset Figure 6-14). This suggests that with an improved set up which further reduces the overpotential even greater capacities could be achieved.

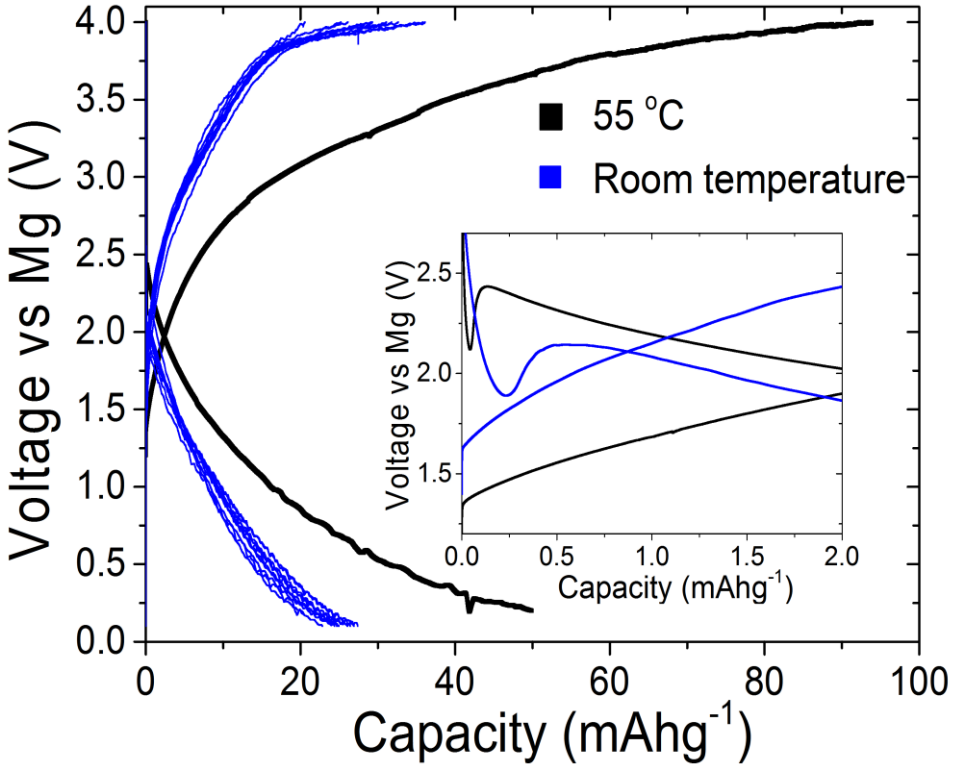

Figure 6-14. Cycling of $MgMnB_2O_5$ with a Mg metal anode and 1M $Mg(ClO_4)_2$ in acetonitrile electrolyte at a rate of C/100, at room temperature (blue line) and at 55 °C (black line). Inset shows the onset voltages of the charge and discharge processes at the two temperatures.

As 1M $Mg(TFSI)_2$ in ACN/THF is thought to support Mg^{2+} electrochemistry with a smaller overpotential than the perchlorate electrolyte, this was also used as the electrolyte in full Mg-ion cells. On charge to 4.0 V a shoulder is observed at ~3.2 V vs. Mg indicating the start of an electrochemical process, Figure 6-15. The voltage continues to increase up to 3.9 V, achieving a capacity of ~75 mAh g^{-1} (0.25 Mg^{2+} ions), at which point a plateau is reached and continuous capacity is observed. This is attributed to electrolyte breakdown, however the desired redox reaction may be occurring simultaneously. This suggests that Mg can be removed from the structure in the full Mg-ion cell, however significant electrolyte breakdown hinders assessing the actual useful capacity achieved. Discharge results in the insertion of 0.38 Mg^{2+} (112 mAh g^{-1}) into the structure, further confirming Mg was removed on charge, and demonstrating that $MgMnB_2O_5$ can support reversible Mg intercalation. Subsequent cycling leads to continuous capacity on charge at ~2.5 V, however reasonable discharge capacities are maintained, with a capacity of 90 mAh g^{-1} on 5th discharge.

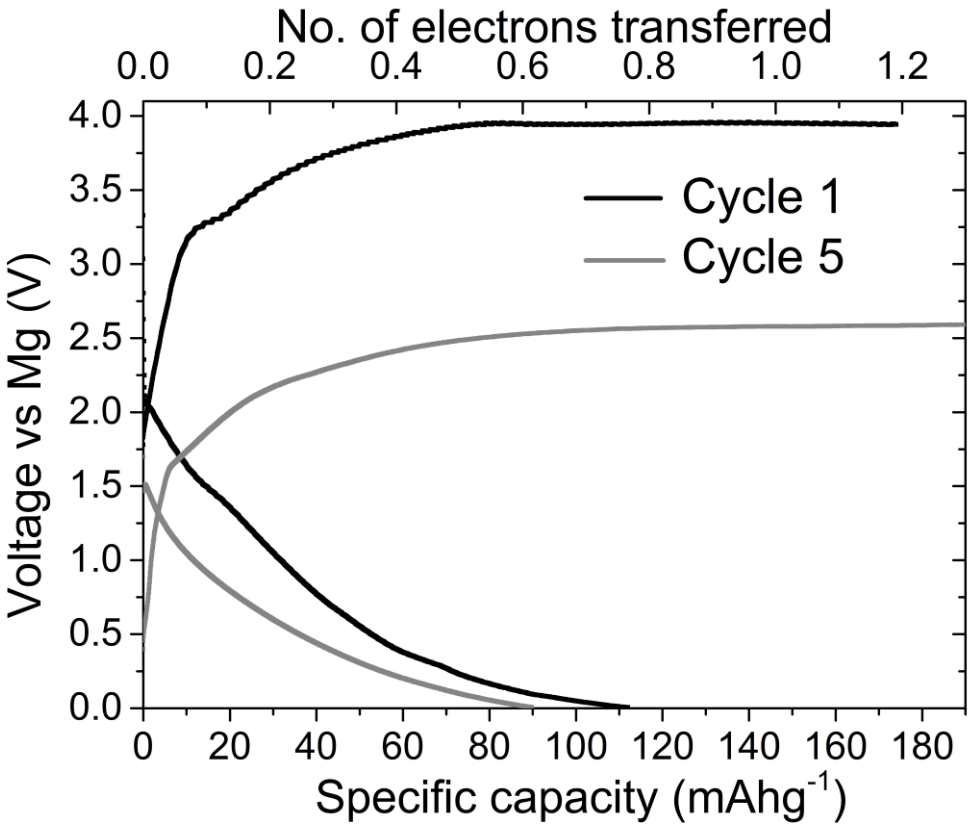

Figure 6-15. Cycling behaviour of $MgMnB_2O_5$ in a Mg-ion cell with 1M $Mg(TFSI)_2$ in ACN/THF electrolyte and Mg metal anode at a rate of C/25.

Cells were cycled with a limiting charge voltage of 3.5 V vs. Mg with the aim of avoiding the significant electrolyte breakdown on first charge. Figure 6-16 shows that on first charge a feature is observed below 3.5 V and a capacity of 24.5 mAh g^{-1} is reached by 3.5 V. This is consistent with the electrochemistry seen in Figure 6-15, where the same feature is observed and 26 mAh g^{-1} had been achieved by 3.5 V. The first discharge capacity is greater than first charge, reaching 56.2 mAh g^{-1} (0.19 Mg^{2+}) by 0.005 V. The excess discharge capacity could be Mg insertion (as seen in the Li-ion cells, where Li could be inserted into pristine material) or a surface / degradation reaction. On 2nd charge an increased capacity of 104.2 mAh g^{-1} is observed with a sloping voltage profile and the feature at ~3.4 V is absent. This is followed by a discharge capacity similar to the 1st (58.8 mAh g^{-1}). On the 3rd and all subsequent charges, continuous capacity is observed, never reaching the 3.5 V limit (the program was set to switch to discharge when the equivalent of 1.5 times the full theoretical capacity had been reached). Although this suggests significant electrolyte breakdown, the observation that discharge capacity continues to gradually increase, reaching 138.6 mAh g^{-1} (0.47 Mg^{2+}) by cycle 10, indicates that at least some of this capacity is due to the desired deintercalation reaction.

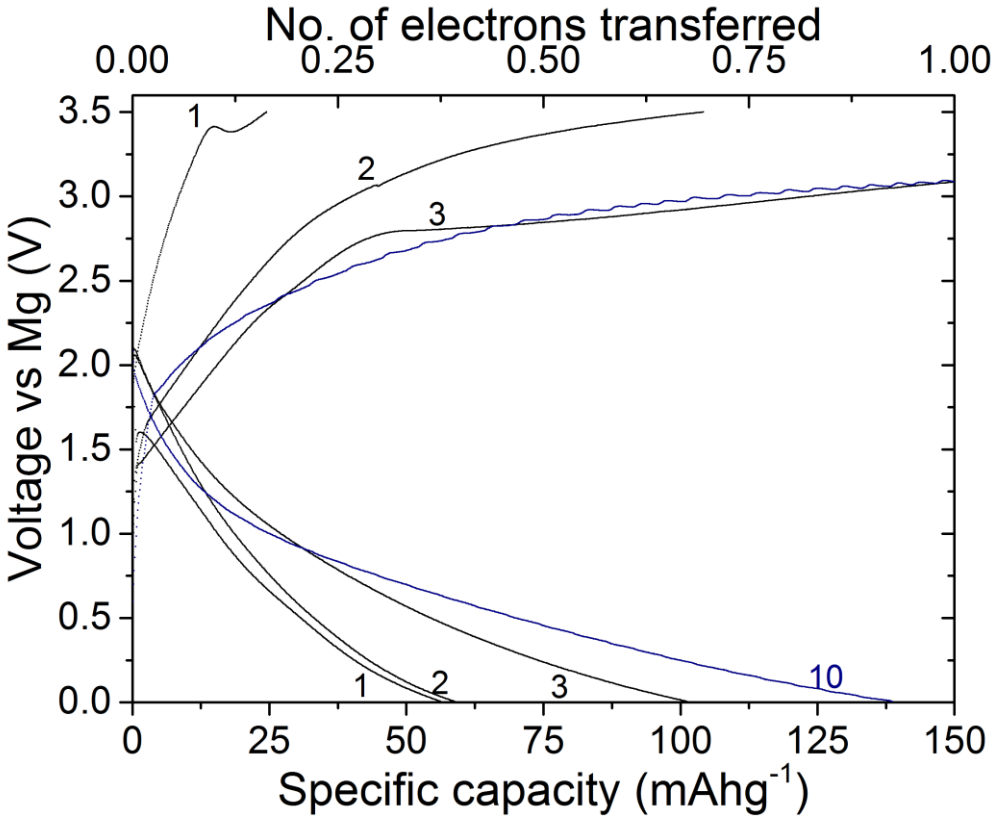

Figure 6-16. Cycling behaviour of $MgMnB_2O_5$ vs. a Mg metal anode with 1M $Mg(TFSI)_2$ in ACN/THF electrolyte at a rate of C/25 with a limiting voltage of 3.5 V vs. Mg.

Limiting the voltage range further to 2.5 V results in reduced charge capacity as would be expected, Figure 6-17. However, the initial discharge appears unaffected, with 64.8 mAh g^{-1} achieved on first discharge. Again, this could be due to insertion into the structure or a surface reaction with the electrolyte. Subsequent cycling results in fully reversible insertion of ~38 mAh g^{-1} or 0.12 Mg^{2+} ions, indicating that some Mg is removed from the structure < 2.5 V, but that higher capacities require the higher voltages previously used.

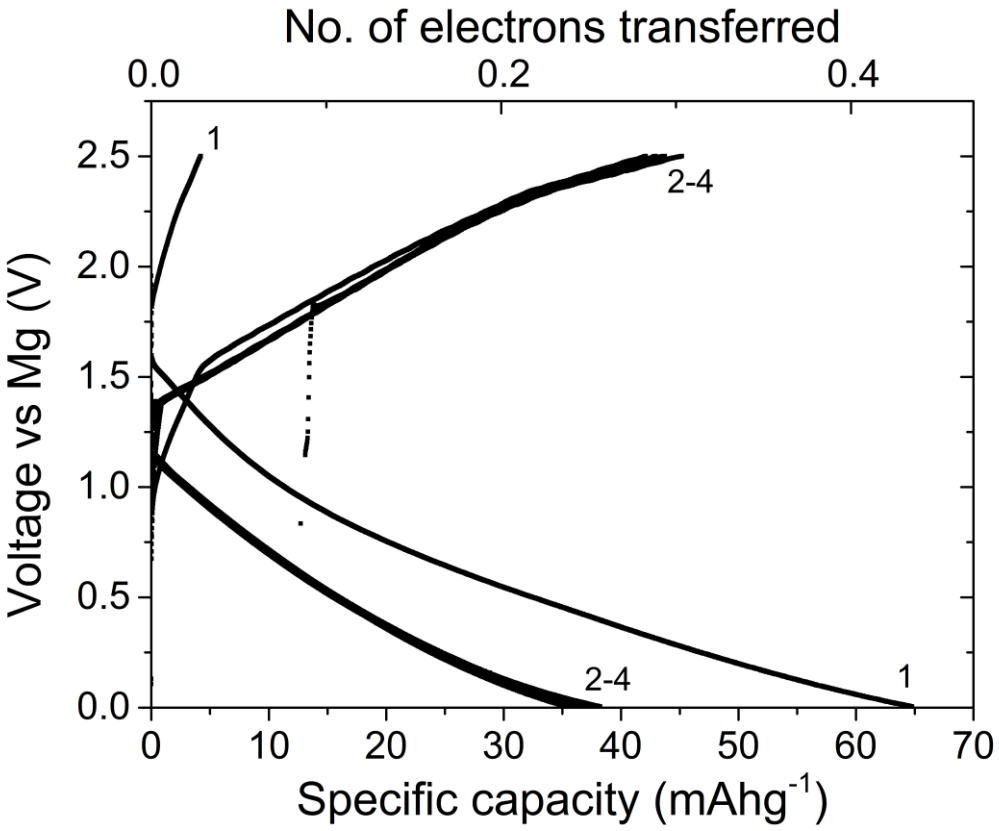

Figure 6-17. Cycling behaviour of $MgMnB_2O_5$ vs. a Mg metal anode with 1M $Mg(TFSI)_2$ in ACN/THF electrolyte at a rate of C/25 with a limiting voltage of 2.5 V vs. Mg.

By charging vs. a Li anode we have previously shown that all the Mg can be removed from the structure. Material that had been demagnesiated in a Li-ion coin cell was then cycled in a Mg-ion cell in order to assess if Mg intercalation is subsequently improved. Figure 6-18 shows that on 1st discharge in the Mg-ion cell 75.9 mAh g^{-1} is achieved, less than achieved in the Mg-ion cell charged to 4.0 V but more than the 3.5 or 2.5 V cell. Therefore, it seems that the Mg^{2+} intercalation capacities are not limited by the charge capacities achieved in the Mg-ion cells, instead the intercalation process itself is limited in these conditions. This is further supported by the increased capacities observed at the slower rate of C/100 (Figure 6-19) where 166.6 mAh g^{-1} is achieved on 1st discharge, greater than that achieved in any of the C/25 cells, indicating that the intercalation process is kinetically hindered. Neither the charged vs. Li first or cycled at C/100 cells display the low capacity 1st charge observed in the C/25 Mg-ion cells, suggesting that the initial hindrance to Mg^{2+} removal is reduced in these systems. Further study of the cells at C/100 was not possible as the reduced rate increased electrolyte side reactions significantly and lead to failure of the cell after the 1st cycle.

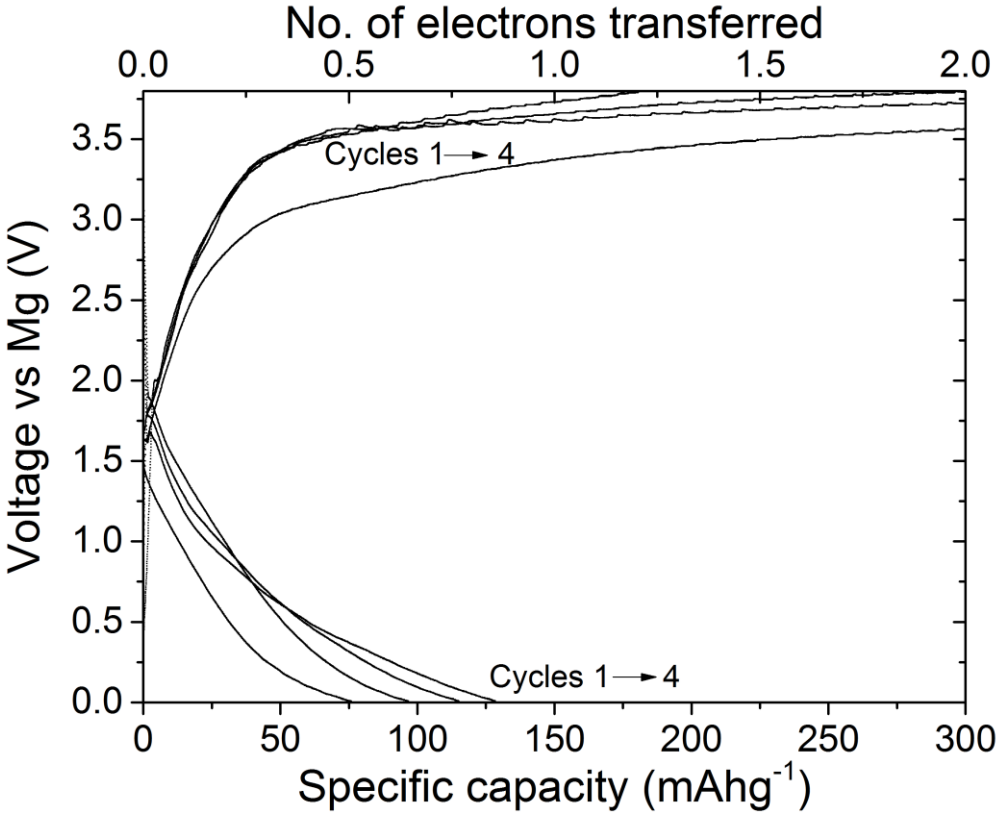

Figure 6-18. Cycling behaviour of $Mg_xMnB_2O_5$ that has been previously charged vs. a Li anode. Material was cycling in a Mg-ion coin cell with 1M Mg(TFSI)2 in ACN/THF electrolyte at a rate of C/25.

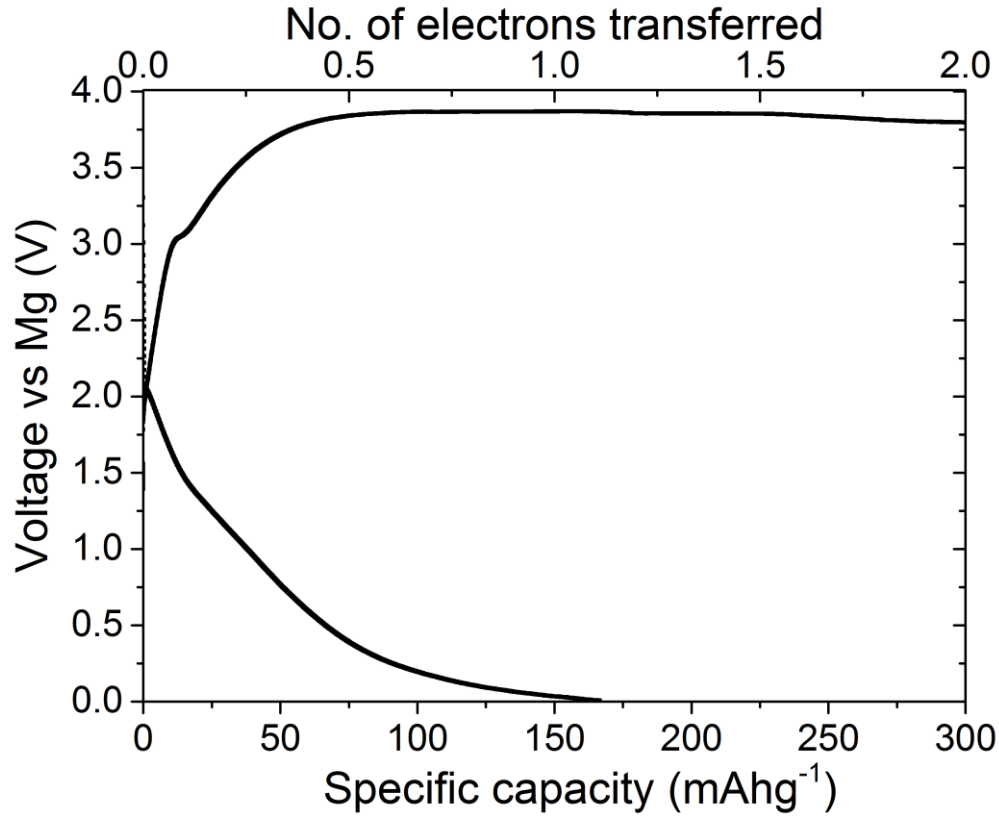

Figure 6-19. Cycling behaviour of $MgMnB_2O_5$ in a Mg-ion coin cell with 1M Mg(TFSI)2 in ACN/THF electrolyte at a rate of C/100.

6.4.2 $MgMnB_2O_5$ in 3-electrode flooded cells

The $MgMnB_2O_5$ cathode has been shown to give reversible capacity in Mg-ion coin cells but electrolyte breakdown leads to inefficient cycling and short cycle life. The electrolyte decomposition reaction is thought to be predominantly due to reaction with the cell casing, as has been previously reported, and on disassembly discoloration of the current collectors was observed.[89,202] Therefore, cyclic voltammetry on the material in a 3-electrode flooded cell was used to assess the voltages at which the desired electrochemical reactions occur.

$MgMnB_2O_5$ film was coated onto Pt wire and immersed in $Mg(TFSI)_2$ in ACN/THF electrolyte. A Mg wire pseudo-reference and capacitive carbon counter electrode complete the circuit. When cycled between 0.5 V and 3.5 V at 10 mV s^{-1} vs. Mg a large positive current is observed above 2.6 V, peaking ~3.0 V, associated with oxidation of the cathode and therefore Mg removal, Figure 6-20. Above this the current decreases slightly until 3.5 V is reached. As the current is swept back towards more negative potentials the current remains positive and flat until 2.9 V, where the current rapidly drops. This flat current response is unusual and could be attributed to capacitive behaviour induced by relatively fast cycle rates. The current continues to drop and turns negative (reductive) at 2.6 V and a reductive peak is observed at 2.3 V. This is thought to be the reversal of the oxidative process at 3.0 V, i.e. Mg insertions. A smaller but still negative current is observed down to 0.5 V, with a broad feature below 1.1 V that diminishes with increased cycle number, indicating further reductive processes are occurring. On the following oxidative sweep a relatively sharp peak is observed at 1.65 V, which also diminishes on increased cycle life so is likely the reversal of the broad low voltage process.

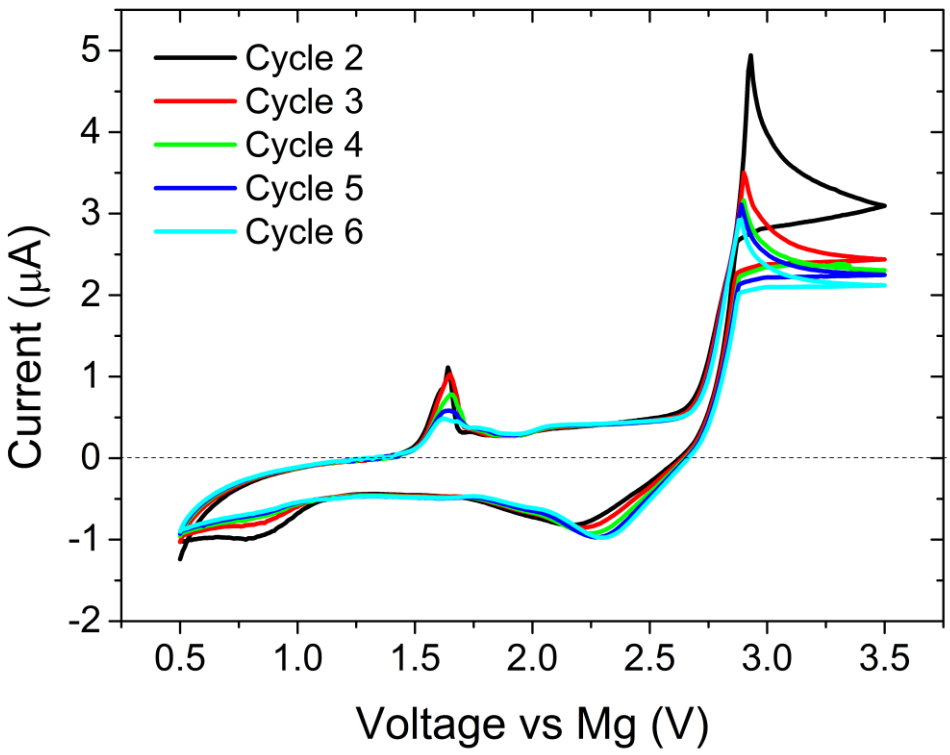

Figure 6-20. Cyclic voltammetry of $MgMnB_2O_5$ in a 3-electrode flooded cell with $Mg(TFSI)_2$ in ACN/THF electrolyte. Voltage was swept at a rate of 10 mV s^{-1}.

After 50 cycles the peak capacity has reduced, however the high voltage processes are still apparent, and occur with reduced overpotential (at 2.8 V and 2.55 V), Figure 6-21. There is also significant capacity at lower voltages, consistent with the sloping voltage profile seen in the coin cell electrochemistry. Two new, smaller and reversible features are also present at lower voltages (indicated by dotted lines on Figure 6-21), and with increased cycling the high voltage processes decrease further and these become more obvious, Figure 6-22. The cause of these 3 individual processes is not understood, however their reversibility and broad peak shape is consistent with Mg^{2+} intercalation in other systems.[78,94]

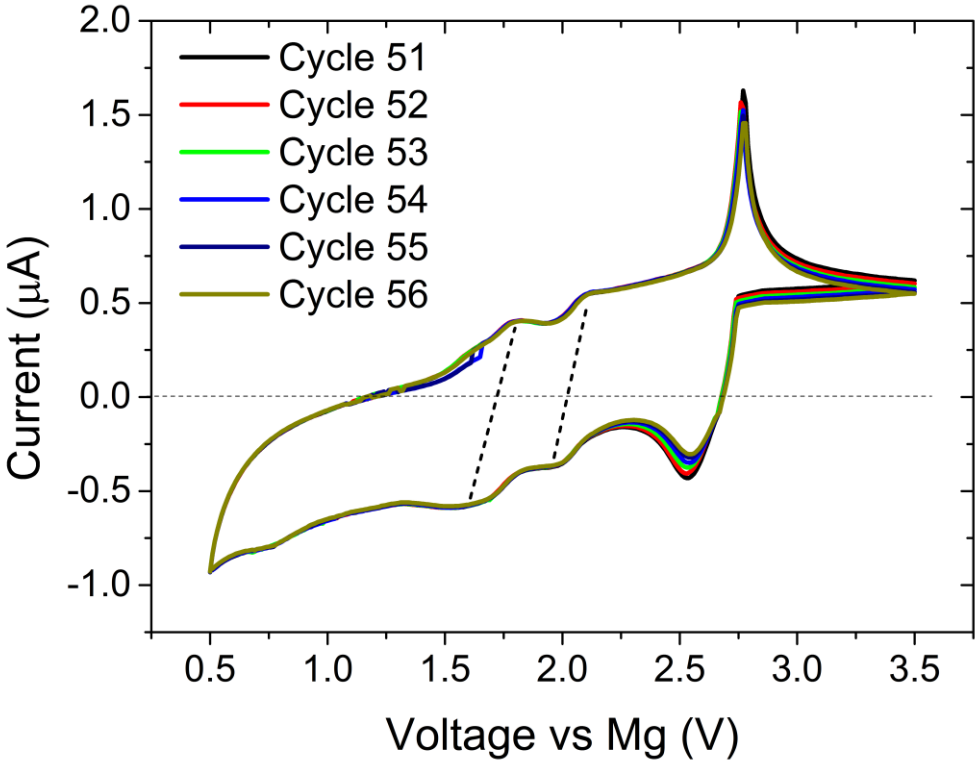

Figure 6-21. Cycles 51-56 of cyclic voltammetry of $MgMnB_2O_5$ in $Mg(TFSI)_2$ in ACNTHF electrolyte swept at a rate of 10 mV s^{-1}. Dotted lines indicate the reversible features which were not observed in the initial cycles.

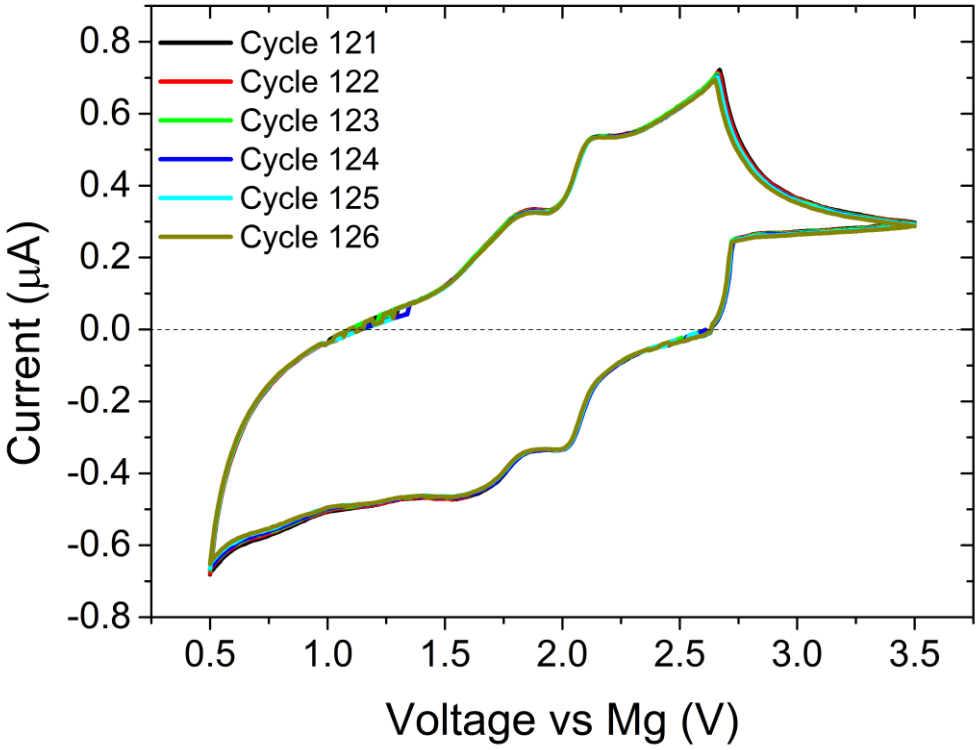

Figure 6-22. Cyclic voltammetry cycles 121-126 of $MgMnB_2O_5$ in $Mg(TFSI)_2$ in ACN/THF electrolyte, with voltage sweep rate of 10 mV s^{-1}.

To assess if the flat current region above 3 V was due to capacitive effects, a slower sweep rate was used (1 mV s^{-1}), Figure 6-23. This shows similar features to the fast sweep rate data and the high voltage region has a more standard current response, confirming that the unusual response was due to capacitive effects. However, at the slower rate the high voltage oxidative current is far greater than the reductive, indicating that an irreversible reaction is occurring as well as a reversible one. This is consistent with the coin cell data where continuous electrolyte breakdown was observed occurring at similar voltages to a reversible process, and where slower rates induced more side reactions and faster cell failure.

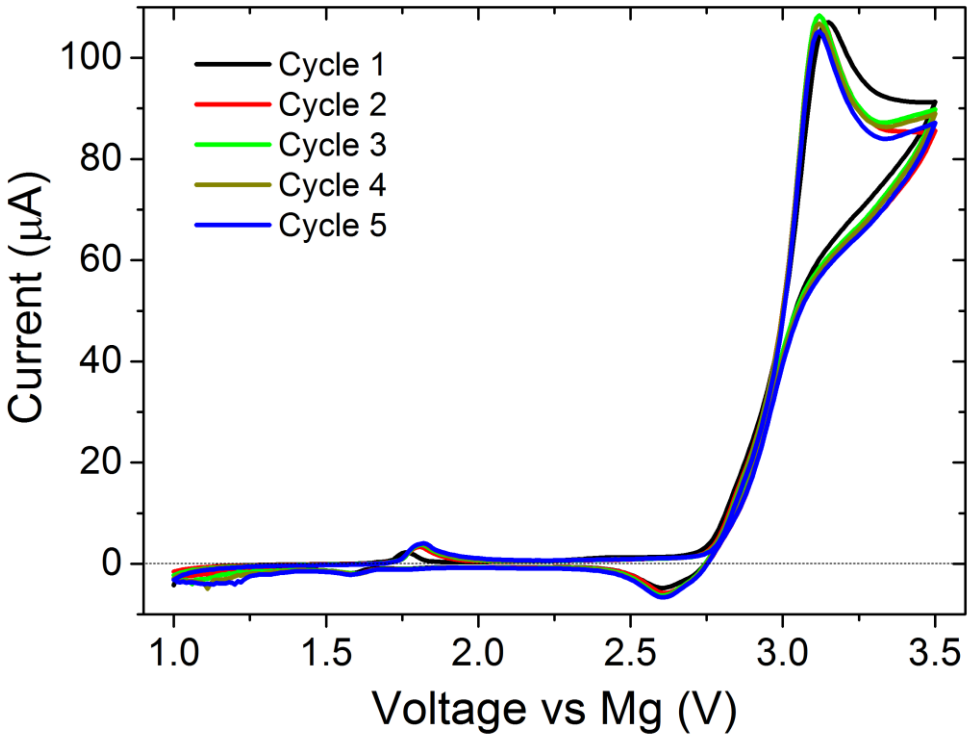

Figure 6-23. Cyclic voltammetry of $MgMnB_2O_5$ at the slower sweep rate of 1mV s^{-1}.

6.4.3 Ex-situ analysis

6.4.3.1 Ex-situ PXRD

$MgMnB_2O_5$ was charged vs. Mg in a Mg-ion coin cell with $Mg(TFSI)_2$ in ACN/THF electrolyte and the voltage was held at 3.5 V until full theoretical capacity was achieved. Ex-situ Le Bail refinement of the resulting material gives a unit cell volume of 362.3(1) $Å^3$ compared to 367.07 $Å^3$ in the pristine material, a reduction of 1.3%. This is just under half the contraction observed for the charged vs. Li material, suggesting ~½ the Mg is removed, Figure 6-24. This is consistent with the electrochemistry where on discharge up to 0.47 Mg^{2+} are inserted per unit cell, indicating removal of at least this much Mg^{2+} on charge. The peak associated with doubling the unit cell in the *c* direction is again observed after charge, indicating the same process that occurs in the Li-ion cell (Chapter 4), is occurring in this Mg-ion cell.

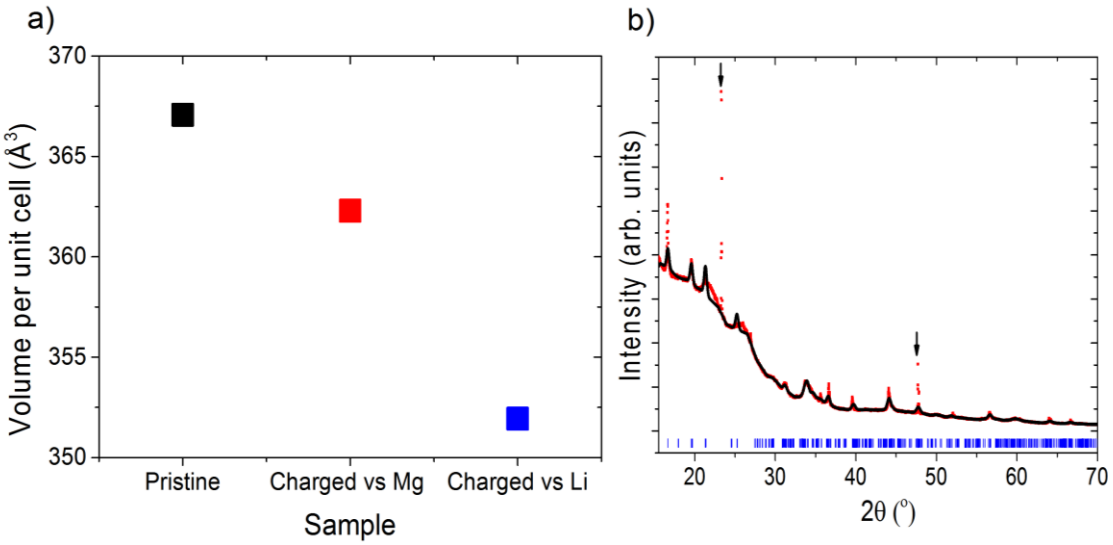

Figure 6-24. a) Refined unit cell volumes for uncycled, charged vs. Mg and charged vs. Li $MgMnB_2O_5$. b) Le Bail refinement of the charged vs. Mg material. Arrows indicate peaks due to residual electrolyte.

6.4.3.2 SQUID magnetometry

As discussed in Chapter 4, SQUID magnetometry can be used to calculate the magnetic moment of the Mn ion in a cycled cathode, and therefore investigate oxidation changes. $MgMnB_2O_5$ was cycled in a full Mg-ion coin cells using the $Mg(TFSI)_2$ electrolyte to produce a charged only and charged-discharged sample, Figure 6-25. The charge regions were allowed to reach capacities well above theoretical capacity, under the assumption that the real deintercalation process happens simultaneous to electrolyte breakdown. After diamagnetic correction, the magnetic moments of the samples were found to be: Pristine, 5.98 μ_B; Charge only, 5.0 μ_B; charged-discharge, 5.6 μ_B. The pristine cathode gives a magnetic moment consistent with Mn^{2+},

the expected starting oxidation state. The reduced moment in the charged sample is indicative of Mn oxidation to nearly Mn^{3+} (expected moment for Mn^{3+} is 4.9 μ_B). This suggests that around half the Mg has been removed from the cell (~150 mAh g^{-1} of the charge capacity is due redox reactions in the cathode material). Discharging the material leads to an increase in magnetic moment and therefore a reduction to between Mn^{2+} and Mn^{3+}, consistent with the electrochemistry where ~0.25 of a Mg^{2+} ion is inserted per cell on discharge (78.6 mAh g^{-1}). Full reduction back to Mn^{2+} is not observed, which was also the case for Li^+ insertion, suggesting that the material remains Mg deficient ($Mg_{1-x}MnB_2O_5$, $x \sim 0.25$).

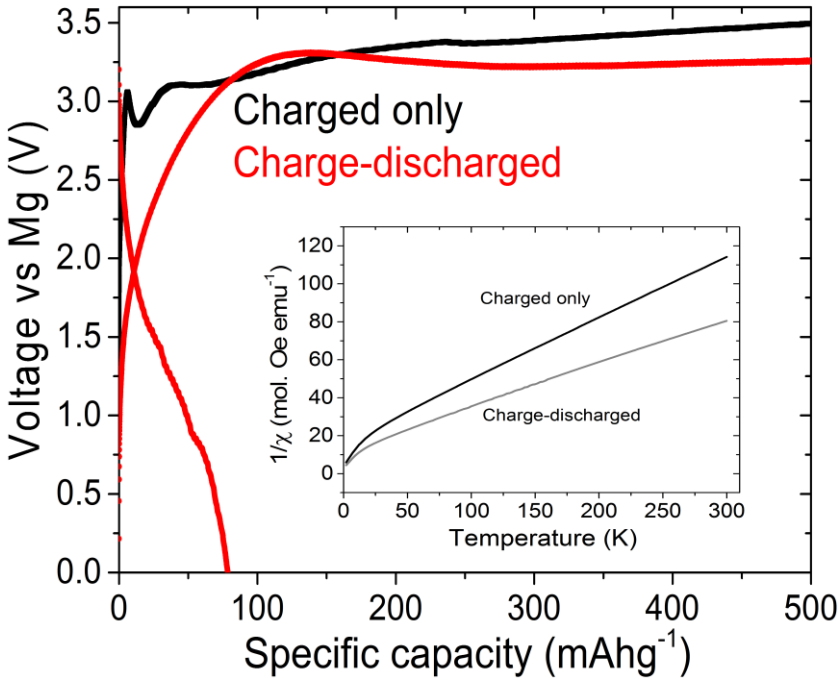

Figure 6-25. Cycling of $MgMnB_2O_5$ in a Mg-ion coin cell. Cells were disassembled and cathode magnetisation measured in a SQUID magnetometer (inset).

6.4.3.1 XANES

X-ray absorption structure spectra were measured for the Mn K-edge in the pristine cathode material and after charge vs. a Mg anode, Figure 6-26. Comparison of the spectra shows that on charge a slight blue shift is observed in the K-edge, indicating oxidation of the Mn. This is accompanied by a reduction in the peak at 6552 eV and a more distinct feature at 6557 eV, consistent with oxidation of Mn^{2+}. As with the Li-ion ex-situ samples (Chapter 4), the changes are less pronounced than would be expected from the electrochemistry and SQUID measurements. As previously discussed this may be due to hybridization of O 2*p* states and Mn

3*d* states leading to predominantly O 2*p* character below the Fermi level in these materials, and therefore oxidation is concentrated on the oxygen.

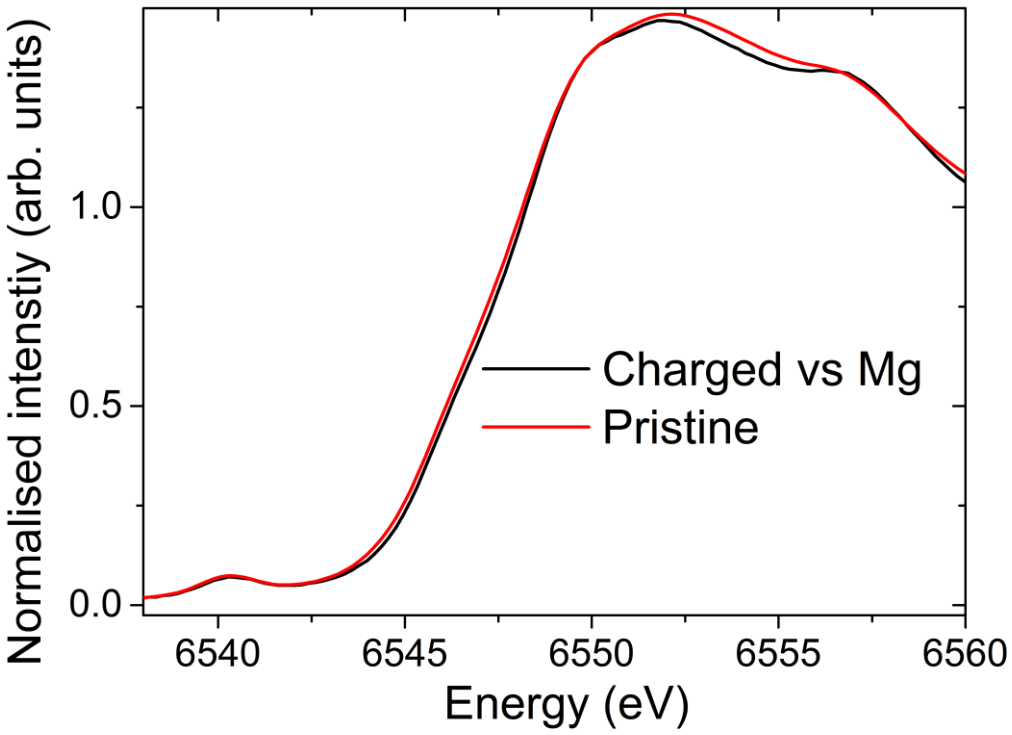

Figure 6-26. XANES spectra for ex-situ cycled $MgMnB_2O_5$ samples vs. a Mg anode at the Mn K-edge.

6.5 Conclusions

Various electrolytes were tested in the 3-electrode flooded cell set up and $Mg(TFSI)_2$ in ACN/THF was chosen for use with the cathode material due to its combination of reversible Mg plating and relatively large stability window.

$Mg(PF_6)_2$ in ACN was synthesised by the Wright group and been shown to facilitate reversible Mg deposition with high efficiencies and anodic stability, especially on Al current collectors, where large oxidation currents are not observed up to 4.0 V vs. Mg. This suggests the Al surface is passivated towards the breakdown of electrolyte, as observed in the Li system.[138] SEM and EDX measurements confirmed the Mg anode surface remains electrochemically active after cycling for 250 hours in a Mg symmetrical cell (0.5 V overpotential and >99.96% efficiency), with little evidence of a fluoride passivation layer. This is contrary to previous reports that suggested this type of simple inorganic salt would be unsuitable for Mg-ion batteries.[75] Reversible intercalation into the Chevrel phase when Al coin cell components were used is demonstrated, achieving ~50% theoretical capacity at room temperature.

$MgMnB_2O_5$ was chosen for testing as a Mg-ion cathode due to the high capacity of Mg removal and reversible intercalation achieved in the Li-ion cells. When cycled in a Mg-ion coin cell with $Mg(ClO_4)_2$ electrolyte and a Mg metal anode reversible electrochemistry is observed with discharge capacities up to 43.8 mAh g^{-1}, equivalent to insertion of 0.14 Mg^{2+} ions. This capacity is achieved over a sloping voltage region starting at 2.4 V vs. Mg. There is excess capacity on charge, likely due to electrolyte breakdown.

When a $Mg(TFSI)_2$ based electrolyte is used, the reversible capacities are increased, achieving up to 138.6 mAh g^{-1} (0.47 Mg^{2+}) after 10 cycles at a rate of C/25. However, this is accompanied by a greater irreversible component with electrolyte breakdown occurring at a lower voltage than observed for the perchlorate electrolyte. The desired charge process appears to occur with a feature ~3.3 V vs. Mg on first charge, though with extended cycling this smooths out to give a sloping voltage profile. This is consistent with the Li-ion electrochemistry where Mg removal was observed with a plateau >4.0 V vs. Li (~3.3 vs. Mg) while subsequent cycling showed a sloping profile.

The capacities achieved in the full Mg-ion cells are similar to those achieved with solid state V_2O_5 and the manganese oxides after optimisation (Table 1-2), and if the overpotential and efficiency could be improved (i.e. reliable high voltage electrolytes) then a much higher average voltage than V_2O_5 could also be realised. The electrolyte used and the synthesis route has a large effect on the capacities and voltages achieved in other intercalation compounds,

demonstrating the potential for improvement in this system that could be achieved by forming nanowires or gels, or improving the electrolyte.

Further study of this system in a 3-electrode flooded cell demonstrates that a reversible process above 2.6 V vs. Mg occurs with a high current, irreversible, oxidative process also occurring at high voltages. Extended cycling results in multiple reversible processes between 1.5 and 3.0 V vs. Mg.

Ex-situ PXRD shows a reduction in volume on charge vs. a Mg anode. The change in volume is just under half that observed on full Mg removal in the Li anode cell, consistent with the electrochemistry where up to 0.47 Mg^{2+} are inserted meaning at least this is much removed on charge.

SQUID magnetometry shows Mn oxidation from Mn^{2+} to Mn^{3+} on charge in a Mg-ion coin cell. Confirming that at least some of the capacity achieved on charge is due to redox reactions in the cathode material. The 1 electron oxidation state change suggests around 150 mAh g^{-1} is due to Mg^{2+} removal, which equates to 0.5 Mg. Subsequent discharge results in Mn reduction back to between $Mn^{2+/3+}$, consistent with the electrochemistry showing insertion of 70 mAh g^{-1} or 0.25 Mg.

These results show that despite electrolyte compatibility issues, $MgMnB_2O_5$ allows reversible, high capacity cycling of Mg^{2+} ions. Demonstration of Mg electrochemistry in polyanions is rare, therefore this study opens up the possibility to investigate a range of borate polyanions as potential high voltage electrodes for Mg-ion batteries.

Chapter 7. Conclusions

The aim of this project was to investigate the use of borate-based polyanions that contain a transition metal and a magnesium cation as Li-ion and Mg-ion cathode materials. Polyanions offer higher voltages and greater stability than oxide based cathodes, though the extra weight of the framework can lead to lower specific capacities in some cases. Borate-based polyanions are of particular interest as they are the lightest frameworks, so capacities are greater than the phosphate or silicate analogues, while voltages are generally greater than silicates and approaching those of the phosphates (dependent on connectivity and geometry). Of the wide variety of structures the versatile borate group form, the orthoborates and pyroborates were chosen for study as they contain M^{2+} transition metals, form layers or tunnels that may allow Mg^{2+} ion transport, and have high theoretical capacities. As Li containing orthoborates and pyroborates cannot be synthesised directly, replacement of the divalent Mg for 2 Li in an electrochemical cell was attempted, forming a Li-ion cathode in-situ.

7.1 Orthoborates

Although orthoborates containing Mg have been previously described, the synthesis of mixed metal orthoborates, the effect of the transition metal and stoichiometry on cation ordering, and the potential for cation diffusion has not been studied. To this end $(Mg,Co)_3(BO_3)_2$, $(Mg,Mn)_3(BO_3)_2$ $(Mg,Ni)_3(BO_3)_2$, and $(Mg,Co,Ni)_3(BO_3)$ were synthesised, their structures characterised by PXRD and PND and electrochemistry explored. As the layered orthoborate structure contains two distinct *M* sites in a 2:1 ratio, the $Mg_2M(BO_3)_2$ and $MgM_2(BO_3)_2$ stoichiometries were synthesised for each phase. Each system was shown to form solid solutions, with some deviation from a linear change in volume with average cation size caused by preferential occupation of Mg and the transition metal over the two sites. The structures containing transition metals with directional *d* orbitals (Co, Ni) display a preference to occupy the higher symmetry site *M*1, with $MgNi_2(BO_3)_2$ and $MgCo_2(BO_3)_2$ both having *M*1 almost wholly occupied by the transition metal (100% and 94% respectively), with the excess residing on *M*2. While the d^5 Mn^{2+} shows a preference for the *M*2 site, with this ordering driven by cation size. The 3-metal $Mg_2Co_{0.5}Ni_{0.5}(BO_3)_2$ has also been synthesised and shows that transition metal mixing is possible in the materials, which is important for future optimisation of the voltage and stability of the system.

Bond valence sum (BVS) calculations show that a Mg^{2+} percolating network is formed along the *M* layers with a bond valence variance of ± 0.7 v.u. This relatively high value suggests Mg^{2+}

diffusion may be structurally hindered, however Li^+ diffusion is expected to be easier, with a percolating network formed at $\pm$0.45 v.u. Therefore, if Mg can be removed while retaining the polyanion framework, Li cycling is plausible. The diffusion pathway links all *M*1 sites, but requires ions on *M*2 to pass through the *M*1 sites, so the presence of immobile transition metals on *M*1 may hinder diffusion. Therefore, cation ordering where Mg preferentially occupies *M*1 may be preferable.

Cycling vs. a Li anode at 55 °C demonstrates that 0.86 Mg^{2+} can be removed from the $Mg_2Mn(BO_2)_2$ material over two distinct voltage regions associated with oxidation to Mn^{3+} and Mn^{4+}. This gives a 1st charge capacity of 209.9 mAh g^{-1} and an associated unit cell contraction of 2.8% is observed in ex-situ PXRD. The removed Mg^{2+} is replaced by 0.61 Li^+ on discharge, resulting in a capacity of 83.5 mAh g^{-1}. This is reversible but gradual capacity fade is observed with extended cycling.

Cycling $MgMn_2(BO_3)_2$ vs. a Li anode results in the removal of up to 0.2 Mg per formula unit (44.5 mAh g^{-1}) over two high voltage plateaus (3.4 V and 4.0 V), though temperatures of 55 °C are required to achieved this. Achieving greater capacities at increased temperatures is indicative of a kinetically hindered process, which is consistent with the BVS results. For each Mg removed roughly 1 Li is inserted, giving a capacity of 26.1 mAh g^{-1} to 1.5 V, which is significantly less than achieved on charge, as only one electron is transferred for each Li compared to 2 for Mg. The 1:1 exchange contrasts with the pyroborates where 2:1 ion exchange (1:1 electron exchange) is observed.

In the Mg rich $Mg_2Co(BO_3)_2$ up to 0.13 Mg is removed from the structure over three voltage regions (3.3, 3.7 and >4.0 V), and no improvement is seen by cycling at slower rates or increased temperatures. Again 1 Li replaces each Mg removed, achieving a maximum capacity of 25.0 mAh g^{-1} when discharged to 1.5 V. The limitations to Mg and Li diffusion may be that Co preferentially occupies the *M*1, which BVS calculations suggest will have better diffusion characteristics. The results suggest the diffusion channels are blocked by immobile Co, or that the material is inherently insulating, as $LiCoBO_3$ was shown to be.[153]

These results clearly demonstrate that the orthoborates are electrochemically active, and in materials with high Mg occupancy on site *M*1, large Mg^{2+} removal capacities are achieved. In the materials studied, for each Mg^{2+} removed, up to 1 Li^+ is inserted, indicating intercalation is limited by the number of crystallographic sites available. This difference in Li^+ uptake behaviour compared to the pyroborates can be explained by the BVS calculations, where the pyroborates have a higher volume fraction of the cell available to accommodate Li^+ ions than

the orthoborates. Therefore, extra Li^+ sites can be envisioned in the pyroborate materials, that are not present in the orthoborates, limiting Li^+ to occupy only the vacated Mg^{2+} sites.

The performance of the cathodes may be improved by forming carbon coated nanoparticles or mixed transition metal systems as has been displayed in other polyanion systems. The versatility of the structures also allows for optimisation of the transition metal redox couple used and the Mg available for removal, giving variation of the voltage and theoretical capacity.

7.2 Pyroborates

The use of pyroborates ($M_2B_2O_5$) in Mg-ion batteries has been previously been suggested and BVS calculations suggested the Mg may be mobile,[98] however the electrochemistry has not been explored in Mg-ion or Li-ion cells. Pyroborates where *M* is a combination of Mg and one of Mn, Co, Fe, or Ni have been synthesised and characterised, and their electrochemical properties explored in Li-ion and Mg-ion cells.

7.2.1 $Mg_xMn_{2-x}B_2O_5$

Three points of the solid solution $Mg_xMn_{2-x}B_2O_5$ where x = 2/3, 1 and 4/3 have been synthesised, and each display some preference for Mn to occupy the larger of the two octahedral sites. The propensity for Mg to occupy the *M*2 site may aid diffusion kinetics as previous BVS calculations show a percolating pathway is formed with a lower valance variance on this site than on *M*1. The ability to tune the stoichiometry allows for optimisation of the theoretical capacity and may help tune stability and reversibility properties in the future.

The two Mg rich phases (x = 1 and 4/3) both show considerable Mg^{2+} removal from the structure vs. a Li metal anode; 100% from the x = 1 phase and 78% from the x = 4/3 at a rate of C/25. PXRD and PND show that the pyroborate structure is retained after removal of Mg and a 5% volume contraction is observed in $MgMnB_2O_5$. Confirming the previous suggestions that Mg^{2+} removal from these materials is facile. Mn oxidation to balance the Mg^{2+} removal was confirmed by SQUID magnetometry.

Inserting Li into the demagnesiated x = 1 structure in a Li-ion cell at a rate of C/25 results in 220 mAh g^{-1} or 1.4 Li^+ intercalating into the cell on first discharge, and after 100 cycles 193 mAh g^{-1} is achieved, which is 88% capacity retention. Li insertion occurs with a sloping voltage profile down to 1.5 V however two features are observed at 2.5 V and 4.0 V. ^{7}Li solid state NMR on ex-situ cycled samples confirms that the Li content increases on charge and decreases on discharge. Quantitative analysis of the NMR shows that the 100th discharge contains ~80%

of the Li observed on the first discharge, and matches the electrochemical data. The suggestion that Li is reversibly intercalated into the structure is further supported by PND, which shows a 1% volume change in the structure on charge, and SQUID magnetometry, which shows Mn reduction on discharge and oxidation on charge. XANES spectroscopy also shows a change in Mn oxidation state on cycling, though the shift in energy is not as large as would be expected. There have been previous suggestions that Mn containing polyanions may undergo oxygen redox chemistry which would account for the lack of shift in the Mn K-edge.

Cycling at higher rates (2C) reduces the initial capacity, though 97.4 mAh g^{-1} is still achieved. Extended high rate cycling results in a gradual increase in capacity until near full theoretical capacity is achieved, with reversible cycling of 1.82 Li^+ ions per unit cell (314 mAh g^{-1}) after 1000 cycles. The increase in capacity could be caused by mechanical grinding improving diffusion into the material, but as full Mg^{2+} capacity was achieved this seems unlikely. It is more likely that structural rearrangements or amorphisation to accommodate the increased number of ions is occurring.

Full Li^+ capacity is achieved at C/25 by reducing the voltage to below 1.5 V, with 344 mAh g^{-1} achieved by 0.88 V. This suggests that although full replacement of 1 Mg^+ with 2 Li^+ is possible there is a barrier to insertion, likely a structural one with electrostatic repulsion between neighbouring Li^+ hindering further insertion.

After removal of 0.51 Mg from the x = 4/3 material (161.4 mAh g^{-1}, 78% of the theoretical capacity) 0.75 Li can be inserted in a Li-ion cell (130.0 mAh g^{-1}) above 1.5 V at a rate of C/25, increasing to 0.83 Li^+ (145 mAh g^{-1}) after 10 cycles. Therefore, for each Mg^{2+} removed, 1.6 Li^+ are inserted. By cycling at the slower rate of C/100 the Li^+ insertion capacity is improved to 1.1 Li^+ (94.8 mAh g^{-1}, 84% of theoretical) meaning a 2:1 replacement of Li^+ for Mg^{2+} in the structure. The electrochemical processes occur with the same voltage profile and features as observed in the x = 1 material.

The lower Mg content x = 2/3 material displays a far lower reversible capacity with just 17.6 mAh g^{-1} after 10 cycles at a rate of C/50, just 9.4% of the theoretical capacity. The low capacity is explained by the large overpotential to Mg^{2+} removal observed in the GITT experiments (>1 V) meaning ion diffusion is severely hindered. However, a 2:1 replacement of Li^+ for Mg^{2+} is still observed suggesting that if the overpotential could be reduced, greater Li-ion capacity could be achieved.

7.2.2 $Mg_xFe_{2-x}B_2O_5$

In the *M* = Fe phases the stabilisation of Fe^{2+} proved challenging, leading to only the $x = 2/3$ material being synthesised as a phase pure sample. With the $x = 1$ and $x = 2/3$ samples having significant fractions of Fe^{3+} borate impurities.

Charging the $x = 2/3$ material vs. Li results in the removal of 0.5 Mg^{2+} from the cell (134.0 mAh g^{-1}, 76% of theoretical) over two plateaus at 3.7 V and 4.0 V attributed to removal from the two distinct *M* sites for the $Fe^{2+/3+}$ redox couple. Up to 0.26 Li^+ are inserted (39.4 mAh g^{-1}, ~19.6% of theoretical) on discharge, with 50% of the capacity achieved between 3.2 V and 3.0 V. This is a higher discharge voltage than observed in the $LiFeBO_3$ system,[46] supporting the prediction that pyroborates may give higher voltages than other borate polyanions.[29]

Cycling at the increased temperature of 55 °C results in an increase in Li insertion capacities with 0.46 Li^+ inserted on first discharge (~70 mAh g^{-1}, 34.5% of theoretical capacity). The capacity then quickly increases with further cycling until full theoretical capacity is reached after 13 cycles. The capacity of 204.4 mAh g^{-1} equates to reversible Li^+ cycling between $Li_{4/3}Fe^{2+}_{4/3}B_2O_5$ and $Fe^{3+}_{4/3}B_2O_5$. Only around 50 mAh g^{-1} of this capacity occurs over the 3.2 V plateau observed at room temperature, with the majority achieved over a sloping profile down to 1.5 V, with a feature at ~2.0 V. Despite the difficulty synthesising pure phases, the *M* = Fe system provides promising electrochemical performance.

7.2.3 $Mg_xCo_{2-x}B_2O_5$

When *M* = Co the three phases, $x = 2/3$, 1 and 4/3 are again stable and have a linear change in volume, indicating the formation of a solid solution. In contrast to the *M* = Mn system cation ordering is not observed, this is thought to be due to the similarity in ionic radii of Mg^{2+} and Co^{2+}.

Cycling of the $x = 2/3$ and $x = 1$ vs. Li at room temperature at a rate of C/25 results in low Mg removal capacities (<20 mAh g^{-1}), however two clear, high voltage, plateaus are observed at 3.9 V and 4.35 V associated with Mg removal from the two distinct *M* sites in the pyroborate. By cycling at increased temperatures (55 °C) capacities were improved to 93.7 mAh g^{-1} for the $x = 2/3$ material (52% of theoretical capacity, 0.34 Mg^{2+}) with plateaus observed at 3.25 V and 4.2 V. An initial Li insertion capacity of 43.8 mAh g^{-1} was observed (0.27 Li ions 20% of theoretical capacity) meaning that less than 1 Li replaces each Mg removed. However, on extended cycling to >100 cycles the capacity gradually increases to 264.4 mAh g^{-1} which equates to reversible insertion of 1.5 Li and approaches the replacement of 2 Li for each Mg

removed. As with the Mn system the increase in capacity may be due to structural rearrangements to accommodate the chemically different, and more numerous Li^+ ions.

High temperatures are also required for significant Li-ion capacity to be achieved in the $x = 1$ phase, with 61.8 mAh g^{-1} achieved at 55 °C (0.21 Mg^{2+}, 21% of theoretical with plateaus at 3.3 V and 4.5 V on first charge). As with the $x = 2/3$ there is a significant barrier to Li insertion with less than 14 mAh g^{-1} (0.04 Li^+) achieved.

The low capacity of the Co system compared to the Mn and Fe materials is similar to that observed in the Li*M*BO_3 system, where the higher voltage redox couple and low electrical conductivity of the Co materials hinders electrochemical reactions. These issues were mitigated by a combination of nanoparticle synthesis and formation of mixed transition metal phases.

7.2.4 $Mg_xNi_{2-x}B_2O_5$

The presence of Ni in polyanion cathode systems is limited, with no previous description of $Ni_2B_2O_5$ or $NiBO_3$. To assess the use of this high voltage redox ion in the pyroborates, $MgNiB_2O_5$ was synthesised and PXRD analysis showed that it crystallises in the same triclinic structure as previous examples. Partial cation ordering is observed driven by the small Ni^{2+} cation preferring the smaller *M*2 site.

On first charge in a Li-ion cell a capacity of 10.6 mAh g^{-1} is achieved (0.07 Mg^{2+}, 7% of theoretical) over a high voltage plateau corresponding to Mg removal at 4.15 V. The plateau does not contain any other features, unlike in Mn and Co systems, suggesting Mg is only being removed from one site. The subsequent Li^+ insertion capacity is 6.4 mAh g^{-1} or 0.04 Li^+ meaning only ~ ½ the number of Li^+ replace the removed Mg^{2+}. The capacity that is achieved, occurs with a plateau at 2.6 V. By increasing the cycling temperature to 55 °C both the Mg removal (29.3 mAh g^{-1}, 0.1 Mg^{2+}) and Li insertion (13 mAh g^{-1}, 0.08 Li^+) capacities are improved, indicating that the reversible storage of ions is possible, but there is a kinetic barrier to diffusion. The charging plateau occurs at a significantly lower voltage in the higher temperature cell, ~3.3 V rather than 4.15 V, and a second process appears to form approaching 4.5 V. As with the low temperature cells, a large amount of the capacity occurs during the 2.6 V process. Subsequent Li charging is not fully reversible and the capacity appears to match that achieved over the 2.6 V process only, suggesting either that the excess capacity on discharge is due to an irreversible reaction, or that the charging voltage is not high enough to reverse the reaction.

7.2.5 Mg-ion batteries

The electrochemical results in Li-ion cells demonstrate the Mg is mobile in these structures, this contrasts with other Mg containing Li cathodes such as Mg-doped $LiFePO_4$ and $LiCoO_2$ where it is presumed the Mg is structural only.[185,186] The labile nature of Mg makes these materials of interest for Mg-ion batteries, and as $MgMnB_2O_5$ was shown to retain its structure even on removal of all the Mg, this material was chosen for further investigation.

One of the main barriers to Mg-ion cells is currently the electrolyte, with electrolytes that support facile Mg deposition having narrow electrolyte windows, and those with larger windows having lower efficiency Mg stripping, as well as plating and corrosion issues. Therefore, a number of electrolyte systems were tested to demonstrate how they act in the 2-electrode coin cell and 3-electrode flooded cell, at the voltage at which electrolyte breakdown is expected.

The Grignard based electrolytes were not used for testing the cathode material as their electrolyte stability window is not large enough. $Mg(ClO_4)_2$ in ACN has a large stability window but Mg stripping and plating occurs with a large overpotential. $Mg(TFSI)_2$ in ACN/THF showed a good combination of relatively high stability (~3.5 V vs. Mg) and reversible Mg stripping and plating. The new electrolyte $Mg(PF_6)_2$ in ACN synthesised in the Wright group was shown to support reversible Mg stripping and plating in both a 3-elcetrode and 2-electrode cell, and reversible intercalation into the Chevrel phase when Al coin cell components were used.

In a 2-electrode coin cell using a Mg metal anode and $Mg(TFSI)_2$ in ACN/THF electrolyte reversible capacities of up to 138.6 mAh g^{-1} (0.47 Mg^{2+}) were achieved, with a feature in the voltage profile ~3.3 V. This is consistent with the Li chemistry where most of the capacity was achieved above 4.0 V vs. Li, which is ~3.3 V vs. Mg. On continued cycling the profile smooths out, as was observed in the Li-ion cells. There is significant excess capacity on charge associated with electrolyte breakdown, however as the discharge capacities are relatively stable it is thought at least some of this capacity is the desired electrochemical reaction.

By cycling in a 3-electrode flooded cell it was shown that a reversible process occurs above 2.6 V vs. Mg, and on extended cycling multiple reversible processes become apparent between 1.5 V and 3.0 V vs. Mg. As with the 2-electrode cell significant electrolyte breakdown at high voltages is observed.

The assertion that reversible Mg intercalation is occurring is supported by PXRD which shows a decrease in unit cell volume on charge. The change is ~½ that observed on charge vs. Li which

is consistent with the electrochemistry where ~½ the capacity is achieved. SQUID magnetometry also shows a change in Mn oxidation state consistent with redox reactions occurring to balance the removal or insertion of Mg.

These results show that despite electrolyte stability issues, the pyroborate $MgMnB_2O_5$ supports reversible, high capacity cycling in a full Mg-ion cell. The use of polyanion structures where Li can replace labile Mg, without disrupting crystal structure, opens up a new avenue for novel Li-ion cathode materials with high energy densities.

7.3 Summary

This study shows that the pyroborates and orthoborates are promising families of materials for Li- and Mg-ion cathodes, with the light weight structure leading to high specific capacities. In the pyroborates each Mg^{2+} removed can be replaced by 2 Li^+, demonstrating the unusual property of reversible 2-electron cycling. Full theoretical capacities for Li^+ cycling are achieved in the Mn, Fe and Co pyroborate systems. In the orthoborates each Mg^{2+} removed is replaced by up to 1 Li^+, with insertion perhaps hindered by the number of available crystallographic sites. The amount of Mg^{2+} removed is strongly related to the amount of Mg occupying site *M*1, therefore optimisation of stoichiometries and cation ordering could lead to improvements in performance. A summary of the materials discussed in the thesis and their structure, cycling parameters and theoretical and achieved capacities are given in Appendix Table A7-1. The demonstration of two new classes of cathode material opens the door to further understanding and optimisation of these materials for both Li- and Mg-ion batteries. The voltage and capacity of these materials could be optimised by synthesising mixed transition metal borates, while the Mg-ion chemistry could be improved by formation of nanocomposites with carbon and improved understanding of the electrolyte interactions.

The ability to replace Mg for Li in polyanion materials without disrupting the crystal structure opens a new way to search for novel, high energy density, Li-ion cathodes, creating interest into other Mg containing borate structures, some of which are outlined in Table A7-2. It also demonstrates that Mg can be mobile in polyanions, therefore investigation of other Mg containing polyanions, such as phosphates or sulphates, for Mg-ion batteries could prove fruitful.

7.4 Appendix

Table A7-1. Summary of the electrochemistry carried out in this thesis on the ortho and pyroborates in Li- and Mg-ion cells. Δ indicates trigonal planar BO_3 units with the subscript denoting how many oxygens are shared with other units.

Material (Redox couple)	**Borate connectivity**	**Theoretical capacity for Mg^{2+} removal / mAh g^{-1} (compound formed on full charge)**	**Achieved Mg^{2+} capacity / mAh g^{-1} (no. of Mg^{2+})**	**Theoretical capacity for Li+ insertion / mAh g^{-1} (compound formed on full discharge)**	**Achieved Li^{+} capacity / mAh g^{-1} (no. of Li^{2+})**	**Cycling parameters**	**Notes**
$MgMn_2(BO_3)_2$ (2+/3+)	Δ_0	212.87 ($Mn_2(BO_3)_2$)	44.5 (0.20)	235.6 ($Li_2Mn_2(BO_3)_2$)	26.1 (0.22)	Li anode, 4.6 to 1.5 V, 55 °C, C/25	~1:1 replacement of Mg^{2+} for Li.
$Mg_2Mn(BO_3)_2$ (2+/4+)	Δ_0	242.3 ($MgMn(BO_3)_2$)	209.9 (0.86)	272.3 ($Li_2MgMn(BO_3)_2$)	83.5 (0.6)	Li anode, 4.6 to 1.5 V, 55 °C, C/25	2 Plateaus associated with 2 electron process.
$Mg_2Co(BO_3)_2$ (2+/4+)	Δ_0	238.1 ($MgCo(BO_3)_2$)	34.7 (0.15)	266.9 ($Li_2MgCo(BO_3)_2$)	25.0 (0.19)	Li anode, 4.6 to 1.5 V, 55 °C, C/25	Little difference between 25 °C and 55 °C.
$MgMnB_2O_5$ (2+/4+)	Δ_1	296.6 (MnB_2O_5)	330 (1.1)	342.5 ($Li_2MnB_2O_5$)	240 (1.4)	Li anode, 4.6 to 1.5 V, 25 °C, C/25	Full Li capacity achieved after extended cycling at high rates.
$Mg_{2/3}Mn_{4/3}B_2O_5$ (2+/3+)	Δ_1	187.3 ($Mn_{4/3}B_2O_5$)	13.7 (0.05)	204.1 ($Li_{4/3}Mn_{4/3}B_2O_5$)	17.6 (0.11)	Li anode, 4.6 to 1.5 V, 25 °C, C/25	>1 V overpotential.

$Mg_{4/3}Mn_{2/3}B_2O_5$ (2+/4+)	Δ_1	207.9 ($Mg_{2/3}Mn_{2/3}B_2O_5$)	169.3 (0.54)	231.6 ($Li_{4/3}Mg_{2/3}Mn_{2/3}B_2O_5$)	194.8 (1.1)	Li anode, 4.6 to 1.5 V, 25 °C, C/25	
$Mg_{2/3}Co_{4/3}B_2O_5$ (2+/3+)	Δ_1	180.45 ($Co_{4/3}B_2O_5$)	93.7 (0.34)	207.5 ($Li_{4/3}Co_{4/3}B_2O_5$)	43.8 (0.21)	Li anode, 4.6 to 1.5 V, 55 °C, C/25	Extended cycling leads 264.4 mAh g^{-1}, which is greater than theoretical capacity.
$MgCoB_2O_5$ (2+/4+)	Δ_1	289.9 (CoB_2O_5)	61.8 (0.21)	333.8 ($Li_2CoB_2O_5$)	13.2 (0.04)	Li anode, 4.6 to 1.5 V, 55 °C, C/100	Capacity fades on extended cycling.
$MgNiB_2O_5$ (2+/4+)	Δ_1	290.3 (NiB_2O_5)	29.3 (0.1)	334.3 ($Li_2NiB_2O_5$)	13.0 (0.08)	Li anode, 4.6 to 1.5 V, 55 °C, C/25	2 clear plateaus but limited capacity.
$Mg_{2/3}Fe_{4/3}B_2O_5$ (2+/3+)	Δ_1	180.3 ($Fe_{4/3}B_2O_5$)	134.0 (0.5)	201.3 ($Li_{4/3}Fe_{4/3}B_2O_5$)	205.2 (1.33)	Li anode, 4.6 to 1.5 V, 55 °C, C/25	Full capacity reached after 16 cycles. Initial discharge capacity ~70 mAh g^{-1}.
$MgFeB_2O_5$ (2+/4+)	Δ_1	294.9 (FeB_2O_5)	10.0 (0.03)	340.4 ($Li_2FeB_2O_5$)	<5 (0.015)	Li anode, 4.6 to 1.5 V, 55 °C, C/25	Fe^{3+} borate impurities
$MgMnB_2O_5$ (2+/4+)	Δ_1	296.6 (MnB_2O_5)	138.6 (0.47)	n/a	n/a	**Mg anode,** 3.5 V to 0.1 V, C/25	Excess capacity on charge, but cycling of ~0.5 Mg^{2+} is reversible for 10's of cycles.

Table A7-2. A selection of other borate structures, their connectivity and theoretical Mg removal capacities. Δ indicates trigonal planar BO_3 units and $\square$ BO_4 tetrahedra, with the subscript denoting how many oxygens are shared with other units.

Structure	**Connectivity**	**Examples (theoretical capacity / mAh g^{-1})**
$M_2^{2+}BO_4$	Δ_0	$MgFeBO_4 \rightarrow FeBO_4$ (147.4)
$M_3^{2+/3+}BO_5$	Δ_0	$MgFe_2BO_5 \rightarrow Fe_2BO_5$ (118.2) $Mg_2FeBO_5 \rightarrow Mg1.5FeBO_5$ (68.6)
$M^{2+}B_4O_7$	$\square_4$	$M_{0.5}Fe_{0.5}B_4O_7 \rightarrow Fe_{0.5}B_4O_7$ (68.5)
$M^{2+}B_2O_4$	$\square_4$	$M_{0.5}Fe_{0.5}B_2O_8 \rightarrow Fe_{0.5}B_2O_8$ (106.1)
$M^{1+}BO_2$	$\Delta_2\square_4$	$Mg_{0.5}Cu_{0.5}BO_2 \rightarrow Cu_{0.5}BO_2$ (154.6)

Chapter 8. References

(1) Dunn, B.; Kamath, H.; Tarascon, J.-M. Electrical Energy Storage for the Grid: A Battery of Choices. *Science* **2011**, *334* (6058), 928–935.

(2) Pieper, H. Mixed Drive For Autovehicles, 1909.

(3) Thielman, A.; Sauer, A.; Isenmann, R.; Wietschel, M. Technology Roadmap Energy Storage for Electric Mobility 2030. *Fraunhofer ISI* **2013**.

(4) International-Energy-Agency. *Global EV Outlook 2016*; Paris, 2016.

(5) Armand, M.; Tarascon, J.-M. Building Better Batteries. *Nature* **2008**, *451* (7179), 652–657.

(6) Goodenough, J. B.; Kim, Y. Challenges for Rechargeable Li Batteries. *Chem. Mater.* **2010**, *22* (3), 587–603.

(7) Nagaura, T.; Tozawa, K. Lithium Ion Rechargeable Battery. *Prog. Batter. Sol. Cells* **1990**, *9*, 209–217.

(8) Goodenough, J. B. Changing Outlook for Rechargeable Batteries. *ACS Catal.* **2017**, *7*, 1132–1135.

(9) Huggins, A. R. *Advanced Batteries: Material Science Aspects*; Springer: New York, 2009.

(10) Porter, D. A.; Easterling, K. E.; Sherif, M. Y. *Phase Transformations in Metals and Alloys.*; CRC Press, 2009.

(11) Aurbach, D.; Levi, M. D.; Levi, E. A Review on the Solid-State Ionics of Electrochemical Intercalation Processes: How to Interpret Properly Their Electrochemical Response. *Solid State Ionics* **2008**, *179* (21–26), 742–751.

(12) Brandt, K. Historical Development of Secondary Lithium Batteries. *Solid State Ionics* **1994**, *69*, 173–183.

(13) Ohzuku, T.; Ueda, A. Why Transition Metal (Di)Oxides Are the Most Attractive Materials for Batteries. *Solid State Ionics* **1994**, *69*, 201–211.

(14) Whittingham, M. S. Lithium Batteries and Cathode Materials. *Chem. Rev.* **2004**, *104* (10), 4271–4301.

(15) The Committee on Climate Change. *Cost and Performance of EV Batteries*; Element

Energy Limited, 2012.

(16) Doeff, M. M. *Encyclopedia of Sustainability Science and Technology - Battery Cathodes*; Meyers, R. A., Ed.; Springer New York: New York, NY, 2012.

(17) Thackeray, M.; David, W.; Bruce, P. G.; Goodenough, J. B. Lithium Insertion into Manganese Spinels. *Mater. Res. Bull.* **1983**, *18* (4), 461–472.

(18) Goodenough, J. B.; Park, K.-S. The Li-Ion Rechargeable Battery: A Perspective. *J. Am. Chem. Soc.* **2013**, *135* (4), 1167–1176.

(19) Reddy, M. V.; Raju, M. J. S.; Sharma, N.; Quan, P. Y.; Nowshad, S. H.; Emmanuel, H. E.-C.; Peterson, V. K.; Chowdari, B. V. R. Preparation of $Li_{1.03}Mn_{1.97}O_4$ and $Li_{1.06}Mn_{1.94}O_4$ by the Polymer Precursor Method and X-Ray, Neutron Diffraction and Electrochemical Studies. *J. Electrochem. Soc.* **2011**, *158* (11), A1231.

(20) Yamada, A.; Tanaka, M. Jahn-Teller Structural Phase Transition around 280K in LiMn2O4. *Mater. Res. Bull.* **1995**, *30* (6), 715–721.

(21) Hunter, J. C. Preparation of a New Crystal Form of Manganese Dioxide: λ-MnO_2. *J. Solid State Chem.* **1981**, *39* (2), 142–147.

(22) Padhi, A. K.; Nanjundaswamy, K. S.; Goodenough, J. B. Phospho-Olivines as Positive-Electrode Materials for Rechargeable Lithium Batteries. *J. Electrochem. Soc.* **1997**, *144* (4), 1188–1194.

(23) Yamada, A.; Hosoya, M.; Chung, S. C.; Kudo, Y.; Hinokuma, K.; Liu, K. Y.; Nishi, Y. Olivine-Type Cathodes: Achievements and Problems. *J. Power Sources* **2003**, *119–121*, 232–238.

(24) Li, G.; Azuma, H.; Tohda, M. $LiMnPO_4$ as the Cathode for Lithium Batteries. *Electrochem. Solid-State Lett.* **2002**, *5* (6), A135–A137.

(25) Chung, S.-Y.; Bloking, J. T.; Chiang, Y.-M. Electronically Conductive Phospho-Olivines as Lithium Storage Electrodes. *Nat. Mater.* **2002**, *1* (2), 123–128.

(26) Morgan, D.; Van der Ven, A.; Ceder, G. Li Conductivity in Li_xMPO_4 (M = Mn, Fe, Co, Ni) Olivine Materials. *Electrochem. Solid-State Lett.* **2004**, *7* (2), A30–A32.

(27) Thackeray, M. M.; David, W. I. F.; Goodenough, J. B. Structural Characterization of the Lithiated Iron Oxides $Li_xFe_3O_4$ and $Li_xFe_2O_3$ ($0<x<2$). *Mater. Res. Bull.* **1982**, *17* (6), 785–793.

(28) Gutierrez, A.; Benedek, N. A.; Manthiram, A. Crystal-Chemical Guide for Understanding Redox Energy Variations of $M^{2+/3+}$ Couples in Polyanion Cathodes for Lithium-Ion Batteries. *Chem. Mater.* **2013**, *25* (20), 4010–4016.

(29) Jain, A.; Hautier, G.; Ong, S. P.; Dacek, S.; Ceder, G. Relating Voltage and Thermal Safety in Li-Ion Battery Cathodes: A High-Throughput Computational Study. *Phys. Chem. Chem. Phys.* **2015**, *17* (8), 5942–5953.

(30) Mori, T.; Masese, T. N.; Okado, T.; Yamamoto, K.; Huang, Z.; Kim, J.; Orikasa, Y.; Minato, T.; Uchimoto, Y. Anti-Site Mixing Governs Electrochemical Performances of Olivine Type $MgMnSiO_4$ for Magnesium Ion Battery Cathode. **2010**, 4123.

(31) Kang, B.; Ceder, G. Battery Materials for Ultrafast Charging and Discharging. *Nature* **2009**, *458*, 190–193.

(32) Perea, A.; Belanger, D.; Zaghib, K.; Delaporte, N.; Amin, R. Chemical Grafted Carbon-Coated $LiFePO_4$ Olivine Using Diazonium Chemistry. **2011**, 5884.

(33) Amine, K.; Yasuda, H.; Yamachi, M. Olivine $LiCoPO_4$ as 4.8 V Electrode Material for Lithium Batteries. *Electrochem. Solid-State Lett.* **1999**, *3* (4), 178.

(34) Zhou, F.; Cococcioni, M.; Kang, K.; Ceder, G. The Li Intercalation Potential of Li*M*PO_4 and Li*M*SiO_4 Olivines with *M* = Fe, Mn, Co, Ni. *Electrochem. commun.* **2004**, *6* (11), 1144–1148.

(35) Yang, S. M. G.; Aravindan, V.; Cho, W. I.; Chang, D. R.; Kim, H. S.; Lee, Y. S. Realizing the Performance of $LiCoPO_4$ Cathodes by Fe Substitution with Off-Stoichiometry. *J. Electrochem. Soc.* **2012**, *159* (7), A1013–A1018.

(36) Yang, Z.; Yu, H.; Wu, C.; Cao, G.; Xie, J.; Zhao, X. Preparation of Nano-Structured $LiFe_xMn_{1-x}PO_4$ (x=0, 0.2, 0.4) by Reflux Method and Research on the Influences of Fe(II) Substitution. *J. Mater. Sci. Technol.* **2012**, *28* (9), 823–827.

(37) Roberts, M. R.; Vitins, G.; Owen, J. R. High-Throughput Studies of $Li_{1-x}Mg_{x/2}FePO_4$ and $LiFe_{1-y}Mg_yPO_4$ and the Effect of Carbon Coating. *J. Power Sources* **2008**, *179* (2), 754–762.

(38) Wen, B.; Liu, J.; Chernova, N. A.; Wang, X.; Janssen, Y.; Omenya, F.; Khalifah, P. G.; Whittingham, M. S. $Li_3Mo_4P_5O_{24}$: A Two-Electron Cathode for Lithium-Ion Batteries with Three-Dimensional Diffusion Pathways. *Chem. Mater.* **2016**, *28* (7), 2229–2235.

(39) Yamada, A.; Nishimura, S. New Lithium Iron Pyrophosphate $Li_2FeP_2O_7$ as 3.5 V Class

Cathode Material for Lithium-Ion Battery. *JACS Commun.* **2010**, *132*, 13596–13597.

(40) Chen, H.; Hao, Q.; Zivkovic, O.; Hautier, G.; Du, L. S.; Tang, Y.; Hu, Y. Y.; Ma, X.; Grey, C. P.; Ceder, G. Sidorenkite ($Na_3MnPO_4CO_3$): A New Intercalation Cathode Material for Na-Ion Batteries. *Chem. Mater.* **2013**, *25* (14), 2777–2786.

(41) Kraytsberg, A.; Ein-Eli, Y. Higher, Stronger, Better. A Review of 5 Volt Cathode Materials for Advanced Lithium-Ion Batteries. *Adv. Energy Mater.* **2012**, *2* (8), 922–939.

(42) Nitta, N.; Wu, F.; Lee, J. T.; Yushin, G. Li-Ion Battery Materials: Present and Future. *Mater. Today* **2015**, *18* (5), 252–264.

(43) Barpanda, P.; Yamashita, Y.; Yamada, Y.; Yamada, A. High-Throughput Solution Combustion Synthesis of High-Capacity $LiFeBO_3$ Cathode. *J. Electrochem. Soc.* **2013**, *160* (5), A3095–A3099.

(44) Legagneur, V.; An, Y.; Mosbah, A. $LiMBO_3$(M= Mn, Fe, Co): Synthesis, Crystal Structure and Lithium Deinsertion/insertion Properties. *Solid State Ionics* **2001**, *139*, 37–46.

(45) Dong, Y. Z.; Zhao, Y. M.; Shi, Z. D.; An, X. N.; Fu, P.; Chen, L. The Structure and Electrochemical Performance of $LiFeBO_3$ as a Novel Li-Battery Cathode Material. *Electrochim. Acta* **2008**, *53* (5), 2339–2345.

(46) Bo, S.-H.; Wang, F.; Janssen, Y.; Zeng, D.; Nam, K.-W.; Xu, W.; Du, L.-S.; Graetz, J.; Yang, X.-Q.; Zhu, Y.; Parise, J. B.; Grey, C. P.; Khalifah, P. G. Degradation and (De)lithiation Processes in the High Capacity Battery Material $LiFeBO_3$. *J. Mater. Chem.* **2012**, *22* (18), 8799–8809.

(47) Afyon, S.; Kundu, D.; Krumeich, F.; Nesper, R. Nano $LiMnBO_3$, a High-Capacity Cathode Material for Li-Ion Batteries. *J. Power Sources* **2013**, *224*, 145–151.

(48) Le Roux, B.; Bourbon, C.; Lebedev, O. I.; Colin, J. F.; Pralong, V. Synthesis and Characterization of the $LiMnBO_3$-$LiCoBO_3$ Solid Solution and Its Use as a Lithium-Ion Cathode Material. *Inorg Chem* **2015**, *54* (11), 5273–5279.

(49) Nazri, G.; Pistoia, G. *Lithium Batteries: Science and Technology*; Springer US, 2003.

(50) Pinson, M. B.; Bazant, M. Z. Theory of SEI Formation in Rechargeable Batteries: Capacity Fade, Accelerated Aging and Lifetime Prediction. *J. Electrochem. Soc.* **2012**, *160* (2), A243–A250.

(51) Berg, E. J.; Villevieille, C.; Streich, D.; Trabesinger, S.; Novák, P. Rechargeable Batteries: Grasping for the Limits of Chemistry. *J. Electrochem. Soc.* **2015**, *162* (14), A2468–A2475.

(52) Li, W.; Zheng, G.; Yang, Y.; Seh, Z. W.; Liu, N.; Cui, Y. High-Performance Hollow Sulfur Nanostructured Battery Cathode through a Scalable, Room Temperature, One-Step, Bottom-up Approach. *Proc. Natl. Acad. Sci. U. S. A.* **2013**, *110* (18), 7148–7153.

(53) Jayaprakash, N.; Shen, J.; Moganty, S. S.; Corona, A.; Archer, L. A. Porous Hollow Carbon@sulfur Composites for High-Power Lithium-Sulfur Batteries. *Angew. Chemie - Int. Ed.* **2011**, *50* (26), 5904–5908.

(54) Wu, F.; Kim, H.; Magasinski, A.; Lee, J. T.; Lin, H.-T.; Yushin, G. Harnessing Steric Separation of Freshly Nucleated Li_2S Nanoparticles for Bottom-Up Assembly of High-Performance Cathodes for Lithium-Sulfur and Lithium-Ion Batteries. *Adv. Energy Mater.* **2014**, *4* (11), 1400196.

(55) Aurbach, D.; Pollak, E.; Elazari, R.; Salitra, G.; Kelley, C. S.; Affinito, J. On the Surface Chemical Aspects of Very High Energy Density, Rechargeable Li – Sulfur Batteries. *J. Electrochem. Soc.* **2009**, *156* (8), 694–702.

(56) Michan, A. L.; Divitini, G.; Pell, A. J.; Leskes, M.; Ducati, C.; Grey, C. P. Solid Electrolyte Interphase Growth and Capacity Loss in Silicon Electrodes. *J. Am. Chem. Soc.* **2016**, *138* (25), 7918–7931.

(57) Kamali, A. R.; Fray, D. J. Review on Carbon and Silicon Based Materials as Anode Materials for Lithium Ion Batteries. *J. New Mater. Electrochem. Syst.* **2010**, *13* (2), 147–160.

(58) Ashuri, M.; He, Q.; Shaw, L. L. Silicon as a Potential Anode Material for Li-Ion Batteries: Where Size, Geometry and Structure Matter. *Nanoscale* **2016**, *8* (1), 74–103.

(59) Guo, S.; Sun, Y.; Yi, J.; Zhu, K.; Liu, P.; Zhu, Y.; Zhu, G.; Chen, M.; Ishida, M.; Zhou, H. Understanding Sodium-Ion Diffusion in Layered P2 and P3 Oxides via Experiments and First-Principles Calculations: A Bridge between Crystal Structure and Electrochemical Performance. *NPG Asia Mater.* **2016**, *8* (4), e266.

(60) Clément, R. J.; Bruce, P. G.; Grey, C. P. Review—Manganese-Based P2-Type Transition Metal Oxides as Sodium-Ion Battery Cathode Materials. *J. Electrochem. Soc.* **2015**, *162* (14), A2589–A2604.

(61) Stevens, D. A.; Dahn, J. R. The Mechanisms of Lithium and Sodium Insertion in Carbon Materials. *J. Electrochem. Soc.* **2001**, *148* (8), A803–A811.

(62) Cabana, J.; Monconduit, L.; Larcher, D.; Palacín, M. R. Beyond Intercalation-Based Li-Ion Batteries: The State of the Art and Challenges of Electrode Materials Reacting through Conversion Reactions. *Adv. Mater.* **2010**, *22* (35), E170-92.

(63) Hu, J.; Li, H.; Huang, X. Cr_2O_3-Based Anode Materials for Li-Ion Batteries. *Electrochem. Solid-State Lett.* **2005**, *8* (1), A66.

(64) Hua, X.; Robert, R.; Du, L. S.; Wiaderek, K. M.; Leskes, M.; Chapman, K. W.; Chupas, P. J.; Grey, C. P. Comprehensive Study of the CuF_2 Conversion Reaction Mechanism in a Lithium Ion Battery. *J. Phys. Chem. C* **2014**, *118* (28), 15169–15184.

(65) Parzych, G.; Mikhailova, D.; Oswald, S.; Eckert, J.; Ehrenberg, H. Study of the Conversion Reaction Mechanism for Copper Borate as Electrode Material in Lithium-Ion Batteries. *J. Electrochem. Soc.* **2011**, *158* (8), A898.

(66) Liu, M.; Rong, Z.; Malik, R.; Canepa, P.; Jain, A.; Ceder, G.; Persson, K. A.; Liu, M. Spinel Compounds as Multivalent Battery Cathodes: A Systematic Evaluation Based on Ab Initio Calculations. *Energy Environ. Sci* **2015**, *8* (3), 964–974.

(67) Guduru, R.; Icaza, J. A Brief Review on Multivalent Intercalation Batteries with Aqueous Electrolytes. *Nanomaterials* **2016**, *6* (3), 41.

(68) Gregory, T.; Hoffman, R.; Winterton, R. Nonaqueous Electrochemistry of Magnesium Applications to Energy Storage. *J. Electrochem. Soc.* **1990**, *137* (3), 775–780.

(69) Aurbach, D.; Lu, Z.; Schechter, A.; Gofer, Y.; Gizbar, H.; Turgeman, R.; Cohen, Y.; Moshkovich, M.; Levi, E. Prototype Systems for Rechargeable Magnesium Batteries. *Nature* **2000**, *407* (6805), 724–727.

(70) Muldoon, J.; Bucur, C. B.; Gregory, T. Quest for Nonaqueous Multivalent Secondary Batteries: Magnesium and Beyond. *Chem. Rev.* **2014**, *114* (23), 11683–11720.

(71) Brown, I. D. What Factors Determine Cation Coordination Numbers? *Acta Crystallogr. Sect. B* **1988**, *44* (6), 545–553.

(72) Rong, Z.; Malik, R.; Canepa, P.; Sai Gautam, G.; Liu, M.; Jain, A.; Persson, K.; Ceder, G. Materials Design Rules for Multivalent Ion Mobility in Intercalation Structures. *Chem. Mater.* **2015**, *27* (17), 6016–6021.

(73) Gummow, R.; Sharma, N.; Peterson, V.; He, Y. Synthesis, Structure, and Electrochemical Performance of Magnesium-Substituted Lithium Manganese Orthosilicate Cathode Materials for Lithium-Ion Batteries. *J. Power Sources* **2012**, *197*, 231–237.

(74) Muldoon, J.; Bucur, C. B.; Oliver, A. G.; Sugimoto, T.; Matsui, M.; Kim, H. S.; Allred, G. D.; Zajicek, J.; Kotani, Y. Electrolyte Roadblocks to a Magnesium Rechargeable Battery. *Energy Environ. Sci.* **2012**, *5* (3), 5941.

(75) Bucur, C. B.; Gregory, T.; Oliver, A. G.; Muldoon, J. Confession of a Magnesium Battery. *J. Phys. Chem. Lett.* **2015**, *6* (18), 3578–3591.

(76) Levi, E.; Mitelman, a; Isnard, O.; Brunelli, M.; Aurbach, D. Phase Diagram of Mg Insertion into Chevrel Phases, $Mg_xMo_6T_8$ (T = S, Se). 3. The Crystal Structure of Triclinic $Mg_2Mo_6Se_8$. *Inorg. Chem.* **2008**, *47* (6), 1975–1983.

(77) Aurbach, D.; Suresh, G. S.; Levi, E.; Mitelman, A.; Mizrahi, O.; Chusid, O.; Brunelli, M. Progress in Rechargeable Magnesium Battery Technology. *Adv. Mater.* **2007**, *19* (23), 4260–4267.

(78) Gershinsky, G.; Yoo, H. D.; Gofer, Y.; Aurbach, D. Electrochemical and Spectroscopic Analysis of Mg(2+) Intercalation into Thin Film Electrodes of Layered Oxides: V_2O_5 and MoO_3. *Langmuir* **2013**, *29* (34), 10964–10972.

(79) Ramadoss, A.; Kim, S. J. Enhanced Supercapacitor Performance of Graphene/V_2O_5 Nanocomposites. **2013**, *230*, 2013.

(80) Wang, Z.; Su, Q.; Deng, H. Single-Layered V_2O_5 a Promising Cathode Material for Rechargeable Li and Mg Ion Batteries: An Ab Initio Study. *Phys. Chem. Chem. Phys.* **2013**, *15* (22), 8705–8709.

(81) Sa, N.; Wang, H.; Proffit, D. L.; Lipson, A. L.; Key, B.; Liu, M.; Feng, Z.; Fister, T. T.; Ren, Y.; Sun, C. J.; Vaughey, J. T.; Fenter, P. A.; Persson, K. A.; Burrell, A. K. Is Alpha-V_2O_5 a Cathode Material for Mg Insertion Batteries? *J. Power Sources* **2016**, *323*, 44–50.

(82) Novák, P.; Desilvestro, J. Electrochemical Insertion of Magnesium in Metal Oxides and Sulfides from Aprotic Electrolytes. *J. Electrochem. Soc.* **1993**, *140* (1), 140–144.

(83) Canepa, P.; Sai Gautam, G.; Hannah, D. C.; Malik, R.; Liu, M.; Gallagher, K. G.; Persson, K. A.; Ceder, G. Odyssey of Multivalent Cathode Materials: Open Questions

and Future Challenges. *Chem. Rev.* **2017**, acs.chemrev.6b00614.

(84) Lee, S. H.; DiLeo, R. a.; Marschilok, a. C.; Takeuchi, K. J.; Takeuchi, E. S. Sol Gel Based Synthesis and Electrochemistry of Magnesium Vanadium Oxide: A Promising Cathode Material for Secondary Magnesium Ion Batteries. *ECS Electrochem. Lett.* **2014**, *3* (8), A87–A90.

(85) Arthur, T. S.; Kato, K.; Germain, J.; Guo, J.; Glans, P.-A.; Liu, Y.-S.; Holmes, D.; Fan, X.; Mizuno, F. Amorphous V_2O_5–P_2O_5 as High-Voltage Cathodes for Magnesium Batteries. *Chem. Commun.* **2015**, *51* (86), 15657–15660.

(86) Nam, K. W.; Kim, S.; Lee, S.; Salama, M.; Shterenberg, I.; Gofer, Y.; Kim, J.-S.; Yang, E.; Park, C. S.; Kim, J.-S.; Seok-Soo, L.; Chang, W.-S.; Doo, S.-G.; Jo, Y. N.; Jung, Y.; Aurbach, D.; Choi, J. W. The High Performance of Crystal Water Containing Manganese Birnessite Cathodes for Magnesium Batteries. *Nano Lett.* **2015**, *15* (6), 4071–4079.

(87) Yin, J.; Takeuchi, E. S.; Takeuchi, K. J.; Marschilok, A. C. Synthetic Control of Manganese Birnessite: Impact of Crystallite Size on Li, Na, and Mg Based Electrochemistry. *Inorganica Chim. Acta* **2016**, *453*, 230–237.

(88) Sun, X.; Duffort, V.; Mehdi, B. L.; Browning, N. D.; Nazar, L. F. Investigation of the Mechanism of Mg Insertion in Birnessite in Nonaqueous and Aqueous Rechargeable Mg-Ion Batteries. *Chem. Mater.* **2016**, *28* (2), 534–542.

(89) Saha, P.; Datta, M. K.; Velikokhatnyi, O. I.; Manivannan, A.; Alman, D.; Kumta, P. N. Rechargeable Magnesium Battery: Current Status and Key Challenges for the Future. *Prog. Mater. Sci.* **2014**, *66*, 1–86.

(90) Ichitsubo, T.; Adachi, T.; Yagi, S.; Doi, T. Potential Positive Electrodes for High-Voltage Magnesium-Ion Batteries. *J. Mater. Chem.* **2011**, *21* (32), 11764.

(91) Knight, J. C.; Therese, S.; Manthiram, A. On the Utility of Spinel Oxide Hosts for Magnesium-Ion Batteries. *ACS Appl. Mater. Interfaces* **2015**, *7* (41), 22953–22961.

(92) Kim, C.; Phillips, P. J.; Key, B.; Yi, T.; Nordlund, D.; Yu, Y. S.; Bayliss, R. D.; Han, S. D.; He, M.; Zhang, Z.; Burrell, A. K.; Klie, R. F.; Cabana, J. Direct Observation of Reversible Magnesium Ion Intercalation into a Spinel Oxide Host. *Adv. Mater.* **2015**, *27* (22), 3377–3384.

(93) Huang, J.; Poyraz, A. S.; Takeuchi, K. J.; Takeuchi, E. S.; Marschilok, A. C. $M_xMn_8O_{16}$ (M = Ag or K) as Promising Cathode Materials for Secondary Mg Based Batteries: The

Role of the Cation M. *Chem. Commun.* **2016**, *52* (21), 4088–4091.

(94) Li, Y.; Nuli, Y.; Yang, J.; Yilinuer, T.; Wang, J. $MgFeSiO_4$ Prepared via a Molten Salt Method as a New Cathode Material for Rechargeable Magnesium Batteries. *Chinese Sci. Bull.* **2011**, *56* (4–5), 386–390.

(95) Orikasa, Y.; Masese, T.; Koyama, Y.; Mori, T.; Hattori, M.; Yamamoto, K.; Okado, T.; Huang, Z.-D.; Minato, T.; Tassel, C.; Kim, J.; Kobayashi, Y.; Abe, T.; Kageyama, H.; Uchimoto, Y. High Energy Density Rechargeable Magnesium Battery Using Earth-Abundant and Non-Toxic Elements. *Sci. Rep.* **2014**, *4*, 5622.

(96) NuLi, Y.; Zheng, Y.; Wang, Y.; Yang, J.; Wang, J. Electrochemical Intercalation of Mg^{2+} in 3D Hierarchically Porous Magnesium Cobalt Silicate and Its Application as an Advanced Cathode Material in Rechargeable Magnesium Batteries. *J. Mater. Chem.* **2011**, *21* (33), 12437–12443.

(97) Zheng, Y.; Nuli, Y.; Chen, Q.; Wang, Y.; Yang, J.; Wang, J. Magnesium Cobalt Silicate Materials for Reversible Magnesium Ion Storage. *Electrochim. Acta* **2012**, *66*, 75–81.

(98) Bo, S.-H.; Grey, C. P.; Khalifah, P. G. Defect-Tolerant Diffusion Channels for Mg^{2+} Ions in Ribbon-Type Borates: Structural Insights into Potential Battery Cathodes $MgVBO_4$ and $Mg_xFe_{2-x}B_2O_5$. *Chem. Mater.* **2015**, *27* (13), 4630–4639.

(99) Levi, E.; Levi, M. D.; Chasid, O.; Aurbach, D. A Review on the Problems of the Solid State Ions Diffusion in Cathodes for Rechargeable Mg Batteries. *J. Electroceramics* **2009**, *22* (1–3), 13–19.

(100) Amir, N.; Vestfrid, Y.; Chusid, O.; Gofer, Y.; Aurbach, D. Progress in Nonaqueous Magnesium Electrochemistry. *J. Power Sources* **2007**, *174* (2), 1234–1240.

(101) Sun, X.; Bonnick, P.; Duffort, V.; Liu, M.; Ceder, G.; Nazar, L. F. A High Capacity Thiospinel Cathode for Mg Batteries Xiaoqi. *Energy Environ. Sci.* **2016**, *9*, 2273–2277.

(102) Li, X. L.; Li, Y. D. MoS_2 Nanostructures: Synthesis and Electrochemical Mg^{2+} Intercalation. *J. Phys. Chem. B* **2004**, *108* (37), 13893–13900.

(103) Liang, Y.; Yoo, H. D.; Li, Y.; Shuai, J.; Calderon, H. A.; Robles Hernandez, F. C.; Grabow, L. C.; Yao, Y. Interlayer-Expanded Molybdenum Disulfide Nanocomposites for Electrochemical Magnesium Storage. *Nano Lett.* **2015**, *15* (3), 2194–2202.

(104) Gu, Y.; Katsura, Y.; Yoshino, T.; Takagi, H.; Taniguchi, K. Rechargeable Magnesium-Ion Battery Based on a $TiSe_2$-Cathode with D-P Orbital Hybridized Electronic Structure.

Sci. Rep. **2015**, *5* (April), 12486.

(105) Liu, B.; Luo, T.; Mu, G.; Wang, X.; Chen, D.; Shen, G. Rechargeable Mg-Ion Batteries Based on WSe_2 Nanowire Cathodes. *ACS Nano* **2013**, *7* (9), 8051–8058.

(106) Wu, N.; Lyu, Y.-C.; Xiao, R.-J.; Yu, X.; Yin, Y.-X.; Yang, X.-Q.; Li, H.; Gu, L.; Guo, Y.-G. A Highly Reversible, Low-Strain Mg-Ion Insertion Anode Material for Rechargeable Mg-Ion Batteries. *NPG Asia Mater.* **2014**, *6* (8), e120.

(107) Wang, H.; Senguttuvan, P.; Proffit, D. L.; Pan, B.; Liao, C.; Burrell, A. K.; Vaughey, J. T.; Key, B. Formation of MgO during Chemical Magnesiation of Mg-Ion Battery Materials. *ECS Electrochem. Lett.* **2015**, *4* (8), A90–A93.

(108) Feng, Z.; Yang, J.; NuLi, Y.; Wang, J.; Wang, X.; Wang, Z. Preparation and Electrochemical Study of a New Magnesium Intercalation Material Mg1.03Mn0.97SiO4. *Electrochem. commun.* **2008**, *10* (9), 1291–1294.

(109) Zhang, R.; Ling, C. Unveil the Chemistry of Olivine $FePO_4$ as Magnesium Battery Cathode. *ACS Appl. Mater. Interfaces* **2016**, *8* (28), 18018–18026.

(110) Huang, Z.; Masese, T.; Orikasa, Y.; Mori, T.; Minato, T.; Tassel, C.; Kobayashi, Y.; Kageyama, H.; Uchimoto, Y. $MgFePO_4F$ as a Feasible Cathode Material for Magnesium Batteries. *J. Mater. Chem. A* **2014**, *2*, 11578–11582.

(111) Wang, N.; Wang, R.; Peng, C.; Hu, C.; Feng, Y.; Peng, B. Research Progress of Magnesium Anodes and Their Applications in Chemical Power Sources. *Trans. Nonferrous Met. Soc. China* **2014**, *24* (8), 2427–2439.

(112) Singh, N.; Arthur, T. S.; Ling, C.; Matsui, M.; Mizuno, F. A High Energy-Density Tin Anode for Rechargeable Magnesium-Ion Batteries. *Chem. Commun.* **2013**, *49* (2), 149–151.

(113) Liu, Z.; Lee, J.; Xiang, G.; Glass, H. F. J.; Keyzer, E. N.; Dutton, S. E.; Grey, C. P. Insights into the Electrochemical Performances of Bi Anodes for Mg Ion Batteries Using ^{25}Mg Solid State NMR Spectroscopy. *Chem. Commun.* **2017**, *53* (4), 743–746.

(114) Siegal, M. P.; Yelton, W. G.; Perdue, B. R.; Gallis, D. F. S.; Schwarz, H. L. Nanoporous-Carbon as a Potential Host Material for Reversible Mg Ion Intercalation. *J. Electrochem. Soc.* **2016**, *163* (6), A1030–A1035.

(115) Lu, Z.; Schechter, a.; Moshkovich, M.; Aurbach, D. On the Electrochemical Behavior of Magnesium Electrodes in Polar Aprotic Electrolyte Solutions. *J. Electroanal. Chem.*

1999, *466* (2), 203–217.

(116) Benmayza, A.; Ramanathan, M.; Arthur, T. S.; Matsui, M.; Mizuno, F.; Guo, J.; Glans, P. A.; Prakash, J. Effect of Electrolytic Properties of a Magnesium Organohaloaluminate Electrolyte on Magnesium Deposition. *J. Phys. Chem. C* **2013**, *117* (51), 26881–26888.

(117) Doe, R. E.; Han, R.; Hwang, J.; Gmitter, A. J.; Shterenberg, I.; Yoo, H. D.; Pour, N.; Aurbach, D. Novel, Electrolyte Solutions Comprising Fully Inorganic Salts with High Anodic Stability for Rechargeable Magnesium Batteries. *Chem. Commun.* **2014**, *50* (2), 243–245.

(118) Barile, C. J.; Barile, E. C.; Zavadil, K. R.; Nuzzo, R. G.; Gewirth, A. A. Electrolytic Conditioning of a Magnesium Aluminum Chloride Complex for Reversible Magnesium Deposition. *J. Phys. Chem. C* **2014**, *118* (48), 27623–27630.

(119) See, K. A.; Chapman, K. W.; Zhu, L.; Wiaderek, K. M.; Borkiewicz, O. J.; Barile, C. J.; Chupas, P. J.; Gewirth, A. A. The Interplay of Al and Mg Speciation in Advanced Mg Battery Electrolyte Solutions. *J. Am. Chem. Soc.* **2016**, *138* (1), 328–337.

(120) Pan, B.; Huang, J.; Sa, N.; Brombosz, S. M.; Vaughey, J. T.; Zhang, L.; Burrell, A. K.; Zhang, Z.; Liao, C. $MgCl_2$: The Key Ingredient to Improve Chloride Containing Electrolytes for Rechargeable Magnesium-Ion Batteries. *J. Electrochem. Soc.* **2016**, *163* (8), A1672–A1677.

(121) Bertasi, F.; Hettige, C.; Sepehr, F.; Bogle, X.; Pagot, G.; Vezzu, K.; Negro, E.; Paddison, S. J.; Greenbaum, S. G.; Vittadello, M.; Di Noto, V. A Key Concept in Magnesium Secondary Battery Electrolytes. *ChemSusChem* **2015**, *8* (18), 3069–3076.

(122) Tutusaus, O.; Mohtadi, R.; Arthur, T. S.; Mizuno, F.; Nelson, E. G.; Sevryugina, Y. V. An Efficient Halogen-Free Electrolyte for Use in Rechargeable Magnesium Batteries. *Angew. Chemie - Int. Ed.* **2015**, *54* (27), 7900–7904.

(123) Ha, S.; Lee, Y.; Woo, S. W.; Koo, B.; Kim, J.; Cho, J.; Lee, K. T.; Choi, N. Magnesium(II)Bi(TriFluoromethanesulfonyl)Imide-Based Electrolytes with Wide Electrochemical Windows for Rechargeable Magnesium Batteries. *Appl. Mater. Interfaces* **2014**, *6*, 4063–4073.

(124) Segal, D. Chemical Synthesis of Ceramic Materials. *J. Mater. Chem.* **1997**, *7* (8), 1297–1305.

(125) Ring, T. A. *Fundamentals of Ceramic Powder Processing and Synthesis*; *Elsevier*. 1996.

81-83

(126) Smart, L. E.; Moore, E. A. *Solid State Chemistry: An Introduction*; Third, Ed.; Taylor and Francis, 2005.

(127) Harris, K. D. M.; Tremayne, M.; Kariuki, B. M. Contemporary Advances in the Use of Powder X-Ray Diffraction for Structure Determination. *Angew. Chemie* **2001**, *40*, 1626–1651.

(128) Rietveld, H. A Profile Refinement Method for Nuclear and Magnetic Structures. *J. Appl. Crystallogr.* **1969**, *2*, 65–71.

(129) Langford, J. I.; Louer, D. Powder Diffraction. *Reports Prog. Phys.* **1996**, *131* (59), 131–234.

(130) Guicovazzo, C.; Monaco, H. L.; Artioli, G.; Viterbo, D.; Ferraris, G.; Gilli, G.; Zanotti, G.; Catti, M. *Fundamentals of Crystallography*; International Union of Crystallography, 2002.

(131) Institut für Mikro-und Nanomaterialien. *Versuch B : Röntgenbeugung (XRD)*; 2013.

(132) Bragg, W. H.; Bragg, W. L.; James, R. W.; Lipson, H. *The Crystalline State*; The Macmillan Company: New York, 1934; Vol. 1.

(133) Le Bail, A.; Duroy, H.; Fourquet, J. L. Ab-Initio Structure Determination of $LiSbWO_6$ by X-Ray Powder Diffraction. *Mater. Res. Bull.* **1988**, *23* (3), 447–452.

(134) Rodríguez-carvajal. An Introduction to the Program FullProf 2000. *Laboratoire Léon Brillouin* **2001**.

(135) Langford, J. I.; Wilson, A. J. C. Scherrer after Sixty Years: A Survey and Some New Results in the Determination of Crystallite Size. *J. Appl. Crystallogr.* **1978**, *11* (2), 102–113.

(136) Scherrer, P. *Determination of the Size and the Internal Structure of Colloid Particles by X-Ray Radiation*; Springer Berlin Heidelberg, 1912.

(137) Rodríguez-Carvajal, J. Recent Advances in Magnetic Structure Determination by Neutron Powder Diffraction. *Phys. B Condens. Matter* **1993**, *192*, 55–69.

(138) Keyzer, E. N.; Glass, H. F. J.; Liu, Z.; Bayley, P. M.; Dutton, S. E.; Grey, C. P.; Wright, D. S. $Mg(PF_6)_2$-Based Electrolyte Systems: Understanding Electrolyte-Electrode Interactions for the Development of Mg-Ion Batteries. *J. Am. Chem. Soc.* **2016**, *138* (28),

8682–8685.

(139) Grey, C. P.; Dupre, N. NMR Studies of Cathode Materials for Lithium-Ion Rechargeable Batteries. *Chem. Rev.* **2004**, *104* (10), 4493–4512.

(140) Pecher, O.; Carretero-González, J.; Griffith, K. J.; Grey, C. P. Materials Methods : NMR in Battery Research. *Chem. Mater.* **2016**.

(141) Griffith, K. J.; Forse, A. C.; Griffin, J. M.; Grey, C. P. High-Rate Intercalation without Nanostructuring in Metastable Nb_2O_5 Bronze Phases. *J. Am. Chem. Soc.* **2016**, 138, 8888-8899.

(142) Letellier, M.; Chevallier, F.; Clinard, C.; Frackowiak, E.; Rouzaud, J.-N.; Béguin, F.; Morcrette, M.; Tarascon, J.-M. The First in Situ ^{7}Li Nuclear Magnetic Resonance Study of Lithium Insertion in Hard-Carbon Anode Materials for Li-Ion Batteries. *J. Chem. Phys.* **2003**, *118* (13), 6038.

(143) Chang, H. J.; Ilott, A. J.; Trease, N. M.; Mohammadi, M.; Jerschow, A.; Grey, C. P. Correlating Microstructural Lithium Metal Growth with Electrolyte Salt Depletion in Lithium Batteries Using ^{7}Li MRI. *J. Am. Chem. Soc.* **2015**, *137* (48), 15209–15216.

(144) Michan, A. L.; Parimalam, B. S.; Leskes, M.; Kerber, R. N.; Yoon, T.; Grey, C. P.; Lucht, B. L. Fluoroethylene Carbonate and Vinylene Carbonate Reduction: Understanding Lithium-Ion Battery Electrolyte Additives and Solid Electrolyte Interphase Formation. *Chem. Mater.* **2016**, *28* (22), 8149–8159.

(145) Laws, D. D.; Bitter, H.-M. L.; Jerschow, A. Solid-State NMR Spectroscopic Methods in Chemistry. *Angew. Chemie Int. Ed.* **2002**, *41* (17), 3096–3129.

(146) Brown, I. D.; Shannon, R. D. Empirical Bond-Strength-Bond-Length Curves for Oxides. *Acta Crystallogr. Sect. A* **1973**, *29* (3), 266–282.

(147) Brown, I. D.; Altermatt, D. Bond-Valence Parameters Obtained from a Systematic Analysis of the Inorganic Crystal Structure Database. *Acta Crystallogr. Sect. B* **1985**, *41* (4), 244–247.

(148) He, G.; Huq, A.; Kan, W. H.; Manthiram, A. β-$NaVOPO_4$ Obtained by a Low-Temperature Synthesis Process: A New 3.3 V Cathode for Sodium-Ion Batteries. *Chem. Mater.* **2016**, *28* (5), 1503–1512.

(149) Henderson, G. S.; De Groot, F. M. F.; Moulton, B. J. A. X-Ray Absorption Near-Edge Structure (XANES) Spectroscopy. *Rev. Mineral. Geochemistry* **2014**, *78*, 75–138.

(150) Yano, J.; Yachandra, V. K. X-Ray Absorption Spectroscopy. *Photosynth Res* **2009**, *102*, 241–254.

(151) Gaur, A.; Shrivastava, B. D.; Nigam, H. L. X-Ray Absorption Fine Structure (XAFS) Spectroscopy – A Review. *Proc Indian Natn Sci Acad Spl. Issue, Part B* **2013**, *79* (4), 921–966.

(152) Goncharuk, N. A.; Kucera, J.; Smrcka, L. Pre-Edge XANES Structure of Mn in (Ga,Mn)As from First Principles. *Chem. Met. Alloy.* **2009**, *2*, 34–38.

(153) Bo, S.-H.; Veith, G. M.; Saccomanno, M. R.; Huang, H.; Burmistrova, P. V; Malingowski, A. C.; Sacci, R. L.; Kittilstved, K. R.; Grey, C. P.; Khalifah, P. G. Thin-Film and Bulk Investigations of $LiCoBO_3$ as a Li-Ion Battery Cathode. *ACS Appl. Mater. Interfaces* **2014**, *6* (14), 10840–10848.

(154) Glass, H. F. J.; Liu, Z.; Bayley, P. M.; Suard, E.; Bo, S.-H.; Khalifah, P. G.; Grey, C. P.; Dutton, S. E. $Mg_xMn_{2-x}B_2O_5$ Pyroborates ($2/3 \leq x \leq 4/3$): High Capacity and High Rate Cathodes for Li-Ion Batteries. *Chem. Mater.* **2017**, *29*, 3118–3125.

(155) Arun Kumar, R. Borate Crystals for Nonlinear Optical and Laser Applications: A Review. *J. Chem.* **2013**, *2013*, 1–7.

(156) Touboul, M.; Bétourné, E. $LiB_2O_3(OH).H_2O$ as Precursor of Lithium Boron Oxide $LiB_2O_{3.5}$: Synthesis and Dehydration Process. *Solid State Ionics* **1993**, *63–65* (C), 340–345.

(157) Weir, C. E.; Schroeder, R. a. Infrared Spectra of the Crystalline Inorganic Borates. *J. Res. Natl. Bur. Stand. Sect. A Phys. Chem.* **1964**, *68A* (5), 465.

(158) Guo, G. C.; Cheng, W. D.; Chen, J. T.; Huang, J. S.; Zhang, Q. E. Triclinic $Mg_2B_2O_5$. *Acta Crystallogr. Sect. C Cryst. Struct. Commun.* **1995**, *51* (3), 351–353.

(159) Ebelmen. Magneso-Borates. *Ann. Chim. Phys.* **1851**, *33*, 50.

(160) Mallard, E. Borates de Magnesie, de Manganes, de Cobalt et de Zinc. *Comptes Rendus Chim.* **1887**, *105*, 1263.

(161) Watanabe, T. $Mg_3(BO_3)_2$. *Min. Petro. Mitt* **1938**, *50*, 459.

(162) Sadanaga, R.; Nishimura, T.; Watanabe, T. The Structrue of Jimboite, $Mn_3(BO_3)_2$ and Relationship With The Structure Of Kotoite. *Mineral. J.* **1965**, *4* (5), 380–388.

(163) Watanabé, T.; Kato, A.; Matsumoto, T.; Ito, J. Limboite, $Mn_3(BO_3)_2$, a New Mineral

from the Kaso Mine, Tochigi Prefecture, Japan. *Proc. Japan Acad.* **1963**, *39* (3), 170.

(164) Berger, S. V.; Hägg, G.; Sillén, L. G. The Crystal Structure of the Isomorphous Orthoborates of Cobalt and Magnesium. *Acta Chemica Scandinavica*. 1949, pp 660–675.

(165) Kusachi, I.; Henmi, C.; Kobayashi, S. Takedaite, a New Mineral from Fuka, Okayama Prefecture, Japan. *Mineral. Mag.* **1995**, *59*, 549–552.

(166) Newnham, R. E.; Santoro, R. P.; Seal, P. F.; Stallings, G. R. Antiferromagnestism in $Mn_3B_2O_6$ $Co_3B_2O_6$ and $Ni_3B_2O_6$. *Phys. status solidi* **1966**, *K17*, 17–19.

(167) Voort, D. Van Der; Rijk, J. M. E. de; Doorn, R. van; Blasse, G. Luminescence of Rare-Earth Ions in $Ca_3(BO_3)_2$. *Mater. Chem. Phys.* **1992**, *31*, 333–339.

(168) Pardo, J.; Martinex-Ripoll, M.; Garcia-Blanco, S. The Crystal Structure of Nickel Orthoborate, $Ni_3(BO_3)_2$. *Acta Crystallogr.* **1974**, *37*, 37.

(169) Güler, H.; Tekin, B. Synthesis and Crystal Structure $CoNi_2(BO_3)_2$. *Inorg. Mater.* **2009**, *45* (5), 538–542.

(170) M.E. Fleet. Distortion Parameters for Coordination Polyhedra. *Mineral. Mag.* **1976**, *40*, 531–533.

(171) Cambaz, M. A.; Anji Reddy, M.; Vinayan, B. P.; Witte, R.; Pohl, A. H.; Mu, X.; Chakravadhanula, V. S. K.; Kübel, C.; Fichtner, M. Mechanical Milling Assisted Synthesis and Electrochemical Performance of High Capacity $LiFeBO_3$ for Lithium Batteries. *ACS Appl. Mater. Interfaces* **2015**, acsami.5b10747.

(172) Kim, J. C.; Seo, D. H.; Chen, H.; Ceder, G. The Effect of Antisite Disorder and Particle Size on Li Intercalation Kinetics in Monoclinic $LiMnBO_3$. *Adv. Energy Mater.* **2015**, *5* (8), 1401916–1401924.

(173) Yang, Y.; Su, X.; Pan, S.; Yang, Z. Effect of Cation Substitution on Structural Transition: Synthesis, Characterization and Theoretical Studies of $NaCa_4B_3O_9$, $NaCaBO_3$, NaSrBO and $Li_4CaB_2O_6$. *Phys. Chem. Chem. Phys.* **2015**, *17* (39), 26359–26368.

(174) Shannon, R. D. Revised Effective Ionic Radii and Systematic Studies of Interatomic Distances in Halides and Chalcogenides. *Acta Crystallogr. Sect. A* **1976**, *32* (5), 751–767.

(175) Du, L.; Tang, Y.; Hu, Y. Sidorenkite ($Na_3MnPO_4CO_3$), a New Intercalation Cathode Material for Na-Ion Batteries. **2012**, *24* (11), 19627.

(176) Takeuchi, Y. The Crystal Structure of Magnesium Pyroborate. *Acta Cryst.* **1952**, *5* (5), 574–581.

(177) Block, S.; Burley, G.; Perloff, A.; Mason, R. D. Refinement of the Crystal Structure of Triclinic Magnesium Pyroborate. *J. Res. Natl. Bur. Stand. (1934).* **1959**, *62* (3), 95–100.

(178) Norrestam, R; Nielsen, K; Sotofte, I; Thorup, N. Structural Investigation of Two Synthetic Oxyborates : The Mixed Magnesium-Manganese and the Pure Cobalt Ludwigites , $Mg_{1.93(2)}Mn_{1.07(2)}O_2BO_3$ and $CO_3O_2BO_3$. *Zeitschrift fuer Krist.* **1989**, *41*, 33–41.

(179) Guo, G. C.; Cheng, W. D.; Chen, J. T.; Zhuang, H. H.; Huang, J. S.; Zhang, Q. E. Monoclinic $Mg_2B_2O_5$. *Acta Crystallogr. Sect. C Cryst. Struct. Commun.* **1995**, *51* (12), 2469–2471.

(180) Kawano, T.; Morito, H.; Yamada, T.; Onuma, T.; Chichibu, S. F.; Yamane, H. Synthesis, Crystal Structure and Characterization of Iron Pyroborate ($Fe_2B_2O_5$) Single Crystals. *J. Solid State Chem.* **2009**, *182* (8), 2004–2009.

(181) Utzolino, A.; Karsten, B. Synthesis and Crystal Structure of Manganese Pyrobates $MnCo(B_2O_5)$ and $MnMg(B_2O_5)$. *Z.Naturforsch* **1996**, No. 51 b, 912–916.

(182) Bovin, J.; O'Keeffe, M.; O'Keefe, M. Electron Microscopy of Oxyborates. I. Defect Structures in the Minerals Pinakiolite, Ludwigite, Orthopinakiolite and Takeuchiite. *Acta Crystallogr. Sect. A* **1981**, No. 1972, 307–318.

(183) Hautier, G.; Jain, A.; Ong, S. P.; Kang, B.; Moore, C.; Doe, R.; Ceder, G. ChemInform Abstract: Phosphates as Lithium-Ion Battery Cathodes: An Evaluation Based on High-Throughput Ab Initio Calculations. *ChemInform* **2011**, *23*, 3495–3508.

(184) Ucyildiz, A.; Girgin, I. Controlled Synthesis, Characterization and Thermal Properties of $Mg_2B_2O_5$. *Cent. Eur. J. Chem.* **2010**, *8* (4), 758.

(185) Luo, W.; Li, X.; Dahn, J. R. Synthesis and Characterization of Mg Substituted $LiCoO_2$. *J. Electrochem. Soc.* **2010**, *157* (7), A782–A790.

(186) Arumangam, D.; Paruthimal, K.; Manisankar, P. Synthesis and Electrochemical Characterizations of Nano-Crystalline $LiFePO_4$ and Mg-Doped $LiFePO_4$ Cathode Materials for Rechargeable Lithium-Ion Batteries. *J Solid State Electrochem* **2009**, *13*, 301–307.

(187) Liu, C.; Neale, Z. G.; Cao, G. Understanding Electrochemical Potentials of Cathode

Materials in Rechargeable Batteries. *Mater. Today* **2016**, *19* (2), 109–123.

(188) Parzych, G.; Mikhailova, D.; Oswald, S.; Christine, T.; Ritschel, M.; Leonhardt, A. Improved Electrochemical Performance of $Cu_3B_2O_6$-Based Conversion Model Electrodes by Composite Formation with Different Carbon Additives. *J Electrochem Soc* **2014**, *161* (9), 1224–1230.

(189) Reimers, J. N.; Dahn, J. Electrochemical and In Situ X-Ray Diffraction Studies of Lithium Intercalation in Li_xCoO_2. *J. Electrochem. Soc.* **1992**, *139* (8), 2091–2097.

(190) Kim, J. C.; Li, X.; Moore, C. J.; Bo, S. H.; Khalifah, P. G.; Grey, C. P.; Ceder, G. Analysis of Charged State Stability for Monoclinic $LiMnBO_3$ Cathode. *Chem. Mater.* **2014**, *26* (14), 4200–4206.

(191) Chernova, N. A.; Nolis, G. M.; Omenya, F. O.; Zhou, H.; Li, Z.; Whittingham, M. S. What Can We Learn about Battery Materials from Their Magnetic Properties? *J. Mater. Chem.* **2011**, *21* (27), 9865–9875.

(192) Lee, J.; Seymour, I.; Pell, A.; Dutton, S.; Grey, C. A Systematic Study of ^{25}Mg NMR in Paramagnetic Transition Metal Oxides: Applications to Mg-Ion Battery Materials. *Phys. Chem. Chem. Phys.* **2017**, *19*, 613–625.

(193) Yamada, A.; Kudo, Y.; Liu, K.-Y. Reaction Mechanism of the Olivine-Type $Li_xMn_{0.6}Fe_{0.4}PO_4$ ($0 \leq x \leq 1$). *J. Electrochem. Soc.* **2001**, *148* (7), A747.

(194) Yamada, A.; Iwane, N.; Nishimura, S.; Koyama, Y.; Tanaka, I. Synthesis and Electrochemistry of Monoclinic $Li(Mn_xFe_{1-x})BO_3$: A Combined Experimental and Computational Study. *J. Mater. Chem.* **2011**, *21* (29), 10690.

(195) Luo, K.; Roberts, M. R.; Hao, R.; Guerrini, N.; Pickup, D. M.; Liu, Y.-S.; Edström, K.; Guo, J.; Chadwick, A. V; Duda, L. C.; Bruce, P. G. Charge-Compensation in 3d-Transition-Metal-Oxide Intercalation Cathodes through the Generation of Localized Electron Holes on Oxygen. *Nat. Chem.* **2016**, March, 1–17.

(196) Saubanere, M.; McCalla, E.; Tarascon, J.-M.; Doublet, M.-L. The Intriguing Question of Anionic Redox in High-Energy Density Cathodes for Li-Ion Batteries. *Energy Environ. Sci.* **2016**, *9* (3), 984–991.

(197) Britto, S.; Leskes, M.; Hua, X.; Hebert, C. A.; Shin, H. S.; Clarke, S.; Borkiewicz, O.; Chapman, K. W.; Seshadri, R.; Cho, J.; Grey, C. P. Multiple Redox Modes in the Reversible Lithiation of High-Capacity, Peierls-Distorted Vanadium Sulfide. *J. Am.*

Chem. Soc. **2015**, *137* (26), 8499–8508.

(198) Minakshi, M.; Singh, P.; Appadoo, D.; Martin, D. E. Synthesis and Characterization of Olivine $LiNiPO_4$ for Aqueous Rechargeable Battery. *Electrochim. Acta* **2011**, *56* (11), 4356–4360.

(199) NuLi, Y.; Yang, J.; Wang, J.; Li, Y. Electrochemical Intercalation of Mg^{2+} in Magnesium Manganese Silicate and Its Application as High-Energy Rechargeable Magnesium Battery Cathode. *J. Phys. Chem. C* **2009**, *113*, 12594–12597.

(200) Aurbach, D.; Yoo, H.; Shterenberg, I.; Gofer, Y. Non-Aqueous Mg Electrochemistry for Rechargeable Batteries. *The Electrochemical Society*. 224th ECS Meeting. **2013**.

(201) Lv, D.; Xu, T.; Saha, P.; Datta, M. K.; Gordin, M. L.; Manivannan, a.; Kumta, P. N.; Wang, D. A Scientific Study of Current Collectors for Mg Batteries in $Mg(AlCl_2EtBu)_2$/THF Electrolyte. *J. Electrochem. Soc.* **2012**, *160* (2), A351–A355.

(202) Virginia, W. Study of Mg Batteries: Electrolyte, Current Collectors and Their Compatibility. ECS Meeting Abstracts. **2011**, 6009.

(203) Qian, J.; Henderson, W. A.; Xu, W.; Bhattacharya, P.; Engelhard, M.; Borodin, O.; Zhang, J.-G. High Rate and Stable Cycling of Lithium Metal Anode. *Nat. Commun.* **2015**, *6*, 6362.

(204) Feng, Z.; Chen, X.; Qiao, L.; Lipson, A. L.; Fister, T. T.; Zeng, L.; Kim, C.; Yi, T.; Sa, N.; Proffit, D. L.; Burrell, A. K.; Cabana, J.; Ingram, B. J.; Biegalski, M. D.; Bedzyk, M. J.; Fenter, P. Phase-Controlled Electrochemical Activity of Epitaxial Mg-Spinel Thin Films. *ACS Appl. Mater. Interfaces* **2015**, *7* (51), 28438–28443.